Mechanistic Enzymology of Plasmodium Falciparum Sir2, Structural and Biochemical Studies on Nicotinamidases and the Structure and Function of Enzymes in the Purine Degradative Pathway from Klebsiella Pneumoniae

by Jarrod Bradley French

MECHANISTIC ENZYMOLOGY OF *PLASMODIUM FALCIPARUM* SIR2, STRUCTURAL AND BIOCHEMICAL STUDIES ON NICOTINAMIDASES AND THE STRUCTURE AND FUNCTION OF ENZYMES IN THE PURINE DEGRADATIVE PATHWAY FROM *KLEBSIELLA PNEUMONIAE*

A Dissertation

Presented to the Faculty of the Graduate School

of Cornell University

In Partial Fulfillment of the Requirements for the Degree of

Doctor of Philosophy

by

Jarrod Bradley French

August 2010

MECHANISTIC ENZYMOLOGY OF *PLASMODIUM FALCIPARUM* SIR2, STRUCTURAL AND BIOCHEMICAL STUDIES ON NICOTINAMIDASES AND THE STRUCTURE AND FUNCTION OF ENZYMES IN THE PURINE DEGRADATIVE PATHWAY FROM *KLEBSIELLA PNEUMONIAE*

Jarrod Bradley French, Ph. D.

Cornell University 2010

Enzymes are proteins that catalyze the chemistry of life. Biochemical and structural characterization of an enzyme and the interactions it makes with ligands facilitates our understanding of the processes that make life possible and enables us to devise methods to modulate the enzyme's activity for the benefit of human health. In this work, biochemical and structural studies are presented that aim to expand our understanding of several classes of enzymes. In the first part, analyses of two enzymes that have been shown to have a role in lifespan extension in some organisms are presented. The Sir2 enzyme from the malaria-causing parasite *Plasmodium falciparum* is shown to be an NAD^+-dependent deacetylase and an acetyllysine-dependent and acetyllysine-independent NAD^+ glycohydrolase. In addition, several examples of the Sir2 modulating enzyme, nicotinamidase, are characterized both structurally and biochemically. These works provided additional insights into and valuable tools for the study of Sir2-dependent lifespan extension. In the second part, several studies of enzymes that are responsible for purine degradation in the opportunistic human pathogen, *Klebsiella pneumoniae*, are presented. Using a combination of structural and biochemical methods, we characterize the enzymes responsible for ureidoglycine aminotransfer, 2-oxo-4-hydroxy-4-carboxy-5-

ureidoimidazoline (OHCU) decarboxylase and allantoin racemase. The examination of the aminotransferase from *K. pneumoniae* reveals a novel pathway from ureidoglycine to oxalurate and provides structural evidence for this enzyme's specificity for ureidoglycine. We characterize the first reported inhibitor of OHCU decarboxylase and demonstrate structurally and biochemically how this molecule causes a conformational change, disrupting the organization of the active site. The structures of allantoin racemase, the first for this class of enzyme, shed new light on ligand binding and the mechanism of the racemization reaction. Together, these studies elucidate a great deal of the unique complexity that is present in this important pathway.

BIOGRAPHICAL SKETCH

Jarrod was born in Niagara Falls, Ontario, Canada and is the second son of James and Jeanette French. He grew up immersed in the blissful chaos of a childhood amongst his many adoptive and foster siblings. After attending elementary and high school in Niagara Falls, he went on to enroll in Life Sciences at Queen's University in Kingston, Ontario. After one year Jarrod left Queen's to start up a business, but continued his studies part-time at the University of Waterloo, primarily studying mathematics and computer programming. Several years later, he decided to return to his studies full-time and enrolled at Brock University in St. Catharines, Ontario. Jarrod continued to run his business while carrying a full course load and acting as a teaching assistant in the Chemistry department at Brock.

It was during a second year organic chemistry laboratory course that he got his start in research. The lab demonstrator recruited Jarrod to work in the research laboratory of her husband, Herbert L. Holland. That summer, while carrying out research on biotransformations of sulfides in Professor Holland's laboratory, his eyes were opened and his future was decided. While at Brock, he also had the opportunity to work as a research assistant in an organometallic lab for Costa Metallinos and in a computational chemistry lab with Heather L. Gordon. Jarrod graduated with an Honours Bachelor of Science in Chemistry and Biology and completed his undergraduate thesis work in the laboratory of Heather L. Gordon. Professor Gordon had a tremendous positive influence on Jarrod's work and motivated him to continue his research career.

In 2004, Jarrod entered Cornell as part of the Tri-Institutional Training Program in Chemical Biology. As a part of that program he has had the great honour of discussing science with some of the top minds in the world, including several Nobel Laureates. While at Weill Medical College of Cornell University in New York City,

he carried out research on the mechanistic enzymology of Sirtuins and Nicotinamidase enzymes in the Laboratory of Anthony A. Sauve. After completing his Masters in Biomedical Sciences, Jarrod moved to Ithaca and joined the laboratory of Steven E. Ealick in the Chemistry Department at Cornell. In Professor Ealick's laboratory, he has had the opportunity to work on the structural biology of several different classes of proteins, including nicotinamidases, and enzymes involved in purine degradation and thiamin biosynthesis. Jarrod plans on carrying out post-doctoral work as the next step towards his goal of becoming the head of an internationally competitive research laboratory in an academic environment.

While science is his passion, Jarrod also enjoys many other diverse activities. Among many other pursuits he has coached, refereed and played rugby at a competitive level and has played the drums in several different rock bands. He has torn down and completely rebuilt a house and has completed a starburst pattern quilt by hand, put together from over five hundred individual pieces of fabric. Whether rebuilding the pump from an airless paint sprayer or resolving the complexities of an enzymatic reaction mechanism, he is most at home immersed in a challenging project. Jarrod continues to take on new challenges alongside his wife of four years and lifelong companion, Karen Gillie.

For Karen

ACKNOWLEDGMENTS

I would like to thank Steven Ealick for welcoming me into his lab and giving me the opportunity to learn and grow as a researcher and as a person. My work in this lab was considerably more productive and enjoyable in large part due to the hard work and support of Yang Zhang and Leslie Kinsland. All of the current and former members of the lab, including Andy, Katie, Tim, Debamita, Megan, Katherine, Mike, Mariya, Chris, Siyu and Shridhar greatly promoted by sanity and success. Cynthia Kinsland of the Protein Production facility was also an invaluable resource and respected colleague. I would also like to thank the other members of the Cornell community who provided me with equipment, services and advice, particularly the Protein Production facility, the Mass Spectrometry facility, Anthony Condo of the NMR facility, Hening Lin and members of his lab, Brian Crane and members of his lab, Jon Njardson and members of his lab, and Kenneth Gee for many hours of helpful discussion and debate. I would like to acknowledge the many helpful members of the beam lines at NE-CAT (Argonne National Labs) and MacCHESS for their assistance with data collection and processing as well as the Tri-Institutional Training Program in Chemical Biology for financial assistance. I would like to thank Anthony Sauve for offering me a position in his laboratory and providing me with a strong foundation upon which to build my research skills and knowledge. I would also like to thank Tadhg Begley for serving on my thesis committee and for providing helpful suggestions and advice for my research. My supportive family and friends were essential to my progress through graduate school, including my parents (Jim and Jeanette), Jamie, Becky, Jack and Beth, all of my grandparents and my many aunts, uncles and cousins and all of my friends throughout Canada, the U.S. and abroad. Finally, I must thank my wife, Karen, who not only supported and motivated me, but took care of me when I needed it and, most importantly, loved me unconditionally.

TABLE OF CONTENTS

LIST OF FIGURES

LIST OF TABLES

LIST OF SCHEMES

LIST OF ABBREVIATIONS

NAM	Nicotinamide
NA	Nicotinic Acid
Pnc1	Nicotinamidase
NAD^+	Nicotinamide adenine dinucleotide
Sp	*Streptococcus pneumoniae*
Pf	*Plasmodium falciparum*
Bb	*Borrellia burgdorferri*
Ce	*Caenorhabditis elegans*
GDH	Glutamate dehydrogenase
ADPR	Adenosine diphosphate ribose
AADPR	Acetyl adenosine diphosphate ribose
TFA	Trifluoroacetic acid
HPLC	High performance liquid chromatography
PEG	Polyethylene glycol
Kp	*Klebsiella pneumoniae*
HpxX	Hypoxanthine catabolic enzyme X
AAH	Allantoate amidohydrolase
Ec	*Escherichia coli*
PLP	Pyridoxal-5'-phosphate
PMP	Pyridoxamine phosphate
DABS	Dimethylaminoazobenzenesulfone
HIU	5-Hydroxyisourate
OHCU	2-Oxo-4-hydroxy-4-carboxy-5-ureidoimidazoline

NE-CAT	Northeastern Collaborative access team
CD	Circular Dichroism
OMPDC	Orotodine monophosphate decarboxylase
OPRT	Orotate phosphoribosyl transferase
PNP	Purine nucleoside phosphorylase
RMSD	Root mean square deviation

CHAPTER 1

INTRODUCTION TO SECTION I

Research on aging and age-related diseases has led to several exciting breakthroughs in the recent past. One such discovery is the relationship between calorie restriction and lifespan as modulated by the enzymes called Sirtuins (*1*). The Sirtuins are a class of protein modifying, NAD^+-dependent enzymes that are present in all three domains of life. These proteins consume NAD^+ in the process of deacetylation and/or ADP-ribosyltransfer of their target (*2, 3*). Sirtuins have been shown to play a role in several biological processes, including lifespan regulation, stress response, DNA silencing, transcriptional regulation and metabolic control (*4, 5*). While Sirtuins have highly-conserved active sites, distinct enzymes can catalyze deacetylation (*2, 3*) , ADP-ribosyltransfer to protein nucleophiles (*6-8*) or both.

The NAD^+ dependent deacetylase activity of Sirtuins can be modulated *in vivo* by controlling the level of the known Sir2 inhibitor, nicotinamide (*9-11*). The presence of this molecule is controlled, in part, by the enzyme nicotinamidase (PncA), which hydrolyzes nicotinamide into nicotinic acid. In this way, this enzyme has a direct impact on Sir2 activity and its concomitant roles in cellular pathways. In addition to its ability to modulate Sirtuins, PncA activity is required for activation of the front-line tuberculosis prodrug, pyrazinamide. PncA encoded by *M. tuberculosis* hydrolyzes pyrazinamide to form pyrazinoic acid, the active form of the drug (*12*). Despite the effectiveness of this drug, pyrazinamide resistant strains of *M. tuberculosis*, encoding changes in the PncA gene, have emerged (*13*). These genes have been mapped to catalytic residues as well as to residues predominantly structural in nature (*14, 15*).

The following three chapters contain studies on the Sir2 enzyme from *Plasmodium falciparum* (PfSir2), the organism responsible for the most prevalent

form of malaria, and the nicotinamidase enzyme from several different human pathogens including *Streptococcus pneumoniae* (SpNic), *Borrelia burgdorferi*, and *Plasmodium falciparum*. Chapter 2 details a functional and mechanistic analysis of PfSir2, revealing several novel features of this enzyme. In this report, we reveal that PfSir2 not only catalyzes NAD^+ dependent deacetylation, but can also function as an NAD^+ glycohydrolase in both an acetyllysine-dependent and -independent manner (Figure 1.1).

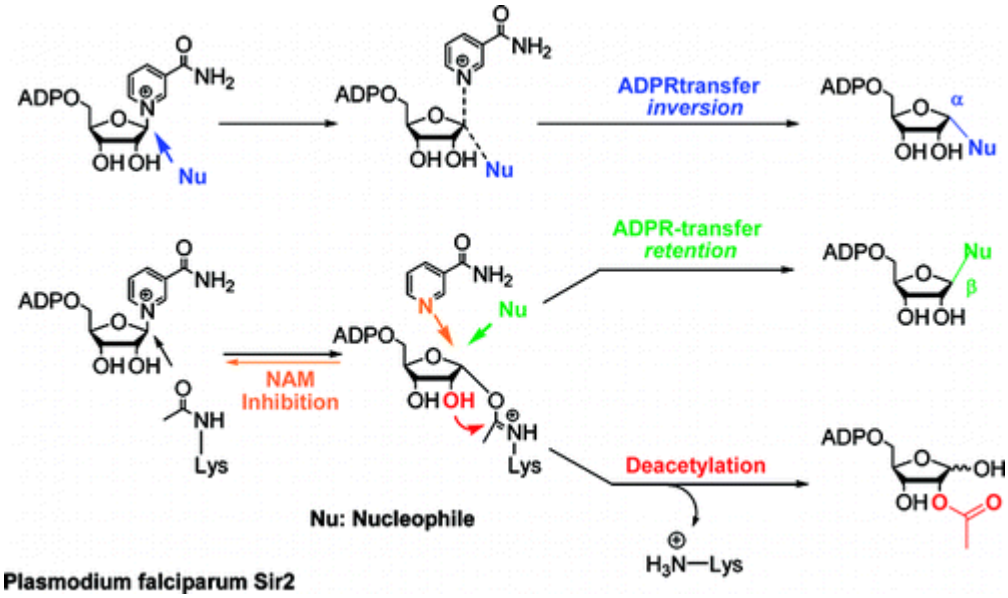

Figure 1.1 Chemistry catalyzed by *Plasmodium falciparum* Sir2.

The final two chapters of this section outline biochemical and structural studies of nicotinamidases, respectively. In Chapter 3, the steady-state kinetics and mechanism of PncA are examined through biochemical analyses of this enzyme from several organisms. In addition, several novel nicotinamidase inhibitors are identified and characterized in this work. Chapter 4 is an extension of the research detailed in Chapter 3 and deals with the structural characterization of SpNic by x-ray crystallography. In this study, structures of SpNic in complex with several ligands reveal important active site features and provide insights into the nicotinamidase

reaction mechanism. The trapped intermediates in the SpNic-ligand structures provide evidence for several putative intermediates along the reaction pathway (Figure 1.2).

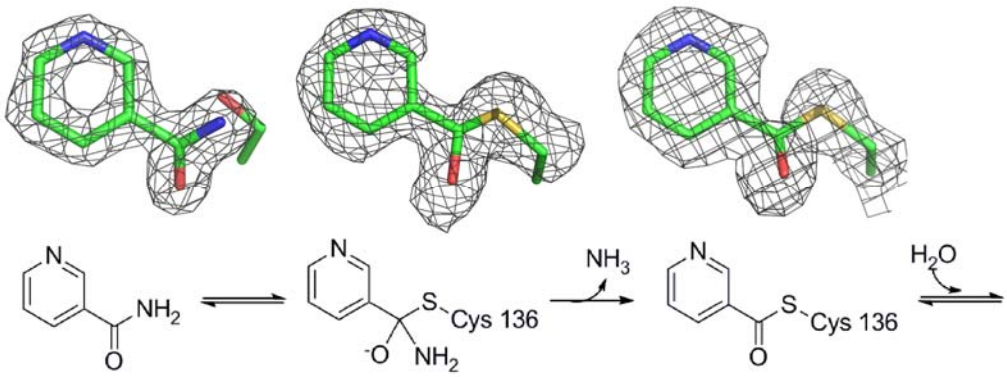

Figure 1.2. Structures of substrate and trapped intermediates in the *Streptococcus pneumoniae* nicotinamidase.

The studies covered in Chapters 2 through 4 identify novel functionality, characterize the steady-state kinetics, examine ligand binding and provide new insights into the reaction mechanism for two important enzymes, Sir2 and PncA. This work expands our understanding of these enzymes, provides the basis for further investigation of their function and provides additional tools to aid in the search for small molecule modulators of their activity.

REFERENCES

1. Bordone, L., and Guarente, L. (2005) Calorie restriction, SIRT1 and metabolism: understanding longevity, *Nat. Rev. Mol. Cell Biol. 6*, 298-305.
2. Sauve, A. A., *et al.* (2006) The biochemistry of sirtuins, *Annu Rev Biochem 75*, 435-465.
3. Blander, G., and Guarente, L. (2004) The Sir2 family of protein deacetylases, *Annu Rev Biochem 73*, 417-435.
4. Guarente, L. (2006) Sirtuins as potential targets for metabolic syndrome, *Nature 444*, 868-874.
5. Haigis, M. C., and Guarente, L. P. (2006) Mammalian sirtuins--emerging roles in physiology, aging, and calorie restriction, *Genes Dev 20*, 2913-2921.
6. Liszt, G., *et al.* (2005) Mouse Sir2 homolog SIRT6 is a nuclear ADP-ribosyltransferase, *J Biol Chem 280*, 21313-21320.
7. Haigis, M. C., *et al.* (2006) SIRT4 inhibits glutamate dehydrogenase and opposes the effects of calorie restriction in pancreatic beta cells, *Cell 126*, 941-954.
8. Garcia-Salcedo, J. A., *et al.* (2003) A chromosomal SIR2 homologue with both histone NAD-dependent ADP-ribosyltransferase and deacetylase activities is involved in DNA repair in Trypanosoma brucei, *Embo J 22*, 5851-5862.
9. van der Horst, A., *et al.* (2007) The *Caenorhabditis elegans* nicotinamidase PNC-1 enhances survival, *Mech. Ageing Dev. 128*, 346-349.
10. Gallo, C. M., *et al.* (2004) Nicotinamide clearence by Pnc1 directly regulates Sir2-mediated silencing and longevity, *Mol. Cell. Biol. 24*, 1301-1312.
11. Anderson, R. M., *et al.* (2003) Nicotinamide and PNC1 govern lifespan extension by calorie restriction in *Saccharomyces cerevisiae*, *Nature 423*, 181-185.

12. Singh, P., *et al.* (2006) The paradox of pyrazinamide: an update on the molecular mechanisms of pyrazinamide resistance in Mycobacteria, *J. Commun. Dis. 38*, 288-298.
13. Konno, K. F., *et al.* (1967) Pyrazinamide susceptibility and amidase activity of tubercle bacilli, *Am. Rev. Respir. Dis. 95*, 461-469.
14. Scorpio, A., *et al.* (1997) Characterization of *pncA* Mutations in Pyrazinamide-Resistant *Mycobacterium tuberculosis*, *Antimicrob. Agents Chemother. 41*, 540-543.
15. Zhang, H., *et al.* (2008) Characterization of *Mycobacterium tuberculosis* nicotinamidase/pyrazinamidase, *FEBS J. 275*, 753-762.

CHAPTER 2

PLASMODIUM FALCIPARUM SIR2 IS AN NAD^+-DEPENDENT DEACETYLASE AND AN ACETYLLYSINE-DEPENDENT AND ACETYLLYSINE-INDEPENDENT NAD^+ GLYCOHYDROLASE

2.1 Abstract

Sirtuins are NAD^+-dependent enzymes that deacetylate a variety of cellular proteins and in some cases catalyze protein ADP-ribosyltransfer. The catalytic mechanism of deacetylation is proposed to involve an ADPR-peptidylimidate, whereas the mechanism of ADP-ribosyltransfer to proteins is undetermined. Herein we characterize a *Plasmodium falciparum* sirtuin that catalyzes deacetylation of histone peptide sequences. Interestingly, the enzyme can also hydrolyze NAD^+. Two mechanisms of hydrolysis were identified and characterized. One is independent of acetyllysine substrate and produces α-stereochemistry as established by reaction of methanol which forms α-1-*O*-methyl-ADPR. This reaction is insensitive to nicotinamide inhibition. The second solvolytic mechanism is dependent on acetylated peptide and is proposed to involve the imidate to generate β-stereochemistry. Stereochemistry was established by isolation of β-1-*O*-methyl-ADPR when methanol was added as a co-solvent. This solvolytic reaction was inhibited by nicotinamide, suggesting that nicotinamide and solvent compete for the imidate. These findings establish new reactions of wildtype sirtuins and suggest possible mechanisms for ADP-ribosylation to proteins. These findings also illustrate the potential utility of nicotinamide as a probe for mechanisms of sirtuin catalyzed ADP-ribosyltransfer.

2.2 Introduction

The sirtuins are protein-modifying enzymes broadly found in all phyla of life that utilize NAD^+ as a substrate to effect protein modification via deacetylation and/or ADP-ribosyltransfer (*1, 2*). Sirtuins have been shown to participate in a variety of

biological processes, including lifespan regulation, stress response, DNA silencing, transcriptional regulation and metabolic control (*3, 4*). Sirtuins have phylogenetically highly-conserved active sites, although distinct enzymes catalyze deacetylation (*1, 2*) , ADP-ribosyltransfer to protein nucleophiles (*5-7*) or both (*7*). The mechanism for the deacetylation reaction catalyzed by sirtuins is consistent with an imidate mechanism (*8*) and is supported by a wealth of data (*9-16*). The protein ADP-ribosyltransfer mechanisms are undetermined and products of ADPR-transfer have been largely uncharacterized (*5, 6, 17*). Sauve and Schramm argued that sirtuin chemistry could be understood by recognizing that ADP-ribosyltransfer is central to their catalytic function (*9*). This mechanistic proposal suggests that sirtuin catalysis of protein deacetylation and ADP-ribosyltransfers could be the consequence of the versatile reactivity of a sirtuin-poised NAD^+ electrophile activated to react directly with different types of nucleophiles (*9*). It has also been suggested that ADPribosyl-transfer can derive from the reactivity of an intermediate complex (*9, 17*). We herein provide evidence for the co-existence of these three different reactive mechanisms (deacetylation, direct-ADPR transfer and intermediate-dependent ADPR-transfer) occurring on the active site of a sirtuin derived from *Plasmodium falciparum*, called Pf-Sir2.

Our preliminary interest in Pf-Sir2 derived from a proposed role for this enzyme in the persistence of malarial infection (300-500 million cases per year worldwide, 1-2 million deaths per year), in which *Plasmodium falciparum* is the most responsible pathogen (*18*). Malaria is difficult to treat, since it typically persists in the host far beyond initial infection or treatment. Persistence of infection is linked to immune avoidance strategies employed by the parasite. The parasite expresses a virulence factor called *P. falciparum* erythrocyte membrane protein 1 (PfEMP1) on infected erythrocytes. Because it is surface-exposed it could enable clearance of the

parasite via an adaptive response of the immune system. However, the parasite swaps the epitope-encoding surface proteins periodically, thereby evading host immunity. Specifically, *P falciparum* has a repertoire of approximately 60 *var* genes that encode functionally similar but epitopically variant PfEMP1 proteins of which only a single gene is typically expressed in the host at a time, with the remainder of the genes kept silent by chromatin silencing mechanisms (*19*). This switching strategy of the parasite is termed *antigenic variation* (*19*). Interestingly, deletion of Pf-Sir2 dysregulates silencing of a major subset of *var* genes (*20, 21*). It has been proposed that the role of Pf-Sir2 in silencing of *var* genes is through the enzymatic activity of histone deacetylation, which can promote or maintain heterochromatin (*20, 21*). In fact, the prototype sirtuin, yeast Sir2 (silencing information regulator 2), is named for its gene silencing functions and it requires intact NAD^+ dependent deacetylase activity for these functions (*2*).

To biochemically characterize the reactivity of Pf-Sir2 we cloned, expressed and purified the enzyme. We confirm it to be a deacetylase of histone H3 and histone H4 and other peptide sequences, as predicted. Unexpectedly, we determined that the enzyme has several additional activities, including the capacity to catalyze NAD^+ solvolysis. The solvolysis chemistry features separate stereochemical modalities, dependent and independent of acetylated substrates. The stereochemically distinct solvolytic reactions also exhibit different behaviors with respect to the universal sirtuin inhibitor nicotinamide. Pf-Sir2 provides an instructive and unusual example of several competing reactivities, including deacetylation and two types of ADP-ribosyltransfer, occurring in one sirtuin active site. The respective solvolysis chemistries are first examples of their kind attributed to a wildtype sirtuin. In addition, these reactions illustrate possible mechanisms of protein ADP-ribosyltransfer catalyzed by the sirtuin family.

2.3 Experimental Procedures.

Reagents and Instrumentation. Synthetic peptides p300: ERSTEL(K-Ac)TEI(K-Ac)EEEDQPSTS, H3: ARTKQTAR(K-Ac)STGG(K-Ac)APRKQLAS and H4: SGRG(K-Ac)GG(K-Ac)GLG(K-Ac)GGA(K-Ac)RHR were synthesized and characterized by the Proteomics Resource Center at Rockefeller University. They were purified by HPLC before use. All other reagents were purchased from Aldrich or VWR and were of the highest purity commercially available. HPLC analyses were performed on a Hitachi elite LaChrom system equipped with Diode array detector using C_{18} reverse phase columns. Radiolabeled samples were counted in a Beckman Coulter LS 6500 multi-purpose scintillation counter.

Plasmid Construction and Protein Expression. The gene encoding Sir2 from *Plasmodium falciparum* (PF13_0152) was cloned from *Plasmodium falciparum* DNA using PCR provide by Kirk Deitsch of Weill Medical College of Cornell University. The coding sequence was initially cloned into a pGEM vector and subsequently recloned into Pet28a (Novagen) to obtain protein expressed with an N-terminal poly-histidine tag. The insert was verified by nucleotide sequencing and checked against the published sequence. PetPFSIR2 vector was transfected into Codon-plus® RIPL cells (Stratagene) and protein synthesis was induced by addition of 0.5 mM isopropyl-β-D-thiogalactopyranoside (IPTG) at OD_{600} = 0.25. Cells were grown for 6 hours at 37 ^{o}C, pelleted and lysed by freeze-thaw cycles. The protein was purified by Ni-column affinity chromatography, dialyzed overnight in 20 mM potassium phosphate buffer pH 7.0, aliquoted in 20% glycerol and 2 mM DTT and flash-frozen and stored at –80 ^{o}C. Enzyme concentrations were determined by the method of Bradford (*22*). The protein molecular weight was determined by MALDI-TOF (Rockefeller Proteomics Resource) and the protein was 95% pure as determined by SDS-polyacrylamide gel

electrophoresis. The presence of a catalytically significant histidine residue (position 162 in our construct) was confirmed by LC-MS/MS analysis of a tryptic digest of the purified enzyme performed at Rockefeller University proteomics facility.

Deacetylation assays. Deacetylation reactions were typically performed in 150 mM phosphate buffer pH 7.3 in reaction volumes of 50 µL. A typical reaction contained 400 µM. NAD^+, 3 µM Pf-Sir2 enzyme and 0-500 µM acetylated peptide (H3, H4 or p300). Reactions were initiated by addition of enzyme, incubated for one hour at 30^o C and then quenched by addition of trifluoroacetic acid. The reactions were placed on ice for one hour after quench to precipitate protein, centrifuged at 13000 *g* for 2 min to pellet insolubles then analyzed by HPLC. Peptides were separated using a Waters Xterra RP-18 column running a gradient of 10% to 40 % acetonitrile in 0.1% TFA and chromatograms collected by multi-wavelength diode array with chromatograms analyzed at wavelength of 215 nm. Reactions were quantified by integrating area of peaks corresponding to deacetylated peptides (identities confirmed by mass spectrometry, Proteomics Resource Center, Rockefeller University). Rates were plotted versus peptide concentration and best fit of points to the Michealis-Menton equation was performed by Kaleidagraph®. HPLC observation of nicotinamide and 2′- and 3′-O-AADPR products was accomplished by performing reaction, quench and injection as above, with HPLC elution with 20 mM ammonium acetate pH 7.5. Chromatograms were analyzed at wavelength of 260 nm. To determine nicotinamide inhibition, reactions were performed similarly but nicotinamide at concentrations ranging from 0-350 µM was also added to reaction mixtures. Rates were plotted and points were fit to the equation $v = v_0 - v_{inh}$ ([I]/(K_i +[I])) where v is the rate observed for a given concentration of nicotinamide, v_0 is the uninhibited rate, v_{inh} is the maximal inhibition, K_i is the apparent inhibition constant and [I] is the concentration of nicotinamide. This equation to fit nicotinamide inhibition of sirtuins has been used previously (*11*).

^{14}C-Nicotinamide Base Exchange Assay. Reactions containing 400 μM NAD^+, 500 μM H3 or 200 μM p300 peptide, and 150 mM phosphate buffer, pH 7.5, with varying concentrations of [carbonyl-^{14}C]nicotinamide (American Radiolabeled Chemicals Inc.) were initiated by addition of Pf-Sir2 enzyme to a concentration of 0.5 μM. Reactions were incubated for one hour at 30 ^{o}C and quenched by addition of trifluoroacetic acid to pH 2. After centrifugation to remove precipitates, reactions were injected on HPLC (0.5% TFA eluant) to separate nicotinamide and NAD^+. Eluant containing nicotinamide and NAD^+ was collected and radioactivity determined by scintillation counting. Reactions were run to no more than 10% of the calculated equilibrium position for nicotinamide exchange. Rates were determined as cpm/s incorporated into NAD^+, and then converted to a turnover rate (s^{-1}) by adjustment for specific radioactivity of nicotinamide and enzyme concentration. Rates were plotted versus nicotinamide concentration and best fit of plotted data to the Michaelis-Menton curve was performed using Kaleidagraph®. Incubations of less than and greater than 1 hour confirmed that product formation versus time was linear during the course of the assay.

Thionicotinamide Base-Exchange Assay. Reactions containing 400 μM NAD^+, 400 μM peptide, and 150 mM phosphate buffer, pH 7.3, were performed in the presence of concentrations 0 to 2000 μM thionicotinamide. Reactions were initiated with addition of Pf-Sir2 enzyme to a final concentration of 1 μM after one hour incubation at 30^{o}C reactions were quenched by addition of trifluoroacetic acid to pH 2. ThioNAD formation was quantified by HPLC on a Waters SymmetryShield RP_8 column running 0.1% TFA with a gradient to 25% MeOH starting at 15 minutes and by comparison to an authentic standard for quantitation and identification, prepared via base exchange of thionicotinamide into NAD^+ catalyzed by CD38 (*23*). Product formation rates were

plotted versus thionicotinamide concentration and points fit to the Michaelis-Menton equation to obtain the Michealis parameters K_m and k_{cat}.

HPLC Assay Measuring Hydrolysis of NAD^+. Reaction mixtures containing 400 μM NAD^+, and one of p300, H3 or H4 peptides (of varying concentrations 0 - 800 μM) in 150 mM phosphate buffer, pH 7.3, were initiated with the addition of Pf-Sir2 (typically 2-4 μM final concentration). Production of ADPR was quantitated by HPLC using a 20 mM ammonium acetate isocratic system on a Waters C-18 column. Comparison to SIRT1 reactions reacted under similar conditions established minimal contribution to apparent hydrolysis from breakdown of AADPR. As stated in the text, Pf-Sir2 added to SIRT1 reactions also did not increase formation of ADPR from AADPR. Moreover, in almost all cases ADPR formation rate exceeded the deacetylation rate that forms AADPR by at least 5 fold. Rate of formation of ADPR was plotted against peptide concentration and fit to a modified curve $k_{obs} = k_{cat(no\ peptide)} + k_{cat(peptide)}[S]/(K_m + [S])$ where k_{obs} is the observed rate, $k_{cat(no\ peptide)}$ is the observed rate of hydrolysis in the absence of peptide, $k_{cat(peptide)}$ is the component of the observed rate of reaction that is dependent on peptide, K_m is the Michaelis constant for peptide and [S] is the peptide concentration.

To analyze nicotinamide effects on reactions (in the presence or absence of added H3 peptide), varying amounts of nicotinamide, 0-1000 μM, were added to reaction mixtures and reactions were assayed as above quantifying rate by observed ADPR. Inhibition curves were of the form $v = v_0 - v_{inh}([I]/(K_i + [I]))$ where v is the rate observed for a given concentration of nicotinamide, v_0 is the uninhibited rate, v_{inh} is the maximal inhibition, K_i is the apparent inhibition constant and [I] is the concentration of nicotinamide.

DEAE-Sephadex Ion-Exchange Assay for Measurement of ADPR formation. Reactions were typically performed in 100 mM phosphate and contained 400 μM [2-, 8-

^{3}H]NAD^{+} or [8-^{14}C]NAD^{+} (synthesized by coupling of NMN and [2-, 8-^{3}H]ATP or [8-^{14}C]-ATP (American Radiolabeled Chemicals Inc.) as previously described (*24*)) with or without peptide. Reactions were initiated by addition of Pf-Sir2 and allowed to incubate for one hour at 37^{o}C. After quenching with TFA, the reactions were centrifuged to remove precipitate and loaded onto columns containing pre-equilibrated DEAE-Sephadex (equilibrated with 5 mM ammonium acetate pH 7). The reaction mixture was then eluted with eight 2 mL fractions of 10 mM ammonium acetate pH 7 and five 2 mL fractions of 100 mM ammonium acetate pH 7. The radioactivity contained in the eluted samples was then quantified by scintillation counter. Radiolabeled NAD^{+} eluted in the 10 mM washes, while ADPR eluted in the 100 mM fractions. Reactions performed with p300 were corrected for AADPR production by HPLC assay of the eluant of 100 mM ammonium acetate (which contained ADPR, major species and AADPR, minor species) and by independent HPLC determination of deacetylation rate of the peptide under identical reaction conditions. Reactions were corrected with appropriate negative controls.

HPLC Assay for Methanolyses of NAD^{+}catalyzed by Pf-Sir2. A β-1-methyl-*O*-ADPR standard was synthesized using the known methanolysis reaction catalyzed by CD-38 (*25*). This enzyme was incubated with NAD^{+} in 150 mM phosphate buffer and 30% MeOH, and monitored by HPLC. A single new peak was formed isolated by HPLC, NMR was taken and confirmed to be β-1-*O*-methyl-ADPR. Mass spectrum by MALDI-TOF confirmed the correct mass (m/z = 574, positive ion). The corresponding α-1-*O*-methyl-ADPR standard was formed by heating NAD^{+} in 30 % methanol in 50 mM phosphate pH 7.5 to 80 ^{o}C. This procedure is known to generate both methanolysis stereochemistries. The methanolysis product α-1-*O*-methyl-ADPR was isolated and identified by NMR and by MALDI-MS (m/z = 574, positive ion).

Methanolysis reactions catalyzed by Pf-Sir2 were carried out in the presence of 400 μM NAD^+, 20% by volume methanol (5.1 M) unless noted otherwise, and varying H3 concentrations in 150 mM phosphate buffer, pH 8.5. The reactions were initiated by addition of Pf-Sir2 (final: 8 μM) and then incubated for one hour at 30 ^oC. After quenching with TFA the solutions were centrifuged to remove precipitate and immediately analyzed by HPLC. Standards of β-1-*O*-methyl-ADPR and α-1-*O*-methyl-ADPR were run on the same day and spiked into reaction mixtures to confirm peak identity. To confirm identity of these compounds in Pf-Sir2 reaction mixtures, eluant of peaks were collected, lyophilized and analyzed by MALDI-TOF (positive ion mode, CHCA matrix).

2.4 Results.

Pf-Sir2 has NAD^+ Dependent Protein Deacetylase Activity. Pf-Sir2 has been found to localize to heterochromatin in *P. falciparum* and is proposed to contribute to *var* gene silencing via deacetylation of histones (*20, 21*). We examined the ability of recombinant Pf-Sir2 to catalyze NAD^+ dependent protein deacetylase activity by using peptides homologous to N-terminal histone sequences of H3 and H4 (see experimental for sequences). Deacetylation activity of Pf-Sir2 was compared with SIRT1 as a positive control. Peptide substrates were reacted with NAD^+ in the presence of enzyme and peptide deacetylation products were determined by HPLC. SIRT1 and Pf-Sir2 reactions generated similar chromatograms for H4 and H3 reactions (Figure 2.1A and 2.1B). It is known that SIRT1 predominantly deacetylates at K16 of tetra-acetylated H4, identical to the sequence used in this study (*26*). Based on retention time, this same residue is deacetylated by Pf-Sir2 (Figure 2.1B) and was confirmed by MS analysis (performed by Rockefeller Proteomics Resource). Deacetylation of a di-acetylated H3 peptide by Pf-Sir2 and SIRT1 produced similar HPLC chromatograms as well (Figure 2.1A). SIRT1 deacetylates positions AcK9 and AcK14 of the N-

terminal H3 sequence (*26*). The single peak was collected in the SIRT1 and Pf-Sir2 HPLC elutions and analyzed by MS (performed by Rockefeller Proteomics Resource). These results confirmed deacetylation of K9 and K14 for both reactions. It was determined that deacetylation depends on the presence of NAD^+, and the K_m for NAD^+ in H3 deacetylation was determined to be 120 μM. These results corroborate a recent study showing that Pf-Sir2 is a histone deacetylase for N-terminal tails of whole histones H3 and H4 (*27*), although Michaelis parameters were not determined and only Westerns were used to identify deacetylated products (*27*).

Interestingly, a human di-acetylated p300 sequence (ERSTEL(K-Ac)TEI(K-Ac)EEEDQPSTS corresponding to amino acid positions 1034-1053 of the full p300 sequence) was determined to be a superior substrate of Pf-Sir2, and the deacetylated peptide product is again similar to that formed by SIRT1 as shown by HPLC (Figure 2.1C). The preferred site of deacetylation for this sequence by SIRT1 has been characterized (*28*) and corresponds to the AcLys in the peptide corresponding to amino acid position 1040 of the full p300 sequence (see above). Acetylation modifications in this sequence have been demonstrated to affect p300 functions as a transcriptional co-regulator (*28*).

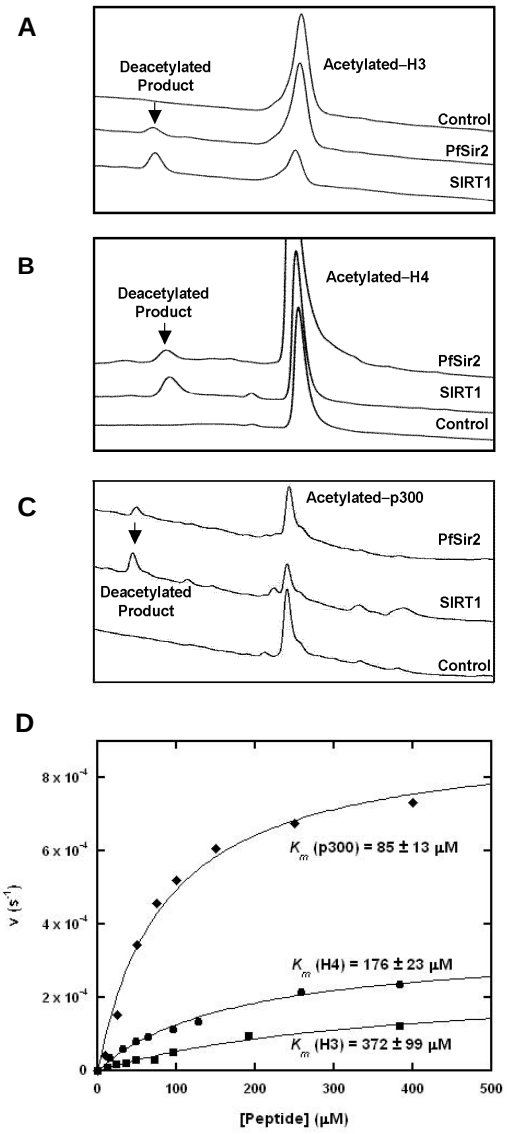

Figure 2.1. Deacetylation of peptide substrates catalyzed by Pf-Sir2. (A) HPLC chromatograms showing the deacetylation of acetylated-H3 by Pf-Sir2 and SirT1 over time. (B) Deacetylation of H4 .(C) Deacetylation of p300. (D)Saturation curves for steady-state deacetylation rates for the three different peptides.

Deacetylation reactions were further studied by HPLC in which peptide concentrations were varied in the presence of enzyme and 400 μM NAD^+. Michaelis-Menton curves fit to determined deacetylation rates versus peptide concentrations are

shown in Figure 2.1D. K_m and k_{cat} values are listed for the different peptide substrates in Table 2.1.

Table 2.1. Parameters for Deacetylation, Exchange, Hydrolysis and Inhibition Reactions for Pf-Sir2 with Various Substrates.

	Deacetylation			**Exchange**[b]		**Hydrolysis**	
	k_{cat} 10^{-4} s^{-1}	K_m μM	$K_{i(NAM)}$[a] μM	k_{cat} 10^{-2} s^{-1}	K_m μM	k_{cat} 10^{-3} s^{-1}	K_m μM
H3[c]	2.5 ± 0.4	372 ± 99	35 ± 2	2.5 ± 0.1	61 ± 5	1.9 ± 0.1	228 ± 28
H4[c]	3.5 ± 0.2	176 ± 23	NM	NM	NM	2.2 ± 0.1	137 ± 29
p300[c]	9.2 ± 0.5	85 ± 13	91 ± 4	6.4 ± 0.2	80 ± 7	3.4 ± 0.2	33 ± 15
NAD^+[d]	NA	NA	NA	ND	NA	1.2 ± 0.2	NM

Conditions for measurements are described in experimental section. All reactions conducted in the presence of 400 μM NAD^+. [a] $K_{i(NAM)}$is the inhibition constant for nicotinamide inhibition of deacetylation. The values are determined by varying nicotinamide (NAM) concentrations, measuring deacetylation by HPLC and plotting rate of deacetylation versus NAM concentration. Fits of points to the inhibition curve described in experimental determines the value of the parameter. [b]The values are determined from the saturation curve for ^{14}C-nicotinamide base-exchange. [c] Peptide primary sequence and acetylation are described in the materials and methods section. NM: Not Measured. ND: Not detected, highest concentration: 5 mM ^{14}C-NAM. [d] No acetylated peptide is added to these reactions. NA: Not applicable.

Maximal rates for deacetylation of H3 and H4 sequences were similar and remarkably slow as indicated by maximal turnover rates of 2.5×10^{-4} s^{-1} and 3.5×10^{-4} s^{-1} respectively (Table 2.1). The p300 peptide reacted at least 2.5 times faster than either H3 or H4 (9×10^{-4} s^{-1}) with a K_m value of 85 μM, 2 times smaller than H4 (176 μM) and 4 times smaller than the K_m of H3 (372 μM). Deacetylation reactions of H3,

H4 and p300 substrates were determined to form 2′- and 3′- *O*-acetyl-ADP-ribose (AADPR), known co-products of sirtuin deacetylation reactions (*8*).

Pf-Sir2 Catalyzes Nicotinamide Exchange and Inhibits Deacetylation. Sirtuin deacetylation reactions are inhibited by the general sirtuin inhibitor nicotinamide, which is a product of sirtuin deacetylation chemistry (*11, 12, 29, 30*). To interrogate inhibition of H3 and p300 deacetylation as a function of nicotinamide concentration, an HPLC assay was employed (see experimental for details). As shown in Figure 2.2A and 2.2B deacetylation was almost completely inhibited by nicotinamide added to reaction mixtures with K_i values for nicotinamide of 35 and 91 μM for H3 and p300 respectively. These results indicate that K_i may be dependent upon the substrate peptide sequence. The inhibition constants are potent and suggest that nicotinamide is likely to exert effects on deacetylation activity of Pf-Sir2 enzymes under physiologic conditions. These nicotinamide inhibition constants are similar to those reported for inhibitions of deacetylation reactions catalyzed by yeast, human and archaeal sirtuins (*11, 12*).

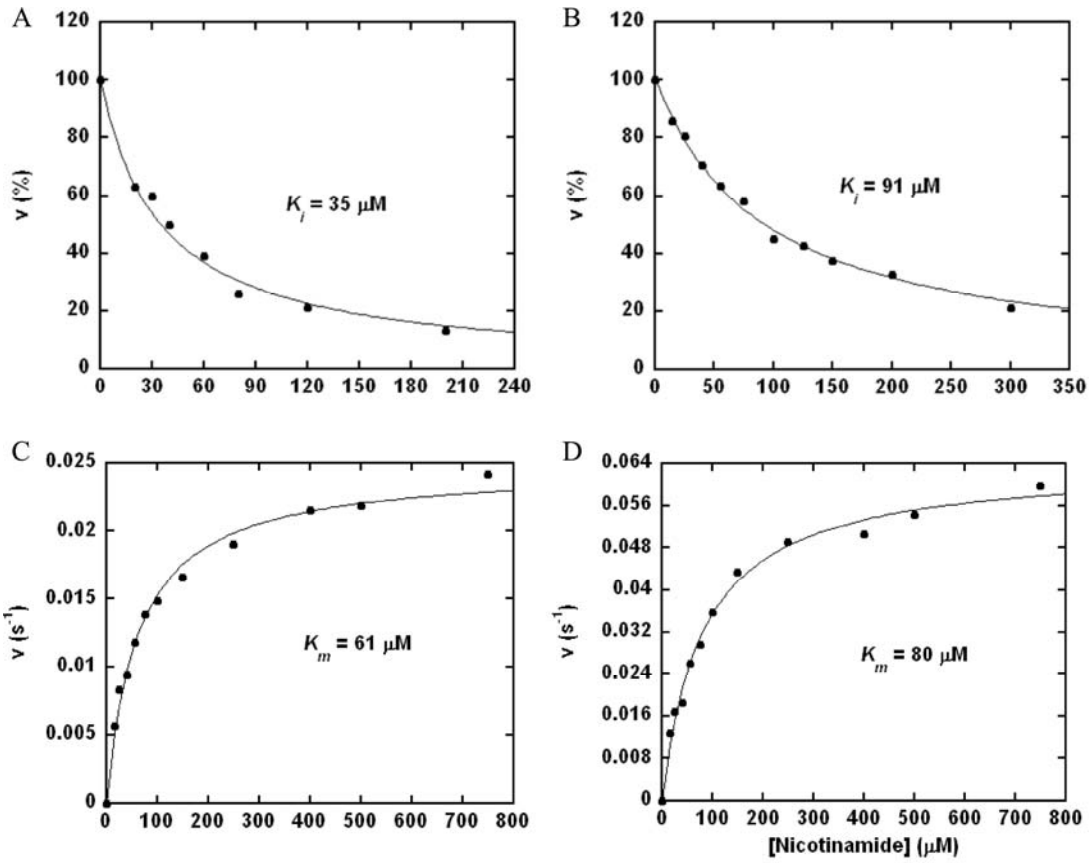

Figure 2.2. Nicotinamide Base-Exchange Catalyzed by Pf-Sir2. (A) and (B): Inhibition of the deacetylation reaction by increasing concentrations of nicotinamide. (A) 500 μM H3 peptide, 250 μM NAD^+ and 150 mM phosphate buffer, pH 7.3, quantified by integration of deacetylated product peaks in the HPLC chromatograms. (B) 200 μM p300 peptide, 400 μM NAD^+ and 150 mM phosphate buffer, pH 7.5, and quantified by integration of deacetylated product peaks in the HPLC chromatograms. (C) and (D): Kinetics of the base-exchange chemistry catalyzed by Pf-Sir2 as measured by exchange of [carbonyl-^{14}C]-nicotinamide into unlabeled NAD^+. (C) 200 μM H3 peptide, 400 μM NAD^+ and 150 mM phosphate buffer, pH 7.5. (D) 200 μM p300 peptide, 400 μM NAD^+ and 150 mM phosphate buffer, pH 7.5.

Nicotinamide inhibition of sirtuin catalyzed deacetylation is linked to a sirtuin reaction which catalyzes nicotinamide exchange into NAD^+ called "base-exchange". The base-exchange reaction is thought to compete with the deacetylation reaction for a common reaction intermediate, called the ADPR-peptidyl-imidate (*11, 12*). Depletion of the imidate by base-exchange inhibits the deacetylation reaction (Scheme 2.1).

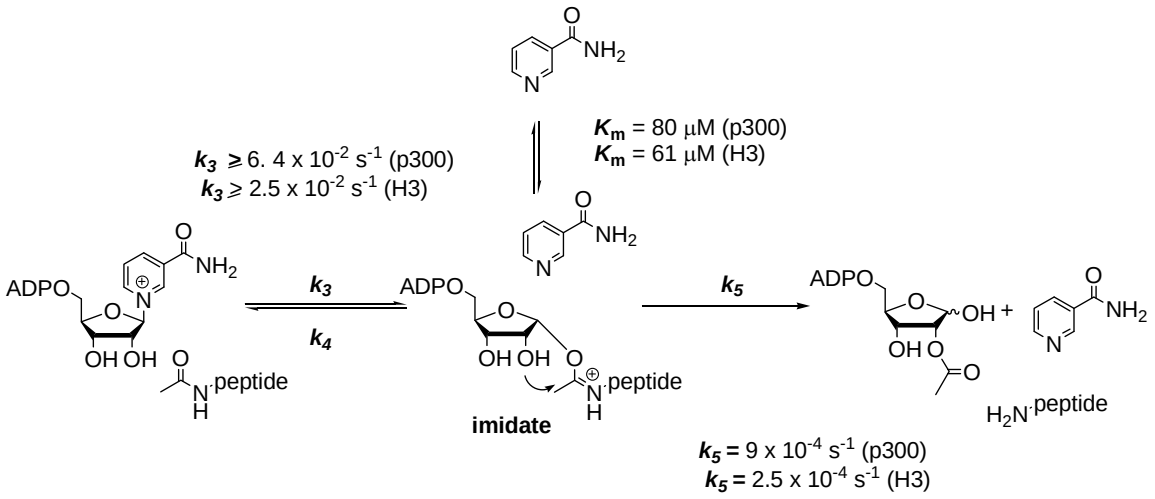

Scheme 2.1. Reactions of acetylysine peptides in base exchange and deacetylation pathways. Rate constants for deacetylation and base exchange are shown for the respective steps.

Correlation of K_m and K_i is expected since base-exchange and inhibition of deacetylation emanate from the same kinetic process (*11*). We measured rates of base-exchange catalyzed by Pf-Sir2 using [carbonyl-^{14}C]nicotinamide as the exchange base, as described previously (*11*). Values for rate versus nicotinamide were plotted and the points fit to the Michaelis-Menten equation (Figure 2.2C and 2.2D). As expected, Pf-Sir2 catalyzed base-exchange with H3 and p300 as substrates and responded saturably with increasing nicotinamide concentrations. Curve fits determined K_m values of 61 μM (H3) and 91 μM (p300). Corresponding k_{cat} values were 0.025 s^{-1} (H3) and 0.064 s^{-1} (p300). These results establish that the kinetic parameter K_m corresponds well to the corresponding K_i values as predicted (*11*). The steady-state rate of base exchange exceeds the corresponding deacetylation rate by 70 fold and 100 fold for p300 and H3 respectively. If deacetylation and base exchange share the imidate as a common intermediate, then the slow deacetylation rate is caused by a rate-limiting step downstream of the imidate, possibly attack of the 2'-OH on the imidate (*11*). The reactivity of the NAD^+ and peptide substrate to form the imidate (Scheme 2.1) must be at least as fast as the steady state base-exchange rate.

To further probe for substrate specificity in the base-exchange reaction, we employed thionicotinamide as the base-exchange substrate. Thionicotinamide has previously been shown to be competent as a base-exchange substrate of the sirtuin HST2 (*12*). Thionicotinamide is proposed to form thioNAD$^+$ upon reaction with an imidate or an ADPR-intermediate complex (*12*). HPLC chromatograms show that thioNAD$^+$ formation is catalyzed by Pf-Sir2 in the presence of thionicotinamide (Figure 2.3A).

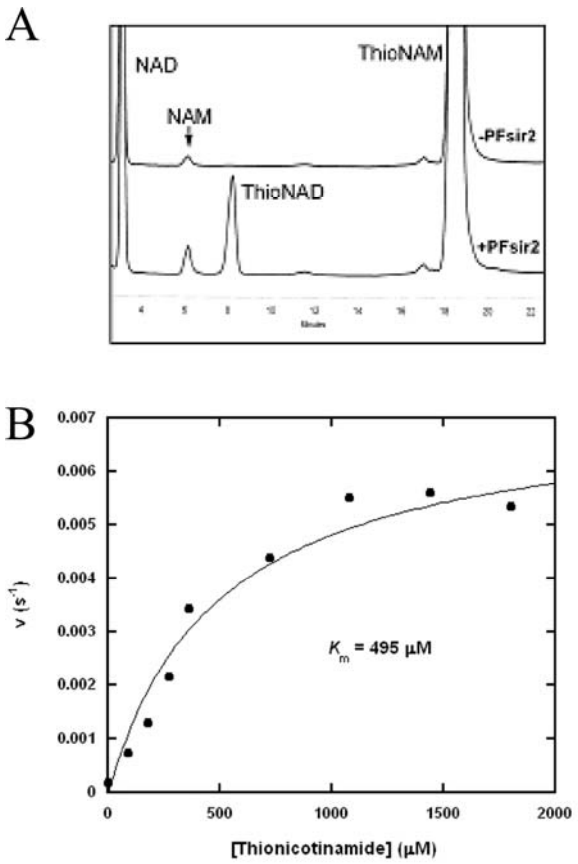

Figure 2.3. Thionicotinamide Base-Exchange Catalyzed by Pf-Sir2. (A) HPLC chromatograms showing the thionicotinamide base-exchange reaction and negative control. (B) Steady-state saturation kinetics of the thionicotinamide base-exchange reaction as catalyzed by Pf-Sir2 in the presence of 400 µM NAD$^+$ and 400 µM H3 peptide and increasing concentrations of thionicotinamide.

To characterize thionicotinamide exchange, thionicotinamide concentrations were varied and the rates of formation of thioNAD$^+$ were determined using H3 as a substrate. Fit of the individual data points to the Michaelis-Menton equation is shown in Figure 2.3B. The K_m of thionicotinamide was 495 μM, and k_{cat} was 6×10^{-3} s^{-1}. Under similar reaction conditions thionicotinamide reacts approximately 4 times slower than nicotinamide and has an 8 times higher K_m. The basis for the slower reaction of thionicotinamide is unlikely to reflect intrinsic reactivity differences, since nicotinamide and thionicotinamide pK_a values are reportedly nearly identical (*12*). The weaker binding of thionicotinamide and slower reaction suggests that substrate binding interactions *and* geometry are less optimal than for reaction of nicotinamide on the active site. These results provide an example of how reactivity differences can emerge with even slight perturbation of substrate structure, not necessarily related to intrinsic reactivity, requiring care in using rate differences in "isosteric substrates" for addressing questions of mechanism.

Pf-Sir2 Catalyzes Hydrolysis of NAD$^+$. The NAD$^+$ hydrolysis product ADPR is often detected in NAD$^+$ dependent deacetylation reactions. ADPR is typically formed by slow non-enzymatic hydrolysis of NAD$^+$, which is the minor pathway, and by the uncatalyzed decomposition of AADPR, the product of deacetylation chemistry (*8*), which is the major pathway. HPLC chromatograms of deacetylation reactions containing NAD$^+$ and Pf-Sir2 showed that amounts of ADPR were much higher than expected in comparison with reaction of SIRT1 under similar conditions of pH, substrates and rate of NAD$^+$ consumption (Figure 2.4A). We considered the possibility that Pf-Sir2 catalyzed decomposition of AADPR. However, purified AADPR in the presence of Pf-Sir2 was not decomposed faster relative to a control (data not shown). Moreover, AADPR was not decomposed when Pf-Sir2 was added to a SIRT1 reaction mixture (data not shown).

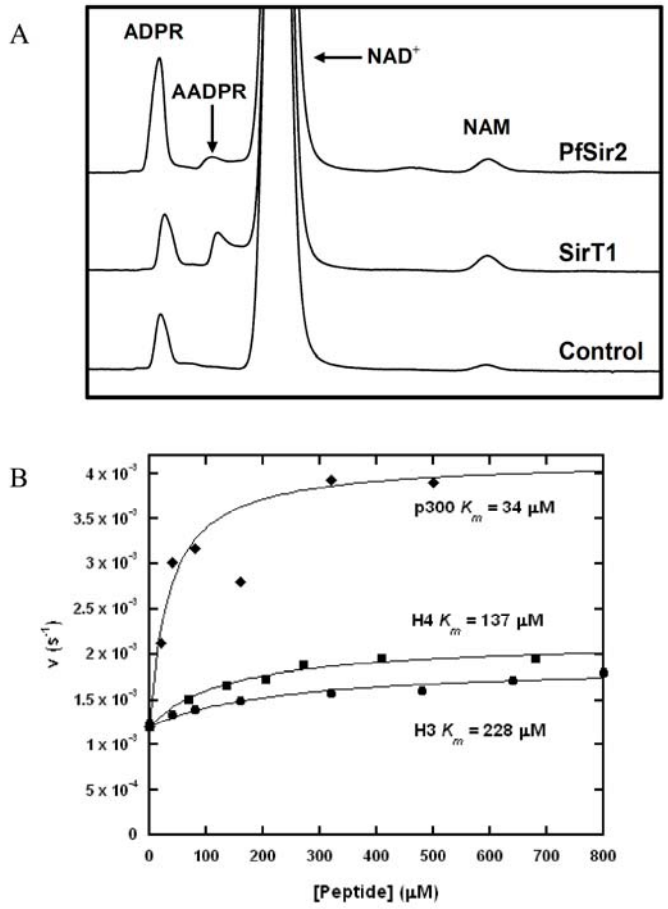

Figure 2.4. Hydrolysis of NAD^+ Catalyzed by Pf-Sir2**.** (A) HPLC chromatograms showing the production of ADPR by SirT1 and Pf-Sir2 under similar conditions. (B) the kinetics of the hydrolysis reaction for varying concentrations of peptide carried out in the presence of 400 µM NAD^+ and 150 mM phosphate buffer, pH 7.3.

This suggested to us that Pf-Sir2 might possess an independent activity capable of catalyzing solvolysis of NAD^+. Although hydrolysis is catalyzed by a mutated sirtuin in which the conserved catalytic histidine in the active site is replaced by alanine (H135A, HST2) (*10*), there are no examples of wildtype sirtuins that have an established NAD^+ glycohydrolase activity. We did check for the presence of the active site histidine in recombinant Pf-Sir2 protein by trypsin digestion. We observed the tryptic peptide containing the catalytic histidine by MS analysis (Rockefeller Proteomics Resource). We also sequenced the vector. Finally, the predicted MW of

the protein was confirmed by MALDI (predicted 32507.6 found 32504.9). Thus, a mutated histidine on Pf-Sir2 could not explain formation of ADPR.

To quantitate ADPR formation we used HPLC conditions similar to those in Figure 2.4 using saturating NAD^+ and different acetylated peptides (see experimental for details). Determined rates of formation of ADPR are shown in Table 2.1. Strikingly, the ADPR formation rate was 3-8 times higher than the maximal deacetylation rate for all peptide substrates (H3, H4 and p300). ADPR formation increased as a function of the peptide concentration and was dependent on substrate identity (H3, H4 or p300) as shown in Figure 2.4. Quantitating rate of ADPR formation as a function of peptide concentration led to the unusual finding that ADPR formation was observable even in the absence of a peptide substrate and occurred at a rate of 1×10^{-3} s^{-1} (Figure 2.4B). We fit the rate of ADPR formation to a modified Michealis-Menton expression that is described in the experimental section (see Figure 2.4B). The K_m values for peptide substrates in deacetylation and in hydrolysis were in good correspondence for all three peptides (Figure 2.1, Figure 2.4B and Table 2.1). The best hydrolysis stimulating substrate was p300. Hydrolysis in the absence of acetylated peptide was intriguing since peptide-independent NAD^+ hydrolysis has not been reported for any sirtuin, mutant or wildtype. In addition, the observation of a peptide-stimulated hydrolysis reaction suggested to us that Pf-Sir2 might catalyze two different types of hydrolysis, which we sought to further elucidate.

In the Absence of Peptide, Pf-Sir2 Catalyzes α-face Methanolysis. We probed the mechanism of peptide independent solvolysis by employing methanol as a co-solvent. Methanol has previously been used to determine the stereochemistry of solvolysis reactions of NAD^+ catalyzed by CD38/NAD^+ glycohydrolase (*25, 31*). Methanol is superior to water for determining stereochemical outcome, because while the hydrolysis product rapidly undergoes mutarotation which randomizes

stereochemistry at the anomeric carbon, the methanolysis product retains its original stereochemistry and thereby reports on the mechanism of its formation. The relevant α-1-*O*-methyl-APDR and β-1-*O*-methyl-ADPR standards were synthesized by known methods (see Methods section), and Pf-Sir2 solvolysis reactions were carried out in the absence of a peptide substrate but in the presence of methanol (30%). HPLC analysis of the reaction revealed a new reaction product that eluted at the same time as the α-1-*O*-methyl-ADPR standard (Figure 2.5A).

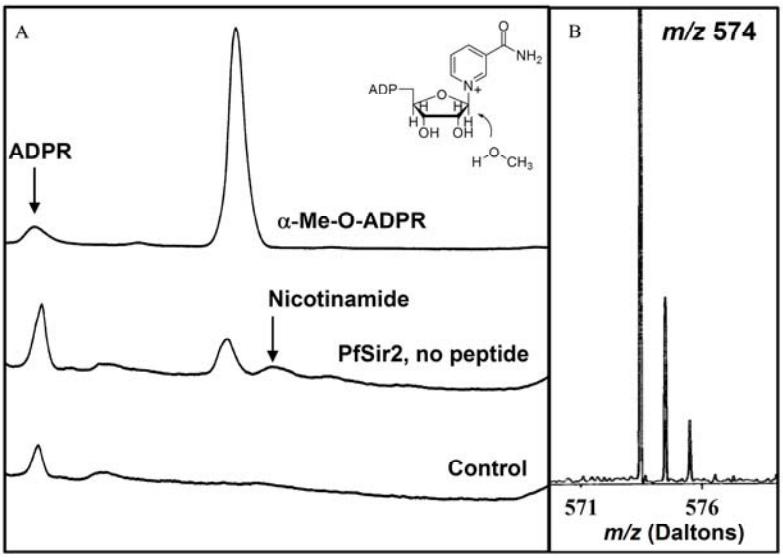

Figure 2.5. Production of α-face Methanolysis Product**.** (A) HPLC chromatograms showing the α-MeOADPR standard, a Pf-Sir2 reaction run without peptide and in the presence of 30% MeOH, and a control reaction containing no enzyme run in the presence of 30% MeOH. (B) MALDI-MS data showing the m/z values for the methanolysis products collected from the Pf-Sir2 catalyzed reactions in the presence of 30% CH_3OH and 30% CD_3OH respectively.

The product was collected and analyzed by MALDI-MS and it behaved identically to the standard, with a positively charged parent ion M/z = 574 (Figure 2.5B). Furthermore, when the reaction was carried out in deuterated methanol, the isolated product gave a positively charged ion of m/z = 577, the expected value for the deuterated compound α-1-*O*-CD_3-ADPR (data not shown). Thus, the reaction that

generates solvolysis in the absence of a peptide substrate generates a product with inverted stereochemistry versus NAD^+. This result confirmed a new mode of chemistry for a sirtuin, namely a single-displacement ADP-ribosyltransfer to solvent independent of acetylated substrate. The solvolysis is envisioned to occur via binding of solvent to the active site pocket typically occupied by an acetylated substrate. The acetylated substrate in the presence of NAD^+ processes forward to form an imidate (Scheme 2.2), whereas in the absence of the acetylated substrate the poised NAD^+ could capture the coordinated solvent to produce a product with inverted stereochemistry (Scheme 2.2).

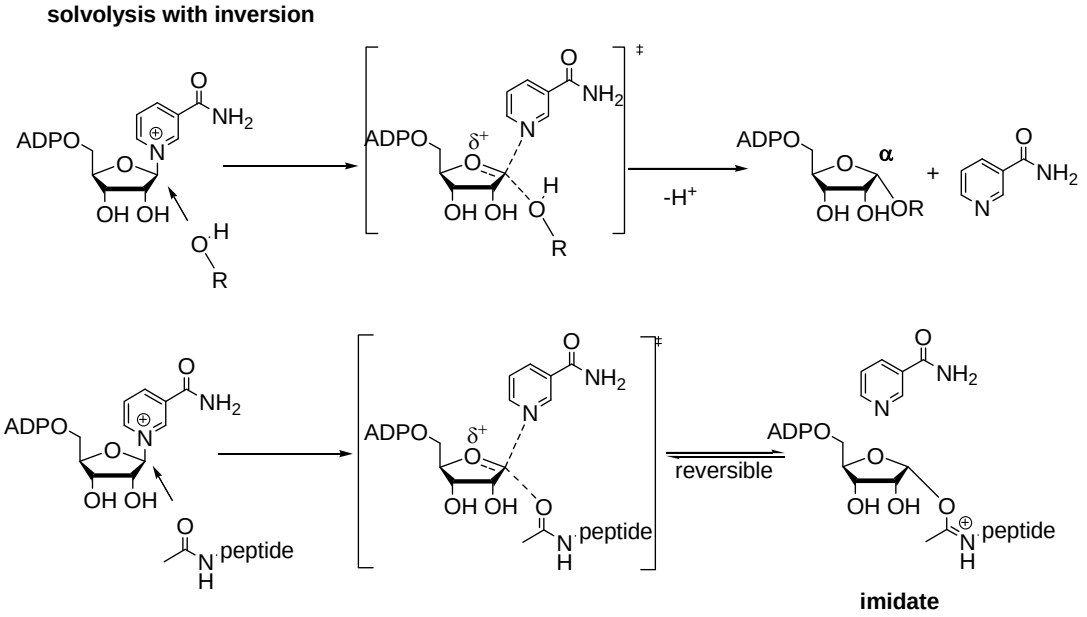

Scheme 2.2 Proposed reaction of NAD^+ in active site of Pf-Sir2 with either solvent of acetyllysine.

In the Presence of Peptide, Pf-Sir2 Catalyzes both α- and β- face Methanolysis.

To investigate the mechanisms of solvolysis reactions stimulated by the presence of acetylated peptide substrate, we conducted solvolysis reactions in which NAD^+ and H3 were reacted in the presence of Pf-Sir2, in which 30% methanol was present as a co-solvent. An HPLC chromatogram of a reaction mixture showed that the α-

methanolysis product appeared again, along with an additional new peak (Figure 2.6A).

The new product had the same elution time as an authentic β-1′-MeO-ADPR standard (Figure 2.6A). We collected this new product and a MALDI-MS spectrum determined the mass of the compound (m/z =574) identical to β-1-*O*-methyl-ADPR. As before, the corresponding reaction run in the presence of d_4-deuterated methanol gave a mass shifted species (m/z = 577) corresponding to the tri-deuterated product. Thus, we conclude that in the presence of peptide Pf-Sir2 produces a new solvolysis product generated with overall retention of stereochemistry versus NAD^+.

In light of this finding, we considered the possibility that two solvolytic mechanisms were occurring on the enzyme, one that happens by one-step single displacement mechanism to produce inverted stereochemistry. The second reaction was hypothesized to be a peptide dependent double-displacement mechanism, probably imidate-dependent, which generates products exhibiting retention of stereochemistry versus NAD^+ (Scheme 2.3). If these are the operative mechanisms, then these two mechanisms should be competitive in nature, given that the solvent and acetylated peptide are proposed to require the same pocket on the enzyme to generate the α-solvolysis products or imidate to generate β-solvolysis products. If this idea is correct, increasing concentration of peptide should increase β- product formation and inhibit α-product formation concomitantly. Thus, a set of reactions were performed varying H3 concentrations and analyzed by HPLC to quantitate ADPR, and both stereochemical methanolysis products.

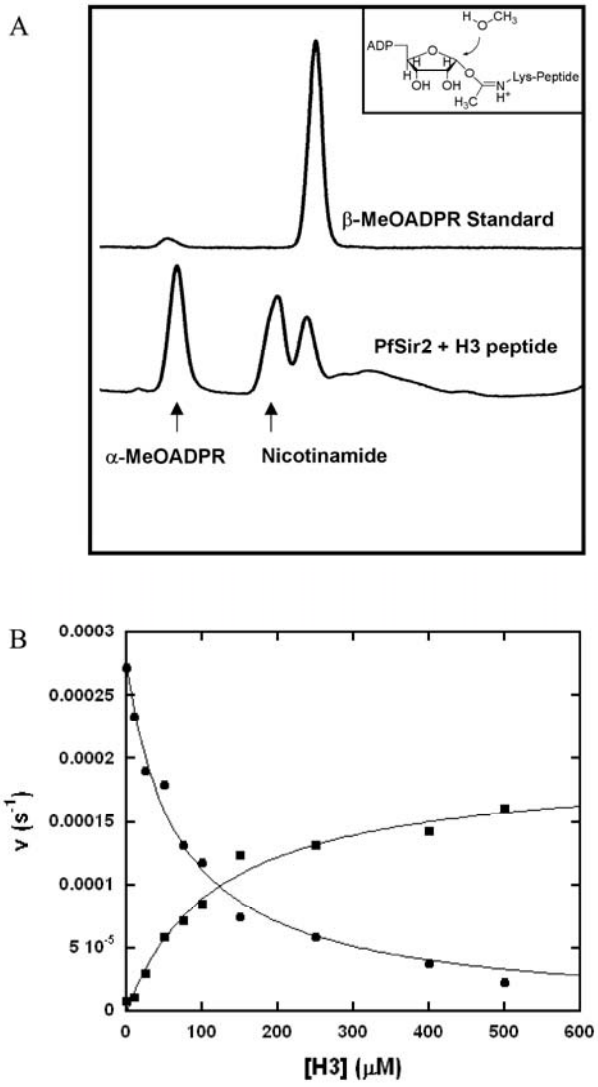

Figure 2.6. Production of β-face Methanolysis Product. (A) HPLC chromatograms showing the β-MeOADPR standard, and a Pf-Sir2 reaction run in the presence of H3 peptide and 30% MeOH. (B) Bottom: Pf-Sir2 catalyzed methanolysis with different concentrations of H3 Productions of α-MeOADPR (circle) and β-MeOADPR (square) with different concentrations of H3 are shown. The reactions contained 400 μM of NAD^+ in 100 mM phosphate buffer with 0, 10, 25, 50, 75, 100, 150, 250, 400 and 500 μM of H3 all at pH 8.5. The following Michaelis parameters were determined by fitting the curves with KaleidaGraph: K_i (α-MeO-ADPR) = 70 μM. k_0 = 2.7 x 10^{-4} s^{-1}. K_m (β-MeO-ADPR) = 119 μM, k_{500} = 1.6 x 10^{-4} s^{-1} $k_{solvolysis}$ ([H3] = 0) = 1.38 x 10^{-3} s^{-1}, $k_{solvolysis}$ ([H3] = 500 μM) = 1.40 x 10^{-3} s^{-1}

As shown, the β-methanolysis product increased with increasing peptide concentrations, eventually saturating with K_m of 120 μM (Figure 2.6B), while the α-product was inhibited to near zero over the same concentration range with a inhibition constant for peptide of K_i = 70 μM. (The lower apparent K_m (and thus K_i) for H3 under these conditions (as compared to the K_m values in Table 2.1) may be a consequence of methanol effects on H3 binding). Interestingly, the overall rate of solvolytic turnover of NAD^+ in the absence and presence of peptide under these conditions are virtually identical but the solvolytic mechanism completely changes (See Figure 2.6 legend for rates of combined ADPR and 1-*O*-methyl-ADPR for these conditions). The result supports the model that acetylated substrate competes for the α-face of C1' of NAD^+, displacing solvent from the active site thus preventing the formation of solvolysis products with inversion of stereochemistry.

Correspondingly, the acetylated substrate can react forward to form the imidate complex, which is proposed to undergo its own solvolysis reaction (Scheme 2.3) to generate overall stereochemical retention and the observed β-1-*O*-methyl ADPR (Scheme 2.3).

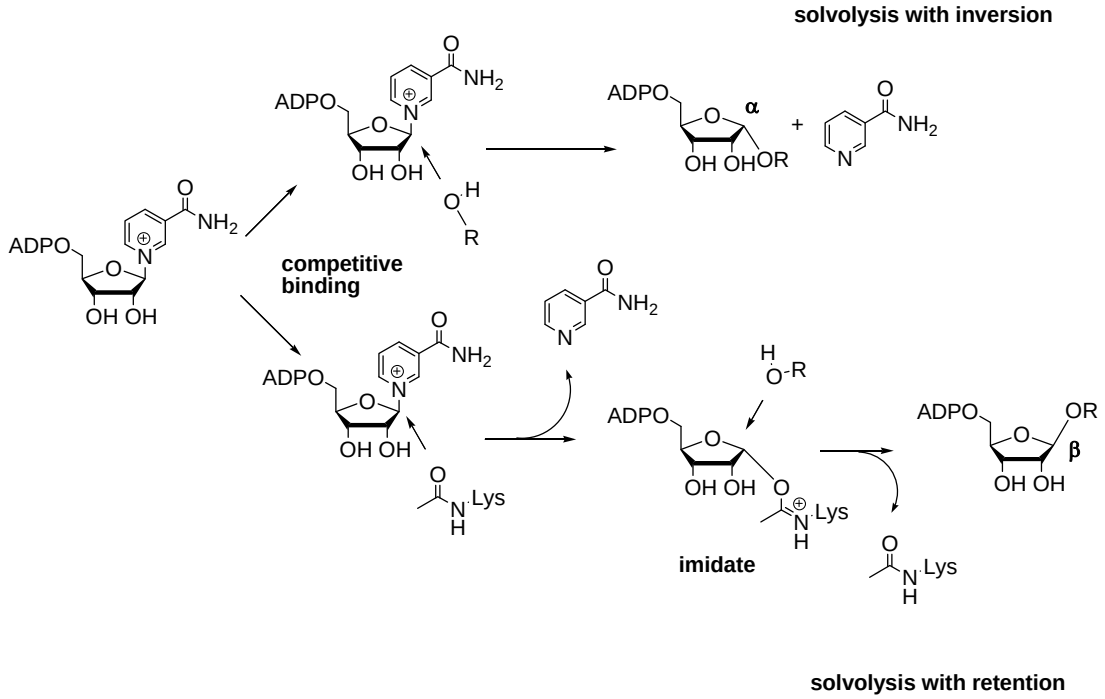

Scheme 2.3. Reaction choices of solvolysis with inversion of stereochemistry or competition reaction of acetyllysine to form imidate which can react with solvent to form product with overall retention of stereochemistry.

Differential Nicotinamide Inhibition of Solvolytic Mechanisms. Observation of two separate solvolytic products, formed through distinct and independent pathways suggested to us that nicotinamide might affect solvolysis differently under conditions in which peptide is present or absent from reaction mixtures. As already discussed, nicotinamide is a general sirtuin inhibitor and inhibits deacetylation of Pf-Sir2 by virtue of its ability to capture the imidate intermediate before it decomposes to products. Nicotinamide does not appear to inhibit Michaelis complex formation, since increasing nicotinamide concentration does not inhibit base-exchange chemistry, even when the base-exchange rate is fully saturated (Figure 2.2, bottom panels). Thus, we would predict that nicotinamide cannot inhibit peptide independent solvolysis, because it does not inhibit NAD^+ binding. Conversely, since peptide dependent chemistry is likely imidate-dependent, we predict that nicotinamide should inhibit peptide-dependent solvolytic reactions.

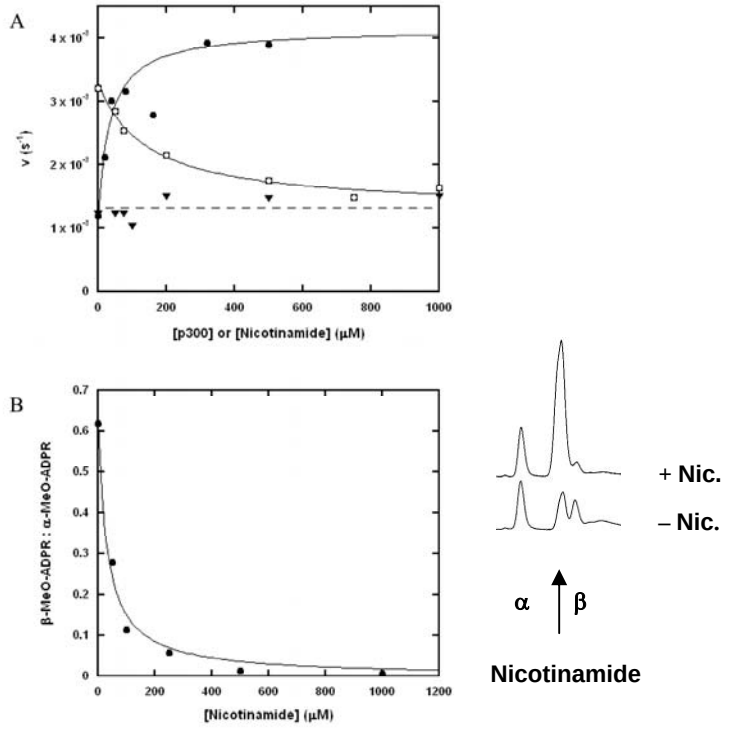

Figure 2.7. Hydrolysis is Incompletely Inhibited by Nicotinamide**.** (A) The effect of nicotinamide on the hydrolytic activity of Pf-Sir2 in the presence and absence of peptide. The curve fit to the data for hydrolysis in increasing P300 concentrations (solid circles) is shown alongside the hydrolysis data obtained by running the reactions in 400 μM P300 and increasing nicotinamide concentrations (circles in squares). The hydrolysis rate is incompletely inhibited and plateaus at a level equal to the rate of peptide independent hydrolysis (dashed line). The data for peptide independent hydrolysis in varying nicotinamide concentrations is shown (triangles) and is fit by a straight line (dashed line). (B) The plot of the ratio of β to α stereochemistry of methanolysis products with increasing nicotinamide concentration as determined by HPLC. The plotted points were fit to a curve of form $r = r_0 - r_{max}$ ([I]/(K_i +[I])) where r is the ratio of stereochemistry observed for a given concentration of nicotinamide, r_0 is the observed stereochemical ratio when no nicotinamide is present, r_{max} is the maximal suppression of the ratio, K_i is the apparent inhibition constant of nicotinamide and [I] is the concentration of nicotinamide. The HPLC chromatograms (B-right) illustrate that when nicotinamide is added there is a decrease in the β-1-*O*-methylADPR peak, but there is little change in the production of α-1-*O*-methylADPR. The nicotinamide visible in the lower trace was produced by the normal hydrolysis and methanolysis of NAD^+ catalyzed by Pf-Sir2.

To examine the effect of nicotinamide on hydrolytic rate in the presence and absence of peptide, we conducted reactions in the presence of NAD^+ with and without

p300 added to solution. In the absence of added peptide, increasing concentrations of nicotinamide have no effect on the rate of hydrolysis, as shown by the line of nearly zero slope in Figure 2.7A.

When p300 is added to reaction, it can stimulate the rate of hydrolysis several fold over the rate in which no peptide is present (overlaid curve Figure 2.7A). Increasing concentrations of nicotinamide inhibit this increase of hydrolysis in the presence of sub-saturating p300 (subsaturating conditions allow both peptide-dependent and peptide-independent mechanisms to occur simultaneously) but does not fully inhibit hydrolysis, as shown by the fit of the inhibition data to a curve for non-linear inhibition (K_i = 75 μM see experimental for details). The uninhibited solvolysis rate is in reasonable agreement with the solvolytic rate when no peptide is present, consistent with the idea that only peptide-dependent hydrolysis is inhibited.

To further probe the idea that only the peptide-dependent solvolysis is sensitive to nicotinamide concentrations, we examined the β-stereochemistry ratio of methanolysis products as a function of increasing nicotinamide concentrations under experimental conditions in which both methanolysis stereoisomers are generated. As shown in the inset of Figure 2.7B, HPLC chromatograms reveal that formation of the β- product is inhibited by nicotinamide, whereas, formation of the β- product is not inhibited. The effect of increasing nicotinamide concentrations on β/α product ratio was determined by HPLC and plotted, with points fit to a predicted curve as described in the figure legend. The ratio decreases to near 0 as a function of increasing nicotinamide concentrations, as predicted if nicotinamide selectively inhibits hydrolysis from the imidate complex, without inhibiting peptide-independent solvolysis of NAD^+ (Figure 2.7B). The peptide-independent hydrolysis of NAD^+ by Pf-Sir2 establishes the first catalytic activity of a sirtuin that is insensitive to

nicotinamide inhibition (other than base-exchange) at concentrations of nicotinamide exceeding the mM range.

2.5 Discussion

Deacetylase activity. Protein deacetylase activity had been previously predicted for Pf-Sir2 based upon biological data implicating this sirtuin in regulation of chromatin structure and in silencing of epitope and virulence associated genes encoded by the var family (20, 21). Patterns of var gene expression are involved in antigenic variation, a process by which P. falciparum avoids the immune system of the host by swapping expression of these genes, while keeping the remainder silent (20, 21). We determined that Pf-Sir2 in the presence of NAD^+ catalyzes deacetylation of N-terminal histone sequences of H3 and H4 identical to N-terminal histone sequences. Pf-Sir2 deacetylates H3 peptides at sequences lysine 9 and 14, and also deacetylates H4 at lysine 16. Pf-Sir2 deacetylation generates AAPDR as a product.

Two other recent reports have confirmed deacetylase activity for this enzyme (27, 32). In the process of examining other substrates for Pf-Sir2 we identified a human p300 sequence to be a superior substrate for Pf-Sir2 as compared with peptide H3 and H4 sequences. Although we currently do not understand the biochemical or functional basis for Pf-Sir2 substrate preference of p300 over histone sequences, we speculate that context-dependent factors such as post-translational modifications of histone sequences or macromolecular structures of histones and Pf-Sir2 localization to histones may affect catalytic efficiency of Pf-Sir2 for histone sequences in a native context. We do not currently know if p300 is a substrate for Pf2-Sir2 in vivo, although P falciparum is an intracellular parasite of human cells and could theoretically act on human protein sequences.

The deacetylation reaction is slow, even relative to sirtuin standards, which are typically slow turnover enzymes and typically have rates of deacetylation of 0.1 -

0.01 s^{-1}. In the case of H3 and H4 sequences, we determined k_{cat} values of 2.5 and 3.5 $\times 10^{-4}$ s^{-1} respectively. For a p300 sequence deacetylation rate was only slightly faster with a maximal rate 9×10^{-4} s^{-1}. A recent study of recombinant Pf-Sir2 with a non-physiologic 8-mer acetylated substrate determined a similarly slow deacetylation rate (32). We propose that the slow rate of deacetylation under steady-state conditions is caused by a stalled imidate complex (Scheme 2.1) which is supported in part by the determination that the nicotinamide cleavage step, which precedes imidate formation, occurs approximately 50-100 times faster (Scheme 2.1). The rate constants for nicotinamide cleavage are no slower than the observed rate of steady-state base-exchange, which for H3 and p300 are 2.5×10^{-2} s^{-1} and 6.5×10^{-2} s^{-1} respectively (Scheme 2.1 and Figure 2.2).

Slow reaction of the imidate and observation of hydrolysis from the imidate. Evidence that imidate forward reaction is rate-limiting for deacetylation includes the observation that the imidate decomposes via hydrolysis at rates that are 4-10 times faster than deacetylation (Table 2.1), suggesting that the 2'-OH attack of the imidate, which commits the imidate to deacetylation chemistry, is slower. Consistently, the imidate hydrolysis reaction is interpreted to be a direct consequence of the slow rate of deacetylation chemistry (Scheme 2.4, step d) . Reaction of solvent at the anomeric carbon of the Pf-Sir2 imidate is predicted to give overall retention of stereochemistry, which was observed in reactions performed in the presence of both acetyllysine peptide and methanol. A literature precedent is available for such a reaction, in which the conserved active site histidine of the sirtuin HST2 was mutated, causing decreased deacetylation rate. In consequence of slowed deacetylation chemistry, imidate hydrolysis was observed, a reaction not observed on the wildtype HST2 enzyme (10).

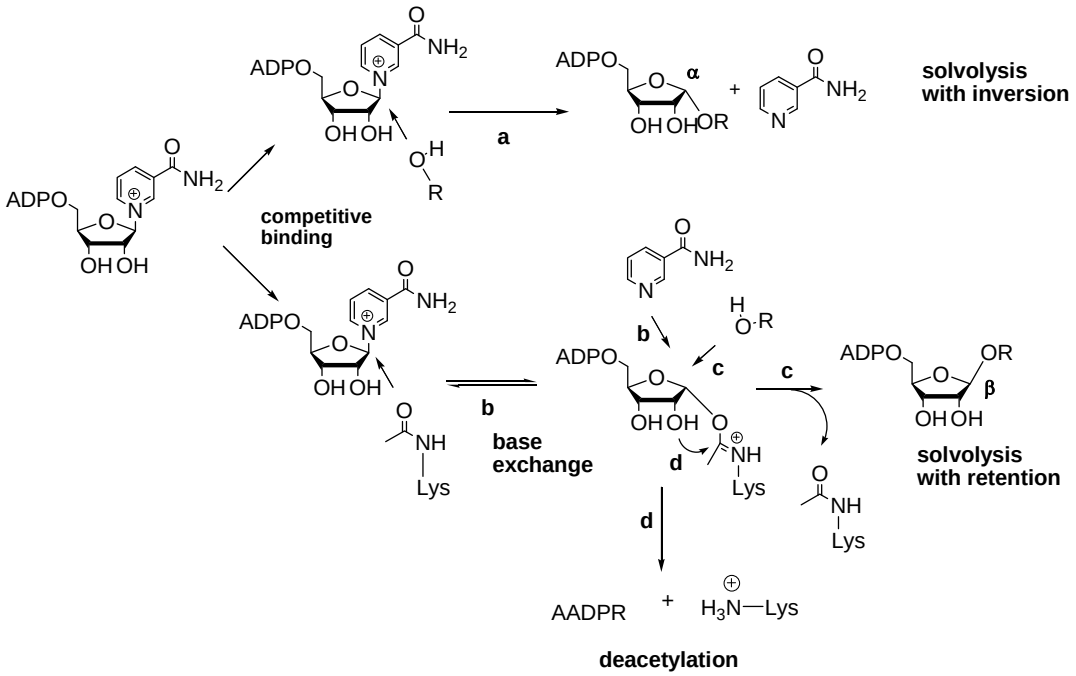

Scheme 2.4**.** Overall reaction scheme of Pf-Sir2 catalyzed reactions. Top scheme depicts solvolytic chemistry in the absence of peptide which gives inversion of stereochemistry (reaction **a**). Bottom scheme depicts acetyllysine dependent chemistries which occur via the imidate including base exchange (reaction **b**), solvolysis from the imidate (reaction **c**) and deacetylation (reaction **d**)

Nicotinamide inhibition of imidate-dependent reactions. Nicotinamide inhibition occurs mainly through the reaction of nicotinamide through the imidate complex. Competitive nicotinamide capture of the imidate (Scheme 2.4 reaction b) is predicted to inhibit the deacetylation (*11, 12*) and imidate solvolysis (Scheme 2.4, reactions d and c respectively). This was observed. Interestingly, the steady-state nicotinamide exchange reaction occurs substantially faster than deacetylation or solvolysis, implying that the imidate and Michaelis complex (NAD^+ and acetylated peptide) pseudo-equilibrate when nicotinamide concentrations saturate base-exchange (Scheme 2.4). Analogous pseudo-equilibration effects of base-exchange with an active site ADPR-intermediate have been observed with the enzyme CD38 (33). We conclude that the imidate is thermodynamically destabilized with respect to the Michaelis complex when nicotinamide saturates the base-exchange reaction, otherwise

the imidate concentration would not be depleted and inhibition of deacetylation would not be observed (11). In contrast, in the absence of nicotinamide re-binding to the active site, the imidate is kinetically stable with respect to return to the Michaelis complex, and partitions between deacetylation and hydrolysis (β-stereochemistry).

Peptide-independent solvolysis and insensitivity to nicotinamide. The Pf-Sir2 enzyme also displayed an unusual capacity to catalyze NAD^+ hydrolysis in the absence of any added acetylated substrate. In the absence of acetylated substrate, we identified only α-1-O-methyl-ADPR as a product (no β) in addition to ADPR when methanol was added as a probe for stereochemistry of reaction. This finding confirmed that the solvolytic reaction in the absence of peptide occurs with inversion of stereochemistry at C1′ (Scheme 2.4, reaction a). This type of direct displacement solvolysis has not been reported for any other sirtuin, although cholera and diphtheria toxins, which are NAD^+ dependent protein ADP-ribosyltransferases, hydrolyze NAD^+ in the absence of cognate substrates, presumably via direct displacement mechanisms, to give inversion in hydrolysis products (34-36). Interestingly, methanolysis appears to be non-reactive in the cholera toxin solvolysis reaction, making confirmation of this prediction problematic (37).

The Pf-Sir2 peptide-independent solvolytic reaction occurs at a rate that exceeds the deacetylation rate for H3, but is inhibited by this peptide, as shown by inhibition of α-stereochemistry methanolysis with increasing concentrations of acetylated peptide. This suggests to us that acetyllysine and water (or methanol) occupy the same site on the enzyme leading to imidate formation or α-hydrolysis, with the ratio determined by the relative occupancy of the site. We also determined that increased H3 peptide concentration, while inhibiting the α-methanolysis concomitantly increases β-methanolysis, implying that H3 peptide provides a mechanism for imidate formation and the intermediate solvolysis pathway. The

peptide-independent solvolysis pathway is not sensitive to inhibition by nicotinamide, since it does not require imidate formation.

Implications of this work for understanding mechanisms of ADP-ribosyl transfer. Our findings on Pf-Sir2 are relevant to reports of stable ADP-ribosyltransfer to proteins catalyzed by sirtuins, which have thus far remained mechanistically uncharacterized. From a general chemical perspective the two different types of solvolysis that occur on Pf-Sir2 define mechanistic examples of two different types of stable ADP-ribosyltransfer to nucleophiles. The first of these examples involves direct displacement of NAD^+ by a nucleophile to furnish an ADP-ribosyltransfer product with α-stereochemistry (inverted) at C1' of ADPR (Scheme 2.5, top). This type of reaction is analogous to that observed for both the ADP-ribosylating toxins and the protein modifying ADPribosyltransfer chemistry proposed for the poly-ADP-ribosylpolymerases. Interestingly, this reaction chemistry occurs independently of an acetylated peptide, although these reactions presumably occur by nucleophile occupation of the "acetyllysine pocket", followed by reaction with enzyme-bound NAD^+. Interestingly, we found that nicotinamide cannot inhibit this reaction (Scheme 2.5), suggesting that nicotinamide only inhibits sirtuin reactions through an imidate complex. We propose that a lack of sensitivity of ADP-ribosyltransfer to nicotinamide can be used to infer the lack of an imidate complex in a sirtuin-catalyzed ADP-ribosyltransfer mechanism.

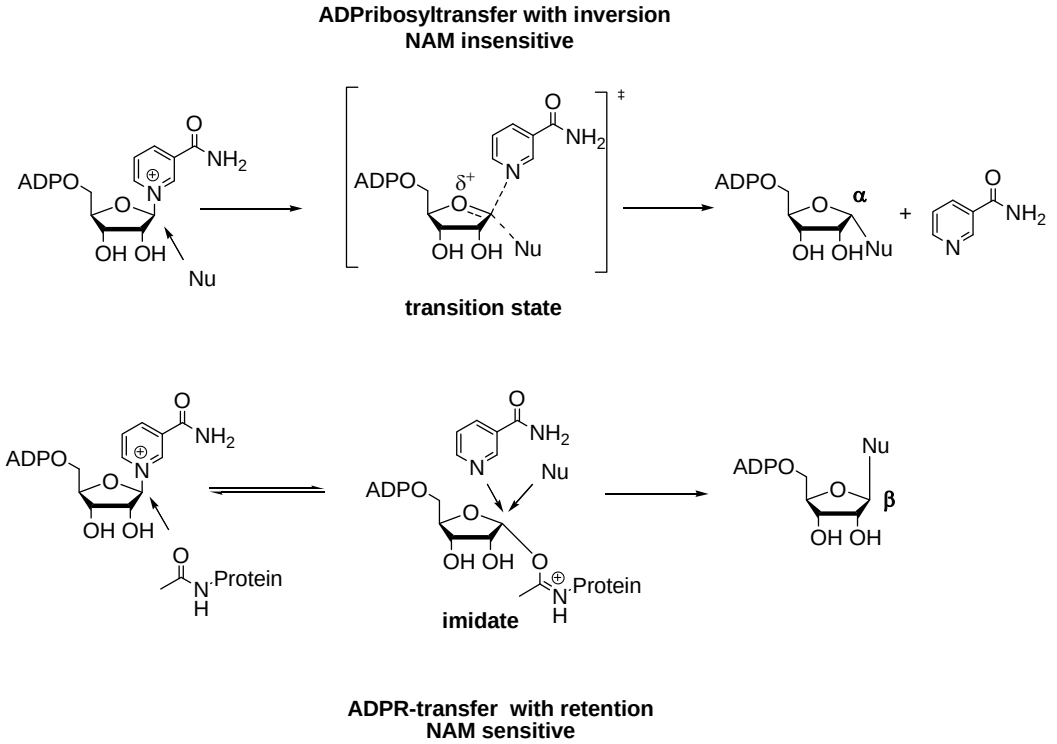

Scheme 2.5**.** Proposed general mechanisms of ADP-ribosyltransfer catalyzed by sirtuins as determined by chemistries reported in this study. Top chemistry is acetyllysine independent, gives inversion of stereochemistry versus NAD^+ and is insensitive to nicotinamide inhibition. Bottom chemistry scheme shows ADP-ribosyltransfer from the imidate complex, to produce ADP-riboysltransfer with retention of stereochemistry versus NAD^+. This reaction is predicted to be sensitive to nicotinamide inhibition.

The second type of ADP-ribosyltransfer mechanism determined in this study is reaction of the imidate complex to produce a product with β-stereochemistry (retention) at C1' of ADPR (Scheme 2.5). This reaction is inherently sensitive to nicotinamide inhibition since nicotinamide can compete for the nucleophile site and for reaction with the imidate (Scheme 2.5). Thus, imidate-dependent ADP-ribosyltransfer can be distinguished by sensitivity to nicotinamide. We propose that nicotinamide sensitivity can help to determine mechanisms of ADP-ribosyltransfer catalyzed by sirtuins. For example, SIRT4 has been demonstrated to ADP-ribosylate glutamate dehydrogenase, and this reaction is inhibited by nicotinamide (6). Based on

our findings, this could imply SIRT4 catalyzes imidate dependent ADP-ribosylation, and we are currently investigating this possibility in our laboratory.

2.6 Conclusions

Plasmodium falciparum Pf-Sir2 is a chromatin associated enzyme implicated in silencing of var genes. We found that it can deacetylate acetyllysine peptide substrates such as histone H3 and H4 N-terminal sequences. Pf-Sir2 was also found to catalyze two stereochemically distinct types of solvolysis, one sensitive to nicotinamide inhibition, the other insensitive to nicotinamide inhibition. These are the first reported NAD^+ glycohydrolase reactions catalyzed by a wildtype sirtuin. The biologic role of these hydrolytic reactions, which would generate ADPR in the nucleus of the parasite, is not known. We speculate that the solvolyses may be occurring in competition with other kinds of Pf-Sir2 ADP-ribosyltransfer reactions in cells, including protein ADP-ribosyl transfer. A recent paper suggests that Pf-Sir2 is able to catalyze protein ADP-ribosyltransfer (27) although the mechanism of ADP-ribosyltransfer remains undetermined. Investigations to elucidate mechanisms of sirtuin-catalyzed protein ADP-ribosyltransfer reactions are underway in our laboratory

REFERENCES

1. Sauve, A. A., *et al.* (2006) The biochemistry of sirtuins, *Annu Rev Biochem 75*, 435-465.
2. Blander, G., and Guarente, L. (2004) The Sir2 family of protein deacetylases, *Annu Rev Biochem 73*, 417-435.
3. Guarente, L. (2006) Sirtuins as potential targets for metabolic syndrome, *Nature 444*, 868-874.
4. Haigis, M. C., and Guarente, L. P. (2006) Mammalian sirtuins--emerging roles in physiology, aging, and calorie restriction, *Genes Dev 20*, 2913-2921.
5. Liszt, G., *et al.* (2005) Mouse Sir2 homolog SIRT6 is a nuclear ADP-ribosyltransferase, *J Biol Chem 280*, 21313-21320.
6. Haigis, M. C., *et al.* (2006) SIRT4 inhibits glutamate dehydrogenase and opposes the effects of calorie restriction in pancreatic beta cells, *Cell 126*, 941-954.
7. Garcia-Salcedo, J. A., *et al.* (2003) A chromosomal SIR2 homologue with both histone NAD-dependent ADP-ribosyltransferase and deacetylase activities is involved in DNA repair in Trypanosoma brucei, *Embo J 22*, 5851-5862.
8. Sauve, A. A., *et al.* (2001) Chemistry of gene silencing: the mechanism of NAD+-dependent deacetylation reactions, *Biochemistry 40*, 15456-15463.
9. Sauve, A. A., and Schramm, V. L. (2004) SIR2: the biochemical mechanism of NAD(+)-dependent protein deacetylation and ADP-ribosyl enzyme intermediates, *Curr Med Chem 11*, 807-826.
10. Smith, B. C., and Denu, J. M. (2006) Sir2 protein deacetylases: evidence for chemical intermediates and functions of a conserved histidine, *Biochemistry 45*, 272-282.

11. Sauve, A. A., and Schramm, V. L. (2003) Sir2 regulation by nicotinamide results from switching between base exchange and deacetylation chemistry, *Biochemistry 42*, 9249-9256.

12. Jackson, M. D.*, et al.* (2003) Mechanism of nicotinamide inhibition and transglycosidation by Sir2 histone/protein deacetylases, *J Biol Chem 278*, 50985-50998.

13. Zhao, K.*, et al.* (2003) Structure of the yeast Hst2 protein deacetylase in ternary complex with 2'-O-acetyl ADP ribose and histone peptide, *Structure 11*, 1403-1411.

14. Marmorstein, R. (2004) Structure and chemistry of the Sir2 family of NAD+-dependent histone/protein deactylases, *Biochem Soc Trans 32*, 904-909.

15. Hoff, K. G.*, et al.* (2006) Insights into the sirtuin mechanism from ternary complexes containing NAD+ and acetylated peptide, *Structure 14*, 1231-1240.

16. Avalos, J. L.*, et al.* (2005) Mechanism of sirtuin inhibition by nicotinamide: altering the NAD(+) cosubstrate specificity of a Sir2 enzyme, *Mol Cell 17*, 855-868.

17. Kowieski, T. M.*, et al.* (2008) Acetylation-dependent ADP-ribosylation by Trypanosoma brucei Sir2, *J Biol Chem 283*, 5317-5326.

18. Guerra, C. A.*, et al.* (2006) Mapping the global extent of malaria in 2005, *Trends Parasitol 22*, 353-358.

19. Kyes, S. A.*, et al.* (2007) Antigenic variation in Plasmodium falciparum: gene organization and regulation of the var multigene family, *Eukaryot Cell 6*, 1511-1520.

20. Duraisingh, M. T.*, et al.* (2005) Heterochromatin silencing and locus repositioning linked to regulation of virulence genes in Plasmodium falciparum, *Cell 121*, 13-24.

21. Freitas-Junior, L. H.*, et al.* (2005) Telomeric heterochromatin propagation and histone acetylation control mutually exclusive expression of antigenic variation genes in malaria parasites, *Cell 121*, 25-36.

22. Bradford, M. M. (1976) A rapid and sensitive method for the quantitation of microgram quantities of protein utilizing the principle of protein-dye binding, *Anal Biochem 72*, 248-254.

23. Yost, D. A., and Anderson, B. M. (1983) Adenosine diphosphoribose transfer reactions catalyzed by Bungarus fasciatus venom NAD glycohydrolase, *J Biol Chem 258*, 3075-3080.

24. Scheuring, J.*, et al.* (1998) Transition-state structure for the ADP-ribosylation of recombinant Gialpha1 subunits by pertussis toxin, *Biochemistry 37*, 2748-2758.

25. Sauve, A. A.*, et al.* (1998) The reaction mechanism for CD38. A single intermediate is responsible for cyclization, hydrolysis, and base-exchange chemistries, *Biochemistry 37*, 13239-13249.

26. Imai, S.*, et al.* (2000) Sir2: an NAD-dependent histone deacetylase that connects chromatin silencing, metabolism, and aging, *Cold Spring Harb Symp Quant Biol 65*, 297-302.

27. Merrick, C. J., and Duraisingh, M. T. (2007) Plasmodium falciparum Sir2: an unusual sirtuin with dual histone deacetylase and ADP-ribosyltransferase activity, *Eukaryot Cell 6*, 2081-2091.

28. Bouras, T.*, et al.* (2005) SIRT1 deacetylation and repression of p300 involves lysine residues 1020/1024 within the cell cycle regulatory domain 1, *J Biol Chem 280*, 10264-10276.

29. Bitterman, K. J.*, et al.* (2002) Inhibition of silencing and accelerated aging by nicotinamide, a putative negative regulator of yeast sir2 and human SIRT1, *J Biol Chem 277*, 45099-45107.

30. Landry, J.*, et al.* (2000) Role of NAD(+) in the deacetylase activity of the SIR2-like proteins, *Biochem Biophys Res Commun 278*, 685-690.

31. Berthelier, V.*, et al.* (1998) Human CD38 is an authentic NAD(P)+ glycohydrolase, *Biochem J 330 (Pt 3)*, 1383-1390.

32. Chakrabarty, S. P.*, et al.* (2008) Biochemical characterization of Plasmodium falciparum Sir2, a NAD(+)-dependent deacetylase, *Mol Biochem Parasitol 158*, 139-151.

33. Sauve, A. A.*, et al.* (2000) A covalent intermediate in CD38 is responsible for ADP-ribosylation and cyclization reactions, *Journal of the American Chemical Society 122*, 7855-7859.

34. Moss, J.*, et al.* (1977) Effect of gangliosides and substrate analogues on the hydrolysis of nicotinamide adenine dinucleotide by choleragen, *Proc Natl Acad Sci U S A 74*, 74-78.

35. Kandel, J.*, et al.* (1974) Interaction of fragment A from diphtheria toxin with nicotinamide adenine dinucleotide, *J Biol Chem 249*, 2088-2097.

36. Bell, C. E., and Eisenberg, D. (1996) Crystal structure of diphtheria toxin bound to nicotinamide adenine dinucleotide, *Biochemistry 35*, 1137-1149.

37. Oppenheimer, N. J. (1978) Structural determination and stereospecificity of the choleragen-catalyzed reaction of NAD+ with guanidines, *J Biol Chem 253*, 4907-4910.

CHAPTER 3

CHARACTERIZATION OF NICOTINAMIDASES: STEADY-STATE KINETIC PARAMETERS, CLASS-WIDE INHIBITION BY NICOTINALDEHYDES AND CATALYTIC MECHANISM

3.1 Abstract

Nicotinamidases are metabolic enzymes that hydrolyze nicotinamide to nicotinic acid. These enzymes are widely distributed across biology, with examples found encoded in the genomes of Mycobacteria, Archaea, Eubacteria, Protozoa, yeast and invertebrates but there are none found in mammals. The catalytic mechanism of these enzymes is not well understood. Recent data shows that nicotinamidases are required for growth and virulence of several pathogenic microbes and the enzymes of *Saccharomyces cerevisiae*, *Drosophila melanogaster* and *Caenorhabditis elegans* regulate lifespan in their respective organisms, consistent with proposed roles in the regulation of NAD^+ metabolism and organismal aging. In this manuscript, we determine the Michaelis-Menten parameters of nicotinamidase enzymes from *C. Elegans*, *S. cerevisiae*, *Streptococcus pnemoniae* (a pathogen responsible for human pneumonia), *Borrelia Burgdorferei* (the pathogen that causes Lyme Disease) and *Plasmodium falciparum* (responsible for most human malaria). Our findings indicate that these enzymes are generally efficient with catalytic rates typically exceeding 1 s^{-1}. The K_m values for nicotinamide are low and are in the range from 5-80 μM. In addition, we show that nicotinaldehydes are potent competitive inhibitors of these enzymes, and bind in the low μM to low nM range for all nicotinamidase enzymes tested. A variety of nicotinaldehyde derivatives were synthesized and evaluated in kinetic assays, demonstrating that optimized binding can be obtained by introducing substitutions to the nicotinaldehyde ring. ^{18}O exchange studies, sequence comparisons and the availability of a complete set of substrate, intermediate and inhibitor crystal

structures (see Chapter 4) provide evidence for a shared catalytic mechanism within this enzyme class. A comprehensive catalytic mechanism that explains nicotinamidase chemistry is presented involving the intermediacy of a thioester moeity and the transient involvement of a Zn-hydroxide complex as an activating base for deprotonation of water that promotes thioester hydrolysis on the enzyme.

3.1 Introduction

The nicotinamidases hydrolyze nicotinamide to nicotinic acid (Scheme 3.1).

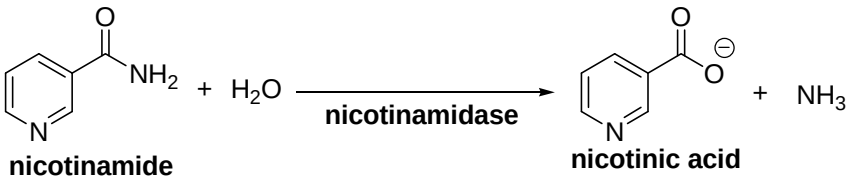

Scheme 3.1. Nicotinamidase hydrolyzes nicotinamide to give nicotinic acid

These enzymes play important roles in nicotinamide salvage in multiple species of bacteria (*1*), mycobacteria (*1-4*), yeast (*5-7*), protozoa (*8*) and are encoded in genomes of plants (*9*) and many metazoan species as well, such as *Drosophila melanogaster (10)* and *Caenorhabditis elegans (10-12)*. Nicotinamide salvage is important since $NAD(P)^+$ is chemically unstable to non-enzymatic hydrolysis even at physiologic temperatures (*13-15*) and because nicotinamide is the product of multiple NAD^+ consuming enzymes (*13, 14*), such as sirtuins that are widely distributed in biology (*16*). Consistent with their centrality to NAD^+ homeostasis, nicotinamidases are essential for the viability of several microorganisms that are pathogenic to humans such as *Borrelia burgdorferi* (which causes Lyme disease) (*17-19*) and *Brucella abortus (20)*. It is possible that a variety of other pathogenic organisms require this enzyme as well, since several of these, including *Plasmodium falciparum* do not appear to encode genes for enzymatic components of de novo NAD^+ biosynthetic

pathways (*21*). Consequently, it is likely that these organisms are highly reliant on salvage of nicotinamide from the human host. Attractively, human genomes do not encode a nicotinamidase, suggesting that small molecule inhibitors of nicotinamidases could serve as antimicrobial agents (*21*).

Biologically interesting roles for nicotinamidases have also been identified as increasers of lifespan in *D. melanogaster (10)* and in *C. elegans (11)* and in the budding yeast *Saccharomyces cerevisiae (22)*. Importantly, endogenous nicotinamide concentrations are implicated in negative regulation of NAD^+ dependent deacetylases, the sirtuins (*16, 23*). Lifespan extending effects of overexpression of nicotinamidases require sirtuin activity in yeast (*24*) and in flies (*10*) consistent with a mechanism in which increased nicotinamidase activity can deplete inhibitory nicotinamide concentrations in cells, leading to sirtuin activity upregulation. Consistently, sirtuin overexpression within *D. melanogaster (25, 26) C. elegans* (*27, 28*) and *S. cerevisiae* (*29, 30*) also causes increased lifespan. Stresses that increase lifespan in the yeast, such as low calorie stress, induce nicotinamidase activity by increasing nicotinamidase transcription and translation (*22*). Similarly, oxidative stress increases nicotinamidase expression in *D. melanogaster (10)*. These data suggest that these enzymes are central to phylogenetically conserved adaptative responses to environmental stress in single-celled eukaryotes and possibly in multicellular eukaryotes as well.

Additional interest in these enzymes stem from an important role in *Mycobacterium tuberculosis*, where the endogenous nicotinamidase is responsible for activation of the pro-drug pyrazinamide to the active antibiotic pyrazinoic acid and mutations in this enzyme are associated with resistance to this drug (Scheme 3.2) (*4*). Recently nicotinamidases have been shown to be important for plant germination as well (*31*). Thus, nicotinamidases are biologically interesting enzymes with diverse biological functions associated with their enzymatic activity.

Scheme 3.2. Nicotinamidase catalyzes the conversion of pyrazinamide to pyrazinoic acid.

The first nicotinamidase activity was reported for the organism *Lactobacillus arabinosus* (*32*), but decades later, there is still limited insight into the chemical and enzymatic mechanisms of these enzymes. Hints to the chemistry of these enzymes was obtained from two unliganded structures of nicotinamidases, one of the *S. cerevisiae* enzyme (*6*), the other from the archaean thermophile *Pyrococcus hirikoshii* (*33*). Both structures revealed an active site coordinated metal ion, proposed to be Zn^{+2}, and similar structural folds. A recent structure of the nicotinamidase from *Acinetobacter baumannii* in complex with nicotinic acid provided new insight into the active site design for these enzymes (*34*). The crystal structure revealed that the pyridine N1 of the product is coordinated to the central metal ion, suggesting that coordination of nicotinamide to the metal center organizes and electrophilically activates the pyridine for attack by a cysteine residue on the amide carbonyl of the substrate (*34*). This cysteine is universally conserved in all nicotinamidases (Figure 3.1) and previously had been proposed to perform a nucleophilic function on the enzyme to form a labile thioester of nicotinic acid, which can further hydrolyse to release the free thiol and nicotinic acid (*33*, *34*).

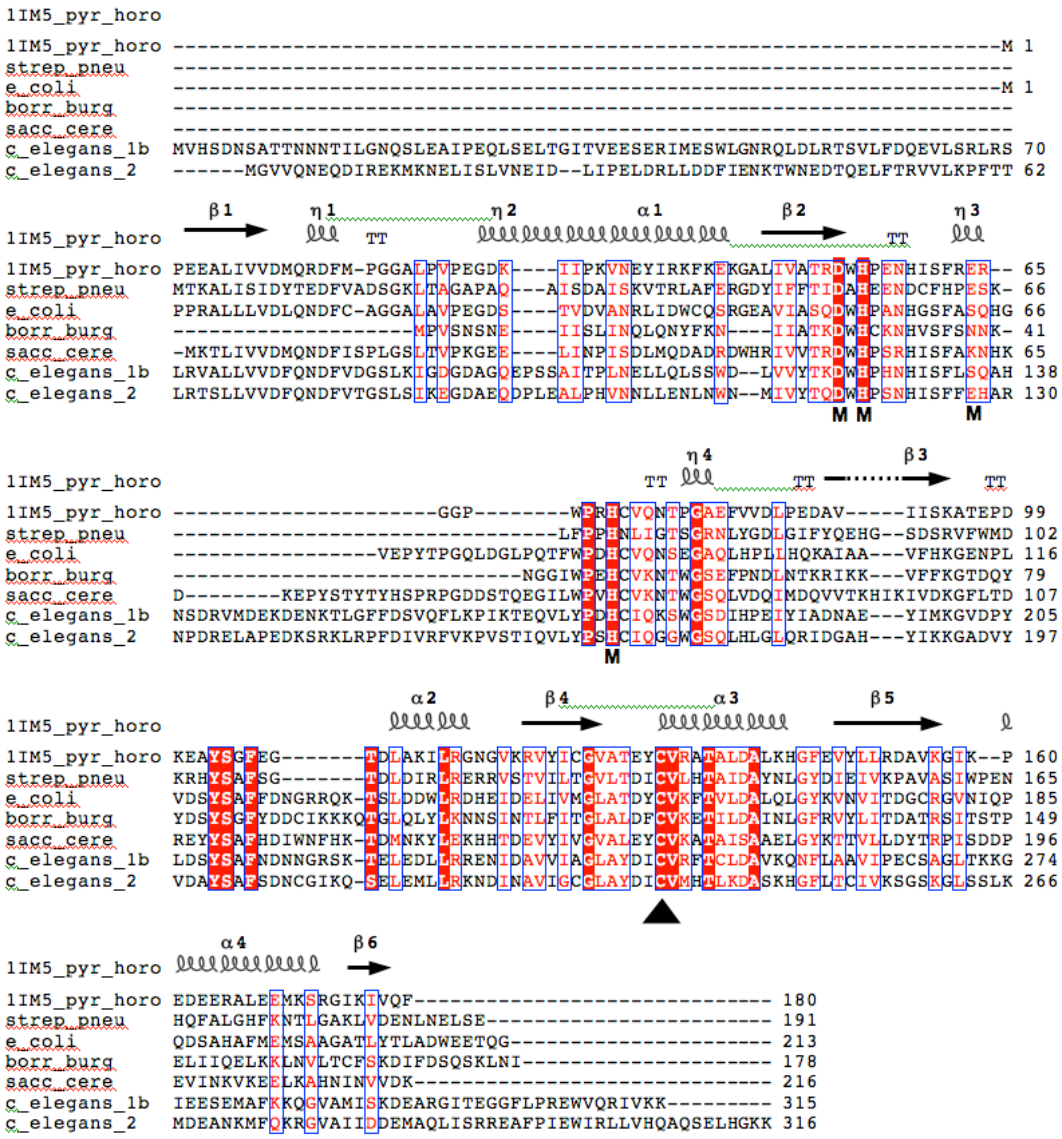

Figure 3.1. Multiple sequence alignment of the *Pyrococcus horikoshii* (PDB entry 1IM5), *Streptococcus pneumoniae, Escherichia Coli, Saccharomyces cerevisiae* , and *Borrelia burgdorferi* nicotinamidases. The alignment was perfomed with ClustalW (*35*) and edited with ESPript (*36*). Identical residues are highlighted, and the secondary structure elements of the solved *P. horikoshii* structure (*37*) are shown above the alignment. Vertical arrows point to the proposed catalytic triad proposed by Du *et al.* that is composed of an aspartate, a cysteine, and a lysine residue. The proposed metal-binding residues are shown with an M under the appropriate residue.

In Chapter 4 we provide extensive structural characterization of a variety of liganded states of the nicotinamidase from *Streptococcus pnemoniae* (SpNic, (*38*))

These structures illuminate important mechanistic states of the enzyme including the substrate bound condition, the probable structure of tetrahedral intermediates as well as the structure of the proposed thioester intermediate. In this paper, we characterize the Michaelis Menten properties for a number of nicotinamidases from multiple sources including *S. cerevisiae* (Pnc1), *B. Burgdorferei* (BbNic), *P. falciparum* (PfNic), *S. pnemoniae* (SpNic) and two nicotinamidase isoforms from *C. elegans* (CePNC1 and CePNC2). We present the first continuous assay to monitor nicotinamidase catalytic function and show that these enzymes have high catalytic efficiency for nicotinamide and can also accept a number of additional substituted nicotinamide substrates. In addition we found that all of these enzymes are inhibited by nicotinaldehyde with K_i values in the range 1.5 μM to 20 nM. The kinetics of inhibition by nicotinaldehyde for these enzymes reveal competitive binding with nicotinamide, consistent with reversible mechanism-based trapping of the enzyme. The mechanism of inhibition was determined by the crystallization of nicotinaldehyde and 5-O-methyl nicotinaldehyde tetrahedral adducts on the *Streptococcus pneumoniae* enzyme, structures presented in Chapter 4 (*38*). Structural variants of nicotinaldehyde were also synthesized and biochemically evaluated, establishing the possibility of developing potent yet selective inhibitors for nicotinamidases derived from different sources. Using information provided by nicotinaldehyde inhibition studies, kinetic studies, sequence comparisons, ^{18}O exchange into nicotinic acid catalysed by SpNic, and the available structural information (*38*) we present a detailed chemical mechanism to explain nicotinamide hydrolysis catalyzed by this enzyme class.

3.3 Materials and Methods

Reagents and Instrumentation. Unless otherwise stated in the text, all reagents were purchased from Sigma-Aldrich or VWR and were of the highest purity commercially available. UV analyses were performed on a Hitachi U-3010

spectrophotometer. Fluorescence analyses were performed on a LJL Biosystems Analyst AD 96.384 microplate reader.

Plasmid Construction and Protein Expression. Standard molecular biology techniques were used to clone the genes of interest. Briefly, the nicotinamidase gene for *Streptococcus pneumoniae* was amplified by PCR from genomic DNA (ATCC 6314D) using primers (5'CAT ATG ATG ACA AAG GCT TTA ATT TGC ATT3' and 5'GGA TCC TTA CTC AAA AAG TTC ATT TAG ATT TTC ATC3') engineered to contain the NdeI and BamHI restriction endonuclease recognition sites. The PCR product was inserted into the pSTBlue vector (Novagen) using the AccepTor vector kit (Novagen). The gene was digested with NdeI and BamHI and ligated into similarly digested Pet28a; the presence of the gene was verified by sequencing. The protein obtained was called SpNic. The nicotinamidase gene from *Borrelia burgdorferi* was cloned from a construct pBBE22 provided by Steven J. Norris, Ph.D. of University of Texas Health Science Center at Houston. As previously reported (*39*) in order to produce a functional nicotinamidase an additional 48 base pairs upstream of the annotated start codon were required. PCR was used to amplify the extended gene using primers engineered to include NdeI and BamHI cut sites (5'CAT ATG ATG CCA GTA TCT AAC AGT AAT GAA ATA ATT TCT TTG ATT3' and 5'GGA TCC TTA TAT ATT AAG CTT ACT TTG GCT GTC GAA GAT GTC C3'). The PCR product was inserted into the pSTBlue vector (Novagen) using the AccepTor vector kit (Novagen). The gene was digested with NdeI and BamHI and ligated into similarly digested Pet28a; the presence of the gene was verified by sequencing. The protein obtained was called BbNic. The nicotinamidase gene for *Plasmodium falciparum* was amplified from cDNA provided by Kirk Deitsch of Weill Medical College using primers engineered to included the EcoRI and HindIII restriction endonuclease sites (5'AGA ATT CAT GAA ATG CCT TGT TAT AGT TGA TGC

ACA A3' and 5'GCA AGC TTA TGA CAA AAG TTT TGA TGA GTT AAT AAA TTT GAT TCC3'). The PCR product was inserted into the pSTBlue vector (Novagen) using the AccepTor vector kit (Novagen). The gene was digested with NdeI and BamHI and ligated into similarly digested Pet28a; the presence of the gene was verified by sequencing. The protein obtained was called PfNic. In all cases the constructs were transformed into Codon+ cells (Stratagene) and grown with shaking at 37^{o}C to an O.D. of 0.6 before inducing with 0.5 mM IPTG. After 6 hours of growth post-induction at 37^{o}C the cells were harvested and lysed using lysozyme followed by three successive freeze-thaw cycles. After treatment with DNAse, the cell debris was pelleted and the supernatant was added to pre-equilibrated Ni-NTA nickel resin (Qiagen). After successive washes with 5 mM and 10 mM imidazole in 10 mM Tris, the protein was eluted from the nickel resin with 250 mM imidazole in 10 mM Tris. The elutions were immediately tested for activity and purity of the samples was assessed by SDS-polyacrylamide gel electrophoresis. Active fractions with purity greater than 90% were pooled and aliquots were flash frozen in 20% glycerol and 2 mM DTT. *C. elegans* PNC1 and PNC2 (CePNC1 and CePNC2) was expressed and purified as described (*12*) and the expression plasmid of *S. cerevisiae* Pnc1 was received as a gift from Dr. Jeffrey Smith of the University of Virginia and expressed and purified as described previously (*24*).

GDH Coupled Nicotinamidase Assay. Nicotinamidase activity was monitored by coupling the production of ammonia with the consumption of NAD(P)H by the enzyme bovine glutamate dehydrogenase (GDH, from Sigma). A typical reaction contained 1 mM α-ketoglutarate, 250 μM NAD(P)H, 1.5 units of GDH per 100 μL of reaction volume, and different concentrations of nicotinamide in 100 mM phosphate buffer, pH 7.3. The components were mixed and placed in cuvettes (for analysis by UV, 340 nm detection wavelength), or into a 96-well plate (for analysis on a plate

reader using fluorescence). The reaction was initiated by addition of the appropriate nicotinamidase enzyme and the absorbance at 340 nm was used to monitor concentration of NAD(P)H with time. In plate reader experiments, fluorescence intensity was used for this purpose (excitation 360 nm, emission 490 nm).

HPLC Assay for Nicotinamidase Activity. All HPLC analyses were performed on a Hitachi Elite Lachrom system equipped with diode array detector. A typical injection (Macherey-Nagel Nucleosil C-18 250 mm x 4.6 mm) employed 20 mM ammonium acetate, pH 6.9 at 1mL/min for 15 min. and was then followed by 20 mM ammonium acetate pH 6.9 10% methanol. Authentic nicotinic acid elutes at 4.2 min. and nicotinamide elutes at 16 min using 260 nm as a detection wavelength (typical chromatograms are available in Figure 3.2).

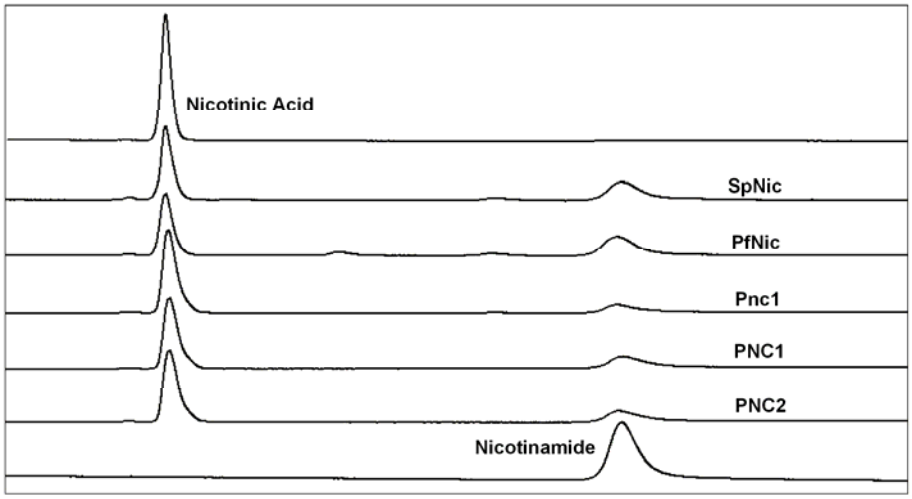

Figure 3.2. HPLC chromatograms showing the conversion of nicotinamide to nicotinic acid by nicotinamidases. A typical reaction was run on a 50 µL scale containing 200 µM of nicotinamide in 100 mM phosphate buffer at pH 7.3. The reaction was initiated by addition of nicotinamidase enzyme and incubated at 25^{o}C to allow approximately 50% nicotinamide conversion. The reaction was quenched by addition of 6 µL of 10% trifluoroacetic acid to a final pH 3 and then allowed to incubate on ice for 30 minutes. Prior to injection on HPLC, the sample was centrifuged at 13,000 g for 2 minutes to remove precipitates. Authentic chemical standards of nicotinamide and nicotinic acid were injected to determine retention times for substrate and product.

In some instances a Waters 300 mm x 7.8 mm Delta-pak C18 column was used for HPLC measurements with slight adjustments to the assay method. A typical reaction was run in 50 μL total volume containing 200 μM nicotinamide in 100 mM phosphate buffer at pH 7.3. The reaction was initiated by addition of nicotinamidase enzyme (10-200 nM final concentration) and allowed to incubate for 20 minutes at 25 ^{o}C. The reaction was quenched by 6 μL addition of 10 % trifluoroacetic acid and incubated on ice for 30 minutes. Prior to injection on HPLC, the sample was centrifuged at 13, 000 g for 2 minutes to remove precipitates.

Michaelis-Menten Initial Rate Analysis. For CePNC1 and CePNC2, the GDH coupled assay described above was used to determine the Michaelis-Menten parameters. Reactions were run in 150 μL total volume containing varying concentrations of nicotinamide (0, 10, 20, 30, 40, 50, 75, 100, 200, 400 and 600 μM) on a 96-well plate. The reactions were initiated by addition of nicotinamidase (final concentration 500 nM PNC1, 2 μM PNC2) and decreasing fluorescence intensity was monitored by a microplate reader for a total of 2,500 seconds at 45 seconds intervals. The initial rates of reactions were derived from the slope of product formed versus time where extent of reaction had not exceeded 15% of substrate in each case. Determined rates were plotted against nicotinamide concentrations and fit with the Michaelis-Menten equation using Kaleidagraph® (Synergy Software).

Michaelis-Menten-Progress Curve Analysis. For SpNic and Pnc1, kinetic parameters were measured by the GDH coupled assay described above and calculated by progress curve analysis. Reactions were run in 600 μL total volume containing 100 μM of nicotinamide in UV cuvettes. The reactions were initiated by addition of nicotinamidase (e.g. final concentration: 200 nM Pnc1). The absorbance at 340 nm was monitored by UV spectrophotometer over a total of 12 to 15 minutes at 16 s intervals for SpNic, and 25 s intervals for Pnc1. Progress curve analysis involved

approximating instantaneous rates at a time t_x, where product formation at t_{x-1} and t_{x+1} was determined and the $\Delta P/\Delta t$ calculated to determine the instantaneous rate. t_x represents the mid time point between t_{x-1} t_{x+1} and the t_{x-1} t_{x+1} represent the start and end points of the time interval. Rates were plotted *vs.* the substrate concentration at each time calculated for each point and the data fit to the Michaelis-Menten equation to determine K_m and V_{max} values. The method is similar to that published for this approach (*40*).

Michaelis-Menten HPLC Analysis. For BbNic and PfNic, The HPLC assay described above was used to measure the Michaelis-Menten parameters. Nicotinamide was incubated at concentrations of 0, 20, 40, 60, 80, 120, 160, 200 and 400 μM. For BbNic, the enzyme was used at a final concentration of 5.4 μM. The chromatograms were analyzed at wavelength of 260 nm. Reactions were quantified by integrating areas of peaks corresponding to nicotinamide and nicotinic acid. Rates were plotted versus nicotinamide concentration and best fit of points to the Michaelis-Menten equation was performed by Kaleidagraph®.

For *P. falciparum* nicotinamidase, reactions containing 0, 2.5, 3.75, 5, 7.5, 10, 20, 25, 50 μM of nicotinamide with 20% [carbonyl-C^{14}]-nicotinamide in 100 mM phosphate budder pH 7.3 were initiated with the addition of PfNic, reactions were incubated at room temperature for 7 minutes and quenched by addition of 8 μL of 10% trifluoroacetic acid. After centrifugation at 13,000 g for 2 minutes, the reactions were injected on HPLC to separate nicotinamide and nicotinic acid. Eluents containing nicotinamide and nicotinic acid were collected and radioactivity was determined by scintillation counting. Rates were determined as cpm/s conversion to nicotinic acid, and then converted to a turnover rate (s^{-1}) by adjustment for specific radioactivity of nicotinamide and enzyme concentration. Rates were plotted versus nicotinamide

concentration and best fit of plotted data to the Michaelis-Menten curve was performed using Kaleidagraph®.

Inhibition Analysis. To determine inhibition, reactions were performed using the GDH coupled assay described above. Reactions containing 1 mM α-ketoglutarate, 250 μM NAD(P)H, 1.5 units of GDH per 100 μL of reaction volume, and 200 μM of nicotinamide, and varying concentrations of inhibitors in 100 mM phosphate buffer, pH 7.3, were initiated with the addition of nicotinamidases. Rates were plotted and points fit to equation (1) using Kaleidagraph®:

$$v_{inh.} = (V_{max}*[S])/([S] + (K_m\,(1 + [I]/K_i) \quad (1)$$

where $v_{inh.}$ is the inhibited rate for a given concentration of inhibitor, V_{max} is the uninhibited rate, [S] is the nicotinamide concentration, K_m is the Michaelis constant for nicotinamide for a given nicotinamidase, [I] is the inhibitor concentration and K_i is the binding constant for competitive inhibition. In some cases relative rates were plotted and points fit to equation (2) using Kaleidagraph®:

$$v_{inh}/V_{max.} = [S]/([S] + (K_m*(1 + [I]/K_i) \quad (2)$$

where $v_{inh.}$ is the inhibited rate for a given concentration of inhibitor, V_{max} is the uninhibited rate, [S] is the nicotinamide concentration, K_m is the Michaelis constant for nicotinamide for a given nicotinamidase, [I] is the inhibitor concentration and K_i is the binding constant for competitive inhibition.

Competition Analysis of Inhibitor. Nicotinaldehyde, characterized as an inhibitor by use of the GDH coupled assay described above, was used for the competitive analysis. Inhibition reactions were performed in 150 μL volumes containing 1 mM α-ketoglutarate, 250 μM NADPH, 2.25 units of GDH, and different concentrations of nicotinamide (50, 100, 250, 500 and 1000 μM) in 100 mM phosphate buffer, pH 7.3. The inhibitor concentrations were from 0 to twice or five times its estimated K_i as indicated in Figure 3.3.

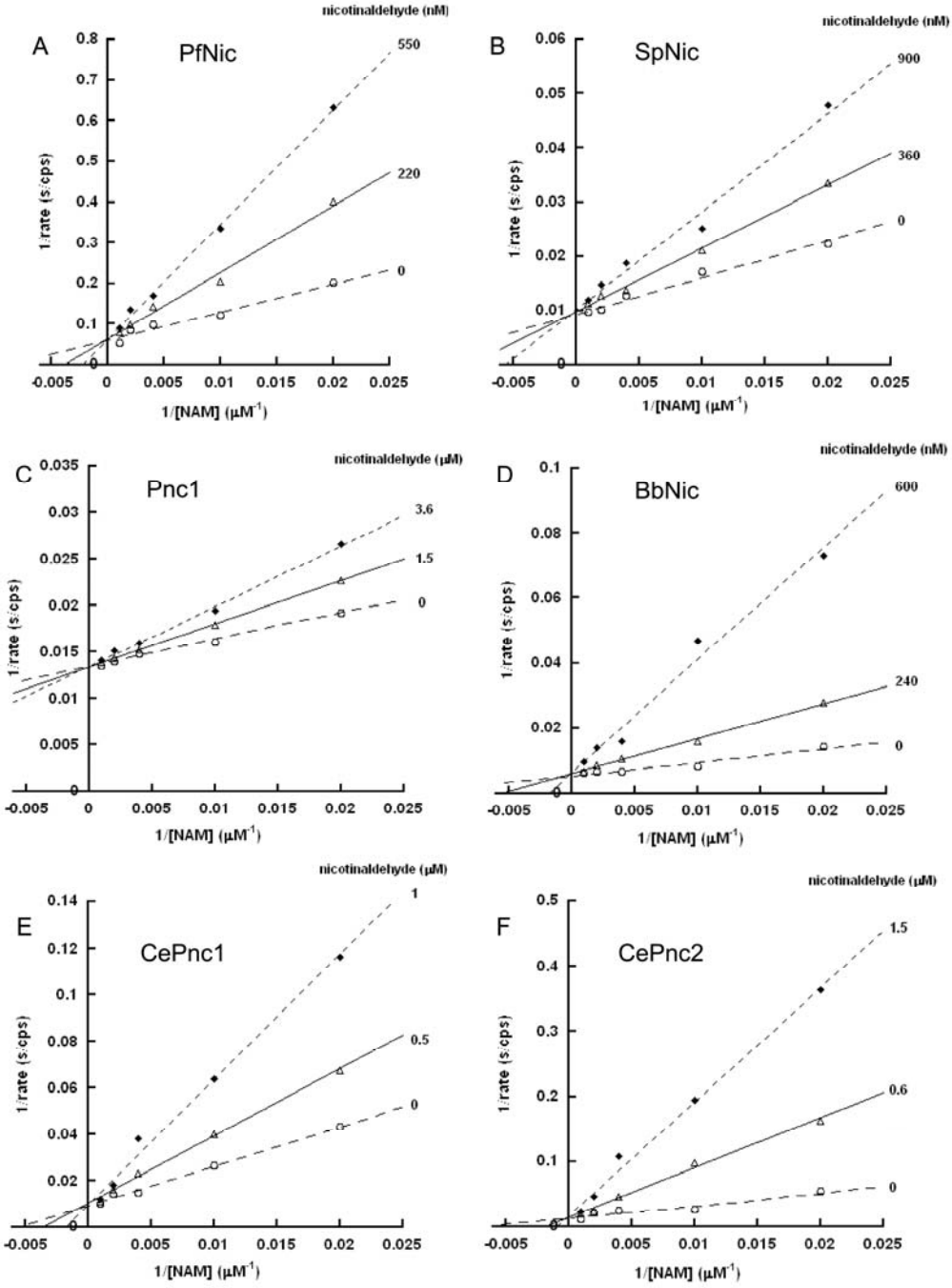

Figure 3.3. The Lineweaver-Burke plots for nicotinamidases. Curves were obtained in the presence of three different concentrations of nicotinaldehyde, demonstrating the competitive nature of the inhibitor with substrate. These curves were used to determine the K_i values for nicotinaldehyde in Table 3.4.

Reactions were initiated by addition of the nicotinamidase enzymes (varying from 20 nM to 5 μM). Double reciprocal plots of 1/*v* versus 1/[Nicotinamide] at different fixed concentrations of the inhibitor were plotted, the intersection of the lines at 1/*v* axis indicated competitive inhibition. All data points were fitted to double reciprocal plots using Kaleidagraph®.

Isotope Exchange catalyzed by Streptococcus pneumoniae nicotinamidase. Reactions of volume 25μL in 40mM phosphate buffer pH 7.0 containing 90% ^{18}O-H_2O, 1 mM nicotinic acid and 6 μM *Streptococcus pneumoniae* nicotinamidase. After incubation for 0 (pre quenched), 2, 10, 30, 60 min at 37 ^{o}C, the reaction was quenched with 4 μL of 10% trifluoroacetic acid. A no enzyme control was run identically for 60 minutes and quenched identically. 20 μL of the solution injected into a C-18 reverse phase column (EC250/4.6 NUCLEODUR 100-5 C18, Macherey-Nagel) to separate nicotinic acid from other components using 20mM ammonia acetate pH 7.0 as the eluent and fractions were collected. Fractions containing nicotinic acid were lyophilized and then dissolved into 10 μL water. 1μL of the sample was spotted on a MALDI plate and after drying 1μL of the matrix composed of 10 mg/mL α-cyano-4-hydroxycinnamic acid (CHCA) and 0.1% TFA (50: 50 v/v) was spotted to the plate and dried. The mass spectrum was acquired by an Applied Biosystems DE-STR MALDI-TOF spectrometer (Rockfeller University, Proteomics Resource Center). For each sample, the intensity of isotope was recorded through 200 shots in each measurement and the measurement was repeated three times. Non-labeled nicotinic acid was detected at m/z = molecular weight of 124.07(5) which represents the twice protonated species. Nicotinic acid incorporating one ^{18}O was detected 126.07(5) and nicotinic acid with two ^{18}O isotopes was detected at 128.07(5). Complete exchange of ^{18}O into nicotinic acid was observed after an hour and significant exchange was measured at 2 minutes. No exchange was observed for control. The rate of exchange

was calculated to be 0.7 s^{-1}. Formation of ^{18}O nicotinic acids (single and double labeled) was confirmed by HRMS (CUNY Hunter Mass Spectrometry Facility). The predicted m/z for single labeled ^{18}O nicotinic acid ($C_6H_5NO[^{18}O]$) was calculated to be 125.0363 and measured to be 125.0365, while for (C_6H_5N[18O]2) the calculated m/z was 127.0405 and the measured m/z was 127.0407.

Synthesis of Substrate Analogues. Nicotinamide, 2-chloronicotinamide, 6-chloronicotinamide, 6-methylnicotinamide, 6-aminonicotinamide, isonicotinamide and ethyl nicotinate were purchased from Aldrich. Thionicotinamide was purchased from Acros. We also thank Peter Tyler of IRL New Zealand for several samples of nicotinamides including 5-methylnicotinamide, 6-chloronicotinamide, 6-methylnicotinamide 6-aminoisonicotinamide and 6-aminonicotinamide used for parts of this study. 5-methylnicotinamide was alternatively synthesized as reported (*21*). *5-Methoxynicotinamide* was synthesized from the corresponding aldehyde (*41*). 5-Methoxy-3-pyridinecarboxaldehyde (400 mg, 2.92 mmol) was dissolved in 4 mL of methanol, to this solution was added hydroxylamine hydrochloride (264 mg, 3.80 mmol). The reaction mixture was allowed to stir at room temperature for 4 hours. Solvent was removed under reduced pressure, residue was redissolved in 3 mL of dry pyridine, and to this solution was added methanesulfonyl chloride (435 mg, 3.80 mmol). The mixture was stirred at room temperature for 2 hours, and then water and ethyl acetate were added. Combined organic layer was dried over Na_2SO_4. Column chromatography (hexanes: ethyl acetate = 4:1) afforded 320 mg (2.39 mmol, 82% yield) of 3-cyano-5-methoxypyridine as a white solid. ^1H NMR (400 MHz, $CDCl_3$), δ ppm: 8.49 (d, *J*= 2.8 Hz, 1H), 8.46 (d, *J*= 1.5 Hz, 1H), 7.37 (dd, *J*= 1.6, 2.8 Hz, 1H), 3.89 (s, 3H). Hydrogen peroxide (4 mL) was added dropwise to a solution of 3-cyano-5-methoxypyridine (320 mg, 2.39 mmol) and K_2CO_3 (790 mg, 5.72 mmol) in 3 mL of DMSO, the mixture was stirred for one hour before it was diluted with water and

lyophilized to dryness. The crude product was purified by column chromatography (ethyl acetate: ethanol = 10:1) followed by recrystallization in ethyl acetate to afford 200 mg (1.32 mmol, 55% yield) of 5-methoxynicotinamide as white solid. ^{1}H NMR (400 MHz, DMSO), δ ppm: 8.62 (d, *J*= 1.7 Hz, 1H), 8.40 (d, *J*= 2.9 Hz, 1H), 8.13 (s, br, 1H), 7.74 (dd, *J*= 1.8, 2.8 Hz, 1H), 7.59 (s, br, 1H), 3.86 (s, 3H).

4-Methoxynicotinamide was synthesized from the corresponding aldehyde (*41*). 4-Methoxy-3-pyridinecarboxaldehyde (180 mg, 1.31 mmol) was dissolved in 2 mL of methanol, to this solution was added hydroxylamine hydrochloride (118 mg, 1.70 mmol). The reaction mixture was allowed to stir at room temperature for 4 hours. Solvent was removed under reduced pressure, residue was redissolved in 2 mL of dry pyridine, and to this solution was added methanesulfonyl chloride (195 mg, 1.70 mmol). The mixture was stirred at room temperature for 2 hours, and then water and ethyl acetate were added. Combined organic layer were dried over Na_2SO_4. Column chromatography (hexanes: ethyl acetate = 1:2) afforded 135 mg (1 mmol, 78% yield) of 3-cyano-4-methoxypyridine as white solid. ^{1}H NMR (400 MHz, $CDCl_3$), δ ppm: 8.67 (s, 1H), 8.62 (d, *J*= 6.0 Hz, 1H), 6.90 (d, *J*= 6.0 Hz, 1H), 3.99 (s, 3H). Hydrogen peroxide (1.67 mL) was added dropwise to a solution of 3-cyano-4-methoxypyridine (135 mg, 1mmol) and K_2CO_3 (333 mg, 2.4 mmol) in 3 mL of DMSO, and the mixture was stirred for one hour before it was diluted with water and lyophilized to dryness. The crude product was purified by column chromatography (ethyl acetate: ethanol = 10:1) followed by recrystallization in ethyl acetate to afford 100 mg (0.66 mmol, 66% yield) of 4-methoxynicotinamide as white solid. ^{1}H NMR (400 MHz, DMSO), δ ppm: 8.70 (s, 1H), 8.51 (d, *J*= 5.8 Hz, 1H), 7.64 (s, br, 1H), 7.61 (s, br, 1H), 7.15 (d, *J*= 5.9 Hz, 1H), 3.93 (s, 3H).

2-Aminoisonicotinamide was synthesized as described before (*42*) with several modifications. Briefly, acetylation of 2-amino-4-picoline followed by oxidation using

$KMnO_4$ gave 2-acetylamino isonicotinic acid. This compound was subjected to amidation in the presence of DCC and ammonia in methanol to yield 2-acetylamino isonicotinamide. Further reaction of 2-acetylamino isonicotinamide with ammonia in methanol provided the desired 2-aminoisonicotinamide in modest yield.

4-Methoxyphenyl nicotinate (12) was synthesized from nicotinoyl chloride hydrochloride. To a 100 mL round-bottom flask were added nicotinoyl chloride hydrochloride (770 mg, 4.33 mmol), 5 mL of triethylamine and 20 mL of THF. To this mixture was added 4 mL of pyridine dropwise. After stirring for 30 minutes at room temperature, *p*-methoxyphenol (805 mg, 6.49 mmol) was added. The reaction was kept at room temperature overnight, precipitate was filtered off and solution was evaporated under reduced pressure. The residue was redissolved in water and extracted with CH_2Cl_2. The combined organic layer was washed with brine and dried over anhydrous Na_2SO_4. Solvent was then concentrated in *vacuo* and crude product was recrystallized from ethyl acetate. ^{1}H NMR (500 MHz, $CDCl_3$), δ ppm: 9.37 (t, *J*= 1.1 Hz, 1H), 8.82 (dd, *J*= 1.7, 4.9 Hz, 1H), 8.42 (dt, *J*= 1.9, 7.9 Hz, 1H), 7.44 (m, 1H), 7.13 (dd, *J*=2.3 Hz, 2H), 6.93 (dd, *J*= 2.3 Hz, 2H), 3.80 (s, 3H).

1-Methylnicotinamide was synthesized similarly to the method reported by Martin and Hull (*43*). Briefly, three equivalents of iodomethane were added to a solution of nicotinamide or isonicotinamide in 2 mL of methanol. The reaction was allowed to stir at room temperature and monitored by TLC. When the reaction was complete (after approximately 30 hours), the solid was filtered off and dried under reduced pressure. The resulting product was purified by recrystallization from methanol. 1-Methylnicotinamide ^{1}H NMR (500 MHz, DMSO), δ ppm: 9.4 (s, 1H), 9.11 (d, *J*= 6.1 Hz, 1H), 8.90 (d, *J*= 8.2 Hz, 1H), 8.51 (s, br, 1H), 8.25 (dd, *J*= 6.1, 8.1 Hz, 1H), 8.14 (s, br, 1H), 4.42 (s, 3H). 1-methyl-isonicotinamide was prepared similarly.

Synthesis of Inhibitors. 3-Pyridinecarboxaldehyde, 5-bromo-3-pyridinecarboxaldehyde, 2-chloro-3-pyridinecarboxaldehyde, 3,5-lutidine, 3,5-dibromopyridine, 4-methoxypyridine, 3-cyanopyridine, 3-acetylpyridine, 3-hydroxypyridine and nicotinic acid were purchased from Aldrich.

5-Methoxy-3-pyridinecarboxaldehyde was synthesized in two steps from 3,5-dibromopyridine (*44*). Sodium methoxide in methanol (4 mL, 9.56 mmol) was stirred under reduced pressure at 65˚C for 10 minutes. The remaining solid was dissolved in 5 mL of DMF. Solid 3,5-dibromopyridine (1.5 g, 6.33 mmol) was added, and the mixture was stirred at 63~68˚C for one hour. This solution was poured into water and then extracted with ethyl acetate. The combined organic layer was washed with brine and dried over anhydrous Na_2SO_4. After solvent was evaporated under reduced pressure, column chromatography afforded 1 g (5.32 mmol, 85% yield) of 3-bromo-5-methoxypyridine as a white solid. ^{1}H NMR (400 MHz, $CDCl_3$), δ ppm: 8.31 (s, 1H), 8.26 (s, 1H), 7.35 (s, 1H), 3.88 (s, 3H). To a stirred solution of 3-bromo-5-methoxypyridine (1 g, 5.3 mmol) in 20 mL of anhydrous THF at -90˚C was added *n*BuLi (2.9 mL, 5.8 mmol) over 5 minutes. The solution was allowed to stir for another 20 minutes at -90˚C, and then DMF (0.53 mL, 6.9 mmol) was added. The reaction mixture was stirred for 30 minutes and the cold mixture was poured directly into brine and extracted with ethyl acetate. The combined organic layer was dried over anhydrous Na_2SO_4. After solvent was evaporated under reduced pressure, column chromatography afforded 0.5 g (3.65 mmol, 68% yield) of 5-methoxy-3-pyridinecarboxaldehyde as a pale yellow solid. ^{1}H NMR (400 MHz, $CDCl_3$), δ ppm: 10.08 (s, 1H), 8.63 (d, J= 1.5 Hz, 1H), 8.53 (d, J= 3 Hz, 1H), 7.58 (dd, J= 1.5, 3 Hz, 1H), 3.89 (s, 3H).

5-Methyl-3-pyridinecarboxaldehyde was synthesized in three steps from 3,5-lutidine. 3,5-lutidine was converted to 5-methylnicotinic acid as described previously

(*45*). 5-methylnicotinic acid (100 mg, 0.73 mmol), triphenylphosphine (382 mg, 1.46 mmol) and methanol (47 mg, 1.46 mmol) were dissolved in 1 mL of anhydrous THF, and to this solution was added DIAD (295 mg, 1.46 mmol) at 0°C dropwise. The reaction mixture was allowed to warm to room temperature and stir overnight. Saturated brine was added to quench the reaction and then the aqueous layer was extracted with ethyl acetate. The combined organic layer was dried over anhydrous Na_2SO_4 and concentrated under reduced pressure. The crude product was purified by column chromatography to afford 70 mg (0.46 mmol, 64% yield) of 5-methylnicotinic acid methyl ester as white solid. ^{1}H NMR (500 MHz, $CDCl_3$), δ ppm: 9.01 (s, 1H), 8.59 (s, 1H), 8.09 (s, 1H), 3.93 (s, 3H), 2.38 (s, 3H). To a solution of 5-methylnicotinic acid methyl ester (70 mg, 0.46 mmol) in 2 mL of toluene was added DIBAL-H (3.2 mL, 3.2 mmol) dropwise at -78°C. The reaction was kept at -78°C for one hour before being quenched by methanol at -20°C. To the reaction mixture was then added 0.1 M HCl and ether, the aqueous phase was extracted with ether, the combined organic phase was washed with saturated $NaHCO_3$, water and brine, and then dried over anhydrous Na_2SO_4. Solvent was evaporated under reduced pressure and crude product was purified by column chromatography to afford 50 mg (0.41 mmol, 89% yield) of 5-methyl-3-pyridinecarboxaldehyde as colorless oil. ^{1}H NMR (500 MHz, $CDCl_3$), δ ppm: 10.08 (s, 1H), 8.87 (s, 1H), 8.67 (s, 1H), 7.95 (s, 1H), 2.43 (s, 3H).

6-Fluoro-3-pyridinecarboxaldehyde was synthesized from the corresponding carboxylic acid. In general, the acid was reduced with 1.1 equivalents of lithium aluminum hydride in refluxing anhydrous THF overnight. After quenching with ethyl acetate and water, the precipitate was filtered off, solvent was removed under reduced pressure and the alcohol was used for the next step without further purification. The alcohol was added to two equivalents of sodium nitrite followed by one equivalent of

acetic anhydride and stirred at 0°C (*46*). The reaction was monitored by TLC and upon completion the product was extracted with diethyl ether. The aldehyde was further purified by column chromatography. ^{1}H NMR (500 MHz, $CDCl_3$), δ ppm: 10.08 (s, 1H), 8.75 (d, *J*= 1.5 Hz, 1H), 8.32 (dt, *J*= 2.1, 8.2 Hz, 1H), 7.11 (dd, *J*= 2.5, 8.4 Hz, 1H).

4-Methoxy-3-pyridinecarboxaldehyde was synthesized in one step from 4-methoxy-pyridine (*44*). To a solution of *t*BuLi (1.7 M in pentane, 16.6 mL, 28 mmol) in 30 mL of anhydrous THF at -78˚C was added 2.2 g of 2-bromomesitylene (1.66 mL, 11 mmol). After strring at -78˚C for 1 hour, a pale yellow heterogeneous mixture was formed. To this mixture was then added 1.09 g of 4-methoxypyridine (1 mL, 10 mmol), and stirring was continued at -78˚C for 1 hour, at -23˚C for 1 hour and at room temperature for 1 hour. The mixture was again cooled to -78˚C, and 0.954 g of DMF (1 mL, 13.1 mmol) was added dropwise. After stirring at -78˚C for another hour, the reaction was quenched by saturated $NaHCO_3$ solution. The aqueous layer was extracted with ethyl acetate (3 x 10 mL), and the organic layers were combined and dried over anhydrous Na_2SO_4. After solvent was evaporated under reduced pressure, column chromatography afforded 0.88 g (6.4 mmol, 64% yield) of 4-methoxy-3-pyridinecarboxaldehyde as a pale yellow solid. ^{1}H NMR (400 MHz, $CDCl_3$), δ ppm: 10.42 (s, 1H), 8.86 (s, 1H), 8.61 (d, *J*= 6 Hz, 1H), 6.91 (d, *J*= 6 Hz, 1H), 3.98 (s, 3H).

3.4 Results

Cloning and Protein Expression. The genes encoding the nicotinamidase enzymes from *Borrelia burgdorferi* (BbNic), *Streptococcus pneumoniae* (SpNic) and *Plasmodium falciparum* (PfNic) were cloned into appropriate expression vectors as described in the Materials and Methods section. Expression plasmids for the two *C. elegans* nicotinamidases, CePNC1 and CePNC2 (*12*), and *S. cerevisiae* Pnc1 (*24*) were previously described. Expression and purification of the respective proteins are

described in the Methods and Materials. When assayed by HPLC under standard reaction conditions (200 μM nicotinamide, 100 mM phosphate, pH 7.3), all enzymes were found to catalyze the conversion of nicotinamide into nicotinic acid as shown by chromatograms stacked in Figure 3.2.

Nicotinamidase Assay Development. In order to monitor the activity of purified enzymes in real time, we developed a robust and straightforward assay that could continuously monitor one of the two products of the nicotinamidase reaction, ammonia. Bovine glutamate dehydrogenase (GDH), which is commercially available, was found to be an ideal enzyme for this purpose. GDH catalyzes the reaction of α-ketoglutarate, ammonia and NADPH (or NADH) to form glutamate and the oxidized dinucleotide (Scheme 3.3). The ammonia produced by conversion of nicotinamide to nicotinic acid is reacted by the coupling enzyme, which in turn consumes NADPH stoichiometrically. NADPH conversion to $NADP^+$ can be measured by absorbance of NADPH at a wavelength of 340 nm where $NADP^+$ has no absorbance ($\Delta\varepsilon_{340nm} = 6200$ M^{-1} cm^{-1}). Alternatively, the method was readily adapted to a plate reader which can detect fluorescence emission of NADPH (360 nm excitation, 490 emission). NADPH is measured by amount of emitted light and rates determined by changes in light emission versus time. Both methods were used to monitor nicotinamidase activity in this study.

A.

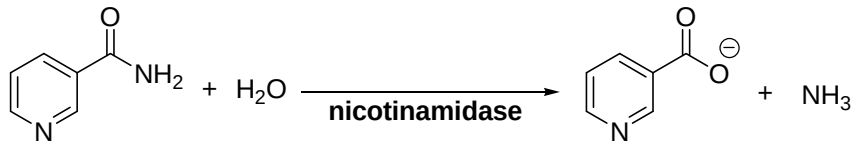

B.

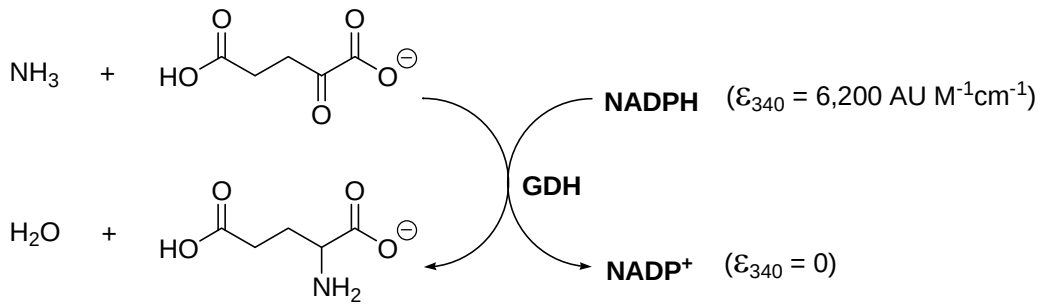

Scheme 3.3. The nicotinamidase assay developed couples the release of ammonia to the consumption of NAD(P)H via glutamate dehydrogenase. The synthesis of glutamate by GDH occurs in the presence of ammonia and α-ketoglutarate and is dependent upon the stoichiometric oxidation of NAD(P)H. The conversion of NAD(P)H to $NAD(P)^+$ can be followed by monitoring the decrease in absorbance at 340 nm or the decrease in fluorescence (excitation 360 nm, emission 490 nm).

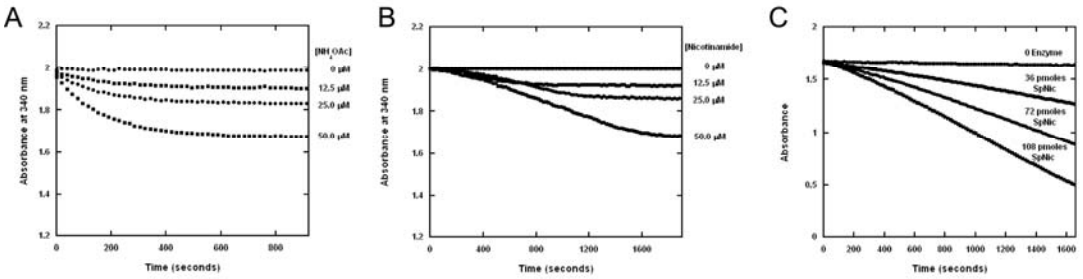

Figure 3.4. Glutamate dehydrogenase assay. (A) The GDH assay was performed with varying concentrations of ammonium acetate. (B) The GDH-coupled assay was performed with varying concentrations of nicotinamide. Reactions containing 1 mM α-ketoglutarate, 250 μM of NADPH, 1.5 units GDH per 100 μL of reaction volume in 100 mM phosphate buffer pH 7.3 were initiated with the addition of PfNic to a final concentration of 320 nM. The reactions were measured by monitoring the absorbance at 340 nm over time. (C) SpNic activity scales nicely with varying concentrations of enzyme. Reactions containing 1 mM α-ketoglutarate, 250 μM of NADPH, 1.5 units GDH per 100 μL of reaction volume in 100 mM phosphate buffer pH 7.3 were initiated with the addition of SpNic to the final concentrations indicated in the figure. The reactions were measured by monitoring the absorbance at 340 nm over time. The slopes for 0, 36, 72 and 108 pmoles of SpNic are -2.23×10^{-5}, -2.39×10^{-4}, -4.79×10^{-4} and -7.30×10^{-4}, respectively.

The quantity of NADPH consumed correlates well to nicotinamide or ammonia quantities added to a sample as shown in Figure 3.4 A and B. In addition, the rate of nicotinamidase activity scales linearly with amount of enzyme added, demonstrating that sufficient coupling enzyme is present so that GDH is not limiting for determination of catalytic velocity (Figure 3.4 C). This assay is effective for monitoring a wide range of nicotinamide concentrations and can accurately detect rates generated by low micromolar concentrations of nicotinamide, particularly because of a low K_m for NADPH of 28 μM, and an excellent rate of turnover (>9 s^{-1}, calculated from kinetic parameters) (*47*). Favorably, the equilibrium position also very strongly favors the oxidized dinucleotide product at pH 7.0 (*48*). Interference of GDH from nicotinamide and nicotinic acid was found to be neglible, and the components of the GDH assay did not interfere with nicotinamidase enzymatic activity as compared against HPLC (data not shown). The components of this assay, nicotinamidase and GDH, were recently combined in a coupled assay to detect and measure activity of nicotinamide forming enzymes, such as sirtuins, that degrade NAD^+ to nicotinamide (*49*).

Kinetics Parameters for Nicotinamidase Enzymes. Kinetic properties of nicotinamidase enzymes cloned or isolated from a variety of organisms have been determined including *Arabidosis thaliana* (*9*), *Mycobacterium tuberculosis* (*3*) *Mycobaceterium smegmatis (2), Lactobaccillus arabinosis (50, 51) Torula cremoris* (*7*), *Flavobacterium peregrinum (52)* and *S. cerevisiae* (*53-58*). Of the enzymes considered in this study, nicotinamidase activity of the *P. falciparum* enzyme was previously detected in crude dialyzed lysates derived from *P. falciparum* infected erythrocytes (*59*). With a reliable assay available, we sought to determine the kinetic parameters for Pnc1 as the prototype enzyme. In addition, the kinetic parameters for the *Streptococcus pneumoniae, Borrelia burgdorferi, Plasmodium falciparum* and

both *Caenorhabditis elegans* nicotinamidases were determined for the first time. Enzymes were expressed in *E. coli* and isolated by Ni^{2+} column chromatography. Although enzymes from different sources have been reported to have different central metal requirements (*3, 9, 34*), enzymes were active as purified without reconstituting them (Figure 3.2).

Employing standard conditions of assay (100 mM potassium phosphate, pH 7.3 with or without GDH components for detection of ammonia formed by nicotinamidase reaction, as described in Materials and Methods) we determined Michaelis-Menten parameters for each enzyme by varying nicotinamide concentration and plotting initial rates versus concentration of nicotinamide to determine K_m and V_{max} values (Figure 3.5, and Table 3.1). Maximum velocities were confirmed by HPLC assay using at least 10 fold K_m concentration of nicotinamide.

Table 3.1. Kinetic parameters of nicotinamidases

Enzyme	K_m (μM)[a]	V_{max} (s^{-1})[a]
BbNic	36.7 ± 7.5	0.0030 ± 0.00017[b]
PfNic	3.1 ± 1.2	0.30 ± 0.032[b]
Pnc1	10.6 ± 0.54	3.8 ± 0.060[b]
SpNic	5.1 ± 0.38	5.5 ± 0.13[b]
PNC1	83.5 ± 12.9	1.9 ± 0.11
PNC2	45.6 ± 6.6	0.12 ± 0.0056

[a]K_m and V_{max} values were determined by fitting the data to the Michaelis-Menten equation using the Kaleidagraph software package (Synergy Software). Error values represent the error in the fit to the data as calculated by the curve-fitting algorithm.
[b]Calculated V_{max} values were confirmed by HPLC assay for several enzyme concentrations.

For the Pnc1 and SpNic enzymes we used progress curve analysis (*40*), which was preferable due to a very low K_m for nicotinamide determined for these enzymes. A potential caveat with these analyses is product inhibition, which generally causes

increases in apparent K_m, but we showed that nicotinamidase rates do not vary when concentrations of nicotinic acid up to 500 μM are present (data not shown). Consistently, the Pnc1 and SpNic were determined to have K_m values of 10 and 5 μM for nicotinamide and corresponding values of k_{cat} of 3.8 s^{-1} and 5.5 s^{-1}.

For other nicotinamidases, we used the GDH method (CePNC1 or CePNC2) or an HPLC method (PfNic and BbNic) to determine initial reaction rates as a function of nicotinamide concentration. All data are summarized in Table 3.1 and shown graphically in Figure 3.5. All K_m values were found to be below 100 μM, with k_{cat} values in the range 0.3-10 s^{-1}. Only the BbNic deviated from the pattern. An examination of the BbNic sequence against the others (Figure 3.1) shows that the genetically encoded enzyme is approximately 20 residues (*52*) shorter at the N-terminus. This region contains a DXQXD sequence that is highly conserved in nicotinamidases (Figure 3.1). Thus, we introduced additional sequence at the N-terminus to create active enzyme (as was originally reported (*19*)). It remains possible that BbNic is imperfectly reconstituted in sequence or in other requirements, accounting for its poor catalytic properties.

Substrate Specificity. We probed the specificity of nicotinamidases to hydrolyze a variety of nicotinamide analogues. Using both HPLC analysis and the GDH coupled assay, we determined relative rates for a number of compounds showing structural similarity to nicotinamide (Table 3.2). In the cases of SpNic, Pnc1, and PfNic substitutions at the 5- position were well tolerated, and interestingly, 5-methyl and 5-O-methyl substitutions caused up to 4 .5 fold rate enhancement (in k_{cat}, see Table 3.3) over nicotinamide. The K_m and k_{cat} values for a small subset of the substrate analogues on the SpNic, Pnc1 and PfNic enzymes are provided in Table 3.3. These data indicate that the pattern of rate enhancement provided by the 5-position

substitutions is not associated with changes in K_m (Table 3.3) suggesting no steric interference in the binding of these substrates to the active site.

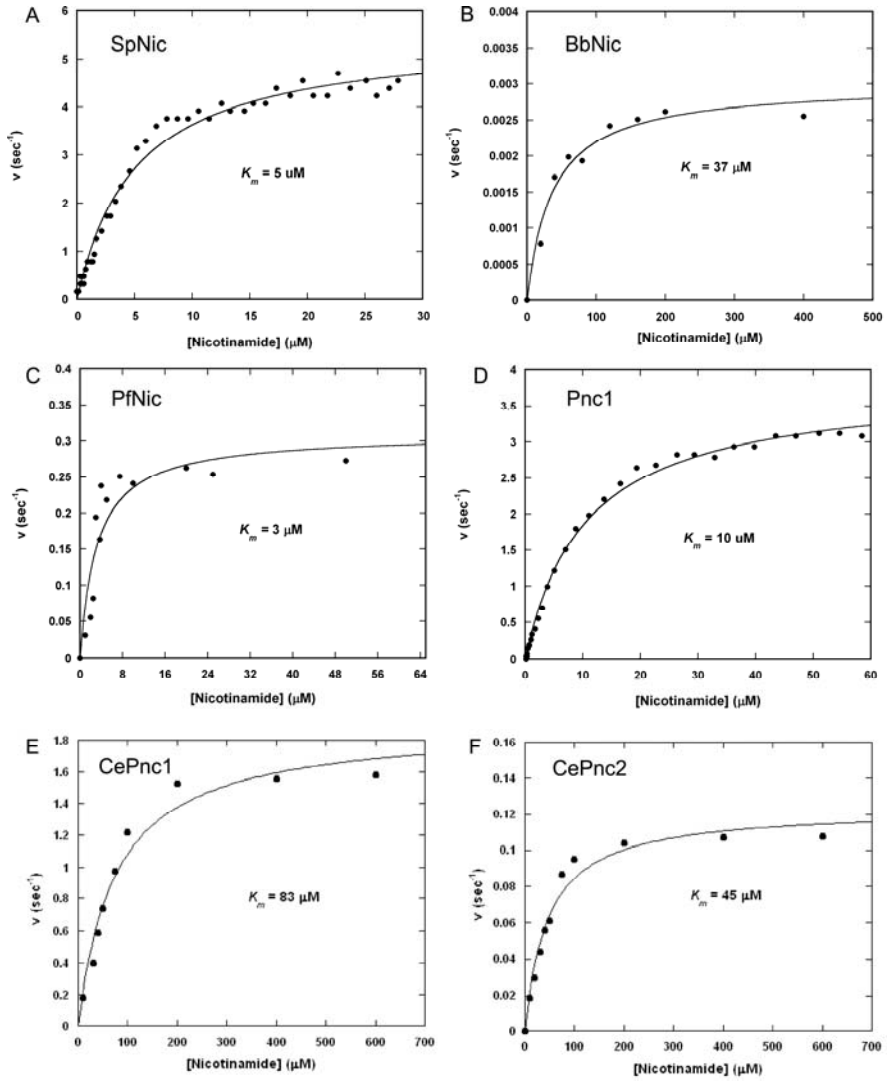

Figure 3.5. The kinetics of the nicotinamidase enzymes from *S. cerevisiae* (A), *B. burgdorferi* (B), *P. falciparum* (C), *S. pneumoniae* (D), *C. elegans PNC1* (E) and *C. elegans PNC2* (F). A and D were derived from progress curve analysis (see experimental) of the nicotinamidase reaction run in the presence of 100 μM nicotinamide, B and C are from HPLC analysis of reactions run in varying nicotinamide concentrations, and E and F are from the GDH coupled fluorescence assay with various concentrations of nicotinamide. In all cases, the data was fit with the Michaelis-Menten equation using KaleidaGraph graphing software.

Table 3.2. Relative rates of nicotinamidase enzymes for nicotinamide analogues[a]

Substrate	BbNic[b]	PfNic	pnc1	SpNic
nicotinamide	1.00	1.00	1.00	1.00
1	0.51	1.50	0.80	1.63
2	2.21	4.80	2.06	1.37
3	0	0	0	0
4	0	0	0.02	0.08
5	0.45	0.40	0	0.11
6	0.78	0.45	0.20	0.36
7	0.20	0.12	0.09	0.10
8	0.94	0.03	0.17	0.02
9	0.57	0.10	0.15	0.03
10	0	0	0.44	0
11	ND	0.39	0.05	0.04
12	ND	0	0.07	0.04
13	ND	0	0	0.03
14	ND	0	0	0

[a] Reactions were run in 150 μL total volume containing 1 mM α-ketoglutarate, 250 μM NADPH, 3 units of GDH, and 500 μM of nicotinamide analogue in 100 mM phosphate buffer, pH 7.3. For control experiments, reactions containing 500 μM of nicotinamide were run in parallel. Reactions were initiated by addition of nicotinamidase enzymes, decreasing of fluorescence intensity was monitored by a microplate reader.

[b]ND = Not determined.

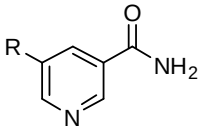

nicotinamide: R = H
1: R = CH_3
2: R = OMe

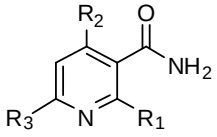

3: R_1 = Cl, R_2, R_3 = H
4: R_1, R_2 = H, R_3 = Cl
5: R_1, R_2 = H, R_3 = CH_3
6: R_1, R_2 = H, R_3 = NH_2
7: R_1, R_3 = H, R_2 = OMe

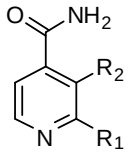

8: R_1, R_2 = H
9: R_1 = NH_2, R_2 = H

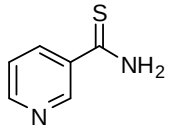

10

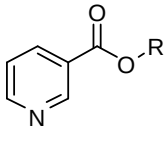

11: R = CH_2CH_3
12: R = *p*-OMe-Ph

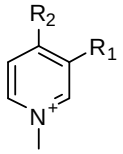

13: R_1 = $CONH_2$, R_2 = H
14: R_1 = H, R_2 = $CONH_2$

Table 3.3. Kinetic parameters of some nicotinamide analogues (μM)[a]

Substrate	pnc1		PfNic		SpNic	
	K_m (μM)	V_{max} (s^{-1})	K_m (μM)	V_{max} (s^{-1})	K_m(μM)	V_{max} (s^{-1})
NAM	10.6 ± 0.54	3.8 ± 0.06	3.1 ± 1.2	0.30 ± 0.03	5.1 ± 0.38	5.5 ± 0.13
5-Me-NAM	8.9 ± 0.7	3.5 ± 0.2	4.2 ± 0.5	0.6 ± 0.1	4.1 ± 0.6	8.8 ± 0.8
5-OMe-NAM	8.2 ± 0.56	7.7 ± 0.27	2.1 ± 0.2	1.9 ± 0.4	6.2 ± 0.4	7.5 ± 0.5
2-Cl-NAM	NS[b]	NS	NS	NS	NS	NS
6-Cl-NAM	NS	NS	1200.3 ± 70.1	0.004 ± 0.00015	1825.6 ± 122.7	0.31 ± 0.015

[a] Reactions containing various concentrations of nicotinamide analogues in 100 mM phosphate buffer at pH 7.3 were initiated by addition of nicotinamidase enzymes and allowed to incubate for 20 minutes at 25°C. The reaction was quenched by addition of 8 μL of 10% trifluoroacetic acid to a final pH of 3 and then allowed to incubate on ice for 30 minutes. Prior to injection on HPLC, the sample was centrifuged at 13, 000 g for 2 minutes to remove precipitates. Chromatograms were analyzed at wavelength of 260 nm. Reactions were quantified by integrating areas of peaks corresponding to nicotinamide analogue and nicotinic acid analogue. Rates were plotted versus nicotinamide analogue concentration and best fit of points to the Michaelis-Menten equation was performed by Kaleidagraph.
[b]NS = not a substrate

The origin of the 5-substitution effect on catalytic rate is unclear, and although it could be a steric effect it could also be an electronic effect. Moving the OMe group to the 4-position caused slowing of all enzymes to 9%-20% of the rate observed for nicotinamide (Table 3.2 and Table 3.3). Again, we are not clear if these changes in reaction rate are largely dictated by steric or electronic effects, although data from inhibitor studies sheds some light on these effects. Nicotinamidases (BbNic, PfNic, Pnc1 and SpNic) were weakly active against isonicotinamides and 1-methyl isonicotinamide and 1-methyl-nicotinamide derivatives. These results suggest that coordination of nicotinamide to the metal center is a prerequisite to catalysis as suggested in a recent mechanistic proposal (*34*), and that the spatial relationship of the carbamide group to the pyridine N is crucial for successful catalysis. The 2-chloronicotinamide and 6-chloronicotinamide were not well accepted either, this again

could be due to steric proximity of the 2 and 6-groups to the coordinating metal and since electron withdrawing groups deactivate ligand interactions with metals. 6-methyl and 6-aminonicotinamide were substrates for the 4 nicotinamidases but these nicotinamides were still slower than nicotinamide (0.09-0.78 relative rate versus nicotinamide, Table 3.2). Nicotinate esters, particularly ethylnicotinate, could be hydrolyzed as well, although more poorly than nicotinamide.

Sensitivity to substitutions showed similar trends for the four enzymes for which substrate specificity was broadly evaluated, although there were differences in the overall tolerance between organisms. *B. burgdorferi* appeared to be the most promiscuous enzyme, turning over at a moderate rate for a wide range of substrates, despite a slower rate of turnover for all substrates versus other enzymes. The Pnc1 and SpNic were the least tolerant of substitutions, showing little or no turnover for a large number of the substrates tested. The *P. falciparum* nicotinamidase saw the largest relative rate increases, with the 5-substituted compounds up to 4.8 times faster than nicotinamide.

Inhibition by Nicotinaldehyde. A report that *S. cerevisiae* nicotinamidase could be weakly inhibited by nicotinaldehyde K_i = 68 μM (*53*) led us to wonder if nicotinaldehydes might be general inhibitors of nicotinamidases. Unusual to this report, it was suggested that nicotinaldehyde inhibited the yeast enzyme by a non-competitive mechanism with nicotinamide, *via* Schiff's base formation. We sought to reinvestigate this inhibition. Nicotinaldehyde could potently inhibit nicotinamidases from all sources we examined (Table 3.4). Double reciprocal plots confirmed competitive inhibition with nicotinamide in all cases, and with surprising potency (Figure 3.3). Table 3.4 shows that the determined K_i values were in the range of 1.5 μM for the yeast enzyme, whereas K_i values were 13, 69 and 88 nM for the corresponding enzymes from *P. falciparum*, *S pnemoniae* and *B burgdorferei*

repsectively. Moreover, nicotinaldehyde could competitively inhibit both *C. elegans* enzymes with 136 nM and 400 nM K_i values for PNC2 and PNC1 respectively (Figure 3.3 and Table 3.4).

Table 3.4. K_i Values of Nicotinamidase Inhibitors (μM)

Substrate	**BbNic**	**PfNic**	**pnc1**	**SpNic**	**CePNC1**	**CePNC2**
15	0.088 ± 0.025	0.013 ± 0.0011	1.5 ± 0.11	0.069 ± 0.0040	0.45 ± 0.11	0.14 ± 0.01
16	1.8 ± 0.20	0.59	4.5 ± 0.80	0.072 ± 0.022	0.20 ± 0.058	0.32 ± 0.055
17	1.3 ± 0.43	0.052 ± 0.0045	5.0 ± 0.54	0.14 ± 0.017	0.54 ± 0.30	0.43 ± 0.12
18	1.1 ± 0.13	0.018 ± 0.0019	0.76 ± 0.070	0.068 ± 0.0054	ND[a]	ND
19	370	NI[b]	5000	110	ND	ND
20	19	4.9	NI	0.83 ± 0.29	ND	ND
21	153	1.1 ± 0.11	68	50	8.7 ± 1.0	1.3 ± 0.19
22	2000	1000	85	500	ND	ND
23	342	10	46	60	ND	ND
24	NI	NI	NI	NI	ND	ND
nicotinic acid	NI	NI	NI	2000	NI	NI

[a] ND= not determined.
[b] NI = no inhibition detected.

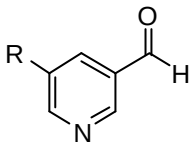

15: R = H
16: R = Br
17: R = OMe
18: R = Me

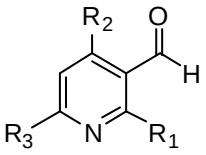

19: R_1 = Cl, R_2, R_3 = H
20: R_1, R_2 = H, R_3 = F
21: R_1, R_3 = H, R_2 = OMe

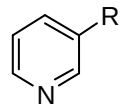

22: R = CN
23: R = Ac
24: R = OH
nicotinic acid: R = COOH

Nicotinaldehydes as inhibitors of nicotinamidases. To more completely explore the potency of nicotinaldehydes as inhibitors of nicotinamidases we synthesized a number of substituted analogues of nicotinaldehyde, with variable

substituents (as shown in Table 3.4). The K_i values for those compounds that showed inhibition of the nicotinamidase activity for the enzymes are listed in Table 3.4. We also tested several other compounds for inhibitory activity including acetylpyridine, 3-cyanopyridine, 3-hydroxypyridine and nicotinic acid (Table 3.4). Consistent with observations that 5-substituted nicotinamides are excellent substrates, 5-substituted nicotinaldehyde analogues were potent inhibitors of all of nicotinamidases tested (Table 3.4). All enzymes tolerated even a bulky 5-bromo substituent (Table 3.4). Consistent with observations that 4-O-methyl substitution was poorly tolerated in substrates, 4-O-methylnicotinaldehydes were weaker inhibitors with higher K_i values (Table 3.4). However, 4-O-methylnicotinaldehyde was a fair inhibitor of the CePNC2 enzyme, with a 6 fold selectivity over CePNC1, suggesting that variations in chemical structure of these compounds can lead to inhibitor specificity for isoforms. It should also be noted that the product of the nicotinamidase reaction, nicotinic acid, was not observed to inhibit the enzymes tested when applied at 1 mM. However, 3-acetylpyridine and 3 cyanopyridine could inhibit some enzymes, although with weaker K_i values than substrate K_m values, suggesting these 3-substituted pyridines bind competitively with nicotinamide. As suggested by the x-ray structures in Chapter 4 (*38*) these compounds likely coordinate to the central metal atom found at the active site of nicotinamidases.

Chemical Exchange of Nicotinic Acid Oxygens with ^{18}O Water. The crystal structure of a stabilized thioester complex co-crystallized on SpNic as reported in Chapter 4 (*38*) indicated to us that the enzyme can react with nicotinic acid reversibly to form the thioester. To more firmly establish this chemistry, we co-incubated nicotinic acid and *S. pneumoniae* enzyme with ^{18}O water and asked if the enzyme could support ^{18}O exchange into the carboxy oxygens of nicotinic acid which would be presumed to occur if nicotinic acid could reform the thioester. The cycling of

nicotinic acid to the thioester and back to nicotinic acid would be predicted to cause loss of ^{16}O in the carboxy oxygens and replacement with ^{18}O. We used mass spectrometry to monitor this exchange. As shown in Figure 3.6, nearly immediate loss of unlabeled nicotinic acid is observed when 1 mM nicotinic acid is treated with 6 μM SPNic enzyme.

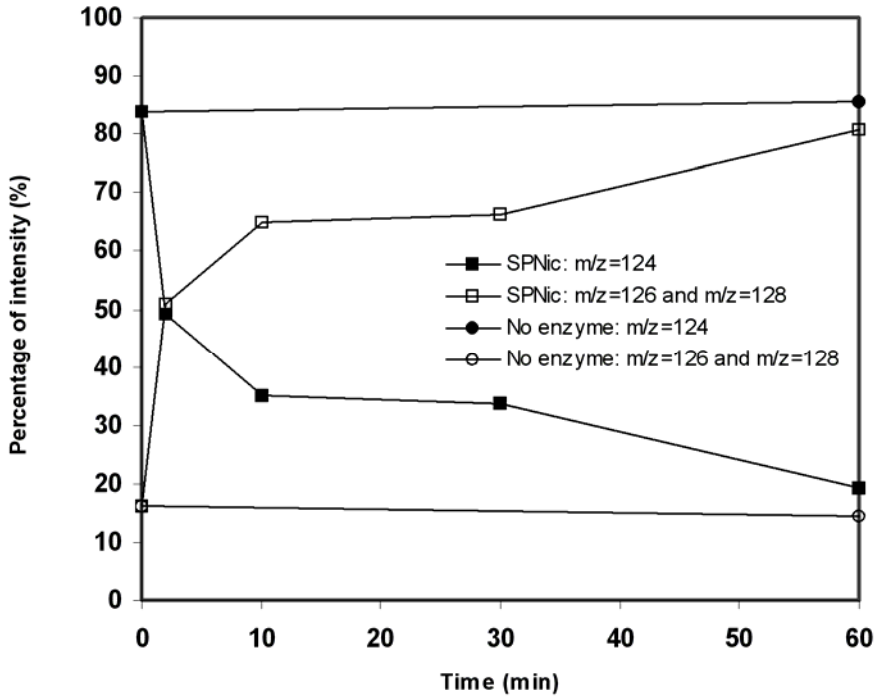

Figure 3.6. Mass spectra demonstrating time dependent ^{18}O exchange catalysed by SpNic. Data is plotted as percent intensity versus time, where the total intensities of peaks in mass spectra at ***m/z*** = 124, 126, 128 are summed to reach 100 percent. 124 is the mass of unlabeled nicotinic acid as a twice protonated cation (M+1). 126 is the molecular mass of nicotinic acid incorporating a single ^{18}O label, and 128 is the mass of nicotinic acid incorporating two ^{18}O atoms. For ease of presentation, mass intensities of single and double labeled nicotinic acid are summed. The data shows that the mass spectrum of nicotinic acid treated with SpNic in the presence of ^{18}O becomes rapidly depleted of intensity for the peak corresponding to ***m/z*** = 124, whereas there is a corresponding enrichment in ***m/z*** = 126 and ***m/z*** = 128 peak intensities, demonstrating rapid ^{18}O incorporation into nicotinic acid. Control does not exchange.

This loss is evident by depletion of m/z= 124 intensity in the MALDI, and is accompanied by increase in intensities for m/z = 126 and 128 (Figure 3.6). This process occurs in as little as 2 minutes, and the calculated rate for the process is 0.7 s^{-1}, indicating it is quite fast at pH 7. To more firmly establish that nicotinic acid was fully exchanged with ^{18}O water, we further analyzed the collected nicotinic acid after incubation with nicotinamidase by HRMS, which corroborated our result (see experimental). These results firmly establish that the nicotinic acid is able to undergo facile ^{18}O exchange, most likely by thioester formation from nicotinic acid catalyzed by the enzyme.

3.5 Discussion

Mechanism of Inhibition. As described in Chapter 4, the mechanism of aldehyde inhibition parallels, to some extent, the mechanism of catalysis (*38*). Nicotinamide initially coordinates the central metal atom, and is attacked by an active site cysteine to form a tetrahedral adduct that subsequently decomposes by elimination of ammonia to yield an enzyme stabilized thioester (*38*). Subsequent hydrolysis of the thioester completes nicotinic acid formation on the enzyme. Nicotinaldehydes bind the enzyme analogously via coordination of the pyridine N and are electrophillically activated by this coordination similar to substrate (Scheme 3.4). The subsequent attack of the cysteine on the aldehyde occurs analogously to that envisioned for substrate, except that instead of forming an unstable intermediate that can decompose to a thioester, the thiohemiacetal tetrahedral adduct is unable to decompose forward and is stalled by enzymatic features that stabilize its tetrahedral geometry, namely the oxyanion hole created by Leu 132 and Cys 136 in the case of SpNic (Scheme 4). An analogous inhibition mechanism has been observed for very potent aldehyde inhibitors that target the caspase enzymes, wherein thiohemiacetal adducts have been demonstrated by x-ray crystallography (*60*).

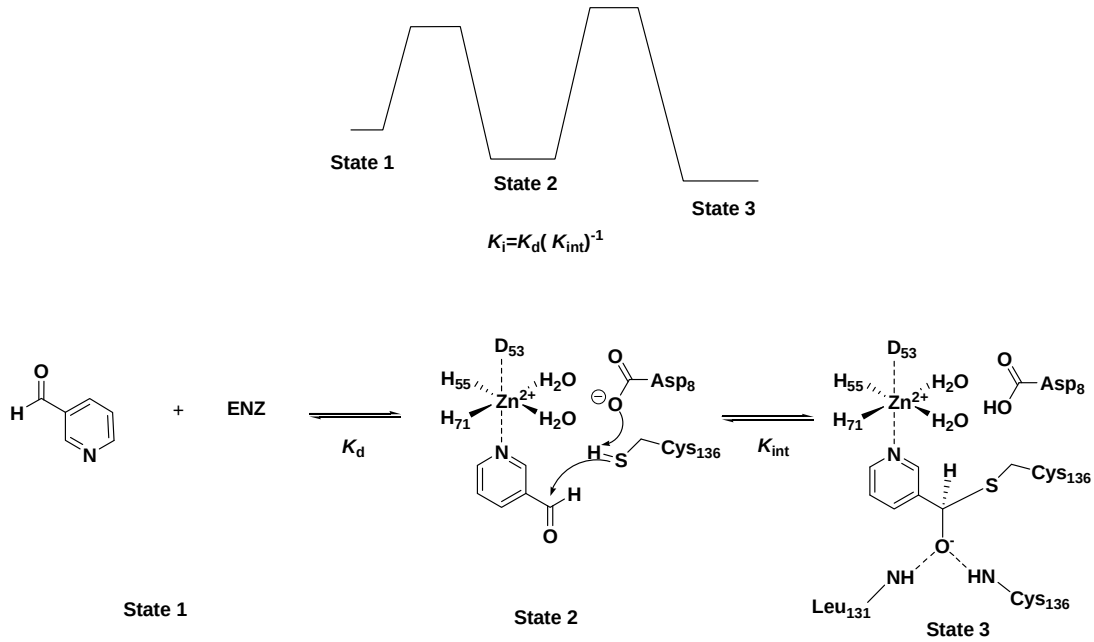

Scheme 3.4. Mechanism for nicotinaldehyde inhibition of *S. pneumoniae* enzyme.

The tetrahedral adduct formed can decompose only by reaction reversal to the initial aldehyde-metal complex. We propose that these adduct formations are fully reversible with solution nicotinaldehyde because the inhibitions observed are clearly competitive with nicotinamide present (Figure 3.3), no bi-phasic onset is apparent for reaction progress curves when aldehydes are present, and preincubation does not change inhibitor potency (data not shown). Since K_i values for nicotinaldehyde are smaller than the K_m for nicotinamide by anywhere from 72-420 across all enzymes studied (with the exception of yeast where K_m/K_i is 6.7), we propose that the enzyme is designed to stabilize the oxy-intermediate formed upon attack of cysteine with the substrate amide. This stabilization is detectable by use of aldehyde, which cannot progress further along the reaction coordinate but because of the tetrahedral intermediate stabilization, it potently inhibits the enzyme. We consider this more

formally in Scheme 3.4, where we depict the inhibition as depending upon the initial coordination of the aldehyde to the metal center, characterized by a binding constant K_d, and then being further stabilized by a factor $1/K_{int}$, where K_{int} is the equilibrium constant for the cysteine adduct that is proposed to be formed (state 3) versus the metal complexed aldehyde (state 2). The inhibition constant can thus be deduced to be $K_i = K_d(K_{int})^{-1}$. This is also qualitatively visualized in the reaction coordinate presented in Scheme 3.5. This thermodynamic explanation is completely supported by the crystallographic demonstration that the aldehydes are stabilized in thioacetal adducts on the enzyme active site (*38*).

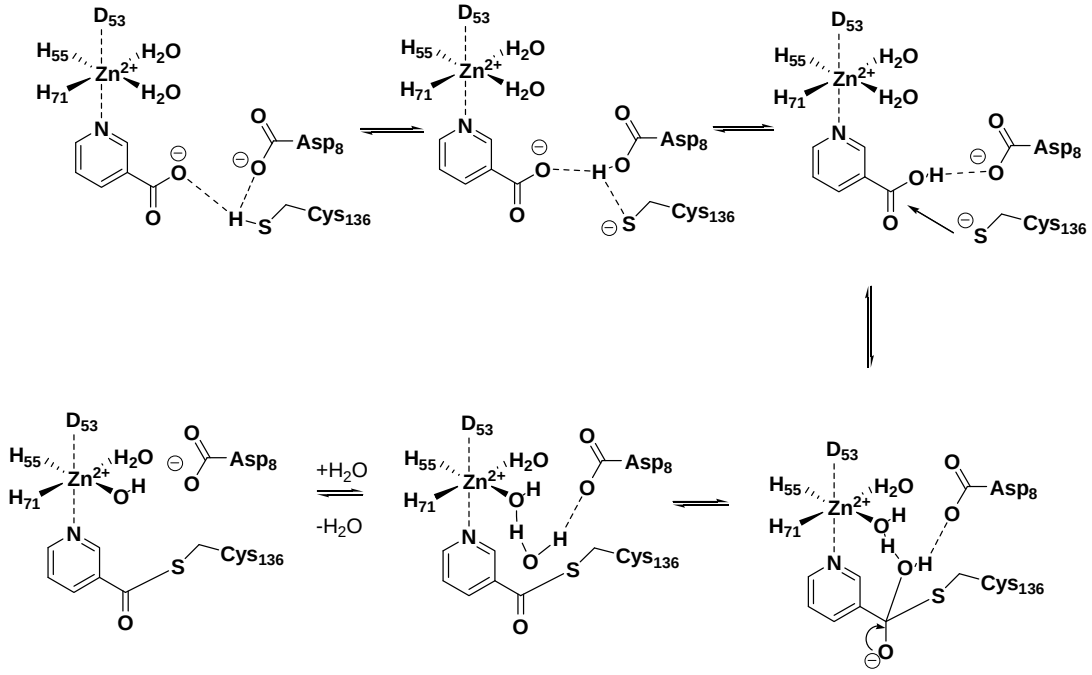

Scheme 3.5. Mechanism for nicotinic acid reversal to the nicotinoyl-thioester complex. The mechanism explains the ability of SpNic to catalyse ^{18}O exchange into nicotinic acid. A key feature of the proposed mechanism is the formation of a Zn-hydroxide complex upon thioester formation from nicotinic acid.

For the most part, with only a few exceptions, inhibition profiles were not significantly improved by 5-substitution. Although data from substrates with 5-substitutions suggests that the enzyme can readily tolerate these groups, and in fact

catalytic acceleration was observed with the electron rich 5-substituted nicotinamides, this was not translated into inhibitor improvement. On the one hand, this seems somewhat surprising, since one imagines that the affinity of the pyridine for the metal atom would be improved by increased basicity (decreased K_d, Scheme 3.4). On the other hand, increased ring electron density can reduce the thiolate ability to react with the aldehyde, and reduced stabilization of the tetrahedral complex is also possible (decreased K_{int}) from increased electron richness, which would seemingly oppose increased metal affinities. Conversely in the case of an electron withdrawing substituent, like 5-bromo, the effects may work in the opposite direction, with weaker metal binding countered by increased intermediate stabilization. Thus, we found no significant improvements in inhibitory potency with 5-substitution, although these compounds are still similarly potent to unsubstituted nicotinaldehyde. These findings suggest that 5-substitution could still be interesting for making bioavailable nicotinamidase inhibitors that are not directly metabolized to nicotinic acid. Also interesting was the development of some isoform selectivity when modifying the nicotinaldehyde substitution pattern. Substitution improved to 5.8 fold for nicotinaldehyde preference on C. elegans PNC2 versus PNC1 with the 4-O-methyl-nicotinaldehyde versus 2.8 fold in the case of nicotinaldehyde

^{18}O Exchange Mechanism and Catalytic Mechanism of Nicotinamidases. Structural data of multiple complexes, including a coordinated nicotinamide adduct, thioacetal tetrahedral adducts from aldehydes and a thioester intermediate provide a remarkably clear picture of how nicotinamidases accomplish chemistry (*38*). However, additional insight was obtained by the measured potencies of inhibitor complexes, which suggest that the enzyme is very good at stabilizing the tetrahedral adduct formed from substrate, as well as from data showing that ^{18}O can be exchanged into the product nicotinic acid. To explain ^{18}O exchange we develop a mechanism to

consider in Scheme 3.5. Coordination of nicotinic acid to the Zn-aqua center is accompanied by a deprotonated Asp 8 residue and a protonated thiol.

Crystallographic data suggests that Asp8 can interact equally with the thiol as well as the nicotinate oxygen, and we suppose that the thiol proton can be transferred between each of the three heteroatoms. When the proton becomes shared between Asp 8 and the nicotinic acid with the Cys 136 in thiolate form, we envision that the nicotinic acid can be reacted and form a tetrahedral adduct in which full deprotonation of Asp 8 occurs, and a tetrahedral intermediate results. This sp^3 center bears a hydroxyl substituent, an oxyanion substituent (which sits in the oxyanion hole) and a thioether substituent (Cys136). Oxyanion electron donation eliminates the hydroxyl substituent. We envision that expulsion of the hydroxyl group would be thermodynamically challenging, but could be facilitated by protonation of the oxygen by the aqua-Zn. This process converts the aqua-Zn to a hydroxyl Zn. We advocate this mechanism because the deprotonation of aqua-Zn should be facile relative to accommodation of naked hydroxide in the active site. There is a 6-8 order of magnitude difference in predicted pK_a of 14 for water, versus the Zn-water species where the pK_a = 7-8 (*61*). This creates a far better thermodynamic tradeoff for the reaction of a thiolate (pK_a = 7-8) with the acid if the species formed has a comparable pK_a value, and this rationalizes the observed ease of reversal of thioester formation on the enzyme. Importantly, at this point, we argue that the thioester is likely decomposed during normal catalytic turnover by a Zn-hydroxide. Water occupying the site for attack of the thioester can be deprotonated by the Zn-hydroxide as shown in Scheme 3.5. The crystallization of the thioester in the form of the aqua-Zn at pH 6.0 in the accompanying manuscript (*38*) may have been a consequence of proton quenching of the hydroxyl-Zn species, which according to the proposed mechanism would stabilize it a slow decomposition to nicotinic acid.

This mechanistic insight brings the total reaction mechanism into better focus and suggests a reason for the incorporation of a Zn^{2+} aqua center in the active site, besides its ability to organize substrate, and to electrophilically activate the nicotinamide substrate for nucleophilic attack. The proposed overall mechanism is shown in Scheme 3.6. Nicotinamide coordinates the Zn water complex as determined by crystallography (*38*). Aspartate 8 deprotonates Cys136 to form the thiolate which can readily proceed to the tetrahedral intermediate. Proton transfer to the amino group of the tetrahedral intermediate facilitates oxyanion electron flow to form the thioester. Interestingly, ammonia is quite basic and with no other protons in vicinity, it can deprotonate the aqua-Zn to form a Zn-hydroxide species prior to its departure from the active site as ammonium. This reaction completes the first half of the reaction coordinate and is probably irreversible (Scheme 3.6). Thus, our argument that the exchange reaction requires a Zn-hydroxide at the thioester complex is probably realistic, as the ammonia product provides the driving force and kinetic access to form the suggested Zn-hydroxide during turnover from substrate. Water then enters the active site to initiate the chemistry that accomplishes hydrolysis of the thioester, in which the water is deprotonated by the Zn-hydroxide acting as the activating base identical to what was suggested in the mechanism for ^{18}O exchange (Scheme 3.5).

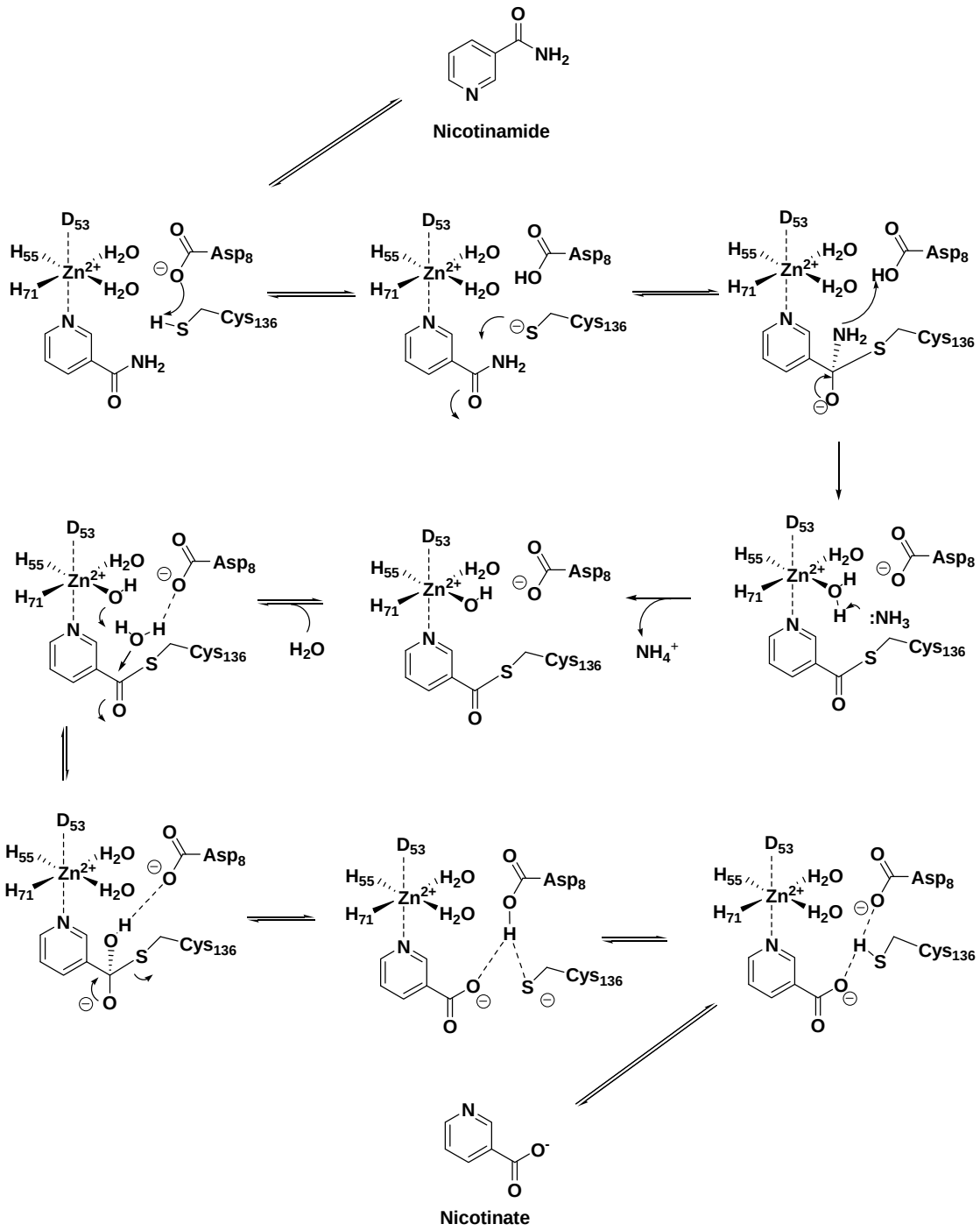

Scheme 3.6. Proposed mechanism of nicotinamidases. Numbering of residues is consistent with that of SpNic. The ammonia generated in the first half of the reaction coordinate generates a Zn-hydroxide by deprotonation prior to departure from the active site. The intermediacy of a Zn-hydroxide is envisioned to act as a base catalyst that activates a solvent derived nucleophilic water in the second half of the catalytic reaction.

With a wealth of new data on nicotinamidase inhibition, crystal structures (*38*), ^{18}O exchange data and the structural identification of the thioester intermediate, we have provided a considerable new perspective on the nicotinamidase enzymes, including providing a comprehensive mechanism that explains the chemistry of these enzymes. Since these enzymes possess so many common residues (Figure 3.1) and are highly conserved, we anticipate that the mechanism we have proposed is likely to apply to individual nicotinamidases from different phylogenetic sources. The advancement of our view of the chemistry of these enzymes increases the likelihood that they can be targeted for inhibitor design, and provides testable hypotheses for further determination of the chemical principles that enable catalysis by nicotinamidases.

REFERENCES

1. Gerdes, S. Y., *et al.* (2002) From genetic footprinting to antimicrobial drug targets: examples in cofactor biosynthetic pathways, *J Bacteriol 184*, 4555-4572.
2. Boshoff, H. I., and Mizrahi, V. (1998) Purification, gene cloning, targeted knockout, overexpression, and biochemical characterization of the major pyrazinamidase from Mycobacterium smegmatis, *J Bacteriol 180*, 5809-5814.
3. Zhang, H., *et al.* (2008) Characterization of Mycobacterium tuberculosis nicotinamidase/pyrazinamidase, *Febs J 275*, 753-762.
4. Scorpio, A., and Zhang, Y. (1996) Mutations in pncA, a gene encoding pyrazinamidase/nicotinamidase, cause resistance to the antituberculous drug pyrazinamide in tubercle bacillus, *Nat Med 2*, 662-667.
5. Ghislain, M., *et al.* (2002) Identification and functional analysis of the Saccharomyces cerevisiae nicotinamidase gene, PNC1, *Yeast 19*, 215-224.
6. Hu, G., *et al.* (2007) Crystal structure of the yeast nicotinamidase Pnc1p, *Arch Biochem Biophys 461*, 66-75.
7. Joshi, J. G., and Handler, P. (1962) Purification and properties of nicotinamidase from *Torula cremoris*, *J. Biol. Chem. 237*, 929-935.
8. Zerez, C. R., *et al.* (1990) Increased nicotinamide adenine dinucleotide content and synthesis in Plasmodium falciparum-infected human erythrocytes, *Blood 75*, 1705-1710.
9. Wang, G., and Pichersky, E. (2007) Nicotinamidase participates in the salvage pathway of NAD biosynthesis in Arabidopsis, *Plant J 49*, 1020-1029.
10. Balan, V., *et al.* (2008) Life span extension and neuronal cell protection by Drosophila nicotinamidase, *J Biol Chem 283*, 27810-27819.

11. van der Horst, A., *et al.* (2007) The Caenorhabditis elegans nicotinamidase PNC-1 enhances survival, *Mech Ageing Dev 128*, 346-349.
12. Vrablik, T. L., *et al.* (2009) Nicotinamidase modulation of NAD+ biosynthesis and nicotinamide levels separately affect reproductive development and cell survival in C. elegans, *Development 136*, 3637-3646.
13. Oppenheimer, N. J. (1994) Nad Hydrolysis - Chemical and Enzymatic Mechanisms, *Molecular and Cellular Biochemistry 138*, 245-251.
14. Handlon, A. L., *et al.* (1994) 2'-Ribose Substituent Effects on the Chemical and Enzymatic-Hydrolysis of Nad(+), *Journal of the American Chemical Society 116*, 12087-12088.
15. Johnson, R. W., *et al.* (1988) Pyridine-Nucleotide Chemistry - a New Mechanism for the Hydroxide-Catalyzed Hydrolysis of the Nicotinamide Glycosyl Bond, *Journal of the American Chemical Society 110*, 2257-2263.
16. Sauve, A. A., *et al.* (2006) The biochemistry of sirtuins, *Annu Rev Biochem 75*, 435-465.
17. Grimm, D., *et al.* (2005) Defining plasmids required by Borrelia burgdorferi for colonization of tick vector Ixodes scapularis (Acari: Ixodidae), *J Med Entomol 42*, 676-684.
18. Kawabata, H., *et al.* (2004) BBE02 disruption mutants of Borrelia burgdorferi B31 have a highly transformable, infectious phenotype, *Infect Immun 72*, 7147-7154.
19. Purser, J. E., *et al.* (2003) A plasmid-encoded nicotinamidase (PncA) is essential for infectivity of Borrelia burgdorferi in a mammalian host, *Mol Microbiol 48*, 753-764.

20. Kim, S., *et al.* (2004) Brucella abortus nicotinamidase (PncA) contributes to its intracellular replication and infectivity in mice, *FEMS Microbiol Lett 234*, 289-295.

21. Sauve, A. A. (2008) NAD+ and vitamin B3: from metabolism to therapies, *J Pharmacol Exp Ther 324*, 883-893.

22. Anderson, R. M., *et al.* (2003) Nicotinamide and PNC1 govern lifespan extension by calorie restriction in Saccharomyces cerevisiae, *Nature 423*, 181-185.

23. Bitterman, K. J., *et al.* (2002) Inhibition of silencing and accelerated aging by nicotinamide, a putative negative regulator of yeast sir2 and human SIRT1, *J Biol Chem 277*, 45099-45107.

24. Gallo, C. M., *et al.* (2004) Nicotinamide clearance by Pnc1 directly regulates Sir2-mediated silencing and longevity, *Mol Cell Biol 24*, 1301-1312.

25. Rogina, B., and Helfand, S. L. (2004) Sir2 mediates longevity in the fly through a pathway related to calorie restriction, *Proc Natl Acad Sci U S A 101*, 15998-16003.

26. Wood, J. G., *et al.* (2004) Sirtuin activators mimic caloric restriction and delay ageing in metazoans, *Nature 430*, 686-689.

27. Tissenbaum, H. A., and Guarente, L. (2001) Increased dosage of a sir-2 gene extends lifespan in Caenorhabditis elegans, *Nature 410*, 227-230.

28. Berdichevsky, A., *et al.* (2006) C. elegans SIR-2.1 interacts with 14-3-3 proteins to activate DAF-16 and extend life span, *Cell 125*, 1165-1177.

29. Kaeberlein, M., *et al.* (1999) The SIR2/3/4 complex and SIR2 alone promote longevity in Saccharomyces cerevisiae by two different mechanisms, *Genes Dev 13*, 2570-2580.

30. Lin, S. J., *et al.* (2000) Requirement of NAD and SIR2 for life-span extension by calorie restriction in Saccharomyces cerevisiae, *Science 289*, 2126-2128.

31. Hunt, L., *et al.* (2007) Nicotinamidase activity is important for germination, *Plant J 51*, 341-351.

32. Hughes, D. E., and Williamson, D. H. (1952) The synthesis of cozymase from nicotinic acid and its derivatives by *Lactobacillus arabinosus*, *Biochem. J.*, 330-338.

33. Du, X., *et al.* (2001) Crystal structure and mechanism of catalysis of a pyrazinamidase from Pyrococcus horikoshii, *Biochemistry 40*, 14166-14172.

34. Fyfe, P. K., *et al.* (2009) Specificity and mechanism of Acinetobacter baumanii nicotinamidase: implications for activation of the front-line tuberculosis drug pyrazinamide, *Angew Chem Int Ed Engl 48*, 9176-9179.

35. Chenna, R., *et al.* (2003) Multiple sequence alignment with the Clustal series of programs, *Nucleic Acids Res 31*, 3497-3500.

36. Gouet, P., Robert, X., and Courcelle, E. (2003) ESPript/ENDscript; extracting and rendering sequence and 3D information from atomic structures of proteins, *Nucleic Acids Res. 31*, 3320-3323.

37. Du, X., *et al.* (2001) Crystal structure and mechanism of catalysis of a pyrazinamidase from *Pyrococcus horikoshii*, *Biochem. 40*, 14166-14172.

38. French JF, C. Y., Sauve AA, Ealick S. (2010) igh Resolution Crystal Structures of Streptococcus pneumoniae Nicotinamidase in Substrate, Intermediate and Inhibitor Complexes *Biochemsitry*.

39. Pruser, J. E., *et al.* (2003) *Mol. Microbiol. 48*, 753-764.

40. Yun, S. L., and Suelter, C. H. (1977) A simple method for calculating Km and V from a single enzyme reaction progress curve, *Biochim Biophys Acta 480*, 1-13.

41. Evans, G. B., *et al.* (2003) 8-Aza-immucillins as transition-state analogue inhibitors of purine nucleoside phosphorylase and nucleoside hydrolases, *J Med Chem 46*, 155-160.

42. Boovanahalli, S. K., *et al.* (2007) Synthesis of (aryloxyacetylamino)-isonicotinic/nicotinic acid analogues as potent hypoxia-inducible factor (HIF)-1alpha inhibitors, *Bioorg Med Chem Lett 17*, 6305-6310.

43. Martin, R. B., and Hull, J. G. (1964) Reactions of N1-Methylnicotinamide Cation + Analogues with Dilute Alkali, *J Biol Chem 239*, 1237-&.

44. Comins, D. L., and Killpack, M. O. (1990) Lithiation of Methoxypyridines Directed by Alpha-Amino Alkoxides, *J Org Chem 55*, 69-73.

45. Carceller, E., *et al.* (1994) [(3-Pyridylalkyl)piperidylidene]benzocycloheptapyridine derivatives as dual antagonists of PAF and histamine, *J Med Chem 37*, 2697-2703.

46. Bandgar, B. P., *et al.* (2000) Selective and rapid oxidation of primary, allylic and benzylic alcohols to the corresponding carbonyl compounds with NaNO2-acetic anhydride under mild and solvent-free conditions, *J Chem Soc Perk T 1*, 3559-3560.

47. Rife, J. E., and Cleland, W. W. (1980) Kinetic mechanism of glutamate dehydrogenase, *Biochemistry 19*, 2321-2328.

48. Engel, P. C., and Dalziel, K. (1967) The equilibrium constants of the glutamate dehydrogenase systems, *Biochem J 105*, 691-695.

49. Smith, B. C., *et al.* (2009) A continuous microplate assay for sirtuins and nicotinamide-producing enzymes, *Anal Biochem 394*, 101-109.

50. Hughes, D. E., and Williamson, D. H. (1953) The deamidation of nicotinamide by bacteria, *Biochem J 55*, 851-856.

51. Hughes, D. E., and Williamson, D. H. (1952) The synthesis of cozymase from nicotinic acid and its derivatives by Lactobacillus arabinosus 17-5, *Biochem J 51*, 330-338.

52. Tanigawa, Y.*, et al.* (1980) Nicotinamide deamidase from Flavobacterium peregrinum, *Methods Enzymol 66*, 132-136.

53. Yan, C., and Sloan, D. L. (1987) Purification and characterization of nicotinamide deamidase from yeast, *J Biol Chem 262*, 9082-9087.

54. Calbreath, D. F., and Joshi, J. G. (1971) Inhibition of nicotinamidase by nicotinamide adenine dinucleotide, *J Biol Chem 246*, 4334-4339.

55. Hu, G.*, et al.* (2007) Crystal structure of the yeast nicotinamidase Pnc1p, *Arch. Biochem. Biophys. 461*, 66-75.

56. Calbreath, D. F., and Joshi, J. G. (1971) Inhibition of nicotinamidase by nicotinamide adenine dinucleotide, *J. Biol. Chem. 246*, 4334-4339.

57. Yan, C., and Sloan, D. L. (1987) Purification and characterization of nicotinamide deamidase from yeast, *J. Biol. Chem. 262*, 9082-9087.

58. Ghislain, M.*, et al.* (2002) Identification and functional analysis of the *Saccharomyces cerevisiae* nicotinamidase gene, PNC1, *Yeast 19*, 215-224.

59. Zerez, C. R.*, et al.* (1990) Increased nicotinamide adenine dinucleotide content and synthesis in *Plasmodium faciparum*-infected human erythrocytes, *Blood 75*, 1705-1710.

60. Margolin, N.*, et al.* (1997) Substrate and inhibitor specificity of interleukin-1 beta-converting enzyme and related caspases, *J Biol Chem 272*, 7223-7228.

61. Groves, J. T., and Olson, J. R. (1985) Models of Zinc-Containing Proteases - Rapid Amide Hydrolysis by an Unusually Acidic Zn2+-Oh2 Complex, *Inorganic Chemistry 24*, 2715-2717.

CHAPTER 4

HIGH RESOLUTION STRUCTURES OF *STREPTOCOCCUS PNEUMONIAE* NICOTINAMIDASE IN INHIBITOR, SUBSTRATE AND INTERMEDIATE COMPLEXES

4.1 Abstract

Nicotinamidases are salvage enzymes that convert nicotinamide to nicotinic acid. These enzymes are essential for the recycling of nicotinamide into NAD^+ in most prokaryotes, most single-celled and multicellular eukaryotes, but not in mammals. The significance of these enzymes for nicotinamide salvage and for NAD^+ homeostasis has increased interest in these enzymes as possible antibiotic targets. Nicotinamidases are also regulators of intracellular nicotinamide concentrations, thereby regulating signaling of downstream NAD^+ consuming enzymes, such as the NAD^+-dependent deacetylases (sirtuins). Here, we report several high resolution crystal structures of the nicotinamidase from *Streptococcus pneumoniae* (SpNic) in unliganded and ligand-bound forms. The structure of the C136S mutant in complex with nicotinamide provides details about substrate binding while a trapped nicotinoyl-thioester complexed with SpNic reveals the structure of a putative thioester reaction intermediate. Examination of the active site of SpNic reveal several important features including a metal ion that coordinates the substrate and the catalytically relevant water molecule, and an oxyanion hole which both orients the substrate and offsets the negative charge that builds up along the reaction coordinate. Structures of this enzyme with bound nicotinaldehyde inhibitors elucidate the mechanism of inhibition and provide further details about the catalytic mechanism. In addition, we provide a biochemical analysis of the identity and role of the metal ion that orients the ligand in the active site and activates the water molecule responsible for hydrolysis of the substrate. These data provide structural evidence for several putative reaction

intermediates and allow for a more complete understanding of the catalytic mechanism of this enzyme.

4.2 Introduction

Nicotinamide adenine dinucleotide (NAD^+) and its phosphorylated and reduced forms, $NADP^+$, NADH, and NADPH, are central to cellular metabolism and energy production. Maintenance of NAD^+ concentrations is important for cell and organism viability, and the strategies of cells to replete NAD^+ from nicotinamide (NAM), nicotinic acid (NA), nicotinamide riboside and via *de novo* routes are quite elaborate (*1*). The complexity of NAD^+ biosynthesis in most organisms is likely linked to the importance of the dinucleotides in central metabolism, and targeting NAD^+ biosynthesis as an antibiotic approach has recently been the subject of increased investigation (*1-3*). In addition to biosynthetic production, salvage pathways operate to offset depletion of NAD^+ stocks by NAD^+ consuming enzymes and non-enzymatic hydrolysis, which can occur even at physiologic temperatures and pH (*4, 5*).

An important difference between human NAD^+ homeostasis and that of most prokaryotes, unicellular eukaryotes and multicellular eukaryotes involves the mechanism of NAD^+ production and/or salvage. In most organisms nicotinamide is recycled back to NAD^+ by first being converted into nicotinic acid by the enzyme nicotinamidase, the genes of which are also known as pyrazinamidase/nicotinamidase (PncA) (Figure 4.1A). Mammalian genomes do not encode nicotinamidases but instead convert NAM directly into nicotinamide mononucleotide (NMN) using nicotinamide phosphoribosyltransferase (Nampt). NMN is then adenylated by nicotinomide mononucleotide adenyltransferase to form NAD^+ (*6, 7*). Mammals also retain the capacity to utilize nicotinic acid to make NAD^+, doing so using the Preiss

Handler pathway. This pathway is biochemically similar to the way most organisms recycle nicotinic acid (Figure 4.1B) (*7*).

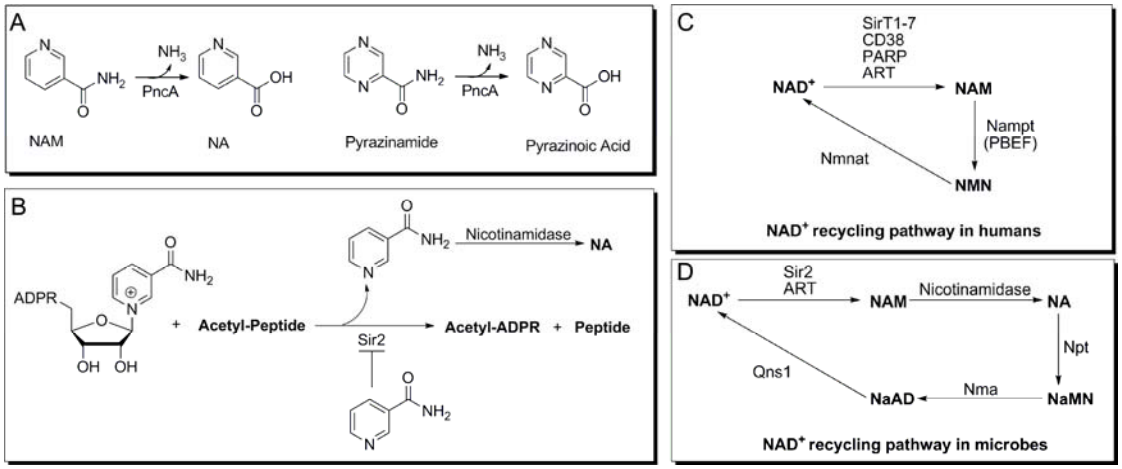

Figure 4.1. Nicotinamidase chemistry and function. (A) PncA hydrolyzes nicotinamide to give nicotinic acid (top reaction) and is also able to catalyze the conversion of the drug pyrazinamide to pyrazinoic acid (bottom reaction). (B) Sirtuin chemistry. Sirtuins deacetylate an acetylated peptide in an NAD^+-dependent manner, releasing nicotinamide in the process. Heightened levels of nicotinamide inhibit sirtuin chemistry. (C) and (D) NAD^+ recycling. A schematic of the NAD^+ recycling pathways in humans (C) and microbes (D).

The importance of the nicotinamidase activity to organisms that are pathogenic to humans, combined with its absence in human NAD^+ biosynthetic pathways has increased interest in this enzyme as a possible drug target. Recent work on the spirochaete *Borrelia burgdorferi* indicates that host nicotinic acid levels are too low to support pathogen survival and that a plasmid-encoded nicotinamidase is essential for viability (*8*). Similarly, a nicotinamidase deficient mutant from *Brucella abortus* failed to replicate in cells but was rescued by the addition of nicotinic acid (*9*). In addition, an increased nicotinamidase activity has been observed in *Plasmodium falciparum* infected erythrocytes (*10*). A need for nicotinamidase activity for viability is consistent with the idea that some organisms lack a *de novo* NAD^+ biosynthetic

pathway and therefore rely upon recycling and salvage of host NAM for growth (*1, 2, 11, 12*).

Nicotinamidase activity was first reported by Williamson and Hughes in extracts from *Lactobacillus arabinosus* (*13*) and this activity was later observed in many other microorganisms (*14-19*). Nicotinamidases have also been confirmed in plants (*20, 21*), *Caenorhabditis elegans (22)*, and *Drosophila melanogaster (23)*. In addition to proposed roles in NAD^+ homeostasis, nicotinamidases are reported to regulate the NAD^+ dependent deacetylase activity of sirtuins (*22, 24, 25*). This is accomplished through modulation of *in vivo* concentrations of nicotinamide, a potent inhibitor of sirtuins (Figure 4.1C) (*26-28*). Increased nicotinamidase expression increases Sir2-dependent gene silencing (*24, 29, 30*) and increases replicative lifespan in yeast (*31*), *D. melanogaster* (*23, 32*) and *C. elegans (22, 33)*.

In addition to its known biological functions, nicotinamidase activity is required for activation of the front-line tuberculosis prodrug, pyrazinamide. Nicotinamidase encoded by *Mycobacterium tuberculosis* hydrolyzes pyrazinamide to form the active form of the drug, pyrazinoic acid (Figure 4.1A). Despite the effectiveness of pyrazinamide, drug resistant strains of *M. tuberculosis* have emerged that are unable to metabolize this drug. Resistance arises from point mutations on the nicotinamidase enzyme (*34*) and these mutations have been mapped to catalytic residues as well as to residues predominantly structural in nature (*35, 36*).

With considerable interest in these enzymes for their biological effects, their potential as antibiotic targets, and a long history of investigation, it is somewhat surprising that the structural and chemical basis for the catalytic function of these enzymes has remained largely undetermined. Until recently, only unliganded crystal structures of nicotinamidases, from *Saccharomyces cerevisiae (37)* and *Pyrococcus horikoshii* (*38*), had been reported. While the active site within both structures was

putatively identified through similarity to known structures and by the presence of a coordinated metal, few conclusions could be made about ligand binding or the reaction mechanism. Recently a structure of the *Acenitobacter baumanii* nicotinamidase with nicotinic acid bound at the active site was reported in which the pyridine nitrogen of the ligand was determined to be coordinated to the central metal ion (*39*). The results suggest that nicotinamidases utilize metal coordination of the pyridine nitrogen to orient the substrate and possibly also to activate it for catalysis.

In this manuscript we report several crystal structures, both unliganded and of several trapped intermediates, of the nicotinamidase from the human pathogen, *Streptococcus pneumoniae* (SpNic). In addition, we provide an analysis of role and identity of the active site metal ion. These structures provide insight into key active site interactions and provide snapshots of several presumed reaction intermediates. The structure of the C136S mutant with nicotinamide bound provides details about substrate binding while the nicotinyl thioester observed in the structure of nicotinic acid treated crystals provides evidence for a thioester intermediate. The structures of the SpNic-aldehyde complexes reveal a covalent adduct with tetrahedral geometry, analogous to another putative reaction intermediate. These structures, along with the biochemical evidence presented, allow us to propose a catalytic mechanism for the nicotinamidase catalyzed reaction and provide a likely rationale for the inhibition by aldehyde analogues of nicotinamide.

4.3 Materials and Methods

Cloning and Mutagenesis. The PncA gene for *S. pneumoniae* TIGR4 (accession number NC_003028) was amplified by PCR from genomic DNA (ATCC 6314D) and engineered to contain the NdeI and BamHI restriction endonuclease recognition sites. The PCR product was inserted into the pSTBlue vector (Novagen) using the AccepTor vector kit (Novagen). The gene was then digested with NdeI and

BamHI restriction endonucleases and ligated into similarly digested Pet28a; the presence of the gene was verified by sequencing. The C136S mutant plasmid was made at the Cornell Protein Characterization and Production Facility by using site-directed mutagenesis of the native gene. Briefly, site-directed mutagenesis was performed on SpNic by a standard PCR protocol using *Pfu*Turbo DNA polymerase (Invitrogen) and *Dpn*I (New England Biolabs) to digest the methylated parental DNA prior to transformation. The presence of the mutated residue was verified by sequencing.

Protein Expression and Purification. Plasmid DNA was transformed into the Rosetta 2(DE3) pLysS (Novagen) *E. coli* cell line. Cells were grown in LB medium at 37 °C with shaking (180 rpm) to an OD_{600} of 0.6. SpNic expression was induced by the addition of 0.5 mM IPTG and cells were incubated at 37 °C with shaking for an additional 10 h. Cells were harvested by centrifugation, resuspended in lysis buffer (300 mM NaCl, 50 mM Na_2PO_4 and 5 mM imidazole, pH 7.6) and lysed by sonication. The lysate was then centrifuged at 30 000 *g* for 60 min at 4 °C. The cleared lysate was loaded onto Ni-NTA resin (Qiagen) that had been pre-equilibrated with the lysis buffer. After loading, the lysate was washed with lysis buffer and then with wash buffer (300 mM NaCl, 50 mM Na_2PO_4, 10% glycerol and 25 mM imidazole, pH 7.6). Finally, the protein was eluted with 300 mM NaCl, 50 mM Na_2PO_4 and 250 mM imidazole, pH 7.6 and then buffered exchanged using an Econo-Pac 10DG column (BioRad) into 30 mM NaCl and 10 mM Tris, pH 7.6. The protein was concentrated using a centrifugal filter with a 10 kDa molecular weight cutoff (Amicon) to a final concentration of 25 mg/mL as measured by the method of Bradford (*40*). Protein purity was verified to be greater than 95 % by SDS-PAGE.

Synthesis of 5-methoxynicotinaldehyde. 5-methoxynicotinaldehyde was synthesized in two steps from 3,5-dibromopyridine as previously reported (*41*).

Protein Crystallization, Data Collection and Structure Determination. Crystallization experiments were conducted using the hanging drop vapor diffusion method at 18 °C by combining equal volumes of protein and reservoir solution. Initial crystallization conditions were determined by sparse matrix screening (Hampton Research, Emerald Biostructures). After optimization, diffraction quality crystals were grown from 18 – 22 % PEG 3350, 0.2 – 0.3 M NaCl and 0.2 M sodium malonate, pH 6.3 at 18 °C. To obtain the SpNic-small molecule complexes, the crystals were soaked for 12 hours in the crystallization solution containing 2 mM $ZnCl_2$, and 2 mM of the ligand (nicotinaldehyde, 5-methoxynicotinaldehyde, NA or NAM). Prior to flash-freezing in liquid nitrogen, crystals were soaked in a solution containing the crystallization buffer, 2 mM $ZnCl_2$, 2 mM ligand and 18% glycerol. Data sets were collected at the Advanced Photon Source (APS) beamline 24-ID-C using an ADSC Quantum 315 detector at a wavelength of 0.9795 Å. The data collection statistics are provided in Table 4.1.

The structure of SpNic was solved by molecular replacement using the program Molrep (*42*) with an all-alanine monomer of *P. horikoshii* pyrazinamidase (PDB code 1IM5) as the search model. The models were refined by iterative cycles of restrained refinement using Refmac5 (*43*) and CNS (*44*) and by manual model building using the interactive graphics program Coot (*45*). Water molecules were added using Coot only after the refinement of the protein structure had converged. Ligands were directly built into the corresponding difference electron density and the model was then subject to an additional round of refinement. Refinement statistics for the model are listed in Table 4.2.

Table 4.1. Summary of Data Collection Statistics

	SpNic-Zn	SpNic-Zn-nicotin-aldehyde	SpNic-Zn-5-OMe-nictotin-aldehyde	SpNic-Zn-NA	SpNic-Cys136Ser-Zn-NAM
resolution (Å)	1.95	1.63	1.9	1.91	1.60
wavelength (Å)	0.9795	0.9795	0.9795	0.9795	0.9795
Space group	$P2_1$	$P2_1$	$P2_12_12_1$	$P2_1$	$P2_1$
a (Å)	60.8	60.8	61.2	61.2	61.2
b (Å)	120.9	120.0	114.5	121.2	120.8
c (Å)	63.2	62.8	120.9	115.3	62.8
β (^{o})	114.3	114.9	90	94.3	114.7
# of reflections	185471	452705	336232	692648	425812
unique reflections	54280	96559	67241	128796	106320
average I/σ	11.3 (2.2)	14.7 (1.9)	14.3 (4.7)	16.5 (4.5)	18.9 (3.8)
Redundancy	3.4 (2.1)	4.7 (2.5)	5.0 (4.9)	5.4 (4.9)	4.0 (3.4)
completeness(%)	88.2 (73.7)	95.1 (79.4)	99.0 (99.9)	99.5 (98.8)	97.7 (86.2)
R_{sym}[a] (%)	13.2 (29.2)	9.3 (17.7)	9.8 (35.3)	9.9 (28.9)	5.1 (18.9)

Numbers in parentheses correspond to the highest resolution shell

[a] $R_{\text{sym}} = \Sigma\Sigma_i \left| I_i - \langle I \rangle \right| / \Sigma \langle I \rangle$, where $\langle I \rangle$ is the mean intensity of the N reflections with intensities I_i and common indices h, k, l

Table 4.2. Summary of Data Refinement Statistics

	SpNic-Zn	SpNic-Zn-nicotin-aldehyde	SpNic-Zn-5-OMe-nicotin-aldehyde	SpNic-Zn-NA	SpNic-Cys136Ser-Zn-NAM
resolution (Å)	1.95	1.63	1.9	1.91	1.60
total no. of atoms	6128	6160	6032	6061	6080
no. of ligand atoms	4	36	44	36	40
no. of water atoms	564	431	606	593	853
reflections in working set	51163	77657	62379	66830	103397
reflections in test set	2719	4097	3328	3542	5312
R factor[a]	20.5	18.4	17.4	20.1	16.4
R_{free}[b]	24.6	21.8	21.7	24.5	20.0
rmsd bonds (Å)	0.021	0.012	0.014	0.023	0.027
rmsd angles (^{o})	1.83	1.35	1.44	1.90	2.18
mean B factor (Å^2)	30.1	30.4	27.3	29.9	15.8
Ramachandran					
most favored (%)	91.2	92.2	92.0	90.3	91.9
additionally allowed (%)	8.8	7.5	7.8	9.2	8.1
generously allowed (%)	0.0	0.3	0.2	0.5	0
disallowed (%)	0	0	0	0	0

[a] R factor $= \Sigma_{hkl} \| F_{obs} | - k | F_{calc} \| / \sum_{hkl} | F_{obs} |$, where F_{obs} and F_{calc} are observed and calculated structure factors respectively.
[b] For R_{free}, the sum is extended over a subset of reflections excluded from all stages of refinement

Estimation of Coordinate Error. While the variances and covariances of parameters used in structural refinement can be obtained through the inversion of the full least-squares matrix, this calculation is computationally very challenging and difficult to realize for protein structures, given the number of parameters needed for refinement. Alternatively, approximations can be used to compute an estimate of coordinate error in a model. To determine the approximate coordinate error for the Zn^{2+} and water atoms bound in the SpNic active site, the method of Cruickshank (*46*), called the diffraction-component precision index (DPI), was used. This method uses the number of atoms in the structure (N_i), the number of reflections (n_{obs}), the completeness of the data (C), the maximum resolution (d_{min}), and the R_{free} value to estimate the mean coordinate error as follows:

$$\sigma_r^{DPI}(B_{avg}) = 3^{1/2} \left(N_i / n_{obs} \right)^{1/2} C^{-1/3} R_{free} d_{\min}$$

Because of the high degree of correlation between the *B*-factor and coordinate error (*46, 47*), individual coordinate errors can be estimated using the following formula (*48*):

$$\tilde{\sigma}_{r,i} = \frac{\sigma_r^{DPI}(B_{avg})}{B_{avg}} B_i .$$

Total Elemental Analysis of Protein Samples. Elemental analysis of protein samples was performed by the Cornell Nutrient Analysis Laboratory (*49*) following EPA protocol 3051-6010. This method involves microwave assisted nitric acid digestion of samples followed by analysis by inductively coupled plasma – atomic emission spectrometry. Prior to treatment of samples, the 6-His tag was cleaved from the protein using TEV protease. An aliquot was set aside to use as an untreated

sample and the remaining was incubated with 2 mM EDTA and 2 mM 1,10-phenanthroline for 24 hours at 4 °C. Samples were buffer exchanged on a centricon 10 kDa cutoff centrifugal device (Millipore) into 30 mM Tris, 10 mM NaCl. Three subsequent centrifugation runs were carried out using a 20:1 ratio of new buffer to concentrated sample on each run. Metal salts were added to a final concentration of 2 mM to 5 mg/mL solutions of protein and incubated for 16 h. These samples were buffer exchanged to remove unbound metal ions as described above and sent for analysis at a concentration of 2 mg/mL.

Metal Dependence Measurements. SpNic protein used for metal dependent kinetics analysis had the 6-His tag removed, treated with chelators and buffer exchanged as detailed above. After addition of $Zn(OCH_3)_2$, $Fe(II)SO_4$, $MnCl_2$, $CoCl_2$, $NiSO_4$, or $Fe(III)Cl_3$, (in concentrations ranging from 0 to 2 mM for each metal salt) the solutions were incubated for 6 h and buffer exchanged using spin columns to remove excess metals. This step is necessary as the metal ions can interfere with the coupling enzyme. The rate of reaction was monitored on a 96-well plate using a glutamate dehydrogenase coupled assay (*41*). Control reactions using ammonium sulfate with each enzyme solution without added NAM were run to ensure that the coupling enzyme was not limiting the reaction.

4.4 Results

Structure of Unliganded SpNic. The stucture of SpNic is a homotetramer (Figure 4.2A), consistent with molecular weight estimates determined by size exclusion chromatography (data not shown).

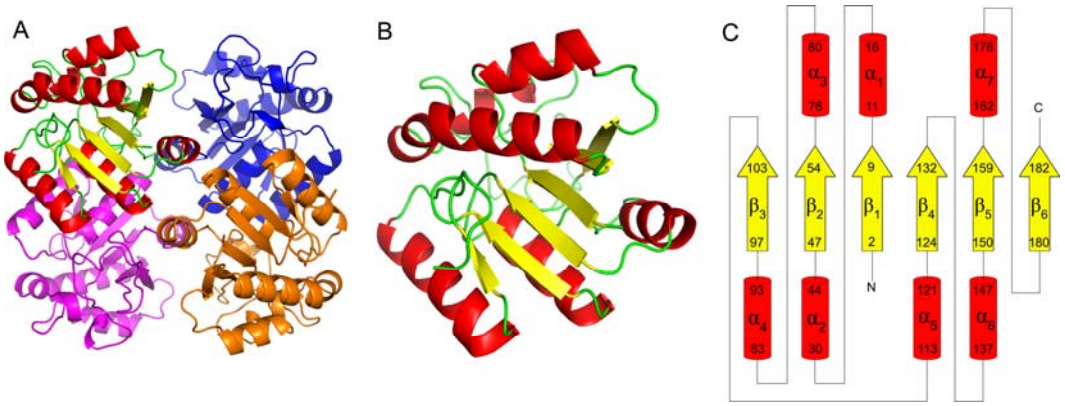

Figure 4.2. Structure of SpNic. (A) SpNic tetramer. (B) SpNic monomer and topology diagram of SpNic. The yellow arrows represent β-strands and red cylinders represent α-helices.

SpNic is an α/β protein with a six-stranded β-sheet flanked by three helices on one side and four helices on the opposite side (Figure 4.2B). The interface between protomers is dominated by polar contacts of α5 on one side and by π-stacking and polar interactions of α6 and α7. The four active sites of the SpNic tetramer are located in solvent-accessible pockets in each protomer that are formed primarily by three loop regions containing residues 55 through 75 (between β_1 and α_3), residues 104 through 112 (between β_3 and α_5) and residues 133 through 136 (between β_4 and α_6). While one of the open sides of the active site is bordered by two residues (Thr176 and His172) of α_7 from a neighboring protomer, all interactions necessary for substrate binding and catalysis, including those that coordinate the metal ion, are provided by a single SpNic protomer.

Organization of Metal Binding Site. The metal center is coordinated by two histidines (His55 and His71), an aspartate (Asp53) and a glutamate (Glu64). Two additional coordination interactions are provided by a single water molecule and by the pyridyl nitrogen of the ligand (Figure 4.3), or by two water molecules in the absence of a ligand, in each case furnishing full octahedral coordination to the metal ion.

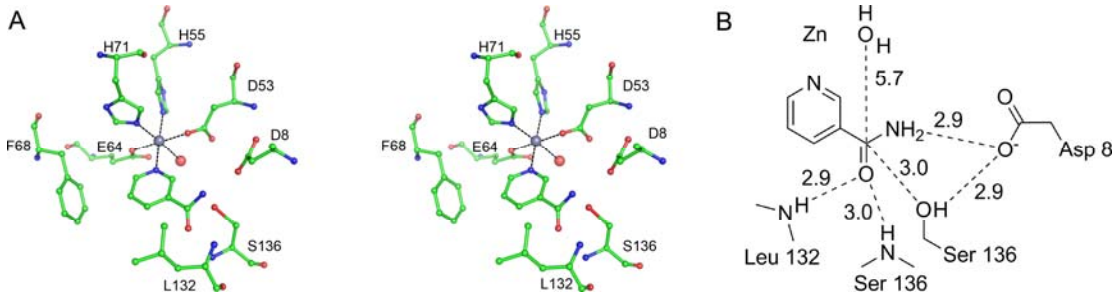

Figure 4.3. SpNic active site. A) Stereoview of the active site of SpNic shown with NAM bound as observed in the Cys136Ser–NAM structure. The grey and red spheres represent zinc and water respectively. Phe-14 (not shown) is situated in front of NAM in the plane of the paper and makes an additional π-stacking interaction with the NAM ring. B) Schematic of the active site of the Cys136Ser SpNic mutant in complex with NAM. The distances shown are heavy atom to heavy atom distances in angstroms.

The magnitude of the electron density peak at the metal ion binding site was low when crystals were grown without exogenous metal added. Crystallization solution supplemented with Zn^{2+} ions, however, led to a clear, strong peak. Supplementation of the well solution with other ions, including Mn^{2+}, Fe^{2+}, Fe^{3+}, Co^{2+}, Ni^{2+} or Ca^{2+} did not lead to improvement over crystals grown in the absence of exogenous metals.

Metal Ion Dependence of SpNic. To determine the metal dependence of SpNic, the enzyme was first treated with EDTA and phenanthroline, buffer exchanged to remove chelators and then treated with various metal ion solutions. These solutions were further buffer exchanged to remove unbound metals and then tested for activity. Addition of Fe^{2+}, Mn^{2+}, Co^{2+}, and Zn^{2+} restored various levels of enzyme activity, with Zn^{2+} showing the highest level (Table 4.3). Addition of Fe^{3+} or Ni^{2+} resulted in no detectable activity. Moreover, analysis of metal content of untreated native enzyme showed the presence of Zn^{2+} ions only (Table 4.3). Similarly, soaks of SpNic by metals after treatment with chelators showed that, while both Fe^{2+} and Mn^{2+} can bind, Zn^{2+} is observed at the highest concentration under equivalent conditions.

Table 4.3. Analysis of Metal Content

Sample	S (μM)	[SpNic][1] (μM)	Mn (μM)	Fe (μM)	Zn (μM)	Co, Cu, Ca, Mg, K (μM)
Untreated	203	34	< det	< det	5	< det
No metal added	119	20	< det	< det	< det	< det
Zn^{2+}	144	24	< det	< det	142	< det
Mn^{2+}	144	24	18	< det	17	< det
Fe^{2+}	122	20	< det	51	< det	< det

< det = below detection limit

[1] [SpNic] was calculated from the sulfur content determined by analysis of metal content

Active Site Water Molecule and Metal-Water Relationship. In addition to four bonds to the enzyme and an interaction with the pyridyl nitrogen of the ligand, a water molecule is coordinated to the metal in the SpNic active site (Figure 4.3, red sphere). This water is located from 5 - 6 Å from the carbonyl carbon of the ligand in the SpNic structures. Water molecules coordinated to metals can be activated for catalysis and the degree of activation of the water has implications for the mechanism of the enzymatic reaction. The length of the metal-water bond can indicate the type of species present in the structure. The distances between the metal ion and the water in the SpNic structures vary from 2.2 Å to 2.4 Å. The method of Cruickshank (*46*) was used to estimate the coordinate error present in the model and from this information and the individual B-factors, approximate coordinate errors for the water and metal ion were calculated (see Materials and Methods). The estimated coordinate error for both the metal ion and the water varied between 0.12 Å and 0.19 Å.

Structure of C136S SpNic with Bound Nicotinamide. To assess the roles of active site residues, the structures of several SpNic complexes were determined. The structure of an inactive form of SpNic, the C136S mutant, reveals several important features of the active site (Figures 4.3 and 4.4A). The orientation of the ligand in the active site is facilitated by several π-stacking interactions of the pyridyl ring with

Phe14, Phe68 and Tyr106 and through coordination of the pyridyl nitrogen to the observed metal ion. Additional contacts are made to the amide nitrogen by Asp8, and the backbone carbonyls of Val131 and Ser136. A putative oxyanion hole, which forms H-bonds with the backbone amines of Leu132 and Ser136 in this structure, is also observed (Figure 4.3A). In addition, the carbonyl carbon of nicotinamide is situated less than 3 Å from the suspected catalytic residue (136) while an aspartate residue (Asp8) is approximately equidistant from the amide nitrogen and the oxygen of Ser136 (Figure 4.3B).

Structures of SpNic-Aldehyde Complexes. To further probe the active site of SpNic, we solved the crystal structures of SpNic in complex with the aldehyde inhibitors nicotinaldehyde and 5-MeO-nicotinaldehyde. While the organization of the active site remains essentially unchanged, the observed geometry about the carbonyl carbon varies in the differently liganded structures of SpNic. In both of the nicotinaldehyde complexes, tetrahedral geometry is observed at what was the carbonyl carbon center (Figure 4.4B and C and Figure 4.5). The difference density observed in these structures allows for the unambiguous placement of the proposed thiohemiacetal in the active site (Figures 4.4B and 4.4C).

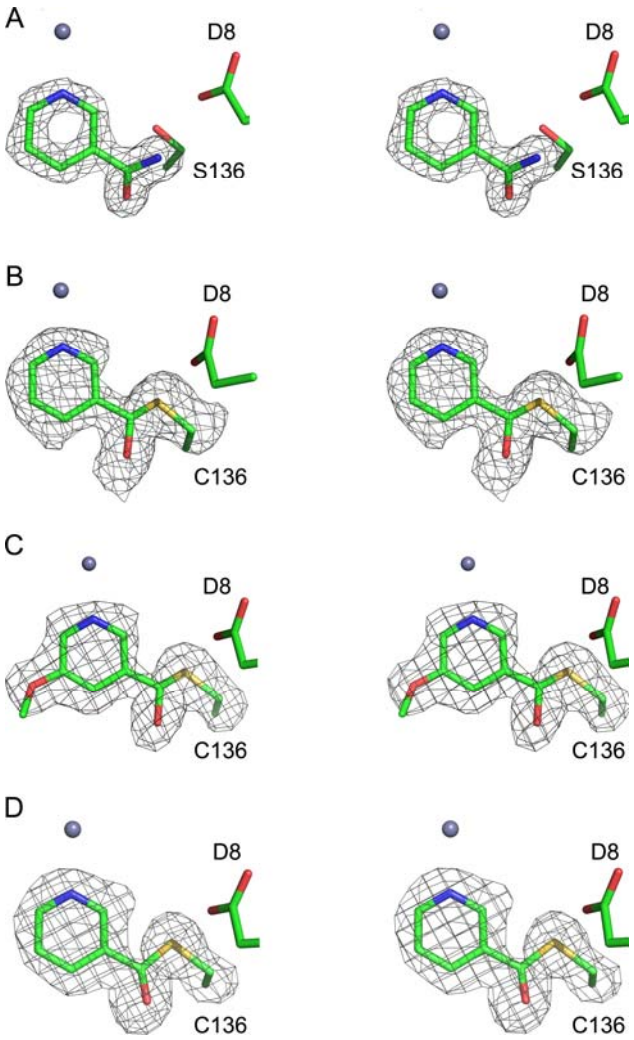

Figure 4.4. Electron densities of bound ligands to SpNic. Each section shows a stereo diagram of the various ligand-bound complexes; the zinc ion (grey sphere) and Asp8 are shown for reference. All electron density shown is from $1F_O - F_C$ maps and density shown, contoured at 2.5σ, was calculated prior to adding the ligand to the model. For the covalent complex maps, the Cys136 side chain was also omitted from the model in order to illustrate the linkage (A) Cys136Ser SpNic mutant with NAM bound. (B) SpNic complex with nicotinaldehyde. (C) SpNic complex with 5-OCH_3-nicotinaldehyde. (D) SpNic thioester complex formed in the presence of nicotinic acid.

Structure of SpNic Treated with Nicotinic Acid. As was observed for the aldehyde soaks of SpNic, treatment of this enzyme with nicotinic acid had little effect on the overall organization of the active site. The observed ligand density, however, was distinct from the other liganded structures. The electron density observed from

data collected on soaks of SpNic treated with nicotinic acid corresponded to a covalent adduct with sp^2 hybridization at the carbonyl carbon. A covalent nicotinyl thioester linkage between the ligand and Cys 136 of SpNic was a good fit to the observed density (Figure 4.4D).

4.5 Discussion

Structural Similarity to Other Proteins. The crystal structure of SpNic was compared to other proteins contained within the PDB using the Dali server (*50*). The overall fold of SpNic is shared by several classes of enzymes, most of which belong to the cysteine hydrolase family. These enzymes predominantly catalyze the hydrolysis of amides, esters or ethers and share a conserved catalytic cysteine residue. The most closely related enzymes, structurally, are the N-carbamoylsarcosine amidases (PDB codes 3EEF and 1NBA), and the isochorismatases (1NF9, 2FQ1 and 2A67). N-carbamoylsarcosine amidohydrolases (CSHases) hydrolyze N-carbomoylsarcosine to sarcosine, carbon dioxide and ammonia. While the fold of this enzyme is quite similar to that of SpNic the shape and nature of substrates accommodated is quite different. In addition, CSHase catalyzes the removal of an amide group and does not employ a metal ion in catalysis or substrate binding (*51*). The isochorismatase enzymes catalyze the conversion of isochorismate to 2,3-dihydroxybenzoate and pyruvate *via* the hydrolysis of a vinyl ether bond. Despite the structural similarities between these enzymes and PncA, isochorismatases lack the conserved cysteine residue and catalyze unrelated chemistry (*52*).

Key Active Site Residues. There are several features of the SpNic active site that are significant for substrate binding and catalysis. Structurally, the pyridine ring of the ligand is oriented in the active site through coordination to the metal ion and through π-interactions made with the aromatic sidechains Phe14, Phe68 and Tyr106; additional polar contacts are made with the amide moiety through both side chain and

backbone atoms. The SpNic-aldehyde complex structures clearly indicate that Cys136 is the catalytic residue responsible for nucleophilic attack of the carbonyl carbon. Asp8, nearly equidistant from Cys136 and the $-NH_2$ of the amide, is poised to both deprotonate the catalytic cysteine and to transfer a proton to the amine leaving group (Figure 4.3). Studies of PncA mutants, predominantly carried out in *Mycobacterium tuberculosis,* have shown that a complete loss of activity occurs upon mutation of either the active site cysteine or aspartate (*35, 36, 53*). One interesting case, the *Borrelia bergdorferri* PncA, is annotated as having an N-terminally truncated PncA which lacks the aspartate residue equivalent to Asp8. Studies on the activity of this enzyme showed that an additional 48 basepairs 5' of the designated start codon (16 amino acid residues) were needed to reconstitute PncA activity (*54*). When aligned with SpNic, this leading sequence contained an aspartate residue equivalent to Asp8 in SpNic.

Another active site mutation known to eliminate PncA activity is Lys96 in *M. tuberculosis* (equivalent to Lys103 in SpNic) (*35, 36*). It has been speculated that, along with the cysteine and aspartate residues, the lysine completes a catalytic triad in the PncA active site (*55*). There has been no evidence put forth, however, to indicate a direct role for the lysine residue in catalysis. Our structures indicate that the role of Lys103 is likely ancillary. This residue makes salt bridges with Asp8 and Asp53 (one of the residues that coordinates the metal ion) as well as interacting with Cys136 in the SpNic active site. Its likely role, therefore, is to orient these residues before and during catalysis and to help to offset the negative charges that develop along the reaction pathway.

A further notable feature of the SpNic active site is the presence of a putative oxyanion hole. In this pocket, the backbone amines of Leu132 and Cys136 make favorable contacts to the carbonyl oxygen of the ligand (Figure 4.3). This site is

structurally configured by a cis-peptide bond between Val131 and Leu132 that is conserved amongst nicotinamidases as well as in two other proteins with a similar fold, *N*-carbamoylsarcosine amidohydrolase from *Arthrobacter sp.* (*56*) and YcaC from *Escherichia coli* (*57*). This oxyanion hole presumably acts by both contributing to the proper orientation of the ligand in the active site, donating hydrogen bonds to the carbonyl oxygen, and by stabilizing negative charge that builds up along the reaction coordinate.

Identity and Role of the Metal Ion. Previous structural and biochemical studies on the PncA from *M. tuberculosis* (*36*) and *P. horikoshii* (*55*) have shown that this enzyme binds a metal ion. For the former, either Fe^{2+} or Mn^{2+} was sufficient to reconstitute activity and a 1:1 stoichiometry of Fe^{2+}:Mn^{2+} was found bound in the native enzyme (*36*). Kinetic analysis of the *P. horikoshii* PncA, however, showed a 19-fold increase in enzyme activity in the presence of zinc (*55*). In the case of SpNic, elemental analysis indicates that both Zn^{2+} and Fe^{2+} can bind to the enzyme, although zinc was the only metal isolated from the native protein. Clearly, Zn^{2+} can occupy the active site of SpNic as both the ligand and metal electron density in our structures was very clear when crystals were grown in the presence of $ZnCl_2$. In addition, our analysis of the metal dependence of SpNic kinetics shows that, while several divalent metals can participate in catalysis, the most catalytically active is Zn^{2+} (Table 4.4) These data suggest that this enzyme is most suited to utilize zinc in the metal site, but can also accommodate other divalent ions.

Table 4.4. Recovery of SpNic activity by addition of metal ions

Sample	Relative Rate[1]
Untreated	1.0
Metals Removed	0.0 ± 0.01
Zn^{2+}	0.90 ± 0.04
Mn^{2+}	0.27 ± 0.02
Fe^{2+}	0.13 ± 0.03
Co^{2+}	0.13 ± 0.02
Fe^{3+} or Ni^{2+}	0.0 ± 0.02

[1]The data are represented as mean of triplicate test ± standard deviation

The number and nature of the amino acid residues coordinated to the metal differs between the *P. horikoshii* PncA, *S. cerevisiae* PncA and SpNic. In both *P. horikoshii* and *S. cerevisiae*, the metal ion is coordinated by two histidine residues and an aspartate (*55, 58*). An additional glutamate residue is present in the SpNic enzyme (Figure 4.3). Mutational studies of the *M. tuberculosis* PncA suggest that this enzyme also coordinates the metal through four sidechain interactions, however these residues are putatively identified as three histidines and one aspartate (*36*). These findings indicate that the identity of the bound metal may depend upon the organism and is dictated by the nature of the coordinating residues. One possible explanation for this phenomenon is a divergent evolved specificity for particular metal(s) in distinct organisms due to differing environmental conditions. In this case, the ability for SpNic to utilize different metals for catalysis could have provided a competitive advantage and thus provided evolutionary pressure towards promiscuity.

Catalytic Water Molecule. In addition to four bonds to the enzyme and an interaction with the pyridyl nitrogen of the ligand, a water molecule is coordinated to the metal in the SpNic active site (Figure 4.3, red sphere). In order to complete the hydrolysis of NAM, an –OH donor is needed, which presumably originates from a water molecule. Since the metal bound water molecule is the only water less than 10

Å from the catalytic cysteine, it is reasonable to assume that this molecule may act as the –OH donor. While the distance from this water to the carbonyl carbon of the ligand is approximately 5.5 Å, all of our SpNic-ligand complexes show the carbonyl of the ligand oriented in such a way that this water molecule has a clear line of attack to the carbonyl carbon (Figure 4.4).

Water molecules coordinated to metals can be activated for catalysis. The degree of activation of the water has implications for the mechanism of the enzymatic reaction. In some cases the water is deprotonated upon coordination to the metal thus being activated as a hydroxide ion. The nature and number of coordinated ligands to a metal affects the overall ligand-metal bond strengths, with higher coordination leading to weaker bonds (*59*). In the case of water coordinated to a zinc ion, bond lengths of less than 2 Å generally indicate a metal-hydroxide moiety, while bonds greater than 2 Å in length indicate zinc-bound water (*59*). The metal-water bond length in our structures ranges from 2.3 to 2.5 Å with an estimated coordinate error at each atom of 0.1 to 0.2 Å. In addition, it has been observed that hydrogen bonds to the metal-bound water/hydroxide moeity orient it for attack (*59*). In the SpNic structure both Glu64 and Asp53 are ideally positioned to accept hydrogen bonds from the water molecule coordinated to zinc (Figure 4.3A). Considering the octahedral coordination, the metal-water bond length and the presence of two hydrogen bond acceptors, it is likely that, while the water may be activated for nucleophilic attack, it is coordinated as a water molecule and not as a hydroxide ion.

SpNic-Inhibitor Complexes and Mechanism of Inhibition. Nicotinaldehydes are known competitive inhibitors of nicotinamidase enzymes (*19, 41*). To examine the mechanism of inhibition we solved the structure of SpNic in complex with both nicotinaldehyde and 5-MeO-nicotinaldehyde (Figures 4.4B and C). These structures reveal a covalent adduct, formed between the carbonyl carbon and Cys136, that has

tetrahedral geometry at the (formerly) carbonyl carbon. This observation is consistent with the hypothesis that Cys136 acts as the nucleophile during catalysis. With the exception of the amide nitrogen, the inhibors are structurally identical to the substrate and therefore share the same enzyme-substrate interactions in the active site. The methoxy group at the 5- position of 5-OMe-nicotinaldehyde extends into a relatively open region of the active site, causing a slight shift in Phe68, but otherwise appears to have little effect on the orientation of the molecule or the active site residues.

The observation of a covalently linked tetrahedral structure suggests that the enzyme is reacting with the inhibitor but is unable to proceed past a relatively stable intermediate. In the absence of a good leaving group, the intermediate formed by reaction of the inhibitor with SpNic persists in the active site for a long enough time period to form the product observed in the structures. The presence of the oxyanion hole, which could stabilize the negative charge of a tetrahedral intermediate, suggests that the observed SpNic-thiohemiacetal adducts are formed as outlined in Figure 4.5B. This mechanism involves deprotonation of Cys136 by the nearby Asp8 followed by attack at the carbonyl carbon of the inhibitor. The charge buildup is stabilized by the oxyanion hole. In the absence of a leaving group the intermediate either proceeds in the reverse direction to reform the inhibitor or gains a proton from the solvent, leading to the structure observed.

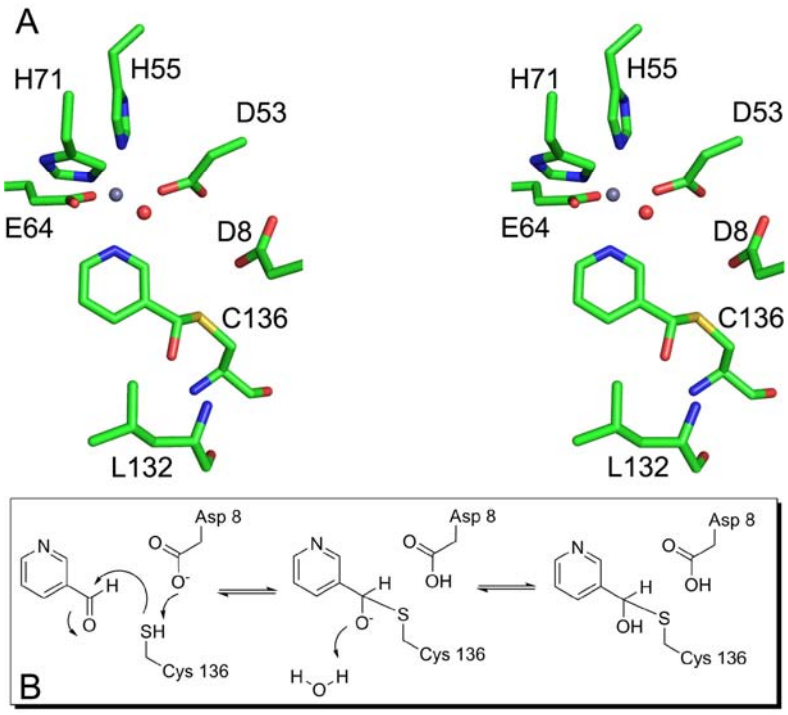

Figure 4.5. Mechanism of SpNic inhibition by nicotinaldehyde. A) Stereo diagram of the structure of the SpNic-nicotinaldehyde complex showing the trapped tetrahedral adduct. In the structure carbon atoms are colored green, oxygen atoms red, nitrogen atoms blue, sulfur is yellow and the zinc atom is grey. The red sphere is the water molecule that is coordinated to the zinc ion. B) The mechanism of inhibition whereby a tetrahedral adduct is formed by reaction with Cys136 to the carbonyl of the inhibitor resulting in a stalled complex due to the inability of the aldehyde hydrogen to act as a leaving group.

Structure of Trapped Thioester. The nicotinamidase reaction has been proposed to proceed through a thioester intermediate formed after attack of the substrate by the catalytic cysteine and concomitant liberation of ammonia (*39*, *55*). While biochemical and structural evidence supports this hypothesis, there has been no direct evidence reported for this type of intermediate. The structure of SpNic from crystals soaked with nicotinic acid, however, suggests that such a reaction intermediate is likely formed along the nicotinamidase reaction pathway. This structure shows a covalently linked intermediate with planar geometry at the carbonyl carbon center. The difference density for the ligand allows for unambiguous

placement of a nicotinyl thioester linked to Cys136 of SpNic (Figure 4.4D). This structure not only provides evidence for a thioester intermediate, but also indicates that the final steps in the reaction are fully reversible. This observation is supported by ^{18}O exchange experiments wherein facile exchange of ^{18}O was observed in the presence of both unlabelled and ^{18}O-nicotinic acid (*41*). These data, together with the C136S SpNic-NAM and SpNic-Inhibitor complexes, suggest a reaction mechanism whereby the putative thioester intermediate is accessible in both the forward and reverse directions.

Implications for Catalysis. The structures presented herein elucidate several important features of substrate binding and catalysis, and provide evidence for two putative intermediates in the nicotinamidase reaction pathway. Our analysis suggests that SpNic catalyzes a ping-pong type reaction that proceeds through two half reactions separated by the reactive thioester intermediate. The proposed mechanism for the SpNic catalyzed reaction is given in Figure 4.6C. Nicotinamide is first oriented in the SpNic active site through π-stacking with several aromatic side chains and by coordination to the active site metal ion, which may also serve to activate the ligand for nucleophilic attack (Figures 4.6A and 4.3A). Additional interactions occur between the carbonyl oxygen of the substrate and the backbone amine groups that constitute the oxyanion hole. Catalysis is initiated by deprotonation of the catalytic cysteine, Cys136, by the nearby Asp8, followed by attack of the carbonyl carbon by the nucleophilic thiol of Cys136. This leads to the formation of the putative tetrahedral intermediate. The negative charge that builds up on the carbonyl oxygen of this species is stabilized by the oxyanion hole. This proposed intermediate is analogous in structure to that observed between SpNic and nicotinaldehyde (Figures 4.4B, 4.4C and 4.5A). The tetrahedral intermediate then collapses to form a thioester, as the amino group of the ligand is protonated by Asp8 and leaves as ammonia. This

aspartate residue is observed in the C136S SpNic-nicotinamide structure to be nearly equidistant from the nucleophile and the leaving group, aligned ideally for proton transfer between these two groups.

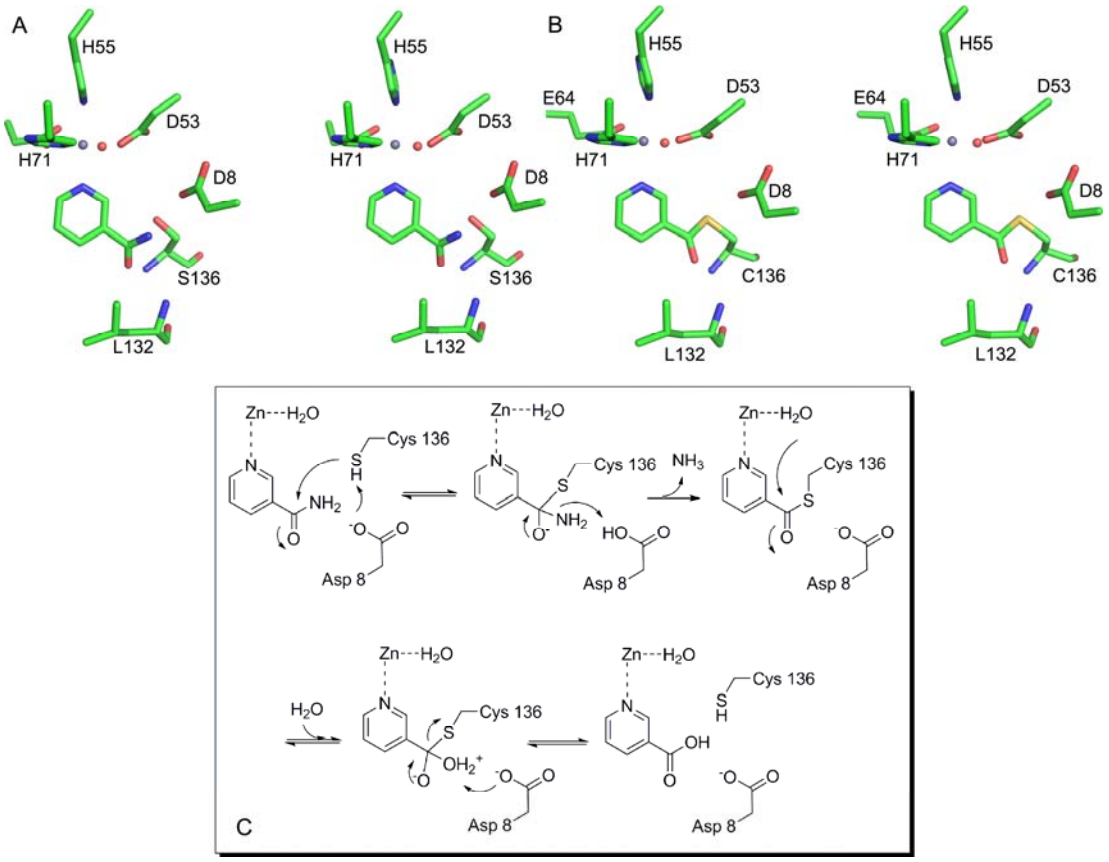

Figure 4.6. Mechanism of SpNic Catalyzed Hydrolysis of Nicotinamide. A) Stereo diagram showing the Cys136Ser mutant in complex with NAM. B) Stereo diagram showing the trapped thioester intermediate formed by soaking native SpNic with NA. For both A) and B) carbon atoms are colored green, oxygen atoms red, nitrogen atoms blue, sulfur is yellow and the zinc atom is grey. The red sphere is the water molecule that is coordinated to the zinc ion. C) The proposed mechanism of the SpNic catalyzed reaction. See text for details of the steps.

The thioester intermediate, presumably equivalent to what is observed for the nicotinic acid treated SpNic, can then undergo nucleophilic attack by a water molecule to lead to a second tetrahedral intermediate. While our structures cannot

unequivocally determine the source of the water that ultimately hydrolyzes the nicotinamide, the most likely source of this nucleophile is the water coordinated to the zinc ion. This water is ideally positioned for attack at the carbonyl carbon and is properly oriented by Asp53 and Glu64 to carry out this chemistry. In addition, coordination to the metal ion likely activates this molecule for attack. Despite this evidence it cannot be ruled out, however, that deprotonation of the water molecule occurs prior to attack, yielding a hydroxide moiety as the nucleophile.

The final stages of the reaction, leading from the second tetrahedral intermediate to product, are analogous to the first steps but occur in the reverse order. Deprotonation of the bound water by Asp8 prevents reversal of the reaction as collapse of the intermediate expels the thiol group of Cys136. The product, nicotinic acid, dissociates, likely driven by unfavorable interactions between Cys136 and Asp8 of the enzyme and the acid group of the product. The catalytic cycle is completed by the return of the proton from Asp8 to Cys136.

In summary, we have presented several crystal structures of the nicotinamidase enzyme from the human pathogen, *Streptococcus pneumoniae*, and provided a biochemical analysis of the role and identity of the active site metal. The structures allow us to define many of the key active site interactions and provide details about the mechanism by which aldehyde analogs of nicotinamide inhibit this enzyme. These structures also provide a glimpse of the putative reaction intermediates and provide much needed insights into the catalytic mechanism of this important enzyme.

REFERENCES

1. Sauve, A. A. (2008) NAD+ and vitamin B3: from metabolism to therapies, *J Pharmacol Exp Ther 324*, 883-893.
2. Gerdes, S. Y., *et al.* (2002) From genetic footprinting to antimicrobial drug targets: examples in cofactor biosynthetic pathways, *J Bacteriol 184*, 4555-4572.
3. Velu, S. E., *et al.* (2007) Antibacterial nicotinamide adenine dinucleotide synthetase inhibitors: amide- and ether-linked tethered dimers with alpha-amino acid end groups, *J Med Chem 50*, 2612-2621.
4. Oppenheimer, N. J. (1994) Nad Hydrolysis - Chemical and Enzymatic Mechanisms, *Molecular and Cellular Biochemistry 138*, 245-251.
5. Handlon, A. L., *et al.* (1994) 2'-Ribose Substituent Effects on the Chemical and Enzymatic-Hydrolysis of Nad(+), *Journal of the American Chemical Society 116*, 12087-12088.
6. Rongvaux, A., *et al.* (2002) Pre-B-cell colony-enhancing factor, whose expression is up-regulated in activated lymphocytes, is a nicotinamide phosphoribosyltransferase, a cytosolic enzyme involved in NAD biosynthesis, *Eur. J. Biochem. 32*, 3225-3234.
7. Belenky, P., *et al.* (2007) NAD+ metabolism in health and disease, *Trends Biochem Sci 32*, 12-19.
8. Pruser, J. E., *et al.* (2003) *Mol. Microbiol. 48*, 753-764.
9. Kim, S., *et al.* (2004) *Brucella abortus* nicotinamidase (PncA) contributes to its intracellular replication and infectivity in mice, *FEMS Microbiol. Lett. 234*, 289-295.

10. Zerez, C. R., *et al.* (1990) Increased nicotinamide adenine dinucleotide content and synthesis in *Plasmodium faciparum*-infected human erythrocytes, *Blood 75*, 1705-1710.
11. Li, Y., and Bao, W. (2007) Why do some yeast species require niacin for growth? Different modes of NAD synthesis, *FEMS Yeast Res. 7*, 657-664.
12. Kurnasov, O. V., *et al.* (2003) Ribosylnicotinamide kinase domain of NadR protein: identification and implications in NAD biosynthesis, *J. Bacteriol. 184*, 6906-6917.
13. Hughes, D. E., and Williamson, D. H. (1952) The synthesis of cozymase from nicotinic acid and its derivatives by *Lactobacillus arabinosus*, *Biochem. J.*, 330-338.
14. Johnson, W. J., and Gadd, R. E. A. (1974) Inhibition of nicotinamide deamidase from *Micrococcus lysodeikticus* by analogues of nicotinamide, *Int. J. Biochem. 5*, 633-641.
15. Foster, J. E., *et al.* (1979) Pyridine nucleotide cycle of *Salmonella typhimurium*: isolation and characterization of pncA, pncB and pncC mutants and utilization of exogenous nicotinamide adenine dinucleotide, *J. Bacteriol. 137*, 1165-1175.
16. Joshi, J. G., and Handler, P. (1961) *J. Biol. Chem. 237*, 929-935.
17. Pardee, A. B., *et al.* (1971) Hyperproduction and purification of nicotinamide deamidase, a microconstituitive enzyme of *Escherichia coli*, *J. Biol. Chem. 246*, 6792-6796.
18. Tanigawa, Y., *et al.* (1972) Purification and properties of nicotinamide deamidase from *Flavobacterium peregrinum*, *J. Biol. Chem. 247*, 8036-8042.

19. Yan, C., and Sloan, D. L. (1987) Purification and characterization of nicotinamide deamidase from yeast, *J. Biol. Chem. 262*, 9082-9087.

20. Joshi, J. G., and Handler, P. (1960) Biosynthesis of trigonelline, *J. Biol. Chem. 235*, 2981-2986.

21. Wang, G., and Pichersky, E. (2007) Nicotinamidase participates in the salvage pathway of NAD biosynthesis in *Arabidopsis*, *Plant J. 49*, 1020-1029.

22. van der Horst, A., *et al.* (2007) The *Caenorhabditis elegans* nicotinamidase PNC-1 enhances survival, *Mech. Ageing Dev. 128*, 346-349.

23. Balan, V., *et al.* (2008) Life span extension and neuronal cell protection by Drosophila nicotinamidase, *J Biol Chem 283*, 27810-27819.

24. Gallo, C. M., *et al.* (2004) Nicotinamide clearence by Pnc1 directly regulates Sir2-mediated silencing and longevity, *Mol. Cell. Biol. 24*, 1301-1312.

25. Anderson, R. M., *et al.* (2003) Nicotinamide and PNC1 govern lifespan extension by calorie restriction in *Saccharomyces cerevisiae*, *Nature 423*, 181-185.

26. Sauve, A. A., and Schramm, V. L. (2003) Sir2 regulation by nicotinamide results from switching between base exchange and deacetylation chemistry, *Biochem. 42*, 9249-9256.

27. Jackson, M. D., *et al.* (2003) Mechanism of nicotinamide inhibition and transglycosidation by Sir2 histone/protein deacetylases, *J. Biol. Chem. 278*, 50985-50998.

28. Avalos, J. L., *et al.* (2004) Structural basis for the mechanism and regulation of Sir2 enzymes, *Mol. Cell 13*, 639-648.

29. Sauve, A. A., *et al.* (2005) Chemical activation of Sir2-dependent silencing by relief of nicotinamide inhibition, *Mol. Cell 17*, 595-601.

30. Sauve, A. A., *et al.* (2006) The Biochemistry of Sirtuins, *Annu. Rev. Biochem. 75*, 435-465.

31. Anderson, R. M., *et al.* (2003) Nicotinamide and PNC1 govern lifespan extension by calorie restriction in Saccharomyces cerevisiae, *Nature 423*, 181-185.

32. Rogina, B., and Helfand, S. L. (2004) Sir2 mediates longevity in the fly through a pathway related to calorie restriction, *Proc Natl Acad Sci U S A 101*, 15998-16003.

33. Tissenbaum, H. A., and Guarente, L. (2001) Increased dosage of a sir-2 gene extends lifespan in Caenorhabditis elegans, *Nature 410*, 227-230.

34. Konno, K. F., *et al.* (1967) Pyrazinamide susceptibility and amidase activity of tubercle bacilli, *Am. Rev. Respir. Dis. 95*, 461-469.

35. Scorpio, A., *et al.* (1997) Characterization of *pncA* Mutations in Pyrazinamide-Resistant *Mycobacterium tuberculosis*, *Antimicrob. Agents Chemother. 41*, 540-543.

36. Zhang, H., *et al.* (2008) Characterization of *Mycobacterium tuberculosis* nicotinamidase/pyrazinamidase, *FEBS J. 275*, 753-762.

37. Hu, G., *et al.* (2007) Crystal structure of the yeast nicotinamidase Pnc1p, *Arch Biochem Biophys 461*, 66-75.

38. Du, X., *et al.* (2001) Crystal structure and mechanism of catalysis of a pyrazinamidase from Pyrococcus horikoshii, *Biochemistry 40*, 14166-14172.

39. Fyfe, P. K., *et al.* (2009) Specificity and mechanism of Acinetobacter baumanii nicotinamidase: implications for activation of the front-line

tuberculosis drug pyrazinamide, *Angewandte Chemie (International ed 48*, 9176-9179.

40. Bradford, M. (1976) A Rapid and Sensitive Method for the Quantitation of Microgram Quantities of Protein Utilizing the Principle of Protein-Dye Binding, *Anal. Biochem. 72*, 248-254.

41. French, J. B.*, et al.* (2010) Characterization of nicotinamidases: Class-wide inhibition by nicotinaldehydes and mechanism of inhibition and catalysis, *submitted*.

42. Vagin, A., and Teplyakov, A. (2000) An approach to multi-copy search in molecular replacement *Acta Crystallogr., D 56*, 1622-1624.

43. Collaborative Computational Project-Number 4. (1994) The CCP-4 suite: programs for protein crystallography, *Acta Crystallogr., D 50*.

44. Brunger, A. T.*, et al.* (1998) Crystallography & NMR system: A new software suite for macromolecular structure determination, *Acta Crystallogr., D 54*, 905-921.

45. Emsley, P., and Cowtan, K. (2004) Coot: model-building tools for molecular graphics, *Acta Crystallogr., D 60*, 2126-2132.

46. Cruickshank, D. W. J. (1999) Remarks about protein structure precision, *Acta. Cryst. D55*, 583-601.

47. Chambers, J. L., and Stroud, R. M. (1979) The accuracy of refined protein structures: Comparison of two independently refined models of bovine trypsin, *Acta. Cryst. B35*, 1861-1874.

48. Schneider, T. R. (2000) Objective comparison of protein structures: error-scaled difference distance matrices, *Acta. Cryst. D56*, 714-721.

49. Cornell Nutrient Analysis Laboratory. (2008) http://cnal.cals.cornell.edu, Ithaca.

50. Holm, L., and Sander, C. (1993) Protein structure comparison by alignment of distance matrixes, *J. Mol. Biol. 233*, 123-128.

51. Zajc, A., *et al.* (1996) Crystallographic and fluorescence studies of ligand binding to N-carbamoylsarcosine amidohydrolase from *Arthrobacter* sp, *J. Mol. Biol. 263*, 269-283.

52. Parsons, J. F., *et al.* (2003) Structure and Mechanism of *Pseudomonas aeruginosa* PhzD, an Isochorismatase from the Phenazine Biosynthetic Pathway, *Biochemistry 42*, 5684-5693.

53. Lemaitre, N., *et al.* (2001) Study of the structure-activity relationships for the pyrazinamidase (PncA) from *Mycobacterium tuberculosis*, *Biochem. J. 353*, 453-458.

54. Purser, J. E., *et al.* (2003) A plasmid-encoded nicotinamidase (PncA) is essential for infectivity of *Borrelia burgdorferi* in a mammalian host, *Mol. Microbiol. 48*, 753-764.

55. Du, X., *et al.* (2001) Crystal structure and mechanism of catalysis of a pyrazinamidase from *Pyrococcus horikoshii*, *Biochem. 40*, 14166-14172.

56. Zajc, A., *et al.* (1996) Crystallographic and fluorescence studies of ligand binding to N-carbamoylsarcosine amidohydrolase from Arthrobacter sp, *J Mol Biol 263*, 269-283.

57. Colovos, C., *et al.* (1998) The 1.8 Å crystal structure of the ycaC gene product from *Escherichia coli* reveals an octameric hydrolase of unknown specificity, *Structure 6*, 1329-1337.

58. Hu, G., *et al.* (2007) Crystal structure of the yeast nicotinamidase Pnc1p, *Arch. Biochem. Biophys. 461*, 66-75.

59. Christianson, D. W., and Cox, J. D. (1999) Catalysis by metal-activated hydroxide in zinc and manganese metalloenzymes, *Annu. Rev. Biochem. 68*, 33-57.

CHAPTER 5

INTRODUCTION TO PART II

Purines and their derivatives comprise a large percentage of biomass and are essential for many of the processes necessary for life. They are a major component of nucleic acids, are important for protein synthesis and signaling and play a major role in energy transfer and storage. In addition, purines can be a major source of nitrogen and carbon for many plants and microorganisms (*1, 2*).

In some organisms purines can be utilized as the sole nitrogen source, particularly when other sources are limited (*1, 2*). This can occur aerobically or anaerobically, but does so by different pathways. The various purine substrates are first converted to xanthine which is then hydrolyzed to uric acid by xanthine dehydrogenase, steps which are not strongly influenced by the presence of oxygen (*1*). The catabolism of uric acid occurs over many steps and involves a suite of enzymes that can differ between organisms. Two recent genetic studies reported a cluster of genes found to be responsible for the degradation of uric acid in *Klebsiella pneumoniae* (*3, 4*). The proposed pathway for the catabolism of uric acid in this organism is shown in Figure 5.1.

The degradation of uric acid and the intermediates in the pathway are of importance to human health for many reasons. The inability for humans to degrade uric acid can lead to the formation of crystals in joints, causing gout (*5*). The ability of *Klebsiella pneumoniae* to degrade allantoin has been linked to the production of liver abscesses with metastatic complications (*6*). In addition, one of the products of uric acid degradation, allantoin, has seen widespread commercial use. This molecule is commonly added to many cosmetic and pharmaceutical products primarily because of its moisturizing and keratolytic properties.

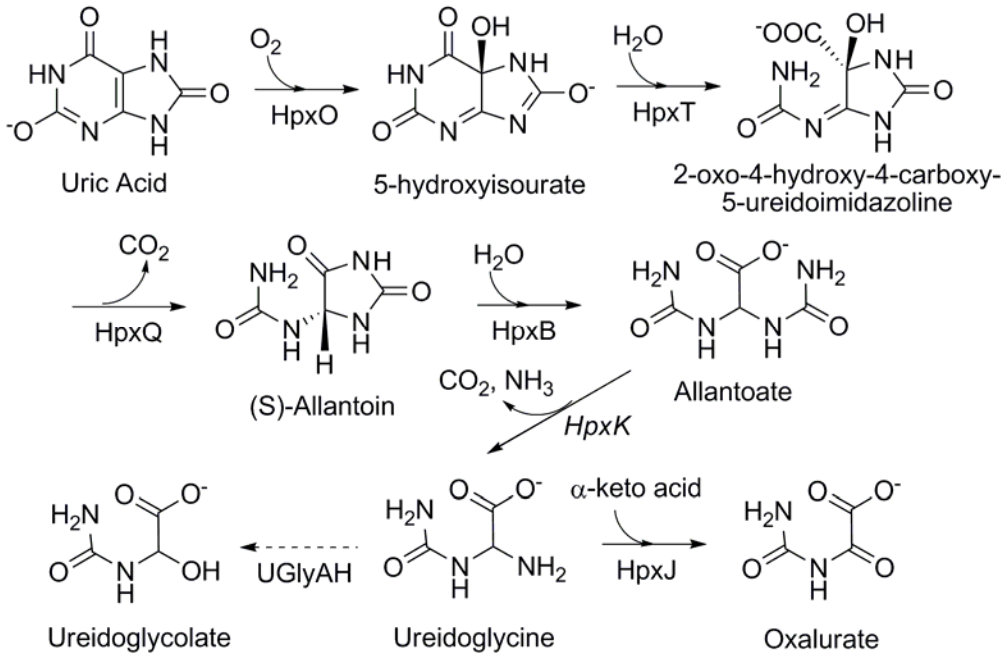

Figure 5.1. Uric acid catabolic pathway in *Klebsiella pneumoniae*. The pathway from uric acid to oxalurate is shown with the compound names given below their structures. The enzyme names from *K. pneumoniae* for each reaction are given below the arrows. The conversion of ureidoglycine to ureidoglycolate is shown as an alternative pathway for ureidoglycine degradation that occurs in other organisms. Oxalurate can be further catabolized by additional enzymes present in *K. pneumoniae*.

In the following three chapters, the structural and biochemical characterization of several of the enzymes that play a role in purine catabolism in *Klebsiella pneumoniae* is presented. In chapter 6, the biochemical and structural characterization of a previously unreported transformation, the aminotransfer between ureidoglycine and an α-keto acid, is reported. *K. pneumoniae* HpxJ is shown, using HPLC, pre-steady state kinetics and x-ray crystallography, to be an aminotransferase that preferentially takes ureidoglycine as a substrate.

Chapter 7 outlines the structural characterization of *K. pneumoniae* HpxQ, the enzyme that converts 2-oxo-4-hydroxy-4-carboxy-5-ureidoimidazoline (OHCU) to (S)-allantoin. This is the first structurally characterized prokaryotic OHCU decarboxylase. In addition to the structures provided, an OHCU decarboxylase

inhibitor is identified and characterized. The structural and biochemical data, along with modeling studies of substrates and intermediates, allow for insights into the mechanism of the HpxQ catalyzed reaction.

The final chapter in this section details the structure and function of an allantoin racemase, HpxA, from *K. pneumoniae*. This work represents the first structural characterization of an allantoin racemase from any organism. The structures, which include an unliganded form and complexes of HpxA mutants with allantoin and with 5-acetyl hydantoin, provide details about ligand binding and the putative two base mechanism of catalysis.

These structural and biochemical studies, along with the studies of *K. pneumoniae* 5-hydroxyisourate hydolase (HpxT - Appendix I) and urate oxidase (HpxO - (*7, 8*)), provide a thorough examination of the enzymes responsible for the conversion of uric acid to oxalurate in this organism. Their characterization provides examples of some previously unknown chemistries, and expands our knowledge of purine metabolism. Further exploration of this unusual pathway will no doubt lead to the discovery of additional interesting and unexpected enzymatic transformations.

REFERENCES

1. Vogels, G. D., and Drift, C. V. D. (1976) Degradation of Purines and Pyrimidines by Microorganisms, *Bacteriol. Rev. 40*, 403-468.
2. Zrenner, R.*, et al.* (2006) Pyrimidine and Purine Biosynthesis and Degradation in Plants, *Ann. Rev. Plant Biol. 57*, 805-836.
3. de la Riva, L.*, et al.* (2008) The hpx genetic system for hypoxanthine assimilation as a nitrogen source in *Klebsiella pneumoniae*: gene organization and transcriptional regulation, *Journal of bacteriology 190*, 7892-7903.
4. Pope, S. D.*, et al.* (2009) Purine utilization by *Klebsiella oxytoca* M5al: genes for ring-oxidizing and -opening enzymes, *Journal of bacteriology 191*, 1006-1017.
5. Richette, P., and Bardin, T. (2010) Gout, *Lancet 375*, 318-328.
6. Chou, H. C.*, et al.* (2004) Isolation of a chromosomal region of Klebsiella pneumoniae associated with allantoin metabolism and liver infection, *Infection and immunity 72*, 3783-3792.
7. Hicks, K. A., and Ealick, S. E. Crystal structures of *Klebsiella pneumoniae* urate oxidase, *Unpublished work.*
8. O'Leary, S. E.*, et al.* (2009) Biochemical characterization of the HpxO enzyme from Klebsiella pneumoniae, a novel FAD-dependent urate oxidase, *Biochemistry 48*, 3033-3035.

CHAPTER 6

BIOCHEMICAL AND STRUCTURAL CHARACTERIZATION OF A UREIDOGLYCINE AMINOTRANSFERASE IN THE *KLEBSIELLA PNEUMONIAE* URIC ACID CATABOLIC PATHWAY

6.1 Abstract

Many plants, fungi, and bacteria catabolize allantoin as a mechanism for nitrogen assimilation. Recent reports have shown that in plants and some bacteria the product of hydrolysis of allantoin by allantoinase is the unstable intermediate ureidoglycine. While this molecule can spontaneously decay, genetic analysis of some bacterial genomes indicates that an aminotransferase may be present in the pathway. Here we present evidence that *Klebsiella pneumoniae* HpxJ is an aminotransferase that preferentially converts ureidoglycine and an α-keto acid into oxalurate and the corresponding amino acid. We determined the crystal structure of HpxJ, allowing us to present an explanation for substrate specificity.

6.2 Introduction, Results and Discussion

The uric acid catabolic pathway is the final stage of purine catabolism and functions in plants and some bacteria to provide a source of nitrogen, particularly when other nitrogen sources are depleted (*1, 2*). Uric acid catabolism begins with the oxidation of uric acid by uricase followed by ring opening and decarboxylation reactions catalyzed by 5-hydroxyisourate hydrolase and 2-oxo-4-hydroxy-4-carboxy-5-ureidoimidazoline decarboxylase, respectively (*3-6*). The latter two steps lead to the production of allantoin, a process that also occurs non-enzymatically after oxidation of uric acid (*1, 4*). Allantoin can then be further degraded to allantoate by an allantoinase enzyme (*1*).

The further catabolism of ureides follows one of two pathways. The degradation of allantoate is catalyzed by either allantoicase or allantoate

amidohydrolase. The former produces urea and ureidoglycolate, both of which require further catabolism for full nitrogen assimilation. The latter pathway, which is found in plants and some bacteria (*1, 2*), also results in ureidoglycolate, but has been demonstrated to proceed *via* ureidoglycine, a molecule now known to be the product of the allantoate amidohydrolase catalyzed reaction (*7*).

Characterization of the fate of ureidoglycine has been complicated by the fact that it is unstable in aqueous environments and is subject to rapid non-enzymatic decay (*7, 8*). A recent report by Werner *et al.*, however, demonstrated that ureidoglycine can be hydrolyzed by ureidoglycine aminohydrolase (*9*). The resulting ureidoglycolate can be consumed by ureidoglycolate amidohydrolase or the urea-releasing ureidoglycolate hydrolase (ureidoglycolate lyase) (*2, 9*). Alternatively, in some organisms, ureidoglycolate can be oxidized to oxalurate which can be used in subsequent reactions to generate ATP and ammonia (*1, 10*).

Two recent genetic studies have identified a gene cluster encoding a purine degradative pathway in *Klebsiella sp.* that proceeds through similar intermediates as those outlined above, but does so using different catalytic strategies (*11, 12*). Scheme 6.1 outlines the proposed enzymes and intermediates in this pathway (*7, 9, 12*). One surprising finding in the gene cluster encoding these enzymes was the presence of a gene for a protein that belongs to the pyridoxal-5′-phosphate (PLP)[1]-dependent aspartate aminotransferase superfamily. An examination of the intermediates along the degradative pathway reveals that only ureidoglycine has the requisite amino group needed to participate in an aminotransfer reaction. Also notable is the absence of an enzyme capable of oxidizing ureidoglycolate to oxalurate. Taken together, this suggests that the pathway could proceed from ureidoglycine to oxalurate directly in some organisms. The presence of an aminotransferase associated with purine degradation is not unique to *Klebsiella sp.* In a recent cross-organism protein

association analysis, a gene encoding an aminotransferase was found linked to allantoate amidohydrolase in several organisms, particularly those lacking a ureidoglycine aminohydrolase (*9*).

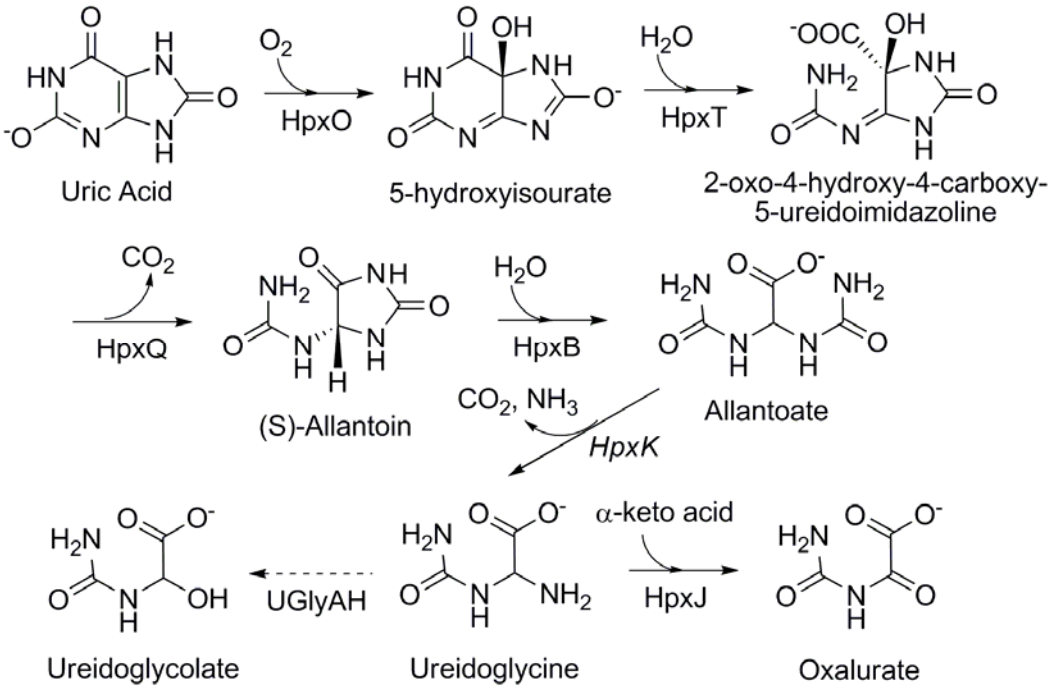

Scheme 6.1. Uric acid catabolic pathway in Klebsiella pneumoniae. The enzyme names are taken from the K. pneumoniae degradative pathway. The dashed line indicates an alternative route that operates in other organisms.

In order to determine if a ureidoglycine aminotransferase participates in the purine degradative pathway, we have biochemically and structurally characterized the *K. pneumoniae* enzyme with this putative function. To establish if HpxJ had aminotransferase activity, we first examined its ability to catalyze the transfers of an amino group between aspartate and glyoxylate. To quantitate the amino acid content in the reaction mixtures, we treated the mixtures with DABS-Cl prior to HPLC analysis. Figure 6.S1 shows HPLC chromatograms of the aminotransfer reaction in the presence and absence of HpxJ. A clear peak that coelutes with the glycine

standard appears in the enzyme catalyzed reaction while the aspartate peak diminishes in size. The production of glycine was enzyme dependent and also required the presence of an amino donor.

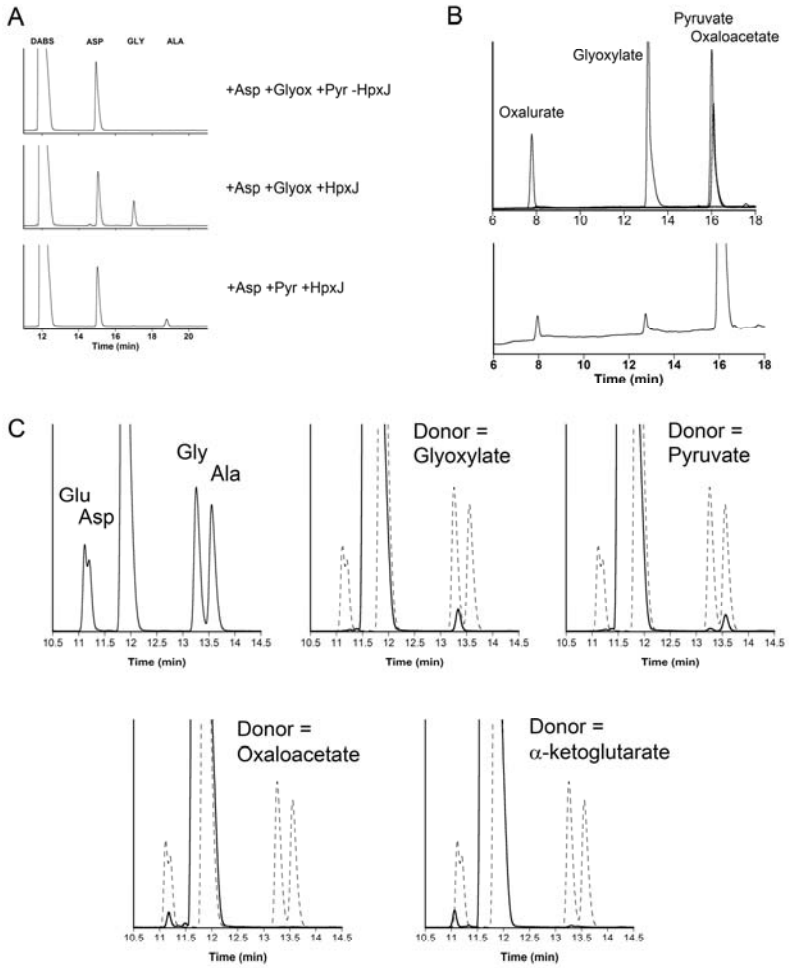

Figure 6.S1: A) HPLC chromatograms of the aminotransfer reaction of aspartate with glyoxylate or pyruvate as catalyzed by KpHpxJ. The top panel is the control reaction run in the absence of KpHpxJ. The second panel is the aminotransfer between aspartate and glyoxylate as monitored by the production of glycine. The third panel shows the aminotransfer reaction between aspartate and pyruvate as measured by the production of alanine. B) Overlaid HPLC chromatograms of keto-acid acceptor molecule standards. The products of the aminotransfer reaction with oxaloacetate and ureidoglycine (from Figure 6.1B - bottom panel) is shown as a reference. C) HPLC chromatograms of the aminotransfer reaction of ureidoglycine with different amino-acceptor molecules. The top left panel shows the amino acid product standards while the other panels show the reaction using the amino-acceptor molecule listed. Note that the gradient used to separate these samples was different than that used for Figure 1.

Having established that HpxJ was capable of catalyzing aminotransfer, we then wished to determine if ureidoglycine would be a substrate for this enzyme. Since this molecule is known to be unstable in solution we employed *E. coli* allantoate amidohydrolase (AAH) to synthesize ureidoglycine *in situ*. This enzyme and the chemistry of the AAH reaction have been recently characterized (*7*). The production of ureidoglycine by AAH reaction can be followed by monitoring the production of ammonia with a glutamate dehydrogenase coupled assay (Figure 6.S2).

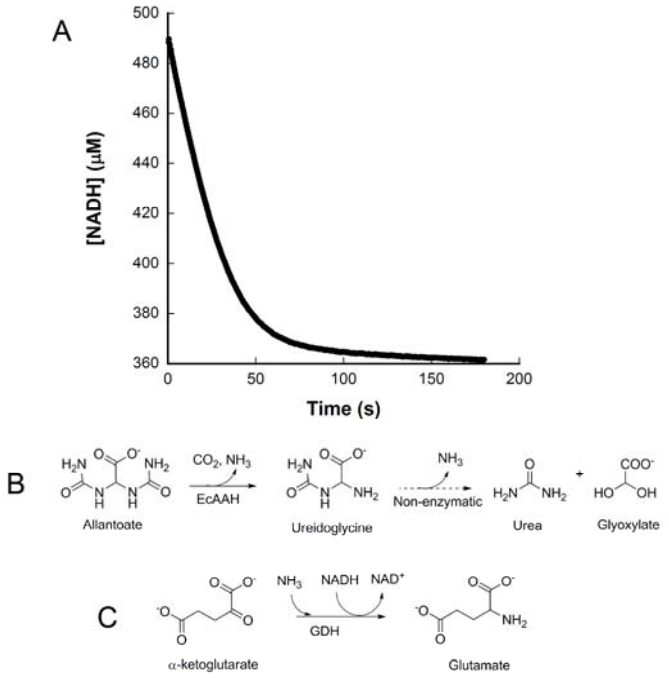

Figure 6.S2. Quantitative conversion of allantoate to ureidoglycine. A) The production of ureidoglycine from allantoate by EcAAH (B) could be monitored by following the release of ammonia. The ammonia produced could be tracked by coupling its release to consumption of NADH by the enzyme glutamate dehydrogenase (GDH). The incorporation of ammonia is accompanied by stoichiometric consumption of NADH (C). Conversion of NADH to NAD can be monitored at 340 nm. For this reaction, 125 μM allantoate was mixed with 1 mM ketoglutarate, 500 μM NADH, and 10 units of glutamate dehydrogenase. The reaction was initiated by the addition of 50 μM EcAAH. The non-enzymatic decay of ureidoglycine could also be monitored with this assay. The rate of decay (approximately 2×10^4 s^{-1}) was negligible over the time scale of the aminotransfer reactions.

The amino acid products of the HpxJ-catalyzed aminotransfer reaction between ureidoglycine and pyruvate were followed by HPLC after derivatization with DABS-Cl. A peak corresponding to alanine was observed in the presence of the enzyme when pyruvate was the amino-acceptor (Figure 6.1A, bottom panel). We also observed a small amount of glycine being produced both in the presence and absence of added pyruvate (Figure 6.1A, bottom two panels). This can be explained by the non-enzymatic decay of ureidoglycine. The decay of this molecule produces glyoxylate (*7, 8*) which can then be used as a substrate for the reaction. HPLC traces of standards and additional aminotransfer reactions are provided in the supporting material.

The products of the aminotransfer reaction between ureidoglycine and an α-keto acid are an amino acid and oxalurate. For further evidence that HpxJ catalyzes the aminotransfer reaction, we derivatized the keto-acid products of the reaction with o-phenylenediamine and followed them by HPLC. Figure 6.1B shows that oxalurate is produced in the presence of either pyruvate (Figure 6.1B, third panel) or oxaloacetate (Figure 6.1B, fourth panel) as amino acceptors. As with the amino products of the reaction, a small oxalurate peak was also observed in the absence of added amino-acceptor (Figure 6.1B, second panel).

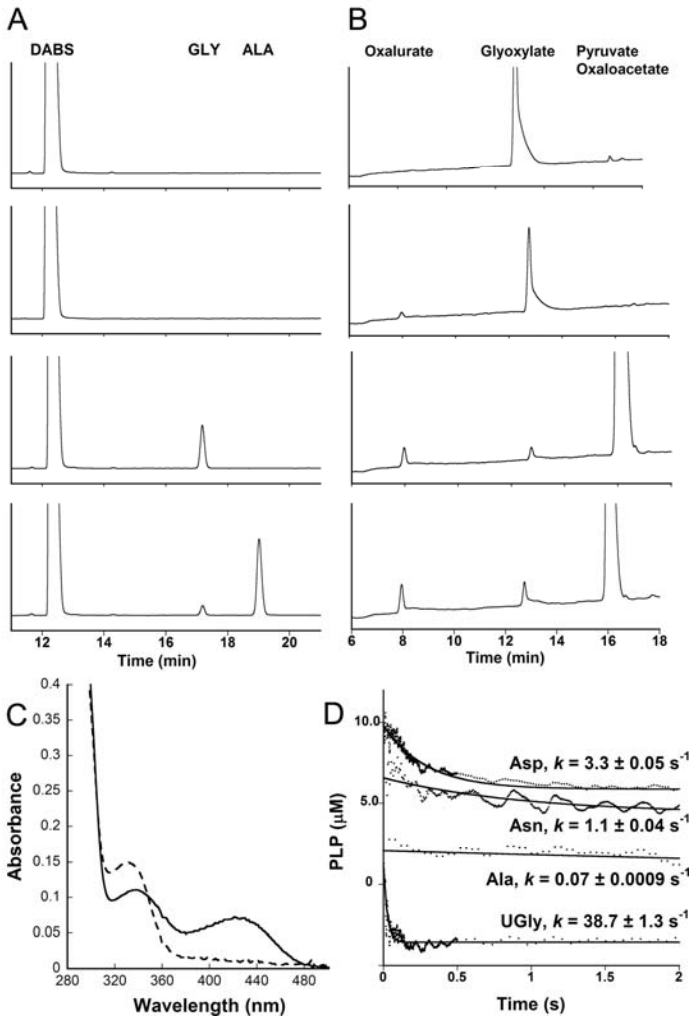

Figure 6.1. Characterization of K. pneumoniae HpxJ. A) HPLC traces of the amino products of the HpxJ aminotransfer reactions. From top to bottom: control reaction run with HpxJ in the absence of ureidoglycine, control reaction run in the absence of HpxJ with all other components present, the reaction with HpxJ and ureidoglycine in the absence of exogenous amino acceptor, and the HpxJ catalyzed reaction run in the presence of ureidoglycine and pyruvate. B) HPLC traces of the keto-acid products of the HpxJ aminotransfer reaction. From top to bottom: control in the absence of HpxJ, reaction with HpxJ and ureidoglycine in the absence of exogenous amino acceptor, transfer reaction in the presence of pyruvate, and the transfer reaction in the presence of oxaloacetate. Note that any unreacted allantoate in the reaction is hydrolyzed to glyoxylate during the derivatization work-up. C) UV absorbance spectra of native HpxJ (solid line) and reduced HpxJ (dashed line). D) Pre-steady state kinetics of the first half reaction catalyzed by HpxJ and rates from a fit to an exponential function. Note that the alanine and ureidoglycine traces have been shifted down the y-axis for clarity.

One of the conserved features of the aspartate aminotransferase family is the dependence upon the cofactor PLP. The absorbance spectrum of HpxJ (Figure 6.1C) is characteristic of enzymes with bound PLP in the imine form. Treatment of this enzyme with sodium borohydride causes the loss of the peak at 420 nm and a shift of the 333 nm peak to a slightly lower wavelength. This is consistent with the reduction of the PLP-imine to the amine form, a phenomenon that is also observed in the first half of the transfer reaction as PLP is converted to PMP (*13*). It was also observed that this reduced form of HpxJ was unable to catalyze the aminotransferase reaction for any of the amino-donor/acceptor pairs that we tried (data not shown).

Aminotransferases are known to be promiscuous in regards to the identity of amino donor and acceptors (*14*, *15*). To examine the specificity of HpxJ for different amino acids, we measured the pre-steady state rate for the first half reaction of the transfer by monitoring the conversion of PLP to PMP. The curves and calculated rates for the different amino acids are shown in Figure 6.1D. It is clear from this data that ureidoglycine is the favored substrate, turning over an order of magnitude faster than the next fastest substrate, aspartate.

In order to further examine this novel aminotransferase and its preference for ureidoglycine, we crystallized and determined the structure of HpxJ using molecular replacement with PDB 1VJ0 (*16*) as a search model. Details about the structure solution and model building, including collection and refinement statistics, can be found in the supplemental material. The crystal structure of HpxJ showed a homotetramer as the biologically relevant unit (Figure 6.S3), an observation that was verified by size exclusion chromatography.

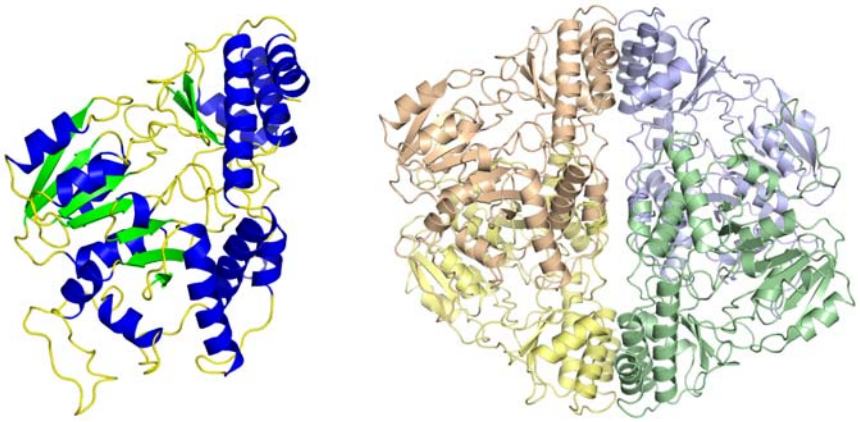

Figure 6.S3. Structure of KpHpxJ. The overall fold of the KpHpxJ monomer is shown on the left and is colored by secondary structure. The tetramer of the enzyme is shown on the right and displays the four molecules colored separately.

Since this enzyme was highly similar to other PLP-dependent aminotransferases, it was not surprising to find a covalently bound PLP molecule in the active site (Figure 6.2A). The electron density allowed for the unambiguous placement of the PLP in an orientation that superimposed well with PLP in homologous structures.

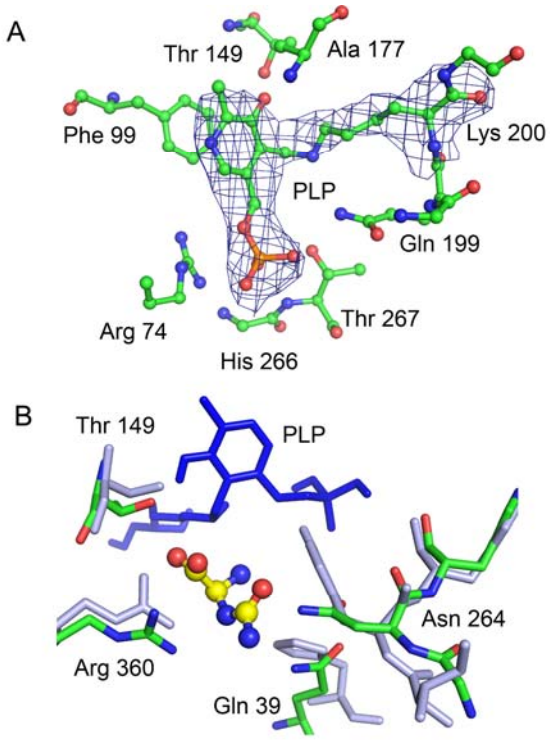

Figure 6.2. The active site of HpxJ. A) The structure of the PLP binding site of HpxJ showing a molecule of PLP covalently bound to lysine 200. F_O - F_C density is shown contoured at 3σ around the PLP and lysine residue. B) Superposition of the active site of HpxJ (green) and *A. aegypti* alanine glyoxylate aminotransferase (grey). Ureidoglycine is shown docked in the active site (yellow, ball and stick).

While the members of the alanine-glyoxylate aminotransferase superfamily are highly structurally conserved, there is a relatively large degree of variation amongst active site residues. With the exception of the highly conserved amino acids that interact with the PLP molecule, differences in active site residues account for the observed differences in substrate selectivity (see Figure 6.S4 for a sequence alignment). A superposition of HpxJ with structurally homologous aminotransferases shows several obvious differences in the active sites of these proteins. The most notable of these is an asparagine (Asn264) in place of a tyrosine residue and a glutamine (Gln39) in place of a histidine. The side chains of these residues point into the active site and are well positioned to make contacts with incoming substrates.

To better understand the selectivity of HpxJ for ureidoglycine over other amino acids, we modeled the ligand into the active site of our solved structure. Despite starting from several different conformers of ureidoglycine, all of the simulations converged to a similar orientation of the ligand in the active site. The structure of the HpxJ active site with the energy minimized ligand bound is shown in Figure 6.2B. What is apparent from this model is that, in addition to interactions with the amino and acid groups made by the PLP molecule, backbone atoms of a conserved proline-proline (Pro19 and Pro20) and a conserved arginine (Arg360), the ureidoglycine tail makes several hydrogen bonding contacts with Asn 264 and Gln39. These amino acids, which replace bulkier tyrosine and histidine residues seen in other aminotransferases, not only allow space for the larger substrate but also appear to directly interact with the substrate.

In summary, we have confirmed that HpxJ is an aminotransferase that catalyzes a novel transfer reaction between ureidoglycine and an α-keto acid. We have provided biochemical and structural evidence for this enzyme's specificity for ureidoglycine. Our data provide an explanation for the presence of this gene in the *K. pneumoniae* Hpx gene cluster and elucidate a novel branch in the ureide catabolic pathway.

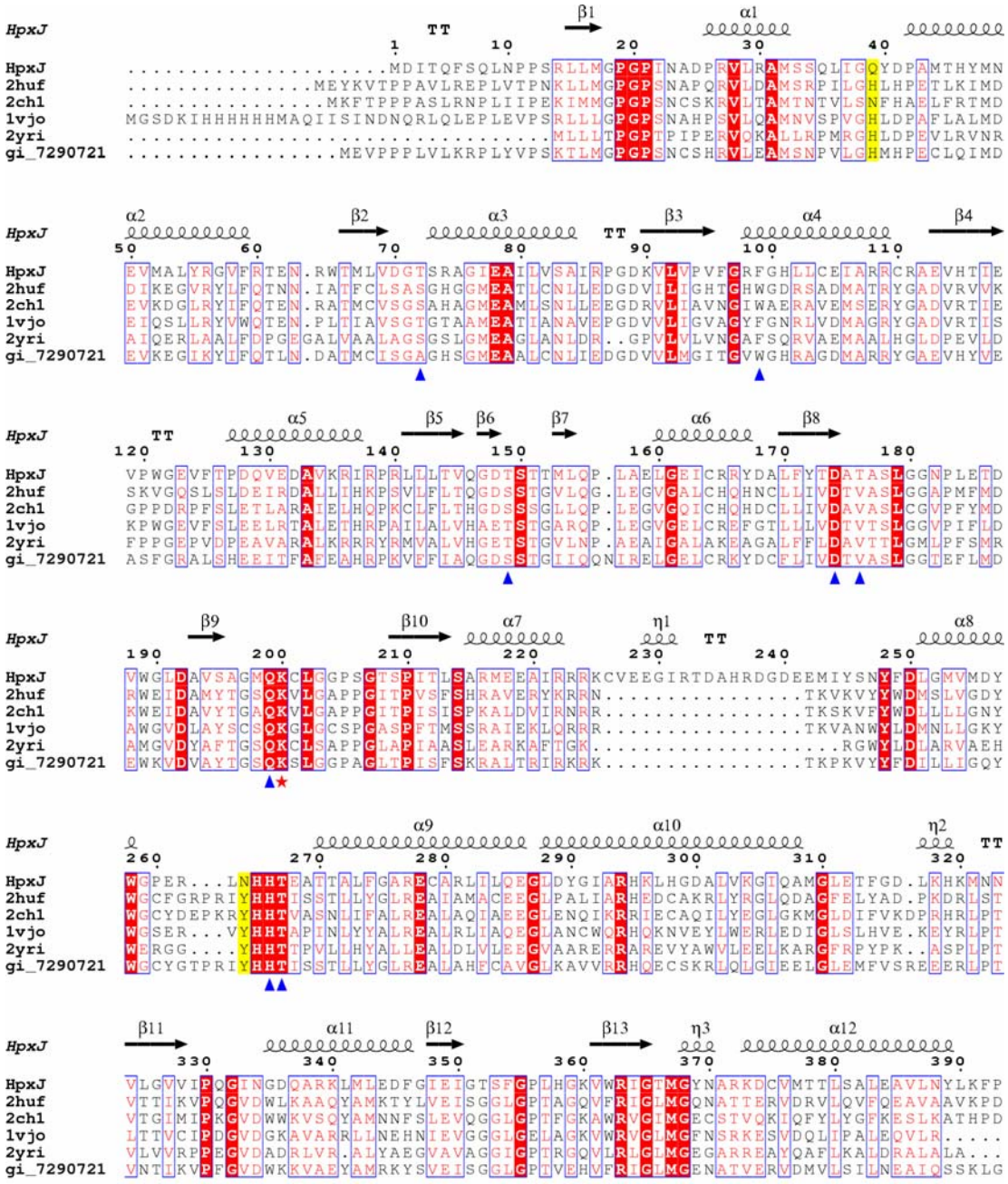

Figure 6.S4. Sequence alignment of KpHpxJ with several similar aspartate aminotransferases (identified by the NCBI conserved domain database; 2HUF (*16*), 2CH1 (*17*), 1VJO (*18*), 2YRI and gi_7290721). Residues highlighted and boxed in red are completely conserved, while those shown with red text are structurally conserved residues. The two residues highlighted in yellow are the two active site residues (Q39 and N64) that are otherwise conserved in the other aminotransferases. Blue arrows indicate residues that make hydrogen bonds with the PLP molecule. The red star is the lysine that forms a covalent attachment to the PLP molecule.

6.3 Supporting Material - Materials and Methods

Cloning, expression and purification of Enzymes. Both *Klebsiella pneumoniae* ureidoglycine-glyoxylate aminotransferase (KpHpxJ, YP_001335423) and *E. coli* allantoate amidohydrolase (EcAAH, NP_415049) were cloned, expressed and purified using the same procedure. The proteins were expressed from a Pet-28 based plasmid containing an N-terminal 6-his tag and a TEV cleavage site. These constructs, denoted HpxJ-THT and EcAAH-THT, were provided by the Cornell Protein Production Facility and were cloned from genomic DNA using standard molecular biology techniques. The KpHpxJ gene was cloned from genomic DNA from *Klebsiella pneumoniae* subsp. *pneumoniae* (Schroeter) Trevisan MGH78578 (ATCC 700721). The EcAAH gene was cloned from *Escherichia coli* (Migula) Castellani and Chalmers, MG1655 (ATCC 700926). BL21(DE3) cells were transformed with these plasmids and grown in LB media supplemented with a final concentration of 50 μg/mL kanamycin. A 10 mL starter culture, grown overnight, was used to inoculate one litre LB cultures. These were grown at 37^{o}C with shaking until the O.D.$_{600}$ reached 0.4. The temperature was reduced to 20^{o}C and after 30 minutes expression was induced with 0.5 mM IPTG. The cells were grown for a further 16 hours and then harvested by centrifugation and stored at – 20^{o}C.

The cells were suspended in 50 mM Tris buffer, pH 7.6, containing 300 mM NaCl and 10 mM imidazole. After lysis by sonication the cellular debris was removed by centrifugation and the cleared lysate applied to a column containing Ni-NTA resin. The column was washed with 100 mL of 50 mM Tris buffer, pH 7.6, containing 300 mM NaCl, 25 mM imidazole and 10% v/v glycerol. The protein was eluted with 50 mM Tris buffer, pH 7.6, containing 300 mM NaCl and 250 mM imidazole. The eluted protein was further purified by gel filtration on a ACTA explorer FPLC with a HiLoad 26/60 Superdex prep grade G200 column running 10 mM Tris, buffer pH 7.6, with 30

mM NaCl. After purification, the protein was concentrated to 12 mg/mL for KpHpxJ and 2 mg/mL for EcAAH and aliquots were flash frozen and stored at – 80°C.

Pre-column Derivatization of Amino Acids with DABS-Cl. In order to quantify amino acid reactants and products, pre-column derivatization with dimethylaminoazobenzenesulfonyl chloride (DABS-Cl) was carried out (*19, 20*). Stock solutions of DABS-Cl were made at 4 mM in acetonitrile just prior to use. To 50 µl of sample was added 50 µl of 100 mM sodium bicarbonate, pH 8.2, and 200 µl of 4 mM DABS-Cl solution. This was vortexed, heated at 80° for 20 minutes and then cooled for 5 minutes on ice. Once cooled, 300 µl of reaction diluent (50 mM sodium phosphate, pH 7.0, in 50% ethanol) was added. The samples were centrifuged at 14 000 rpm on a microcentrifuge for 2 minutes to remove precipitates prior to injection on HPLC.

Synthesis of Oxalurate. Oxalurate was synthesized from uracil as reported (*21*). Briefly, a solution of uracil (0.5 g) in phosphate buffer, pH 7.0 (100 mL), was mixed with a solution of potassium permanganate (1.41 g) in water (80 mL). The mixture was kept at 37° C for 18 hours. Manganese dioxide was removed by centrifugation and the supernatant was concentrated to approximately 5 mL and left at 25° C. White crystals (MP 206-208°C) formed over time, and after 24 hours were removed by filtration. The mass was confirmed by ESI-MS (m/z = 130.99, Figure 6.S5). The purity was estimated to be greater than 90% by analysis of the MS spectrum.

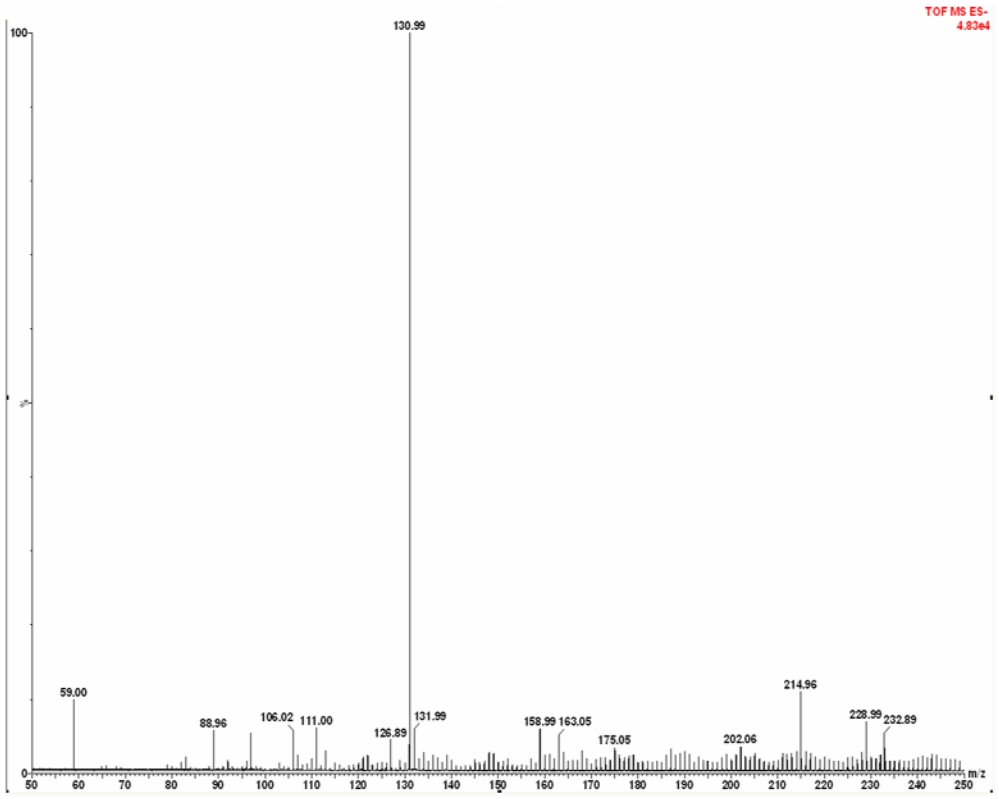

Figure 6.S5. ESI-MS spectrum of oxalurate. The sample was collected in negative ion mode and the observed mass (m/z = 130.99) agrees well with the calculated mass (131).

Pre-Column Derivatization of Keto Acids. In order to quantify keto acids produced in the KpHpxJ reaction, pre-column derivatization with o-phenylenediamine (OPD) was performed. The OPD was purchased from Sigma-Aldrich and used without further purification. To make the keto acid derivatives, 50 µl of sample was added to 100 µl of water and 100 µl of a 100 mM OPD solution (in 2M HCl). The mixture was heated for 30 minutes at 85^{o}C followed by cooling on ice for 5 minutes. Before injecting on the HPLC, 500 µl of 1 M phosphate buffer, pH 7.5, was added and the solution was centrifuged to remove any precipitate.

HPLC Analysis of Aminotransferase Reactions. Aminotransferase reactions were carried out in 100 µl volumes at 25^{o}C. In a typical reaction, 1 mM amino acid and 1 mM α-keto acid were mixed in 50 mM phosphate buffer, pH 7.3. The reaction

was initiated by the addition of 10 µl of 250 µM KpHpxJ. After 30 minutes at 25°C, the reaction was quenched by the addition of 1 µl of 50% acetic acid and then put on ice for 5 minutes. After centrifuging to remove precipitated protein, a sample of the reaction was immediately derivatized with DABS-Cl or OPD. 50 µl of derivatized sample was run on a Hewlett-Packard 1100 Series HPLC with an Agilent Eclipse Plus reverse-phase C18 column (4.6 x 150 mm) using a gradient from 2% acetonitrile to 50% acetonitrile in water with 0.1% TFA. Chromatograms were recorded at 436 nm and 220 nm for DABS-Cl derivatives and 335 and 220 nm for OPD derivatives.

For reactions involving ureidoglycine as a starting material, this compound was made *in situ* immediately prior to running the reaction. To generate ureidoglycine, 1 - 5 mM allantoate (diureidoacetic acid) was mixed with 10 - 50 µl of 100 µM EcAAH in 50 mM phosphate buffer, pH 7.3. The EcAAH protein solution contained 500 µM $MnCl_2$ as this enzyme is known to depend upon manganese for activity (*22, 23*). The rate of reaction could be followed by observing the liberation of ammonia using a glutamate dehydrogenase coupled assay (Figure 6.S2) (*7, 24*). Sufficient EcAAH was used to ensure that complete conversion of allantoate to ureidoglycine was finished within 2 minutes, and the conversion was judged to be quantitative. The enzyme was removed by filtration through a 10 000 MWCO microconcentrator device. The resulting ureidoglycine was used immediately in aminotransferase reactions.

Unless otherwise specified, control reactions were run with all components present, including donor or acceptor molecules, but without adding the enzyme.

Pre-Steady State Measurements. Pre-steady state kinetics measurements were carried out on a Kintek model SF-2004 stopped-flow instrument. The first step of the PLP-dependent reaction was monitored by following the decrease in absorbance at 418 nm as PLP was converted to PMP. For each measurement 1000 time points were

measured over the course of the run. The dead time of the instrument was approximately 15 ms. The experiments were carried out at 15 μM KpHpxJ and 5 mM amino acid and were followed over 1 to 120 seconds. The data was fit by non-linear regression to the following equation (*25*):

$$[PLP] = Ae^{-kt} + C$$

In this equation, *A* is the amplitude of the pseudo-first order process, *k* is the rate, *t* is time and *C* is the initial absorbance.

Crystallization, Data Collection and Processing. The protein was crystallized using the hanging-drop vapor-diffusion method at 18^{o} C. The crystallization conditions for KpHpxJ consisted of 34% 3-methyl-1,5-pentanediol (MPD) and 100 mM NaCl in 100 mM Tris buffer, pH 7.5. The thin rod-shaped crystals grew over seven to ten days and were yellow in color. Prior to data collection, the crystals were cryoprotected using the crystallization solution without additional additives. The data were collected at the NE-CAT 24ID-E beamline of the Advanced Photon Source of Argonne National Lab at a wavelength of 0.979 Å. The data collection statistics are provided in Table 6.S1. Data was collected over 180^{o} with a 1^{o} oscillation angle and an exposure time of 1 s. The data were indexed, integrated and scaled using *HKL-2000 (26)*.

Table 6.S1. Data Collection Statistics

	KpHpxJ ($P2_1$)	KpHpxJ ($P2_12_12$)[a]
resolution (Å)	50.0 - 2.59	50.0 - 2.59
wavelength (Å)	0.9795	0.9795
space group	$P2_1$	$P2_12_12$
a (Å)	142.2	141.7
b (Å)	149.2	146.9
c (Å)	198.0	197.6
β (°)	90.3	90.0
no. of reflections	575 940	529 674
unique reflections	242 484	122 273
Average I/σ	8.6 (1.9)	9.1 (2.0)
redundancy	2.4 (2.3)	4.3 (3.9)
completeness (%)	95.9 (96.8)	94.0 (95.9)
R_{sym}[b] (%)	13.1 (40.9)	13.7 (45.4)

Numbers in parentheses correspond to the highest resolution shell

[a] While the structure was solved using a monoclinic space group, the statistics for the apparent orthorhombic unit cell are included for completeness.

[b] $R_{\mathrm{sym}} = \Sigma\Sigma_{\mathrm{i}} \left| I_i - \langle I \rangle \right| / \Sigma \langle I \rangle$, where $\langle I \rangle$ is the mean intensity of the N reflections with intensities I_i and common indices h, k, l

Structure Solution and Refinement. The initial phases for the structure were provided by molecular replacement using the program Molrep (*27*) with an all-alanine version of PDV 1VJ0 as the model. Initially, the data for the KpHpxJ crystals scaled in an orthorhombic space group with unit cell dimensions of a = 141.7 Å, b = 146.9 Å, and c = 197.6 Å, with eight molecules predicted for the asymmetric unit (data

collection statistics provided in Table 6.S1). All attempts at molecular replacement using this space group failed. After rescaling in $P2_1$ with unit cell dimensions a =142.2 Å, b = 149.2 Å, c = 198.0 Å, and β = 90.3°, a solution with sixteen molecules in the asymmetric unit (four complete tetramers) was found immediately. Examination of the symmetry related molecules in the unit cell showed apparent twofold-screw symmetry along the short axes and apparent twofold symmetry along the long axis, which would result in the non-standard space group $P22_12_1$. Further examination after the appropriate transformation and reindexing of the data revealed that a slight shift of one of the molecules in the unit cell precluded ant symmetry higher than monoclinic. Twinning tests performed by SFCHECK (*28*) and the program xtriage in the Phenix suite (*29*) found a high degree of pseudo-merohedral twinning with a twin operator of h, -k, -l. The twin fraction was estimated to be between 37% and 42% for the monoclinic dataset.

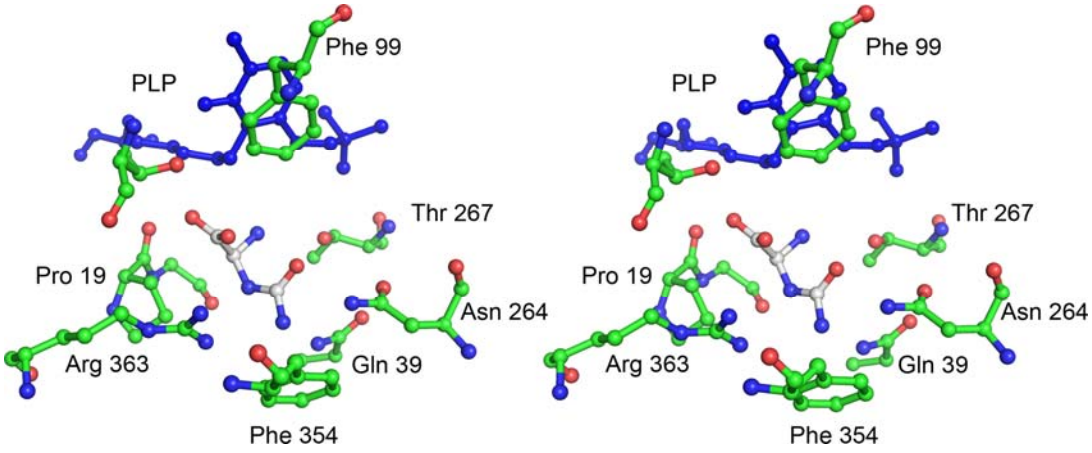

Figure 6.S5. Active site of HpxJ. Stereo diagram of the active site residues of HpxJ with the putative substrate, ureidoglycine (white), modeled in. The PLP molecule (blue) is covalently linked to Lys 200.

The model was refined through successive rounds of manual model building using COOT (*30*) and restrained refinement using Refmac5 (*31*) and Phenix (*29*). Calculation of twin fraction and detwinning was performed automatically by the

refinement program. Water molecules were added only after refinement converged and was followed by additional rounds of refinement. The covalently bound PLP was added directly to difference density and followed by an additional round of refinement. The refinement statistics are given in Table 6.S2.

Table 6.S2. Data Refinement Statistics

	KpHpxJ
resolution (Å)	2.59
no. of protein atoms	50620
no. of ligand atoms	92
no. of water atoms	1228
no. of reflections in working set	230 277
no. of reflections in test set	12 155 (5.3%)
R factor[a]	21.5
R_{free}[b]	23.9
rmsd bonds (Å)	0.006
rmsd angles (^{o})	1.11
mean *B* factor (Å^2)	33.7
Ramachandran plot	
most favored (%)	96.8
additionally allowed (%)	2.7
generously allowed (%)	0.5
disallowed (%)	0.1

[a] R factor $= \Sigma_{hkl} \left\| F_{obs} \right| - k \left| F_{calc} \right\| / \sum_{hkl} \left| F_{obs} \right|$, where F_{obs} and F_{calc} are observed and calculated structure factors respectively.

[b] For R_{free}, the sum is extended over a subset of reflections excluded from all stages of refinement

Modeling of Ureidoglycine in the KpHpxJ Active Site. The modeling of the ligand in the active site of KpHpxJ was performed using version 9.7.211 of the program Macromodel (*32, 33*). The protein was truncated to a shell containing all atoms within 20 Å of the ligand. Water molecules were removed and the protein preparation utility was used to add hydrogens and to ensure proper ionic states of amino acid side chains. In order to model the substrate, ureidoglycine was first placed in the active site by superposition to the alanine from PDB 1H0C (*34*). A conformational search of ureidoglycine was used to generate starting conformers for the calculations. Modeling runs were carried out both allowing only the ligand to move and allowing the ligand and active site residues freedom to move. In order to maintain a reasonable proximity between the PLP to the ligand, the Cα and C1 of ureidoglycine were constrained with a force constant of 100. The calculations were completed using the AMBER* force field (*35, 36*) with a distance dependent dielectric that was further attenuated by a factor of 4. The energy minimization relied upon the truncated Newton conjugate gradient (TNCG) technique (*37*) and was considered to have converged when the energy gradient was less than 0.01 kJ/mol.

All of the figures presented herein were prepared using PyMol (*38*). The structure of KpHpxJ has been deposited in the Protein Data Bank with identifier 3NNK.

REFERENCES

1. Vogels, G. D., and Van der Drift, C. (1976) Degradation of purines and pyrimidines by microorganisms, *Bacteriol. Rev. 40*, 403-468.
2. Zrenner, R., *et al.* (2006) Pyrimidine and purine biosynthesis and degradation in plants, *Annu. Rev. Plant Biol. 57*, 805-836.
3. Modric, N., *et al.* (1992) Tracing and Identification of Uricase Reaction Intermediates, *Tet. Lett. 33*, 6691-6694.
4. Kahn, K., *et al.* (1997) Identification of the true product of the urate oxidation reaction, *J. Am. Chem. Soc. 119*, 5435-5442.
5. Kahn, K., and Tipton, P. A. (1998) Spectroscopic characterization of intermediates in the urate oxidase reaction, *Biochemistry 37*, 11651-11659.
6. Ramazzina, I., *et al.* (2006) Completing the uric acid degradation pathway through phylogenetic comparison of whole genomes, *Nat. Chem. Biol. 2*, 144-148.
7. Serventi, F., *et al.* (2009) Chemical basis of nitrogen recovery through the ureide pathway: formation and hydrolysis of S-ureidoglycine in plants and bacteria, *ACS Chem. Biol. 5*, 203-214.
8. van der Drift, C., *et al.* (1970) Allantoate hydrolysis by allantoate amidohydrolase, *Arch. Biochem. Biophys. 136*, 273-279.
9. Werner, A. K., *et al.* (2009) Ureide catabolism in *Arabidopsis thaliana* and *Escherichia coli*, *Nat. Chem. Biol. 6*, 19-21.
10. Cusa, E., *et al.* (1999) Genetic analysis of a chromosomal region containing genes required for assimilation of allantoin nitrogen and linked glyoxylate metabolism in *Escherichia coli*, *J. Bacteriol. 181*, 7479-7484.
11. de la Riva, L., *et al.* (2008) The hpx genetic system for hypoxanthine assimilation as a nitrogen source in *Klebsiella pneumoniae*: gene organization and transcriptional regulation, *J. Bacteriol. 190*, 7892-7903.

12. Pope, S. D., *et al.* (2009) Purine utilization by *Klebsiella oxytoca* M5al: genes for ring-oxidizing and -opening enzymes, *J. Bacteriol. 191*, 1006-1017.

13. McMurry, J., and Begley, T. (2005) *The Organic Chemistry of Biological Pathways*, Roberts and Company, Englewood, Colorado.

14. Eliot, A. C., and Kirsch, J. F. (2004) Pyridoxal phosphate enzymes: mechanistic, structural and evolutionary considerations, *Annu. Rev. Biochem. 73*, 383-415.

15. Islam, M. M., *et al.* (2003) Reaction of Aspartate Aminotransferase with C5-Dicarboxylic Acids: Comparison with the Reaction with C4-Dicarboxylic Acids, *J. Biochem. 134*, 277-285.

16. Han, G. W. (2005) Crystal structure of an alanine-glyoxylate aminotransferase from *Anabaena sp*. at 1.70 Å resolution reveals a noncovalently linked PLP cofactor, *Proteins 58*, 971-975.

17. Rossi, F., *et al.* (2006) Structure of *Anopheles gambiae* 3-hydroxykynurenine transaminae, *Proc. Natl. Acad. Sci 103*, 5711-5716.

18. Han, G. W., *et al.* (2005) Crystal structure of the Alanine-glyoxylate aminotransferase (ALR1004) from *Nostoc sp.* at 1.70 Å resolution, *Proteins 58*, 971-975.

19. Chang, J. Y., *et al.* (1983) Amino acid analysis in the picomole range by precolumn derivatization and high-performance liquid chromatography, *Methods Enzymol. 91*, 41-48.

20. Schneider, H.-J. (1989) Amino Acid Analysis Using DABS-Cl, *Chromatographia. 28*, 45-48.

21. Chatamra, B., and Jones, A. S. (1963) The Permanganate Oxidation of Uracil and Cytosine and their 1-Substituted Derivatives, *J. Chem. Soc.*, 811-815.

22. Kim, K., *et al.* (2009) Crystal Structure of metal-dependent allantoinase from *Escherichia coli*, *J. Mol. Biol. 387*, 1067-1074.

23. Mulrooney, S. B., and Hausinger, R. P. (2003) Metal ion dependence of recombinant *Escherichia coli* allantoinase, *J. Bacteriol. 185*, 126-134.

24. French, J. B., *et al.* (2010) Characterizaion of nicotinamidases: Class-wide inhibition by nicotinaldehydes and mechanism of inhibition and catalysis, *Submitted*.

25. Johnson, K. A. (1986) Rapid Kinetic Analysis of Mechanochemical Adenosinetriphosphatases, *Methods Enzymol. 134*, 677-705.

26. Otwinowski, Z., and Minor, W. (1997) Processing of X-ray Diffraction Data Collected in Oscillation Mode, *Methods Enzymol. 276*, 307-326.

27. Vagin, A., and Teplyakov, A. (2000) An approach to multi-copy search in molecular replacement, *Acta Crystallogr. D 56*, 1622-1624.

28. Vaguine, A. A., *et al.* (1999) SFCHECK: a unified set of procedures for evaluating the quality of macromolecular structure-factor data and their agreement with the atomic model, *Acta. Crystallogr. D Biol. Crystallogr. 55*, 191-205.

29. Adams, P. D., *et al.* (2010) PHENIX: a comprehensive Python-based system for macromolecular structure solution, *Acta. Crystallogr. D Biol. Crystallogr. 66*, 213-221.

30. Emsley, P., and Cowtan, K. (2004) Coot: model-building tools for molecular graphics, *Acta Crystallogr. D 60*, 2126-2132.

31. Murshudov, G. N., *et al.* (1999) Efficient anisotropic refinement of macromolecular structures using FFT, *Acta Crystallogr. D 55 (Pt 1)*, 247-255.

32. Mohamadi, F., *et al.* (1990) MacroModel - an Integrated Software System for Modeling Organic and Bioorganic Molecules Using Molecular Mechanics, *J. Comput. Chem. 11*, 460-467.

33. Still, W. C., *et al.* (1999) Macromodel, 2.0 ed., Columbia University, New York, NY.

34. Zhang, X., *et al.* (2003) Crystal structure of alanine:glyoxylate aminotransferase and the relationship between genotype and enzymatic phenotype in primary hyperoxaluria type 1, *J. Mol. Biol. 331*, 643-652.

35. Weiner, S. J., *et al.* (1986) An all atom force field for simulations of proteins and nucleic acids, *J. Comput. Chem. 7*, 230-252.

36. Weiner, S. J., *et al.* (1984) A new force field for molecular mechanical simulation of nucleic acids and proteins, *J. Am. Chem. Soc. 106*, 765-784.

37. Ponder, J. W., and Richards, F. M. (1987) An Efficient Newton-like Method for Molecular Mechanics Energy Minimization of Large Molecules, *J. Comput. Chem. 8*, 1016-1024.

38. DeLano, W. L. (2002) The PyMOL Molecular Graphics System, DeLano Scientific, San Carlos, CA.

CHAPTER 7

STRUCTURAL AND MECHANISTIC STUDIES ON *KLEBSIELLA PNEUMONIAE* 2-OXO-4-HYDROXY-4-CARBOXY-5-UREIDOIMIDAZOLE DECARBOXYLASE

7.1 Abstract

The stereospecific oxidative degradation of uric acid to (S)-allantoin was recently shown to proceed *via* three enzymatic steps. The final conversion is a decarboxylation of the unstable intermediate 2-oxo-4-hydroxy-4-carboxy-5-ureidoimidazoline (OHCU) and is catalyzed by OHCU decarboxylase. Here we present the structures of *Klebsiella pneumoniae* OHCU decarboxylase in unliganded form and with bound allantoin. The structures provide evidence that ligand binding organizes the active site residues for catalysis. Modeling of the substrate and intermediates provides additional support for this hypothesis. In addition we characterize the first reported OHCU decarboxylase inhibitor, allopurinol, a structural isomer of hypoxanthine. This molecule is a competitive inhibitor of *K. pneumoniae* OHCU decarboxylase with a K_i of 30 ± 2 μM. Circular dichroism measurements confirm structural observations that this inhibitor prevents the necessary organization of the active site. Our structural and biochemical studies also provide further mechanistic insights into the mechanism of catalysis of OHCU decarboxylation.

7.2 Introduction

The ability to metabolise uric acid, a key intermediate in the degradation of purines, varies by organism. Humans, birds, reptiles and some bacteria, for example, lack the enzymes necessary to break down this compound (*1, 2*). This inability to process uric acid in humans leads to high serum concentrations of urate which can crystallize in joints and cause gout. In plants and some bacteria, however, the high nitrogen content of the ureides make them attractive sources of nitrogen, particularly when other sources are limited. Organisms that possess the ability to degrade uric acid

utilize a conserved pathway that converts this molecule into (*S*)-allantoin (1). Allantoin can be further degraded by plants and some bacteria for use as a nitrogen, carbon and energy source.

The currently accepted degradative pathway from uric acid to allantoin is shown in Scheme 7.1.

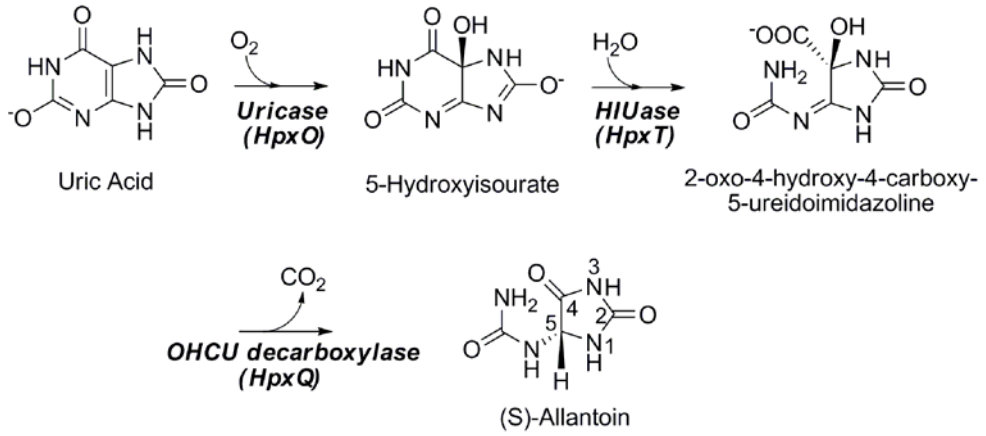

Scheme 7.1. The catabolic pathway from uric acid to allantoin.

Until recently it was believed that only a single enzyme, urate oxidase, was responsible for the conversion of urate to allantoin. Over the last few years, however, several reports have conclusively proven that the pathway proceeds through two intermediates and utilizes two additional enzymes (3-5). The actual product of the urate oxidase reaction is the unstable intermediate, 5-hydroxyisourate (HIU[1]). The conversion of HIU to another unstable compound, 2-oxo-4-hydroxy-4-carboxy-5-ureidoimidazoline (OHCU) is catalyzed by HIU hydrolase. OHCU can then be stereospecifically decarboxylated to yield (*S*)-allantoin.

Despite recent efforts, the enzyme responsible for the final step in this pathway, OHCU decarboxylase, is not well characterized. Very little is known about the mechanism of this decarboxylation reaction, and only two structures of this enzyme, both from eukaryotes, have been solved and deposited in the Protein Data Bank.

These two structures report a similar architecture for OHCU decarboxylase, but display some distinct differences. While both the structure from zebrafish (2O70) (6) and the structure from *Arabadopsis thaliana* (2Q37) (7) report dimeric structures, they differ in how the two monomers interact (*6, 7*). In addition, the structures reported with the bound product, allantoin, differ in which enantiomer is bound in the active site.

Beyond what has been inferred from the crystal structures, very few details about the kinetics or mechanism of the OHCU decarboxylase reaction are known. Sequence analysis of this enzyme reveals that it is unrelated to previously characterized decarboxylases and biochemical analyses of the decarboxylation reaction by circular dichroism (CD) have shown that the reaction proceeds in the absence of exogenous cofactors. With the exception of a few relatively rare radical mechanisms, decarboxylation reactions generally require the presence of an electron sink or a leaving group in order to accommodate the electrons from the cleavage of the bond to the carboxylate moiety (*8*). This role is usually played by cofactors such as PLP or thiamine pyrophosphate (*8, 9*). Few enzymes are known that catalyze decarboxylation reactions independent of cofactors. One notable example is orotidine 5'-monophosphate decarboxylase (OMPDC) (*10, 11*). This protein has been extensively studied, in large part due to its extremely high catalytic proficiency (rate acceleration on the order of 10^{16}) (12).

In this work we report the high resolution crystal structures of the cofactor-independent OHCU decarboxylase from *Klebsiella pneumoniae*, both in unliganded form and with bound allantoin. Our structures reveal a prochiral, enol form of allantoin bound in the active site. This isomer more closely resembles the putative reaction intermediate than either of the individual isomers. The crystal structure with allantoin bound reveals an extensive hydrogen bonding network in the active site.

Modelling of the substrate, putative reaction intermediate and products provides additional details about the likely mode of catalysis. In addition, we have identified a novel competitive inhibitor of this enzyme and examined the method of inhibition using both X-ray crystal structures and circular dichroism measurements. The structure, modeling and kinetic analysis allow us to propose a mechanism for the OHCU decarboxylase catalyzed reaction.

7.3 Experimental Procedures

Cloning and Mutagenesis. KpOHCU decarboxylase was expressed from a pET-28 based plasmid containing an N-terminal 6-His tag and a TEV cleavage site. The *hpxQ* gene was cloned from genomic DNA from *K. pneumoniae* subsp. *pneumoniae* (Schroeter) Trevisan MGH78578 (ATCC 700721). This construct, denoted HpxQ-THT, was provided by the Cornell Protein Production Facility and was cloned using standard molecular biology techniques. The Q88E mutant plasmid was made at the Cornell Protein Production Facility using site-directed mutagenesis of the native gene. Briefly, site-directed mutagenesis was performed on KpOHCU decarboxylase by a standard PCR protocol using *Pfu*Turbo DNA polymerase (Invitrogen) per the manufacturer's instructions and *Dpn*I (New England Biolabs) to digest the methylated parental DNA prior to transformation. Clones were screened for the mutant by PCR with a screening primer and the T7 promoter primer. All clones and the mutant were verified by sequencing.

Protein Expression and Purification. BL21(DE3) cells were transformed with the HpxQ-THT plasmid and grown in LB media supplemented with 50 mg/mL kanamycin. A 10 mL starter culture, grown overnight, was used to inoculate one litre LB cultures. These were grown at 37 °C with shaking until the OD_{600} reached 0.4. The temperature was reduced to 20 °C and after 30 minutes at this temperature

expression was induced with 0.5 mM IPTG. The cells were grown for a further 16 hours and then harvested by centrifugation and stored at –20 °C.

The cells were suspended in 50 mM Tris buffer, pH 7.6, containing 300 mM NaCl and 10 mM imidazole. After lysis by sonication the cellular debris was removed by centrifugation and the cleared lysate applied to a column containing pre-equilibrated Ni-NTA resin. The column was washed with 100 mL of 50 mM Tris buffer, pH 7.6, containing 300 mM NaCl, 25 mM imidazole and 10% v/v glycerol. The protein was eluted with 50 mM Tris buffer, pH 7.6, containing 300 mM NaCl and 250 mM imidazole. The eluted protein was further purified by gel filtration on an ACTA Explorer FPLC with a HiLoad 26/60 Superdex prep grade G200 column running 10 mM Tris buffer, pH 7.6, with 30 mM NaCl. After purification, the protein was concentrated to 12 mg/mL using a centrifugal concentrator and aliquots were flash frozen and stored at –80 °C.

Crystallization, Data Collection and Processing. The protein was crystallized using the hanging-drop vapor-diffusion method at 18 °C. The crystallization conditions for unliganded KpOHCU decarboxylase consisted of either 20 % w/v PEG-3000 in Tris-HCl, pH 7.0, with 0.2 M calcium acetate or 22 – 26 % w/v PEG-8000 in sodium cacodylate, pH 6.5, with 0.25 M sodium acetate. Prior to data collection, the crystals were cryoprotected in the above solutions supplemented with 15 – 20 % ethylene glycol. For the KpOHCU decarboxylase–allantoin complex, crystals were soaked for 5 min in cryosolution that contained 10 mM allantoin. For the allopurinol treated structures, the crystals were either soaked directly in cryosolution containing 10 mM allopurinol or first treated with cryosolution containing 10 mM allantoin for 5 min and then transferred to cryosolution containing 10 mM allopurinol and removed for data collection after either one minute or ten minutes. The crystals of the unliganded protein belonged to space groups $P4_1$ (rod-shaped crystals) and $P1$ (plate-

like crystals). After soaking the latter crystals with allantoin or allopurinol, the space group changed to *C*2. Attempts to soak ligands into the tetragonal crystals caused considerable crystal damage and yielded unusable data.

Data were collected at the NE-CAT 24-ID-E beamline of the Advanced Photon Source of Argonne National Lab at a wavelength of 0.979 Å and at 0.978 Å at the Cornell High Energy Synchrotron Source. In all cases, the data were indexed, integrated and scaled using *HKL-2000* (13). The data collection statistics are summarized in Table 7.1.

Table 7.1. Data Collection Statistics.

	KpOHCU decarboxylase (*P*1)	KpOHCU decarboxylase ($P4_1$)	KpOHCU decarboxylase - allantoin	KpOHCU decarboxylase - allopurinol soak
resolution (Å)	1.79	1.55	2.00	1.98
wavelength (Å)	0.987	0.987	0.987	0.987
beam line	Chess A1	Chess A1	Chess A1	Chess A1
space group	*P*1	$P4_1$	*C*2	*C*2
a (Å)	46.80	88.18	91.18	91.40
b (Å)	49.34	88.18	47.32	46.70
c (Å)	51.69	40.22	50.21	47.30
α (°)	113.18	90	90	90
β (°)	116.49	90	123.13	118.99
γ (°)	94.26	90	90	90
no. of reflections	54 203	367 405	29 217	27333
unique reflections	31 805	49 837	12 101	11639
average I/σ	27.8 (4.7)	28.7 (7.3)	16.5 (2.6)	17.3 (1.9)
redundancy	1.7 (1.5)	7.4 (7.2)	2.4 (2.0)	2.3 (1.8)
completeness (%)	93.8 (75.0)	99.9 (100.0)	98.6 (94.1)	94.7 (58.0)
R_{sym}[a] (%)	3.0 (14.2)	9.6 (37.0)	7.6 (26.3)	6.9 (32.6)

Numbers in parentheses correspond to the highest resolution shell

[a] $R_{\text{sym}} = \Sigma\Sigma_{\text{i}} \left| I_i - \langle I \rangle \right| / \Sigma \langle I \rangle$, where $\langle I \rangle$ is the mean intensity of the *N* reflections with intensities I_i and common indices *h, k, l*

Structure Solution and Refinement. All initial attempts at molecular replacement using Phaser (14), Molrep (15) or CNS (16) with various forms of the *A. thaliana* OHCU decarboxylase (PDB identifier 2Q37) or the OHCU decarboxylase

from zebrafish (PDB identifier 2O70) failed to produce a solution for the higher resolution tetragonal data. Using the *P*1 data, however, a molecular replacement solution was found using Phaser with an all alanine search model derived from 2Q37. The model was refined through successive rounds of manual model building using COOT (17) and restrained refinement using Refmac5 (18). Water molecules were added only after the model converged and followed by two additional rounds of refinement. The solution of the *P*1 crystal form was used as a model for molecular replacement for the other data sets. Refinement of the initial model was carried out as detailed above. For the KpOHCU decarboxylase-allantoin complex structure, the ligand position was added directly to the difference Fourier map after the initial rounds of refinement. For this structure, water molecules were added only after the ligand was placed. The refinement statistics are given in Table 7.2

Table 7.2. Data Refinement Statistics.

	KpOHCU decarb. (*P*1) - unliganded	KpOHCU decarb. (*P*4) - unliganded	KpOHCU decarb. - allantoin	KpOHCU decarb. - allopurinol soak
resolution (Å)	1.79	1.55	2.00	1.98
protein atoms	2440	2273	1260	1057
ligand atoms	0	0	11	0
water atoms	290	655	95	85
reflections in working set	30202	47280	11525	11067
reflections in test set	1603	3493	576	554
R factor[a]	23.8	20.5	22.9	22.5
R_{free}[b]	26.1	22.6	25.4	25.9
rmsd bonds (Å)	0.005	0.005	0.005	0.006
rmsd angles (°)	0.83	0.822	0.91	0.945
mean *B* factor (Å^2)	19.6	10.6	24.5	34.2
Ramachandran plot				
most favored (%)	97.0	97.3	96.6	95.1
additionally allowed (%)	2.7	2.7	3.4	4.9
generously allowed (%)	0.3	0	0	0
disallowed (%)	0	0	0	0

[a] $R \text{ factor} = \Sigma_{hkl} \left\| F_{obs} \right| - k \left| F_{calc} \right\| / \sum_{hkl} \left| F_{obs} \right|$, where F_{obs} and F_{calc} are observed and calculated structure factors respectively.

[b] For R_{free}, the sum is extended over a subset of reflections (5%) excluded from all stages of refinement

Substrate and Product Modeling. The modeling of the ligands in the active site of KpOHCU decarboxylase was performed using version 9.7.211 of MacroModel (*19, 20*). The protein was truncated to a shell containing all atoms within 20 Å of the ligand. Water molecules were removed and the protein preparation utility was used to add hydrogen atoms and to ensure proper ionic states of amino acid side chains. In order to model the substrate, OHCU was positioned in the active site by superposition to the allantoin from the KpOHCU decarboxylase-allantoin complex structure. A conformational search of OHCU was used to generate starting conformers for the calculations. For the modeling runs, both the ligand and active site residues were allowed freedom to move. To model the products of the reaction in the active site, the minimized OHCU molecule was used as a starting point. The calculations were completed using the AMBER* force field (21) with a distance dependent dielectric that was further attenuated by a factor of 4. The energy minimization relied upon the TNCG technique (22) and was considered to have converged when the energy gradient was less than 0.01 kJ/mol.

All of the figures presented herein were prepared using PyMOL (23) and ChemBioDraw (CambridgeSoft). The structures have been deposited in the Protein Data Bank with identifiers XXXX (*P*1 – unliganded), XXXX ($P4_1$ – unliganded), XXXX (*C*2 – allantoin complex), and XXXX (*C*2 – allopurinol soak).

Steady State Kinetics Measurements–The substrate was generated *in situ* by treating a urate solution with uricase and HIU hydrolase enzymes. The OHCU was made just prior to injection by incubating 140 μM urate in 500 μL of 50 mM phosphate buffer, pH 8.0, with 5 μL of a 5 mg/mL uricase solution and 1 μL of a 5 mg/mL HIU hydrolase solution (HpxT from *K. pneumoniae).* This amount of enzyme

was sufficient to completely convert the urate into OHCU in less than one minute (monitored by the disappearance of the absorbance peak at 300 nm (4)). The decarboxylation reaction was initiated by the addition of 20 μL of 2.5 μM KpOHCU decarboxylase (0.024 nmoles). All reactions were carried out at pH 8.0 in 50 mM phosphate buffer in 500 μL total volume. The rate of reaction was monitored by observing the change of absorbance at 256 nm. The initial rate was calculated from the first 15 seconds after addition of the enzyme, at which point the reaction had not proceeded beyond 10% towards completion. Duplicate reactions were carried out at each of the various OHCU concentrations. The initial rate data was plotted and fit to the Michaelis-Menten equation using the Kaleidagraph software package (Synergy Software).

Inhibition by Allopurinol. Reaction rates for inhibition studies were measured as described above. To various concentrations of OHCU (generated *in situ*) was added a solution of 2.5 μM KpOHCU decarboxylase containing allopurinol. The initial rate of reaction, calculated from the first 15 seconds after addition of enzyme, was recorded for the various substrate concentrations. The reaction rates were measured at concentrations of 150, 350 and 600 μM allopurinol. A double reciprocal plot was constructed (Fig. 7.3*C*) and linear fits to the data were extrapolated to the y-intercept to determine the K_i. The reported K_i is the average of the three calculated values from the fits to the data at 150, 350 and 600 μM allopurinol.

Circular Dichroism Measurements. The KpOHCU decarboxylase protein was buffer exchanged into a solution of 10 mM phosphate buffer, pH 7.6 and used at a final concentration of 0.1 mg/mL. Data were collected separately for the protein alone, with 1 mM allantoin added, and with 1 mM allopurinol added. The CD spectra were collected on an AVIV Biomedical (Lakewood, NJ) CD spectrometer, Model 202-01. The data were collected at 25 °C from 190 to 260 nm with a 1 nm step size

and a 1 nm bandwidth. A 1 mm cell was used and in all cases, the data reported are an average of three measurements after subtraction of the background signal. Samples run without enzyme present showed that the ligands tested did not contribute to the CD signal at the concentrations used. The programs K2D2 and DicroProt (*24, 25*) were used for prediction of secondary structure content from the collected data.

7.4 Results

Overall Structure of KpOHCU Decarboxylase. The OHCU decarboxylase of *K. pneumoniae* crystallized with two different morphologies and yielded data in three different space groups. The long rod-shaped crystals that grew in PEG-3000 belonged to space group $P4_1$ with two molecules per asymmetric unit and a calculated solvent content of 42.5%. Crystals grown in the PEG-8000 condition were plate-like and belonged to space group *P*1. This crystal form had two molecules per asymmetric unit with a calculated solvent content of 45.3%. When these crystals were soaked with a solution of mother liquor containing 10 mM allantoin, the space group changed to *C*2 with one molecule per asymmetric unit and the solvent content decreased to 43.6%. KpOHCU decarboxylase is an all α-helical protein that belongs to the newly discovered OHCU decarboxylase fold (as classified by PFAM). It consists of nine helices in two domains, with the N-terminal domain containing the first four helices and the C-terminus of helix nine. Taken together, helices 2 through 4 and helix 8 are consistent with a four-helix bundle. The core of this domain is lined with hydrophobic side chains including two tryptophans, two phenylalanines and several leucine and valine residues. There are no disulfides in this enzyme, and the fold is stabilized primarily by hydrophobic interactions within the two all α-helical domains.

The crystal structures of KpOHCU decarboxylase indicate that this enzyme is a monomer in solution, a conclusion supported by size exclusion chromatography (data not shown). In addition, submission of the structure to the EBI-PISA (26) server,

which examines protein interfaces, surfaces and assemblies, predicted that higher order oligomerization was not likely to be observed. Further evidence comes from the observation that the tetragonal and triclinic/monoclinic crystal forms display completely different packing (Fig. 7.1 and Fig. 7.S1). The monomeric structure of KpHpx with the bound product, allantoin, is shown in Fig. 7.1*A*.

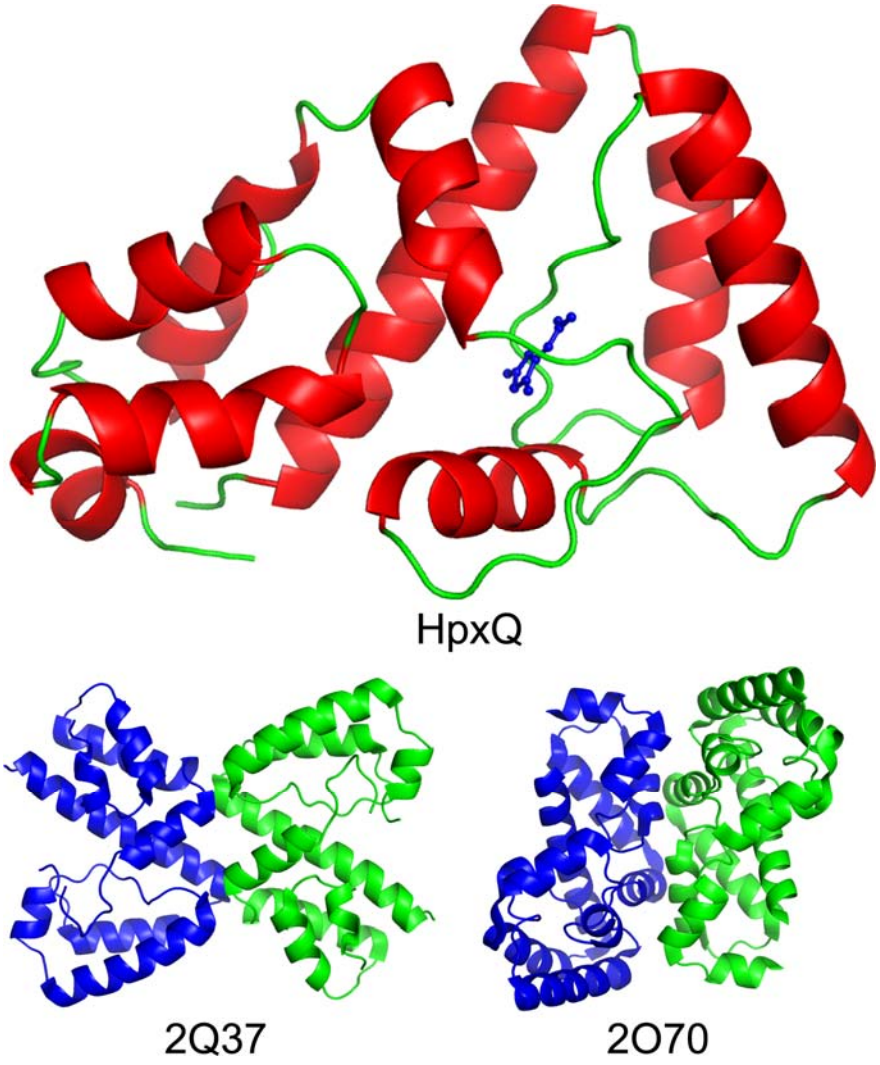

Figure 7.1. Structure of KpOHCU decarboxylase monomer (red helices and green loops) with allantoin bound (blue). Also shown are the proposed OHCU decarboxylase dimers from *A. thaliana* (2Q37 - lower left) and zebrafish (2O70 - lower right)

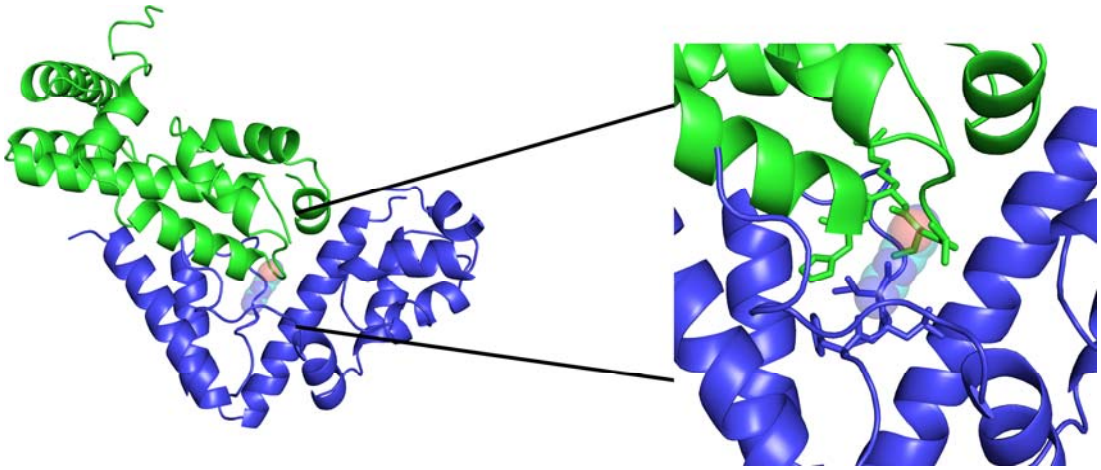

Figure 7.S1. Structure and crystal packing of KpOHCU decarboxylase in tetragonal crystal form. Ribbon representations of two molecules are shown with a semi-transparent space fill model of allantoin to mark the active site. One molecule (green) packs into the active site of the other (blue) where helix 6 of the enzyme is seen in the unliganded (*P*1) and liganded structures.

A search for structurally similar proteins using the DALI server (27) yielded only three homologous structures (Table 7.S1). Two of these, 2Q37 and 2O70, are the OHCU decarboxylase enzymes from *A. thaliana* and zebrafish respectively (Fig. 7.1). The third, 2O8I, is an unpublished structure from *Agrobacterium tumefaciens* with an uncharacterized function (28). Based upon the degree of similarity to 2Q37, 2O70 and KpOHCU decarboxylase, it is likely that this protein is also an OHCU decarboxylase.

Table 7.S1. Results of DALI search for structural homology

PDB ID	Z-Score	RMSD	% identity	Description
2O70	19.1	2.4	22	OHCU Decarboxylase
2Q37	17.1	1.8	29	OHCU Decarboxylase
2O8I	14.1	2.8	23	Hypothetical Protein ATU2327

KpOHCU Decarboxylase Active Site. KpOHCU decarboxylase crystals soaked in mother liquor supplemented with 10 mM allantoin yielded maps with clear difference density in the active site. While a racemic mixture of both (R)- and (S)-allantoin enantiomers was used for soaking, the density observed in the active site

corresponded to a planar molecule, consistent with the enol form of allantoin. The density allowed us to unambiguously place the allantoin molecule in the active site. This placement superimposed well with that of the other OHCU decarboxylase structures.

KpOHCU decarboxylase contains one active site per monomer and all of the contacts with the ligand are made by a single monomer. The active site is formed primarily by the loops connecting helices 5 and 6 and helices 7 and 8. Upon binding, KpOHCU decarboxylase forms a significant number of hydrogen bonds to the ligand (Fig. 7.2). At least eight non-covalent interactions can be seen between the protein and the ligand, with additional bonding occurring through two active site water molecules that are well ordered in the structure. Most of the polar contacts are with backbone atoms of Pro68, Phe117, Ile199, and Ala121 with Ser84 and Glu87 providing addition bonding through their sidechains.

Analysis of the B-factors of the crystal structure of both the unliganded and liganded form of KpOHCU decarboxylase show a relatively even distribution of low B-factors (15 to 20) over the whole protein. The one exception is the helix that spans residues 79 through 88. Fig. 7.S2 shows a ribbon diagram of the KpOHCU decarboxylase structure colored by B-factors. This helix and the adjoining loop regions were examined further both structurally and by CD (see below).

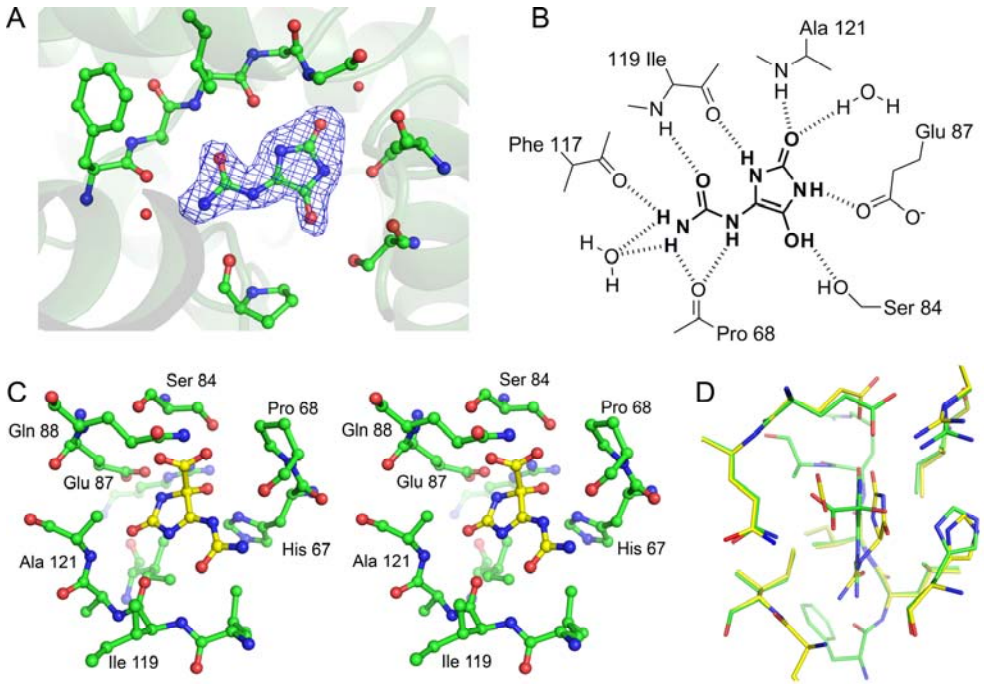

FIGURE 7.2. Active site of KpOHCU decarboxylase and ligand contacts. *A,* Active site with bound product, allantoin, showing $F_O - F_C$ electron density contoured at 3σ. The difference density was calculated before adding the ligand to the model. *B,* Schematic of ligand binding in KpOHCU decarboxylase active site showing hydrogen bonding between the enzyme and the ligand. *C,* Stereoview of KpOHCU decarboxylase active site with modeled OHCU (yellow). *D,* Superposition of the energy minimized active site with bound substrate (OHCU, green) and products ((S)-allantoin and CO_2, yellow).

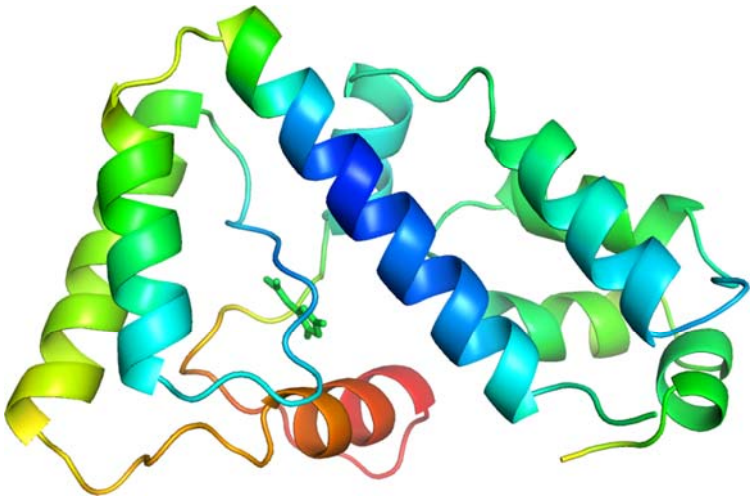

Figure 7.S2. Ribbon diagram of unliganded KpOHCU decarboxylase colored by B-factor. Allantoin is shown in green for reference. The colors indicate the magnitude of the values from low (blue-cyan-green) to high (yellow-orange-red).

A sequence alignment of KpOHCU decarboxylase with the zebrafish and *A. thaliana* OHCU decarboxylases is shown in Fig. 7.S3. Despite the relatively low level of overall similarity between the sequences, there are several conserved regions. In particular, all but one of the active site residues that make polar contacts with the ligand are conserved among the three enzymes (Fig. 7.S3, blue arrows). The exception is Ala74 from the *A. thaliana* OHCU decarboxylase (Ser84 in KpOHCU decarboxylase). A comparison of the different structures at this residue is impossible since Ala74 does not appear in the *A. thaliana* structure as it is part of a presumably disordered loop region.

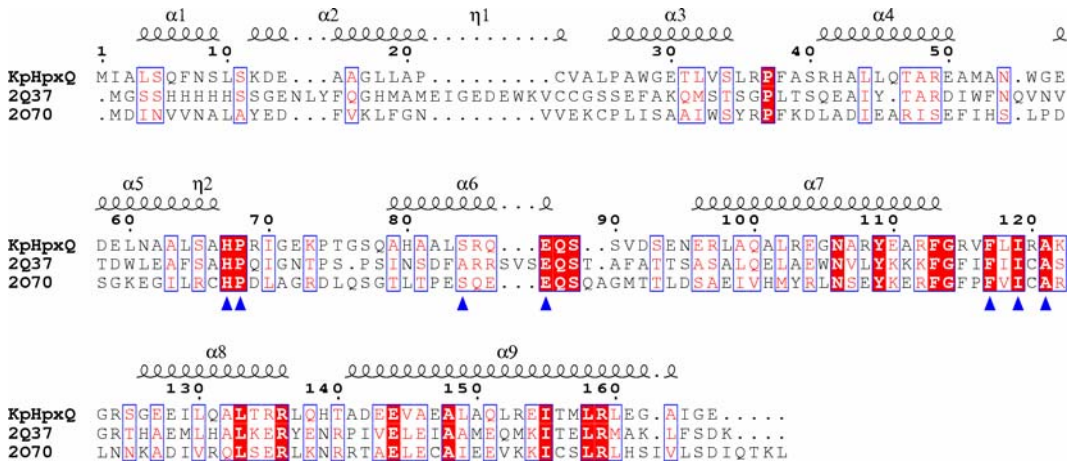

Figure 7.S3. Sequence alignment of KpOHCU decarboxylase, *A. thaliana* OHCU decarboxylase (2Q37), and the OHCU decarboxylase from zebrafish (2O70). The secondary structure elements shown above the alignment correspond to those observed in KpOHCU decarboxylase and the blue arrows indicate residues responsible for making hydrogen bonding contacts to the ligand.

An alignment of the unliganded and allantoin-bound KpOHCU decarboxylase structures reveals a slight difference in the loop between helices 5 and 6. While several residues change position, the shift of this region most notably alters the

position of His67, presumably to accommodate the ligand. The superposition of these two structures, illustrating the motion of His67, is shown in Fig. 7.S4*A*.

Modeling of Substrate and Products. In order to investigate the binding of the substrate and products of the KpOHCU decarboxylase catalyzed reaction, molecular mechanics simulations of OHCU and allantoin/carboxylate in the active site were carried out. Using the structure of the KpOHCU decarboxylase-allantoin complex as a starting point, these molecules were docked into the active site and then energy-minimized using the AMBER* (21) force field. Both the molecules themselves and the active site side-chains were allowed freedom of movement. While most of the residues remain unmoved, the putative active site base, His67, can adopt several low-energy states (Fig. 7.S4*B*,*C*). Modelling of OHCU also reveals additional hydrogen bonds made between the carboxylate group and Gln 88 as well as between the hydroxyl group and His 67. This structure also shows a shift in the position of the allantoin backbone away from Gln 88 and towards His 67.

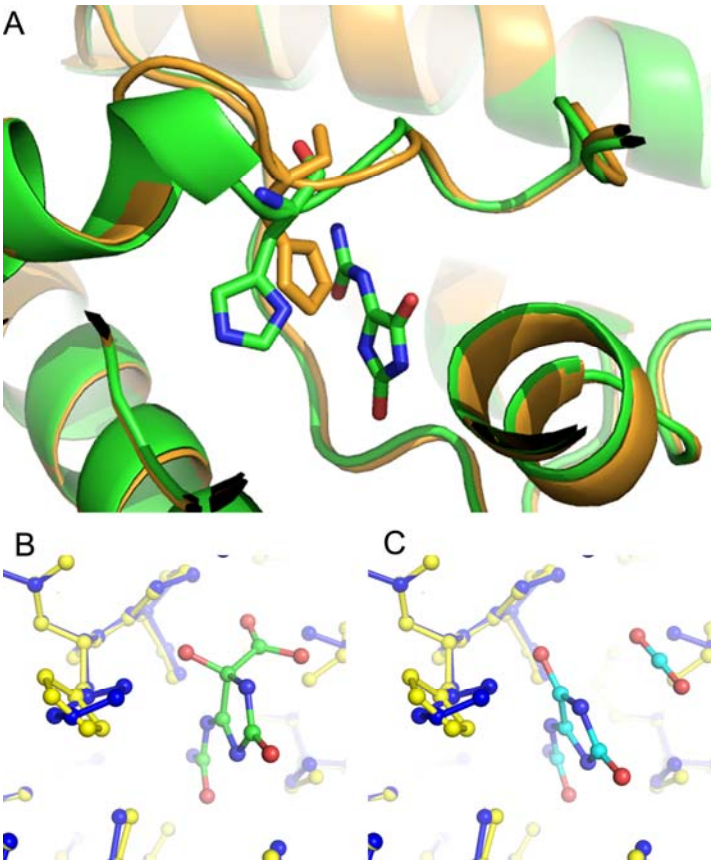

Figure 7.S4. His67 movement in the active site. *A*, Superposition of unliganded KpOHCU decarboxylase (gold) and KpOHCU decarboxylase with allantoin bound (green). His67 is shifted to accommodate the ligand in the KpOHCU decarboxylase-allantoin complex structure. Modeling of the substrate, OHCU (*B*), and the reaction intermediate (*C*) showing two of the predicted low energy conformations of His67. One of the low energy conformers (blue) is positioned to deprotonate the hydroxyl of OHCU, while a second conformer (yellow) is poised to protonate the prochiral carbon of the reaction intermediate. Comparison of the modeled reactant (*B*) and intermediate (*C*) also reveals that, after release of the carboxy moiety, there is a shift of the imidazoline ring towards His67.

Kinetics of KpOHCU Decarboxylase Catalyzed Reaction. The kinetics of conversion of OHCU to allantoin by KpOHCU decarboxylase can be followed spectrophotometrically. Fig. 7.3*A* shows the spectra of uric acid overlaid with the degradation products produced during enzymatic conversion to allantoin. The large difference in absorbance of OHCU and allantoin in the region of 240 - 260 nm allows for the facile measurement of this conversion. By monitoring the change in

absorbance at 256 nm, the initial rates of decarboxylation catalyzed by KpOHCU decarboxylase at various OHCU concentrations were measured and used to calculate the steady state parameters (Fig. 7.3*B*). The calculated background rate of non-enzymatic decay of OHCU ($1.5 \pm 0.1 \times 10^{-3}$ s^{-1}), which was in agreement with the reported value (2.2×10^{-3} s^{-1}, (4)), was accounted for in all cases. The enzyme turns over at a rate of 122 ± 11 s^{-1} and has a k_{cat}/K_M of 9.7×10^5 $M^{-1}s^{-1}$. An attempt to measure pre-steady state kinetics of the reaction showed a linear initial rate with no apparent burst phase observed at any point up to the highest detection limit of the apparatus (0.2 ms). In addition, the kinetics were unaffected by viscosity, showing no difference in rate of reaction in the presence of varying concentrations of sucrose or ethylene glycol (data not shown).

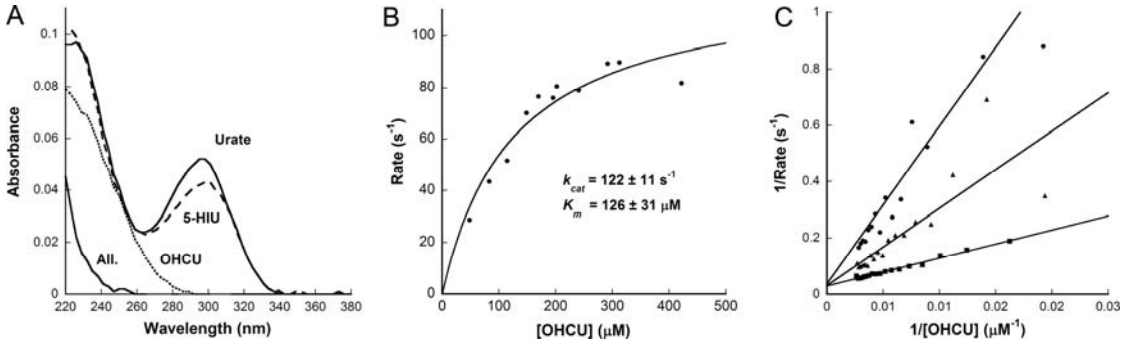

FIGURE 7.3. Kinetics of KpOHCU decarboxylase reaction. *A*, UV traces of the intermediates along the uric acid degradation pathway. Urate (top solid line) is converted to 5-HIU (dashed line) by urate oxidase (HpxO in *K. pneumoniae*); 5-HIU is converted to OHCU (dotted line) by an HIU hydrolase (HpxT in *K. pneumoniae*); and OHCU is converted to allantoin (lower solid line) by KpOHCU decarboxylase. *B*, The steady state kinetics of KpOHCU decarboxylase. The rate of OHCU decarboxylation was measured by monitoring the decrease in absorbance at 256 nm. The reactions were followed using a stopped flow apparatus and the rates were calculated from the first 10 seconds of the reaction (less than 10% completetion). *C*, Double reciprocal plot showing the competitive inhibition of KpOHCU decarboxylase by allopurinol. The rate was measured at 600 μM inhibitor (filled circles), 350 μM inhibitor (filled triangles) and 150 μM inhibitor (filled squares). The average value of K_i from the three datasets is 31 ± 2 μM.

Activity of the Q88E Mutant. To examine the role played by Gln 88 in catalysis, the activity of a glutamine to glutamate mutant was measured. Using the identical protocol and conditions as with the native protein, we measured the rate of conversion of OHCU to allantoin by the mutant enzyme. The Q88E mutant was active, but turned over at a slower pace than the native enzyme. The maximal rate of this mutant ($2.8 \pm 0.2\ s^{-1}$) was 43 fold slower than that of the native rate.

Inhibition of KpOHCU decarboxylase by Allopurinol. As there are currently no OHCU decarboxylase inhibitors reported in the literature, we tested several substrate analogues for their ability to inhibit KpOHCU decarboxylase activity. The xanthine oxidase inhibitor, allopurinol (*29*), was found to reduce the rate of KpOHCU decarboxylase turnover at micromolar concentrations. This compound was determined to be a competitive inhibitor as demonstrated by a double reciprocal plot of inhibition at 150, 350 and 600 μM, (Fig. 7.3*C*) with a calculated K_i of 30 ± 2 μM.

Structural Observations and CD Measurements of Domain Movement–In order to probe the mechanism of inhibition we attempted to structurally characterize a complex of KpOHCU decarboxylase and allopurinol. Soaks of the tetragonal crystal form with allopurinol solutions caused crystal degradation and failed to yield usable data. Similar treatment of the monoclinic crystals yielded high quality data with increased symmetry (*P*1 to *C*2). Examination of the structure revealed that helix 6 was missing from the density and the loop regions connecting this helix to the rest of the structure were displaced from the allantoin-bound structure (Fig. 7.4*A*).

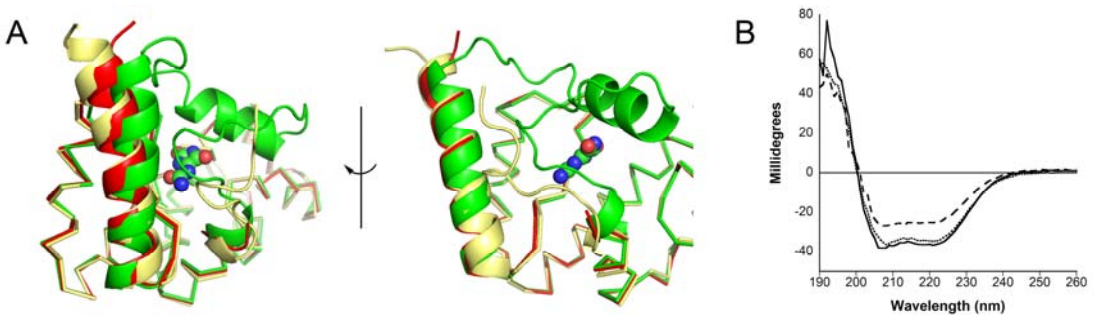

FIGURE 7.4. Conformational change of KpOHCU decarboxylase. *A*, Ribbon diagrams showing the structural superposition of KpOHCU decarboxylase-allantoin complex (green), unliganded KpOHCU decarboxylase in tetragonal form (yellow) and KpOHCU decarboxylase treated with allopurinol (red). Allantoin is shown in space-fill representation. Helix 6 (above allantoin) is visible only in the allantoin bound structure. *B*, Circular dichroism measurements of unliganded KpOHCU decarboxylase (dotted line), KpOHCU decarboxylase treated with allantoin (solid line) and KpOHCU decarboxylase treated with allopurinol (dashed line). The increase in signal at 208 nm and 222 nm and the decrease in signal at 193 nm in the presence of allopurinol are all consistent with a loss of helical content.

To examine the possibility that the inhibitor was disrupting the tertiary structure of the enzyme we examined the CD spectra of KpOHCU decarboxylase in the presence and absence of allantoin or allopurinol. The spectra of the protein alone, in the presence of allantoin and in the presence of allopurinol are shown in Fig. 7.4*B*. While the presence of allantoin has only a minor influence on the structure, a marked decrease in helical content is apparent in the presence of allopurinol. The approximate helical content drops from 93% in the unliganded structure to 82% in the presence of allopurinol (95% in the presence of allantoin).

7.5 Discussion

While KpOHCU decarboxylase bears a high degree of structural homology to previously reported OHCU decarboxylases, there are marked distinctions between these enzymes. The most striking of these is the disparity in the quaternary structures. While both of the eukaryotic OHCU decarboxylases reported dimers as the biological unit, the spatial relationship and interactions between the two protomers are

significantly different (Fig. 7.1). The *K. pneumoniae* enzyme presented herein, however, is clearly a monomer in solution. Considering that all of the protein-ligand interactions are made by a single monomer, these results suggest that the minimal functional unit of OHCU decarboxylase is a monomer. The dimeric forms present in the eukaryotic structures may be a result of evolutionary pressure. Further biochemical comparison of these enzymes is necessary to determine if the dimers are more catalytically efficient or are necessary for some other purpose such as protein-protein complex formation.

The active site residues of OHCU decarboxylases are highly conserved (Fig. 7.S3). Despite this similarity, and the observation that this enzyme produces (S)-allantoin stereospecifically, both the (S)- and (R)- isomers of allantoin have been observed bound in the active site (6, 7). In the KpOHCU decarboxylase structure, however, we observed the enol form of allantoin (Fig. 7.2). Allantoin is known to undergo slow non-enzymatic racemization, with one likely mechanism for this chemistry being the keto-enol tautomerization (*30*). In the presence of KpOHCU decarboxylase, this reaction is likely facilitated by His67, which is well positioned to abstract a proton from allantoin. It is not surprising to see that the enol is stabilized by the active site, as it is structurally more similar to the substrate than either the (R)- or (S)-enantiomers. Thus, the structure of KpOHCU decarboxylase in complex with this isomer of allantoin allows for a clearer picture of how the substrate interacts with this enzyme and provides a snapshot of an important intermediate in the reaction mechanism.

Positioning of OHCU in the KpOHCU decarboxylase active site is facilitated by the degree of similarity between the substrate and the enol observed in the structure. While the stereochemistry of enzymatically produced OHCU has not been well characterized, it can be inferred from structures of urate oxidase with bound

ligands. The addition of the hyroxyl group to urate occurs at the *re*- face leading to the (R)- isomer of OHCU after hydrolysis by HIU hydrolase cleaves the N1-C6 bond (31)[2]. A stereo diagram showing the positioning of OHCU in the KpOHCU decarboxylase active site is provided in Fig. 7.2*B*. In addition to the hydrogen bonding contacts shown in Fig. 7.2*A*, the substrate makes additional bonds to Gln88 through the carboxylate and with His67 through the hydroxyl moiety.

To further our understanding of the OHCU decarboxylation reaction we investigated the kinetics of KpOHCU decarboxylase. To date, there have been no reports on the kinetics of a native OHCU decarboxylase. This is likely due to the difficulty working with the unstable substrate of the reaction. OHCU can be generated *in situ* by the consecutive reactions of urate oxidase and HIU hydrolase on uric acid and 5-HIU, respectively. The conversion from uric acid to OHCU through 5-HIU can be monitored by UV (Fig. 7.3*A*). The clear difference in UV spectra between OHCU and allantoin in the 240 - 260 nm range allows for the facile measurement of reaction rates. The confounding factor of non-enzymatic decay of 5-HIU and OHCU is negligible if reaction times are kept short. Fig. 7.3*B* shows the steady state kinetics of the KpOHCU decarboxylase catalyzed decarboxylation reaction and the calculated kinetic parameters. Even though a cofactor is not required, this enzyme is surprisingly efficient with a k_{cat}/K_M of 9.7×10^5 $M^{-1}s^{-1}$.

Despite the commercial availability of purine derivatives, a search of the literature reveals a paucity of information for small molecule modulators of OHCU decarboxylase activity. There is, however, precedent for binding of such molecules apparent in the crystal structure of zebrafish OHCU decarboxylase in complex with guanine (*6*). Thus, we began our screen for small molecule modulators of KpOHCU decarboxylase activity with purine analogues. Comparison of wild type KpOHCU decarboxylase activity with activity levels in the presence of these molecules

identified allopurinol, a known xanthine oxidase inhibitor. We characterized the inhibition and determined that this molecule is a competitive inhibitor of KpOHCU decarboxylase activity with a K_i of 30 μM.

In order to probe the interactions between allopurinol and KpOHCU decarboxylase, we first attempted to solve the structure of these two molecules in complex. Our efforts to trap the allopurinol-KpOHCU decarboxylase complex revealed some very interesting details about the conformational flexibility of the enzyme and the mechanism of inhibition. Our first evidence that KpOHCU decarboxylase could exist in different conformational states in solution came from the different structures of the two unliganded crystal forms. The structure of the tetragonal form revealed a non-functional conformation where the crystal packing interactions occurred near the active site (Fig. 7.S1). Additionally, soaks of the unliganded or liganded KpOHCU decarboxylase crystals with allopurinol showed a similar unfolded state as was observed for the tetragonal form. A superposition of these different conformational states is shown in Fig. 7.4.

These observations suggested that a region of this enzyme containing helix 6 and bound by the adjoining loop regions was conformationally flexible and was sensitive to active site-ligand interactions. An examination of the B-factors in the full, unliganded, structure suggests that this region of the enzyme has the most dynamic mobility (Fig. 7.S2). For further evidence of the impact of ligand binding on the conformational state of the enzyme we measured the circular dichroism spectra of the enzyme in the absence and presence of allantoin and allopurinol. The results, shown in Fig. 7.4B, indicate that the enzyme has a lower helical content in the presence of the inhibitor. This data, taken together with the structural findings, indicates that the protein-ligand interactions drive conformational change and that binding of the inhibitor prevents the correct organization of the active site.

The structural, biochemical and modelling studies presented herein provide several much needed insights into the mechanism of decarboxylation catalyzed by OHCU decarboxylase enzymes. The proposed mechanism is shown in Scheme 7.2. KpOHCU decarboxylase is a highly efficient enzyme that operates in a cofactor independent manner. It has been proposed that OHCU decarboxylase may use a catalytic strategy similar to OMPDC, a widely studied cofactor-independent decarboxylase (6). While several mechanisms for the decarboxylation reaction catalyzed by OMPDC have been put forth, the mechanism that is most consistent with structural data and quantum mechanical calculations involves ground-state destabilization of the carboxylate group by a proximal aspartate in the active site (*11, 12, 32*).

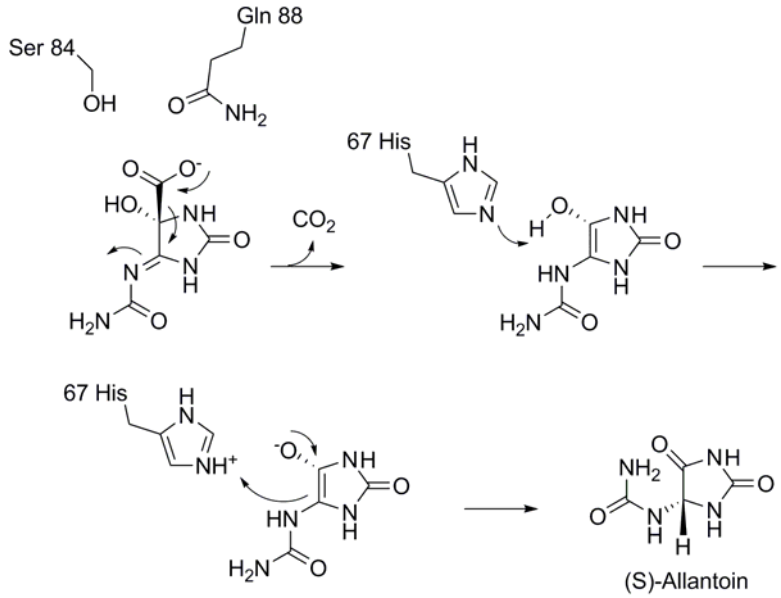

Scheme 7.2. Mechanism of OHCU decarboxylation catalyzed by KpOHCU decarboxylase.

While the active site of KpOHCU decarboxylase contains a large number of hydrogen bonding contacts, locking the substrate into place (as is the case for OMPDC), our data suggests a different mechanism. In the OMPDC decarboxylation reaction, the leaving carboxylate group is destabilized by an unfavourable interaction

with an active site aspartate. Based upon our structure, which allows for an accurate placement of the substrate in the active site, the carboxylate group of OHCU will be in close proximity to Gln88 (Fig. 7.2*C*,*D*). To examine if this residue provides a destabilizing driving force for decarboxylation, we constructed and measured the rate of reaction of the Q88E mutant. If the KpOHCU decarboxylase catalyzed reaction proceeded in an analogous fashion to that of OMPDC, we would expect a rate increase for the mutant enzyme. What we observed, however, was a decrease in enzyme activity by over 40 fold.

Based on this observation we propose that Gln88 instead acts to inductively destabilize the carbon-carbon bond between the carboxylate and C5 of the hydantoin ring in a manner analogous to purine nucleoside phosphorylase (PNP) (33) and related enzymes (34). In the PNP catalyzed reaction, an active site asparagine withdraws electrons from the purine ring through hydrogen bond formation causing a weakening and concomitant heterolysis of the C1′-N9 bond. This type of mechanism is consistent with the positioning of Gln88 in the KpOHCU decarboxylase structure and with the Q88E mutant activity measurements.

Upon decarboxylation, an enol intermediate is formed that resembles the isomer seen in our crystal structure (Fig. 7.2). Modeling of the reaction intermediates suggest that unfavourable interactions between the liberated CO_2 and both the enzyme and intermediate force the hydantoin ring towards His67 (Fig. 7.S4*C*). This histidine is ideally positioned to facilitate proton transfer between the hydroxy and C5 of the hydantoin ring. The structures of liganded and unliganded KpOHCU decarboxylase illustrate the conformational flexibility of this residue (Fig. 7.S4*A*) while our modelling studies support the role of His67 in proton transfer (Fig. 7.S4*B*,*C*). In addition, examination of the H67N mutant in the zebrafish OHCU decarboxylase showed complete loss of activity (6), consistent with its significance for proton

transfer. The enzyme mediated tautomerization, facilitated by His67, yields the product, allantoin, exclusively as the (S)-enantiomer. Pre-steady state kinetic analysis and examination of the effect of viscosity on reaction rate suggest that this latter reaction occurs very rapidly. In addition, as there is no apparent alternative for CO_2 escape from the active site, it is likely that the unfavourable interactions caused by the presence of this molecule drive product release.

In summary, we have presented a structural and biochemical characterization of KpOHCU decarboxylase, identified a novel inhibitor and proposed a mechanism of action for this inhibitor. CD measurements were used to support the structural evidence for dynamic instability of helix 6 and the ability for ligands to modulate this conformational change. The structure of KpOHCU decarboxylase in complex with the enol form of allantoin provides a view of the proposed reaction intermediate and, together with the biochemical data and modeling studies, allows us to provide a mechanistic analysis of the decarboxylation reaction.

REFERENCES

1. Vogels, G. D., and Drift, C. V. D. (1976) Degradation of Purines and Pyrimidines by Microorganisms, *Bacteriol. Rev. 40*, 403-468.
2. Zrenner, R.*, et al.* (2006) Pyrimidine and Purine Biosynthesis and Degradation in Plants, *Ann. Rev. Plant Biol. 57*, 805-836.
3. Kahn, K., and Tipton, P. A. (1997) Kinetic mechanism and cofactor content of soybean root nodule urate oxidase, *Biochemistry 36*, 4731-4738.
4. Kahn, K., and Tipton, P. A. (1998) Spectroscopic characterization of intermediates in the urate oxidase reaction, *Biochemistry 37*, 11651-11659.
5. Ramazzina, I.*, et al.* (2006) Completing the uric acid degradation pathway through phylogenetic comparison of whole genomes, *Nat. Chem. Biol. 2*, 144-148.
6. Cendron, L.*, et al.* (2007) The structure of 2-oxo-4-hydroxy-4-carboxy-5-ureidoimidazoline decarboxylase provides insights into the mechanism of uric acid degradation, *J. Biol. Chem. 282*, 18182-18189.
7. Kim, K.*, et al.* (2007) Structural and functional basis for (S)-allantoin formation in the ureide pathway, *J. Biol. Chem. 282*, 23457-23464.
8. Frey, P. A., and Hegeman, A. D. (2007) *Enzymatic Reaction Mechanisms*, Oxford University Press, New York.
9. McMurry, J. E., and Begley, T. P. (2005) *The Organic Chemistry of Biological Pathways*, Roberts and Company, Englewood, Colorado.
10. Appleby, T. C.*, et al.* (2000) The crystal structure and mechanism of orotidine 5'-monophosphate decarboxylase, *Proc. Natl. Acad. Sci. U.S.A. 97*, 2005-2010.

11. Begley, T. P., *et al.* (2000) The structural basis for the remarkable catalytic proficiency of orotidine 5'-monophosphate decarboxylase, *Curr. Opin. Struct. Biol. 10*, 711-718.
12. Wood, B. M., *et al.* (2009) Mechanism of the orotidine 5'-monophosphate decarboxylase-catalyzed reaction: effect of solvent viscosity on kinetic constants, *Biochemistry 48*, 5510-5517.
13. Otwinowski, Z., and Minor, W. (1997) *Methods Enzymol. 276*, 307-326.
14. McCoy, A. J., *et al.* (2007) Phaser crystallographic software, *J. Appl. Cryst. 40*, 658-674.
15. Vagin, A., and Teplyakov, A. (2000) An approach to multi-copy search in molecular replacement, *Acta Crystallogr. D 56*, 1622-1624.
16. Brünger, A. T., *et al.* (1998) Crystallography & NMR system: A new software suite for macromolecular structure determination, *Acta Crystallogr. D 54*, 905-921.
17. Emsley, P., and Cowtan, K. (2004) Coot: model-building tools for molecular graphics, *Acta Crystallogr. D 60*, 2126-2132.
18. Murshudov, G. N., *et al.* (1999) Efficient anisotropic refinement of macromolecular structures using FFT, *Acta Crystallogr. D 55 (Pt 1)*, 247-255.
19. Mohamadi, F., *et al.* (1990) MacroModel - an Integrated Software System for Modeling Organic and Bioorganic Molecules Using Molecular Mechanics, *J. Comput. Chem. 11*, 460-467.
20. Still, W. C., *et al.* (1999) Macromodel, 2.0 ed., Columbia University, New York, NY.
21. Weiner, S. J., *et al.* (1984) A new force field for molecular mechanical simulation of nucleic acids and proteins, *J. Am. Chem. Soc. 106*, 765-784.

22. Ponder, J. W., and Richards, F. M. (1987) An Efficient Newton-like Method for Molecular Mechanics Energy Minimization of Large Molecules, *J. Comput. Chem. 8*, 1016-1024.

23. DeLano, W. L. (2002) The PyMOL Molecular Graphics System, DeLano Scientific, San Carlos, CA.

24. Deleage, G., and Geourjon, C. (1993) An interactive graphic program for calculating the secondary structure content of proteins from circular dichroism spectrum, *Comput. Appl. Biosci. 2*, 197-199.

25. Perez-Iratxeta, C., and Andrade-Navarro, M. A. (2008) K2D2: Estimation of protein secondary structure from circular dichroism spectra, *BMC Struct. Biol. 8*, 25.

26. Krissinel, E., and Henrick, K. (2005) Detection of Protein Assemblies in Crystals, in *CompLife 2005* (al., B. e., Ed.), pp 163-174, Springer-Verlag, Berlin, Heidelberg.

27. Holm, L.*, et al.* (2008) Searching protein structure databases with DaliLite v.3., *Bioinformatics 24*, 2780-2781.

28. Chang, C.*, et al.* (2007) Crystal structure of protein Atu2327 from *Agrobacterium tumefaciens str*. C58.

29. Borges, F.*, et al.* (2002) Progress towards the discovery of xanthine oxidase inhibitors, *Curr. Med. Chem. 9*, 195-217.

30. Kahn, K., and Tipton, P. A. (2000) Kinetics and Mechanism of Allantoin Racemization, *Bioorg. Chem. 27*, 62-72.

31. Gabison, L.*, et al.* (2008) Structural analysis of urate oxidase in complex with its natural substrate inhibited by cyanide: Mechanistic implications, *BMC Struct. Biol. 8*.

32. Begley, T. P., and Ealick, S. E. (2004) Enzymatic reactions involving novel mechanisms of carbanion stabilization, *Curr. Opin. Chem. Biol. 8*, 508-515.

33. Fedorov, A., *et al.* (2001) Transition State Structure of Purine Nucleoside Phosphorylase and Principles of Atomic Motion in Enzymatic Catalysis, *Biochemistry 40*, 853-860.

34. Doukov, T. I., *et al.* (2007) Structural and Kinetic Evidence for an Extended Hydrogen-bonding Network in Catalysis of Methyl Group Transfer, *J. Biol. Chem. 282*, 6609-6618.

CHAPTER 8

STRUCTURES OF *KLEBSIELLA PNEUMONIAE* ALLANTOIN RACEMASE IN COMPLEX WITH ALLANTOIN AND WITH 5-ACETYL HYDANTION AND THEIR MECHANISTIC IMPLICATIONS

8.1 Abstract

The oxidative catabolism of uric acid produces 5-hydroxy isourate (5HIU) which is further degraded to (S)-allantoin by the actions of two enzymes, 5HIU hydorlase and 2-oxo-4-hydroxy-4-carboxy-5-ureidoimidazoline (OHCU) decarboxylase. Both of the latter two intermediates, HIU and OHCU, are unstable in solution and breakdown nonstereospecifically to allantoin. In addition, slow non-enzymatic racemization of allantoin has been shown to occur at physiological pH. Since the further breakdown of allantoin is catalyzed by an enzyme that is specific for (S)-allantoin, allantoinase, an allantoin racemase is necessary for complete and efficient catabolism of uric acid. In this work we present several crystal structures of allantoin racemase from *Klebsiella pneumoniae* (HpxA). In addition to an unliganded structure solved using SeMet-SAD, structures of HpxA in complex with allantoin and in complex with 5-acetyl hydantoin are presented. These structures reveal several important features of the active site including an oxyanion hole and a polar binding pocket that interacts with the C5 substituent of the ligand and serves to control the orientation of the hydantoin ring. In addition, a highly ordered water molecule is situated near one of the catalytic residues and is ideally situated to participate in catalysis. The data presented provides new insights into the activity and substrate specificity of this enzyme and enables us to propose a mechanism for catalysis that is consistent with the 'two base' mechanism put forth for other members of this family.

8.2 Introduction

The enzymatic degradation of uric acid is the final stage of purine catabolism and serves in plants and some bacteria to provide a source of nitrogen, particularly when other nitrogen sources are depleted (*1, 2*). The first stage of this pathway involves three enzymes and facilitates the stereospecific oxidative decomposition of uric acid to (S)-allantoin. Upon oxidation by urate oxidase, two additional enzymes, 5-hydroxy isourate (HIU[1]) hydrolase and 2-oxo-4-hydroxy-5-ureidoimadozoline (OHCU) decarboxylase, complete the conversion from urate to (S)-allantoin (*3-5*). While the product of these enzymatic conversions is solely the (S)- enantiomer, non-enzymatic decomposition of both HIU and OHCU can occur and does so non-stereospecifically. In addition, slow, non-enzymatic racemization of allantoin has been observed to occur (*6*).

The conversion of allantoin to allantoate by an allantoinase enzyme is a point of convergence in the metabolism of ureides (*1, 2, 7*). This step is present in all organisms that catabolize allantoin. To date two types of allantoinase have been identified, a metal-dependent and a metal-independent form (*8-10*). While these two enzymes may differ in mechanism, what is common is that they both preferentially bind the *(S)*- enantiomer of allantoin. Considering the selectivity of the allantoinase enzymes and the various mechanisms operating to produce racemic mixtures of allantoin, efficient use of this molecule would require the presence of a racemase enzyme. Recent genetic studies on *Klebsiella pneumoniae* and *Klebsiella oxytoca* M5al have identified a gene cluster for purine utilization that encodes several enzymes that catalyze novel chemical transformations, including an enzyme that was putatively identified as an allantoin racemase (*11, 12*). This enzyme shares 45% identity over 96% of its length with the hydantoin racemase from *Pseudomonas sp.* The proposed purine degradative pathway in *Klebsiella sp.* is shown in Scheme 8.1.

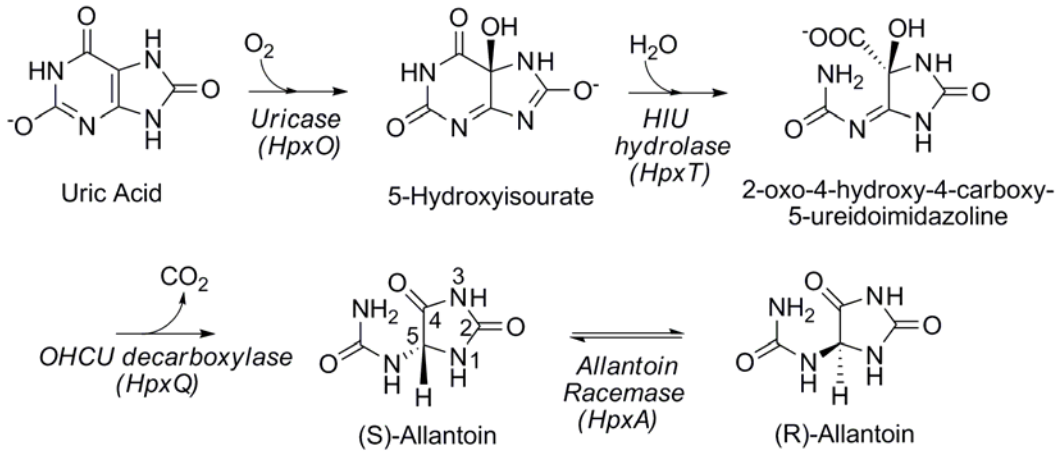

Scheme 8.1 Proposed purine catabolic pathway in *K. pneumoniae* (*11, 12*)

Despite the observation of allantoin racemase activity in the early 1970's (*13-15*), very little is known about this enzyme. In fact, a search of the literature does not yield a single report published on the biochemical or structural characterization of this enzyme since the original work carried out over thirty years ago. Despite this paucity of data for allantoin racemase, some progress has been made on the characterization of a homologous enzyme, hydantoin racemase (*16*). This enzyme belongs to the aspartate/glutamate racemase superfamily and is known to catalyze racemization of 5-substituted hydantoins in a cofactor- and metal-independent fashion. Hydantoin racemase, which catalyzes the racemization of various 5-substituted hydantoins, is a commercially important biocatalyst used in the production of optically pure amino acids (*17*).

Hydantoin racemase and other members of the aspartate/glutamate racemase superfamily are believed to operate using a two base mechanism that involves a pair of highly conserved cysteine residues (*18, 19*). Binding and kinetic studies combined with site-directed mutagenesis have demonstrated the importance of these two cysteines for both substrate recognition and catalysis. While this enzyme can bind and catalyze the conversion of both isomers, it has been reported that it does so with

differing specificity. Much of the binding and catalytic selectivity for the different isomers has been attributed to these two active site cysteines (*19, 20*).

In this work we present the first reported x-ray crystal structures of allantoin racemase in both unliganded and ligand-bound forms. These structures, from the opportunistic human pathogen, *Klebsiella pneumoniae*, provide valuable insights into substrate binding and selectivity. In addition, the structural information allows for a clearer picture of how this enzyme utilizes the conserved 'two base' mechanism to catalyze the racemization of allantoin.

8.3 Results

Structure of Unliganded HpxA. The structure of HpxA was solved using SeMet SAD phasing to 2.2 Å. Other than the polyhistidine tag and the two N-terminal residues, the entire protein was modeled. HpxA is an α/β protein with two domains that form a V shape in the protomer. The two domains share a high degree of similarity (RMSD 3.1 Å), with each containing a 4-stranded parallel β-sheet sandwiched between two pairs of α-helices (Figure 8.1B). When symmetry related molecules were considered, the crystallographic data suggested that HpxA formed a stable hexamer in the crystal (Figure 8.1A). The quaternary structure was verified by size exclusion chromatography (data not shown). The hexamer is made up by a trimer of dimers, with the three identical dimer interfaces occurring at the groove between domains. This interface has an approximate buried surface area of 3 400 $Å^2$ and is dominated by polar contacts between amphipathic helices 4 and 9 of the two protomers. The interface between the dimers is predominantly along helices 2 and 3 and has only slightly less buried surface area (approximately 3 340 $Å^2$) than the dimer interface itself. In addition, the C-terminal 20 residues form a loop that packs along the length of helix 2 of the neighboring molecule providing additional polar contacts.

Overall, this leads to a tightly packed hexamer with a total buried surface area of approximately 22 000 Å^2.

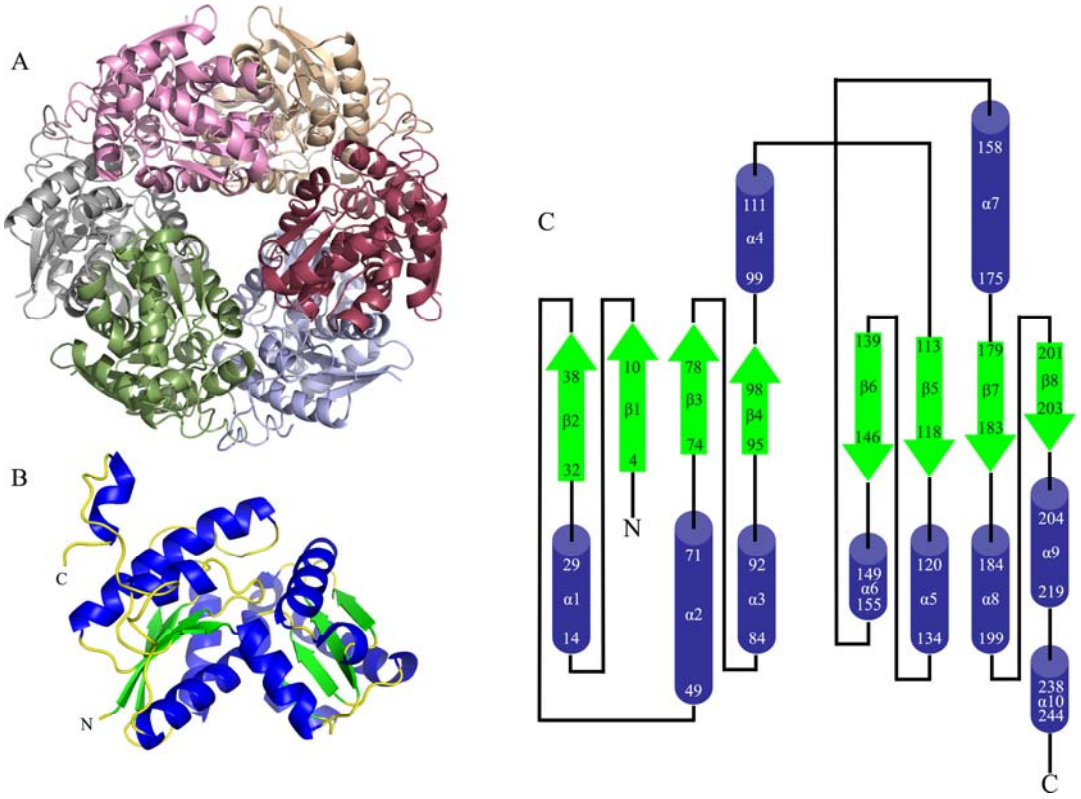

Figure 8.1 Structure of HpxA. A) Hexameric structure of HpxA seen in the crystals and confirmed by size exclusion chromatography. B) HpxA protomer. C) Topology diagram of HpxA. Helixes are shown as blue cylinders and strands as green arrows. The numbers correspond to the residue numbers of the first and last amino acid of each secondary structure element. The N and C termini are marked with an N and C, respectively.

C79S/C184S HpxA - Allantoin Structure. In order to examine active site interactions in HpxA, we constructed the C79S/C184S double mutant and solved the structure in complex with allantoin. The observed difference density in the active site allowed for the unambiguous placement of the ligand (Figure 8.2A). While the solution used for the soaks of the crystals was a mixture of the (R)- and (S)- isomers, the observed density best fit the enol form of allantoin (Figure 8.2B). Most of the interactions between the enzyme and the ligand are made through the backbone of

HpxA. A notable exception to this is a region surrounding the amide tail of the ligand where several hydrogen bonds are made to the sidechains of Thr118, Thr119, the backbone of Gly183 and to a water molecule positioned by Thr123.

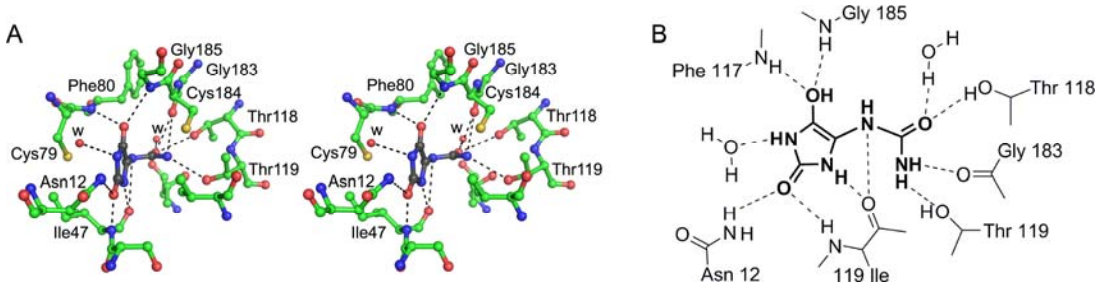

Figure 8.2 Active site of HpxA. A) Stereo diagram of the active site of HpxA in complex with allantoin. The structure shown (C in green, N in blue, O in red) is that of the wild type with allantoin (C in black, N in blue, O in red) placed in the active site as seen in the C79S/C184S structure. Waters are represented as red spheres and are labeled with 'w'. Putative hydrogen bonds are illustrated with dashed lines. B) Schematic drawing of the active site contacts between HpxA and allantoin. Dashed lines indicate putative hydrogen bonds. Cys79 and Cys184 are not shown.

The hydantoin ring of allantoin is positioned in the active site through three major sets of interactions. In addition to the above-mentioned binding pocket that tightly holds the allantoin tail in place, additional interactions are made through the two oxygen atoms of the hydantoin ring. These are each held in place by a pair of residues, the backbone amide nitrogens of Phe80 and Gly185 for the C4 oxygen and the backbone amide nitrogen of Ile47 and the sidechain of Asn12 for the C2 oxygen respectively (Figure 8.2B). Both of these pairs of hydrogen bonding interactions could also provide the necessary stabilizing interactions required for an oxyanion hole. Considering the geometry of the ligand in the active site, however, it is likely that only the former pair of residues would function in this capacity during catalysis.

The two conserved cysteine residues, Cys79 and Cys184, which are substituted by serines in the mutant structure, are situated on opposite sides of allantoin in the

asymmetric active site of HpxA (Figure 8.3A). In the structure of the C79S/C184S HpxA double mutant with allantoin bound the electron density for the Ser79 sidechain was diffuse and was best fit by two rotamers set to have 50% occupancy each (Figure 8.3A). The distances between the two serines and C5 of allantoin in the structure are 3.2 and 4.2 Å for Ser79 (rotamer closest to allantoin) and Ser184, respectively. Also present in the active site is a water molecule situated near Ser79 (Figure 8.3A). This molecule is 2.6 Å from Ser79 and 4.3 Å from C5 of allantoin. The water molecule also makes hydrogen bonds with the backbone nitrogen of Gly81 and the sidechain of Glu53.

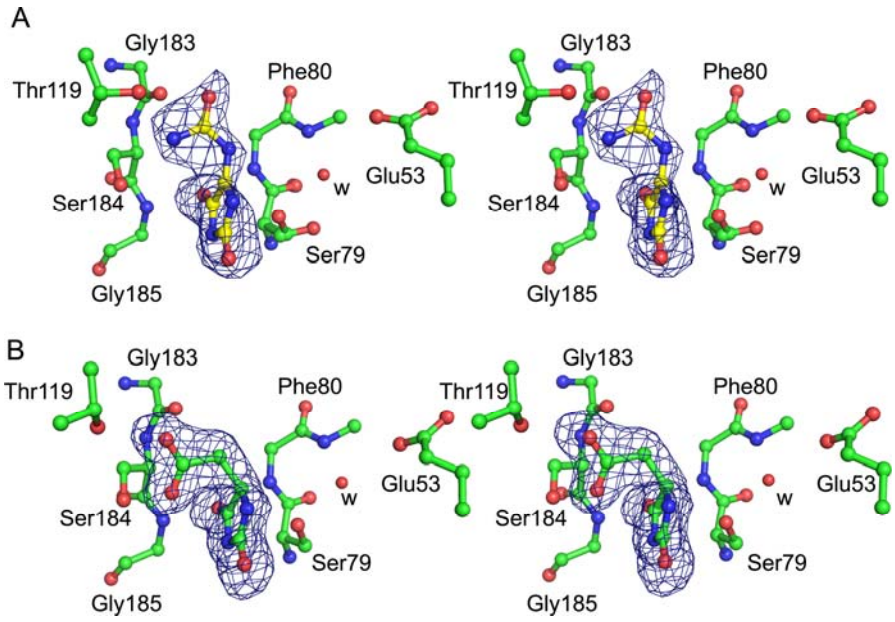

Figure 8.3 Ligands bound to HpxA. A) Stereo diagram of allantoin bound to the C79S/C184S HpxA double mutant. B) Stereo diagram of 5-acetyl hydantoin bound to the C79S/C184S HpxA double mutant. In both cases carbon atoms are green, oxygen atoms are red and nitrogen atoms are blue. The red sphere labeled with 'w' is a water molecule. The sidechain of Phe80 has been omitted for clarity. The electron density in both cases is from difference maps generated before the addition of the ligand molecule into the model and are contoured at 3σ.

Structural Similarity to Other Proteins. A search for structurally homologous proteins using the DALI (*21*) server yielded several related structures (Table 8.1). As expected, all of these structures belonged to the Aspartate/Glutamate racemase superfamily of proteins. The protein of known structure that is most similar to HpxA is the hydantoin racemase from *Pyrococcus horikoshii* (PDB identifier 2EQ5 (*22*)).

Table 8.1 Results of DALI search for structurally similar proteins using PDB90[a]

PDB ID	Z-Score	RMSD	% Identity	Annotated Function
2EQ5	23.4	2.3	20	Hypothetical hydantoin racemase
3EIS	16.6	3.0	18	Arylmalonate decarboxylase
several[b]	12.5 - 16.2	2.9 - 4.1	12 - 20	Glutamate racemase
1JFL	15.1	2.9	12	Aspartate racemase

[a]PDB90 is a representative subset of the PDB structures at 90% sequence identity
[b]2GZM, 2VVT, 1ZUW, 2DWU, 2JFG, 3IST, 2JFU, 2OHO, 2JFY and 1B73

While this protein was also crystallized in a hexagonal space group ($P6_5$), the observed quaternary structure was a dimer. The orientation of the two protamers in the dimeric 2EQ5 is similar to that of hpxA, but the interface is populated primarily by smaller, hydrophobic residues leading to a slightly shorter distance between the two molecules. A structural superposition of HpxA and 2EQ5 shows that the two proteins contain very similar secondary structure elements although some of the helical regions do not align well (Figure 8.4A). In spite of the overal similarity of the two proteins, the active sites display some distinct differences (Figure 8.4B). Superposition of the acitve site residues of HpxA and 2EQ5 show expected similarities in the conserved cysteines and in the putative oxyanion hole. Beyond these features, little similarity exists. Not surprisingly, the tail-binding region of the HpxA active site that is populated by several threonine residues is not present in the hydantoin racemase structure. In 2EQ5, this region is composed of predominantly non-polar residues, presumably to accommodate the typically aliphatic chains present in the 5-substituted hydantoin substrates. Additional interactions observed between allantoin and HpxA,

particularly at the C2 oxygen, are also not present in 2EQ5. Overall the active site of the hydantoin racemase is larger and more open than that observed in the allantoin racemase structure of HpxA.

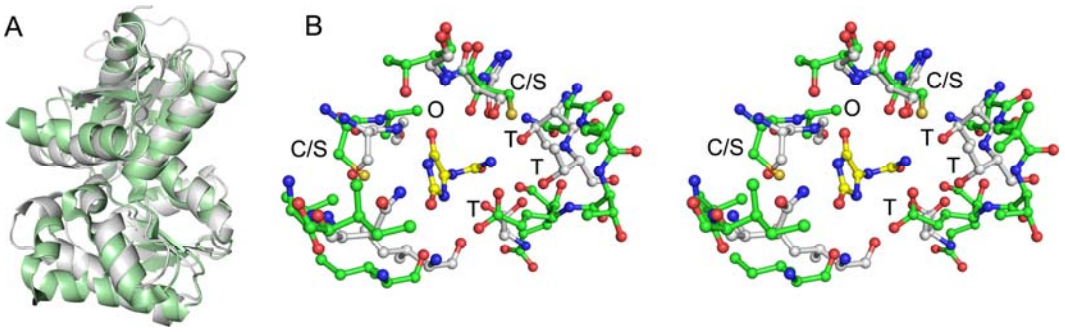

Figure 8.4 Superposition of HpxA and the hydantoin racemase from *P. horikoshii* (2EQ5). A) Secondary structural superposition of the protomers from HpxA (white) and 2EQ5 (green). B) Stereo diagram of the superposition of the active sites of HpxA (white carbon atoms, blue nitrogen atoms, and red oxygen atoms) and 2EQ5 (green carbon atoms) with allantoin shown (yellow carbon atoms). The two active site cysteines (serines in HpxA-allantoin structure) are labeled with C/S, the putative oxyanion hole is designated with an O, and each of the threonine residues that interact with the 'tail' region of allantoin in HpxA are labeled with T.

C79S/C184S HpxA - 5-acetyl Hydantion Structure. To further probe the active site of HpxA and examine how the residues contained within it determine specificity and carry out the racemization reaction, we solved the structure of HpxA in complex with the allantoin analogue, 5-acetyl hydantoin. Unlike allantoin, which is observed as an enol in the active site, the (R)- enantiomer (equivalent to the (S)- enantiomer of allantoin) is clearly bound to HpxA in this structure (Figure 8.3B). While the orientation of the hydantoin ring is similar for the two ligands, the tail region makes distinctly different binding interactions. The substitution of a carbon for N6 of allantoin leads to a different geometry and moves the acetyl group away from the 'threonine pocket' of the active site. This causes a slight shift in the ring and leads to additional hydrogen bonding between the acetyl group of 5-acetyl hydantoin and

Ser184 of the enzyme. What is similar in both structures however, is the electron density for the Ser79 sidechain, which is consistent with the presence of two rotamers, each having approximately 50% occupancy.

8.4 Discussion

Overall Structure of HpxA. *Klebsiella pneumoniae* HpxA is a two domain, α/β protein that is structurally homologous to members of the Glu/Asp racemase superfamily. The two domains of this enzyme share the same secondary structural elements suggesting that a gene duplication event occurred at some point in this protein's evolutionary history (Figures 8.1B and C). A clear hexameric quaternary structure was observed in the crystal structures of this enzyme and was confirmed by size exclusion chromatography (data not shown). Despite having a similar hexagonal space group, the most structurally similar enzyme, hydantoin racemase from the archaea *Pyrococcus horikoshii* (22), was observed as a dimer in the crystal structure. While all of the necessary active site contacts to the ligands are made by a single protomer in HpxA, a very tight dimer, similar to what is observed in the hydantion racemase structure, is formed between neighboring protomers in the hexameric molecule (Figure 8.1A). Size exclusion chromatography on hydantoin racemases from other organisms give results consistent with a hexamer (23) or a tetramer (24, 25). It is possible that the hexamer observed in the *K. pneumoniae* structure provides some evolutionary advantage over the dimer observed in the archael hydantoin racemase, although further research is needed to clarify this point.

Comparison of HpxA to Other Structures. A DALI search for structural homologues of HpxA yielded several proteins of the Glu/Asp racemase superfamily. The proteins of this family also share the two domain, α/β fold that is observed in HpxA. While these proteins have some degree of structural similarity, there is little sequence conservation amongst the members of this group (Figure 8.5). Highly

conserved residues include the two cysteines implicated in catalysis (Figure 8.5, blue triangles) and several other residues that serve predominantly structural roles. Aside from the catalytic cysteines, none of the completely conserved residues appear in the active site of HpxA. Note that the cysteine equivalent to Cys79 in HpxA is not conserved in 3EIS, an arylmalonate decarboxylase, as these enzymes are reported to proceed via a slightly different mechanism than other members of the superfamily.

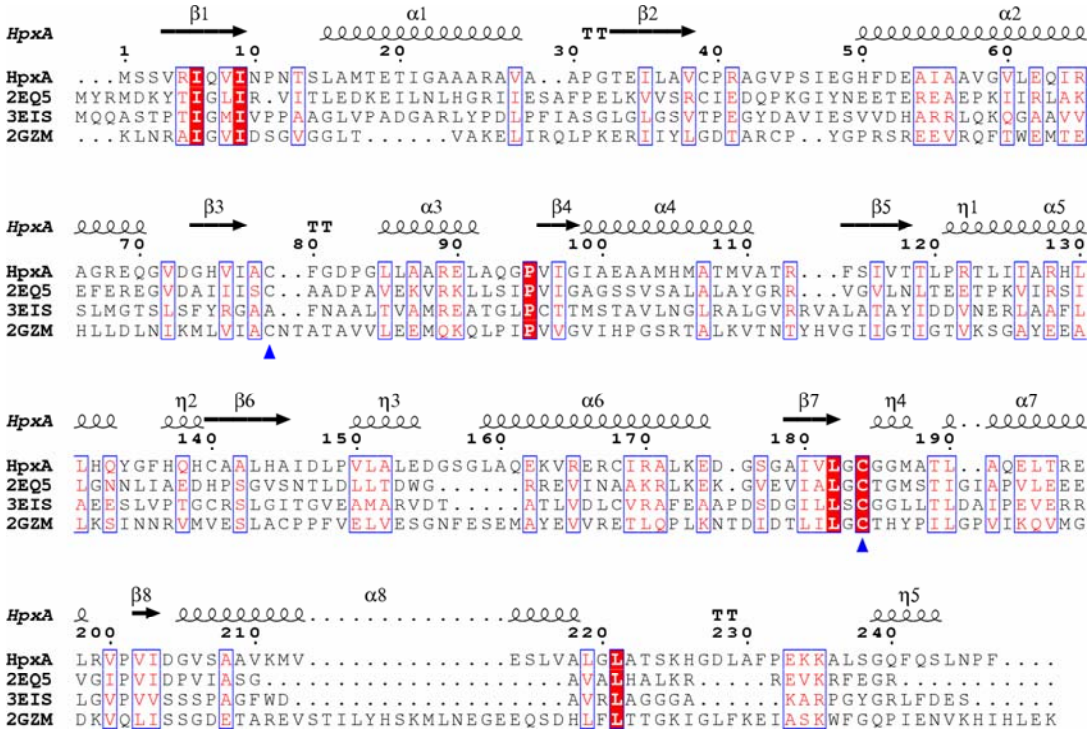

Figure 8.5 Sequence alignment of several Asp/Glu racemase superfamily members. The sequences were aligned using ClustalW (*26*) and the figure was produced using the ESPript server (*27*). The four sequences are the *Klebsiella pneumoniae* allantoin racemase (HpxA), *Pyrococcus horikoshii* hydantoin racemase (2EQ5 (*22*)), *Bordetella bronchiseptica* Arylmalonate decarboxylase (3EIS (*22*)), and *Bacillus anthracis* glutamate racemase (2GZM (*28*)). Red boxes with white lettering are completely conserved residues while boxes with red letters on a white background are regions of sequence similarity. The blue triangles indicate the two conserved cysteines, and the numbering and secondary structural elements shown correspond to the HpxA structure presented herein.

HpxA Active Site and Ligand Binding. A comparison of unliganded and the allantoin-bound complex of HpxA showed that the enzyme does not undergo any structural changes upon ligand binding. Other than a slight difference in the side chain conformation of Glu53, and the fitting of two rotamers to the density for Ser79 in the C79S/C184S HpxA-allantoin structure, all of the residues of the liganded structure align well with those of the unliganded structure. Alternate conformations of Ser79/Cys79 are likely important for catalysis, while the observed flexibility of the Glu53 sidechain suggests that it may act as a gate for the relatively inaccessible active site (Figure 8.6). Glu53 also interacts with an active site water molecule and may participate in catalysis (see discussion of mechanism below).

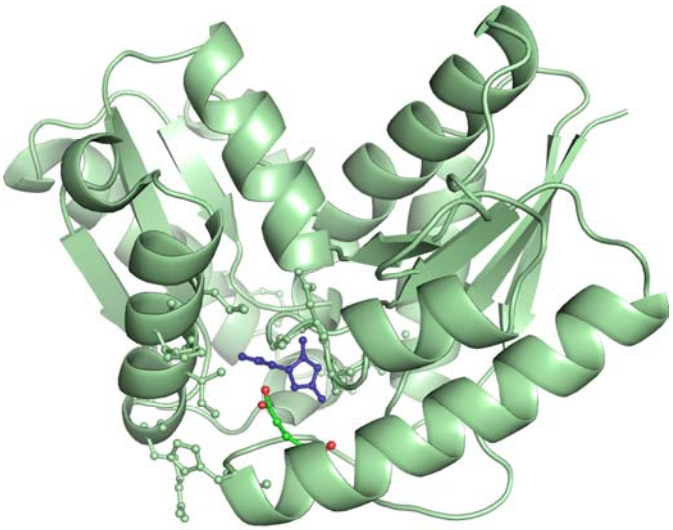

Figure 8.6 Access to the HpxA active site. The structure of HpxA is shown (pale green, ribbon and ball and stick) with allantoin bound (blue, ball and stick). Glu53, which may serve as a gate for the active site, is shown in ball and stick with green carbon atoms and red oxygen atoms.

The electron density observed for the difference maps observed in the active site for the C79S/C184S HpxA-allantoin structure clearly indicates that allantoin is present in its enol form (Figure 8.3A). This is not a surprising result considering that

allantoin is known to undergo slow racemization in solution via keto-enol tautomerization (*6*) and that the putative reaction intermediate for the racemization of allantoin is the enolate. This form of the ligand is not without precedent, and has been observed in the related structures of *Klebsiella pneumoniae* OHCU decarboxylase (*29*) and *Alcaligenes bronchisepticus* arlymalonate decarboxylase (*30*).

The two active site cysteines, which are substituted by serines in the HpxA double mutant, have been reported to play the major roles in a two base mechanism proposed for members of the Asp/Glu racemase superfamily (*19, 31*). In the C79S/C184S HpxA-allantoin structure, these residues are situated on either side of the ligand (Figures 8.2A and 8.3A). The distance between the oxygen atoms of Ser79 and Ser184 in this structure is 6.6 Å (using the rotamer of Ser79 that is closer to Ser184) and would be approximately 6.3 Å between thiols if cysteines were used in place of serine residues. The distance to C5 of allantoin in the structure from Ser79 and Ser184 are 3.2 and 4.2 Å respectively. These distances reflect the asymmetry in the active site and the form of allantoin that is bound.

In the presence of allantoin, a well ordered water molecule is observed in proximity to Ser79 and C5 of the ligand (Figure 8.3A). This water molecule is held in place by interactions with the amide nitrogen of Gly81, and the sidechains of Glu53 and Ser79. The geometry of the water molecule can be determined from the orientation of the three hydrogen bond donating and accepting groups. In the C79S/C184S HpxA-allantoin structure, the Gly81 amide nitrogen acts as a hydrogen bond donor while the polar sidechain of Glu53 accepts a hydrogen bond from the water molecule. This places the second hydrogen of this water molecule in the ideal position to be abstracted by the thiolate of Cys79 (the Ser79 to water distance in the liganded structure is 2.6 Å). Alternatively, when the cysteine sidechain is in the thiol

form, hydrogen bonding between the sulfur and the water will orient the thiol hydrogen ideally for attack by C5 of the hydantoin ring.

An important structural element observed in the liganded HpxA structures is the presence of a putative oxyanion hole. This pocket, created by the backbone amide nitrogens of Phe80 and Gly185 (Figure 8.3), which also serves to orient the hydantoin ring by interacting with the C4 oxygen, could stabilize negative charge that builds up at this oxygen atom along the reaction coordinate. This interaction is observed in both the structures of C79S/C184S HpxA in complex with allantoin (Figure 8.3A) and 5-acetyl hydantoin (Figure 8.3B), indicating its significance for ligand binding. In addition, the enol form of allantoin bound in the active site provides evidence that this pocket may serve to stabilize an oxyanion, as this ligand is structurally similar to the proposed enolate intermediate (see discussion of mechanism below).

One of the observed differences between the HpxA structure and that of hydantoin racemase is the presence of a polar region in the binding pocket of HpxA populated by several threonine side chains. This difference presumably stems from the difference in the substituent at the 5- position of the hydantoin ring. While hydantoin racemase accommodates non-polar, alipatic and aromatic groups such as ethyl, isobutyl and benzyl, the urea group at the 5- position of allantoin would require a more hydrophilic environment. This 'threonine pocket' is also likely to be very important for the selectivity of this enzyme. An examination of the two liganded structures of HpxA (Figure 8.3) indicates that this region provides an anchoring point for the tail region of the ligand and aids in the orientation of the hydantoin ring by securing the 5- substituent in this pocket. The observation of selectivity for the (R)-enantiomer of 5-acetyl hydantoin is likely a result of the interactions at this 'threonine pocket.' Binding of the (S)-5-acetyl hydantoin acetyl group into this pocket would

drive the hydantoin ring to a position almost perpendicular to that observed in the structure and would result in several unfavorable protein-ligand interactions.

Mechanistic Implications. While there are no mechanistic studies reported on allantoin racemase, insights can be gleaned from the structures reported herein with consideration of studies of the other members of the Asp/Glu racemase superfamily (*18-20, 31-33*). Hydantoin racemase is reported to be slightly more active towards the (R)- enantiomers of various 5- substituted hydantoins, although the size of the substituent has an effect upon the degree of selectivity (*32*). The structures of liganded HpxA reveal a polar 'threonine pocket' that interacts with the urea tail group of allantoin and serves to orient the hydantion ring. The other two major interactions with allantoin occur through the oxygen atoms and, while mediating the lateral motion (in reference to the plane of the ring), they do not preclude rotation of the molecule. These three 'anchor points,' therefore, allow for optimal positioning of the two isomers with respect to the two active site cysteines (Figure 8.7).

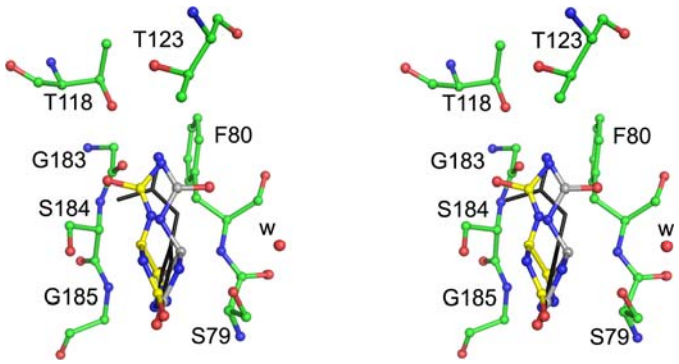

Figure 8.7 Allantoin isomers in HpxA active site. Stereo drawing of the (R)- (white carbon atoms) and the (S)- (yellow carbon atoms) isomers of allantoin docked in the active site of HpxA. The three main interactions in the HpxA active site, the 'threonine pocket,' the oxyanion hole contacts with the C4 oxygen atom and the interactions with the C2 oxygen atom, were used to orient the ligands. The observed enol form of allantoin is shown in black.

Based upon the solved structures of HpxA and the known chemistry of Glu/Asp/Hydantoin racemases, a mechanism for the allantoin racemase reaction is proposed (Scheme 8.2). Upon binding of (R)-allantoin, C5 of the ring is deprotonated by Cys184. This produces the enolate intermediate, with stabilization for the negative charge provided by the oxyanion hole. Abstraction of a proton from the proximal water by Cys79 is facilitated by weakening of the O-H bond as a result of the inductive force of Glu53. Collapse of the reactive oxyanion species drives attack of the thiol of Cys79 and abstraction of this proton. Product release is likely driven by two separate forces, the unfavorable interaction between the hydantoin ring and the protonated Cys184, and the repulsion of both the Cys79 thiolate and Glu53 sidechains by the hydroxide. The latter interaction could drive conformational change of the Glu53 sidechain, which may act as a 'gate' for entry into the active site. This would allow for product release and replacement or reprotonation of the active site water.

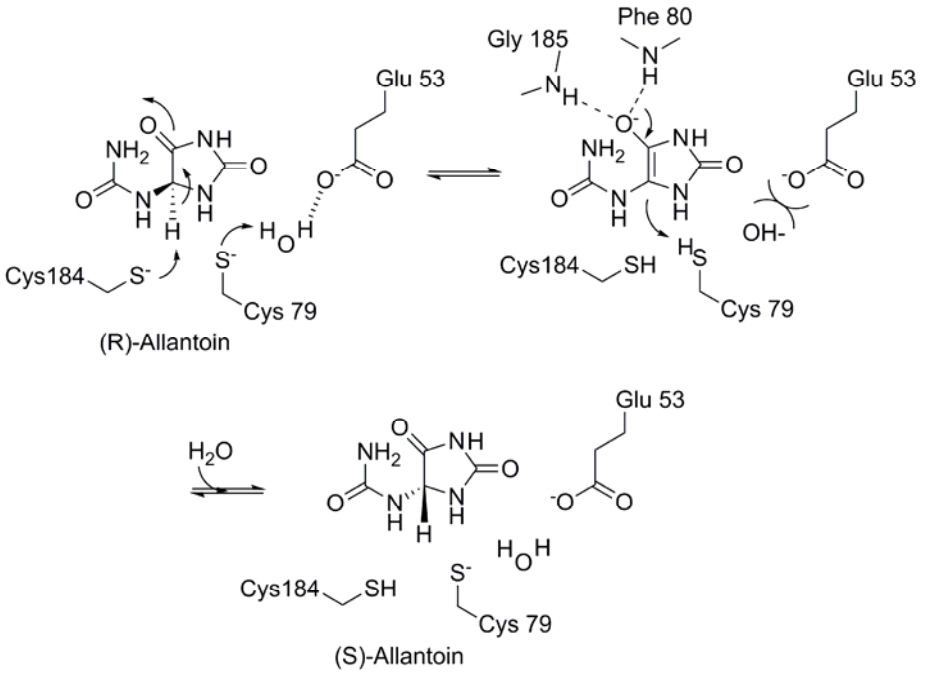

Scheme 8.2 Proposed mechanism of catalysis for racemization of allantoin by HpxA

The asymmetry in the active site suggests that the mechanism for conversion of the (S)- to (R)- enantiomer would likely proceed in a slightly different fashion. While the participation of a nearby water molecule is likely to occur for (R)- to (S)-chemistry, there is no such water molecule in the vicinity of Cys184. Thus, while the mechanisms for the two reactions would be analogous, Cys184 would act as both base and acid for racemization of (S)-allantoin.

In this paper, we have reported the first structural characterization of an allantoin racemase. The structures presented reveal several important features of the active site of this enzyme, including an oxyanion hole and a polar binding region that strongly interacts with the urea tail of allantoin. Analysis of these structures provides insight into the reactivity of this enzyme and allows us to propose a mechanism for the allantoin racemase reaction. Biochemical studies of several active site mutants are currently underway in order to better understand the mechanism and selectivity of the reaction catalyzed by this enzyme.

8.5 Materials and Methods

Protein Purification and Crystallization. The gene encoding *Klebsiella pneumoniae* HpxA was cloned from genomic DNA from *K. pneumoniae* subsp. *pneumoniae* (Schroeter) Trevisan MGH78578 (ATCC 700721) and placed in a modified Pet28 (Novagen) vector encoding an N-terminal 6-His tag by standard molecular biology techniques. The C79S, C184S and C79S/C184S mutant plasmids were made at the Cornell Protein Characterization and Production Facility by using site-directed mutagenesis of the native gene. Briefly, mutagenesis was performed on HpxA by a standard PCR protocol using *Pfu*Turbo DNA polymerase (Invitrogen) and *Dpn*I (New England Biolabs) to digest the methylated parental DNA prior to transformation. The presence of the mutated residue was verified by sequencing.

For protein expression in all cases, the plasmid was transformed into B834(DE3) (methionine auxotrophic) cells and the protein was expressed and purified as follows. For SeMet protein, the cells were grown in M9 minimal media supplemented with 0.4% glucose, MEM vitamin solution, 2 mM $MgSO_4$, 90 mM of $FeSO_4$ (25 mg/L), 100 μM $CaCl_2$, 40 mg/L each of 19 amino acids (methionine excluded), 50 mg/L of seleno-L-methionine and 50 mg/L kanamycin. The cells were grown at 37°C to an $O.D._{600}$ of 0.5 before reducing the temperature to 15°C. After 30 minutes at this temperature the cells were induced with 0.5 mM IPTG and grown for an additional 16 hours. The cells were harvested by centrifugation and the pellet stored at -20°C prior to purification. For native protein, the procedure followed was the same with the exception that LB was used as a growth medium.

For protein purification, the pellets were thawed in buffer containing 300 mM NaCl, 10 mM imidazole, 2 mM DTT and 50 mM sodium phosphate, pH 7.6. The cells were lysed by sonication and centrifuged to remove cellular debris. The cleared lysate was passed through a column containing pre-equilibrated Ni-NTA resin and then washed with a similar buffer containing 20 mM imidazole and 10% glycerol. The protein was eluted with buffer containing 300 mM NaCl, 2 mM DTT and 250 mM imidazole, pH 7.6 and immediately buffer exchanged into 30 mM NaCl, 2 mM DTT and 10 mM sodium acetate, pH 5.6. The protein was concentrated to 15 mg/ml using a centricon centrifugal concentrator (Amicon) and determined to be greater than 95% pure by SDS-PAGE. Aliquots of the protein were flash frozen immediately after buffer exchange and stored at -80°C for crystallization trials. Crystallization was performed by the hanging-drop vapor diffusion method at 18°C. For both the native and SeMet protein, crystals formed after 3 - 5 days in 24 - 34% Peg 400 with 0.1 M sodium acetate, pH 3.7 - 4.1. Crystals were harvested and frozen without additional

cryoprotectant. For allantoin and 5-acetyl-hydantoin complexes, crystals were soaked for 2 hours in solutions of mother liquor supplemented with 5 mM ligand.

Data Collection, Processing, Structure Determination and Refinement. The SeMet data were collected at 100°C at the Northeast Collaborative Access Team (NE-CAT) beam line 24-ID-C of the Advanced Photon Source at Argonne National Labs at the maximum f˝ for selenium as determined by a fluorescence scan of the crystal. The SeMet dataset was collected over 360° using a 1° oscillation range. The space group was determined to be $P6_322$ with 2 molecules per asymmetric unit for a solvent content of 51%. Data was indexed and scaled using HKL2000 (*34*) and heavy atom sites were located using the SHELX suite (*35*). The program autoSHARP (*36*) was used for refinement of heavy atom positions, phasing, calculation of residual maps, density modification and automated model building. The program was able to correctly place 469 of 494 residues in two chains with the correct side chains. Additional residues and water molecules were placed during iterative rounds of manual model building followed by refinement using Refmac5 (*37*).

The data for ligand bound complexes were collected at NE-CAT beam line 24-ID-C and 24-ID-E at a wavelength of 0.979 Å. These data also indexed in space group $P6_322$ and had similar unit cell dimensions and percent solvent content. Refinement was carried out as detailed above using the SeMet structure as a starting point. The ligand was built into difference density only after the refinement had converged. Data collection and refinement statistics for all structures are provided in Tables 8.2 and 8.3, respectively.

Table 8.2. Data Collection Statistics.

	HpxA - SeMet	HpxA - C79S/C184S - allantoin	HpxA - C79S/C184S - 5-acetyl-hydantion
resolution (Å)	50.0 - 2.1	50.0 - 2.0	50.0 - 1.82
wavelength (Å)	0.9792	0.9791	0.9791
beam line	NE-CAT ID-C	NE-CAT ID-E	NE-CAT ID-E
space group	$P6_322$	$P6_322$	$P6_322$
a, b (Å)	124.8	124.9	125.0
c (Å)	126.8	127.0	127.0
no. of reflections	106 706	197 739	805 670
unique reflections	28 561	39 452	52 509
average I/σ	15.0 (2.1)	25.4 (4.3)	47.0 (7.9)
redundancy	3.7 (3.5)	5.0 (4.5)	15.3 (11.3)
completeness (%)	94.6 (99.6)	98.3 (98.2)	99.9 (100.0)
R_{sym}[a] (%)	9.7 (40.1)	9.6 (38.1)	7.0 (30.1)

Numbers in parentheses correspond to the highest resolution shell

[a] $R_{\text{sym}} = \Sigma\Sigma_i \left| I_i - \langle I \rangle \right| / \Sigma \langle I \rangle$, where $\langle I \rangle$ is the mean intensity of the N reflections with intensities I_i and common indices h, k, l

Table 8.3. Data Refinement Statistics.

	HpxA - SeMet	HpxA - C79S/C184S - allantoin	HpxA - C79S/C184S - 5-acetyl-hydantion
resolution (Å)	50.0 - 2.1	50.0 - 2.0	50.0 - 1.82
no. of protein atoms	3542	3573	3518
no. of ligand atoms	0	14	22
no. of water atoms	190	302	446
no. of reflections in working set	32 766	37 463	49 799
no. of reflections in test set	1 740 (5 %)	1 974 (5 %)	2675 (5%)
R factor[a] (%)	20.5	22.2	20.8
R_{free}[b] (%)	23.9	24.6	22.2
rmsd bonds (Å)	0.007	0.005	0.005
rmsd angles (°)	1.013	0.927	0.927
mean B factor (Å^2)	32.9	31.6	19.9
Ramachandran plot			
most favored (%)	94.3	95.2	95.2
additionally allowed (%)	5.7	4.8	4.8
generously allowed (%)	0.0	0.0	0.0
disallowed (%)	0.0	0.0	0.0

[a] R factor $= \Sigma_{hkl} \left| |F_{obs}| - k|F_{calc}| \right| / \sum_{hkl} |F_{obs}|$, where F_{obs} and F_{calc} are observed and calculated structure factors respectively.
[b] For R_{free}, the sum is extended over a subset of reflections (5%) excluded from all stages of refinement

The topology diagram was based upon the results from the PDBsum server (*38*). The sequence alignment was carried out using ClusalW (*26*) and the corresponding figure was made using the ESPript server (*27*). For the superposition of allantoin enantiomers for Figure 8.7, the (R)- and (S)- enantiomers were positioned by aligning the C2 and C4 oxygen atoms and the urea nitrogen atom with the respective atoms from the observed enol form. All other figures were made using PyMol (*39*) and ChemBioDraw (Cambridgesoft).

REFERENCES

1. Vogels, G. D., and Drift, C. V. D. (1976) Degradation of Purines and Pyrimidines by Microorganisms, *Bacteriol. Rev. 40*, 403-468.
2. Zrenner, R., *et al.* (2006) Pyrimidine and Purine Biosynthesis and Degradation in Plants, *Ann. Rev. Plant Biol. 57*, 805-836.
3. Kahn, K., and Tipton, P. A. (1997) Kinetic mechanism and cofactor content of soybean root nodule urate oxidase, *Biochemistry 36*, 4731-4738.
4. Modric, N., *et al.* (1992) Tracing and identification of uricase reaction intermediates, *Tetrahedron Lett. 33*, 6691-6694.
5. Ramazzina, I., *et al.* (2006) Completing the uric acid degradation pathway through phylogenetic comparison of whole genomes, *Nature chemical biology 2*, 144-148.
6. Kahn, K., and Tipton, P. A. (2000) Kinetics and Mechanism of Allantoin Racemization, *Bioorg. Chem. 27*, 62-72.
7. Schubert, K. R. (1986) Products of biological nitrogen fixation in higher plants: synthesis, transport and metabolism, *Ann. Rev. Plant Biol. 37*, 539-574.
8. Kim, K., *et al.* (2009) Crystal structure of metal-dependent allantoinase from *Escherichia coli*, *J. Mol. Biol. 387*, 1067-1074.
9. Mulrooney, S. B., and Hausinger, R. P. (2003) Metal ion dependence of recombinant *Escherichia coli* allantoinase, *J. Bacteriol. 185*, 126-134.
10. Ramazzina, I., *et al.* (2008) Logical identification of an allantoinase analog (puuE) recruited from polysaccharide deacetylases, *J. Biol. Chem. 283*, 23295-29304.
11. de la Riva, L., *et al.* (2008) The hpx genetic system for hypoxanthine assimilation as a nitrogen source in *Klebsiella pneumoniae*: gene organization and transcriptional regulation, *J. Bacteriol. 190*, 7892-7903.

12. Pope, S. D.*, et al.* (2009) Purine utilization by *Klebsiella oxytoca* M5al: genes for ring-oxidizing and -opening enzymes, *J. Bacteriol. 191*, 1006-1017.
13. Okumura, I.*, et al.* (1976) Stereospecificity of conversion of uric acid into allantoic acid by enzymes of Canadida utilis, *Journal of biochemistry 79*, 1013-1019.
14. Okumura, I., and Yamamoto, T. (1978) Enzymic racemization of allantoin, *Journal of biochemistry 84*, 891-895.
15. Van der Drift, L.*, et al.* (1975) Allantoin racemase: a new enzyme from Pseudomonas species, *Biochimica et biophysica acta 391*, 240-248.
16. Nam, S.-H.*, et al.* (2005) Evolutionary relationship and application of a superfamily of cyclic amidohydrolase enzymes, *The Chemical Record 5*, 298-307.
17. Altenbuchner, J.*, et al.* (2001) Hydantoinases and related enzymes as biocatalysts for the synthesis of unnatural chiral amino acids, *Curr. Op. Biotech. 12*, 559-563.
18. Hwang, K. Y.*, et al.* (1999) Structure and mechanism of glutamate racemase from *Aquifex pyrophilus*, *Nat. Struct. Biol. 6*, 422-426.
19. Martinez-Rodriguez, S.*, et al.* (2006) Site-directed mutagenesis indicates an important role of cysteines 76 and 181 in the catalysis of hydantoin racemase from *Sinorhizobium meliloti*, *Protein Sci. 15*, 2729-2738.
20. Andujar-Sanchez, M.*, et al.* (2006) Binding studies of hydantoin racemase from *Sinorhizobium meliloti* by calorimetric and fluorescence analysis, *Biochim. Biophys. Acta 1764*, 292-298.
21. Holm, L.*, et al.* (2008) Searching protein structure databases with DaliLite v.3., *Bioinformatics 24*, 2780-2781.

22. Mizutani, H., and Kunishima, N. (2007) Crystal structure of hydantoin racemase from *Pyrococcus horikoshii* OT3, RIKEN Structural Genomics/Proteomics Initiative (RSGI).

23. Watabe, K.*, et al.* (1992) Purification and characterization of the hydantoin racemase of *Pseudomonas sp.* strain NS671, *J. Bacteriol. 174*, 7989-7995.

24. Martinez-Rodriguez, S.*, et al.* (2004) Biochemical characterization of a novel hydantoin racemase from *Agrobacterium tumefaciens* C58, *Biochimie 86*, 77-81.

25. Suzuki, S.*, et al.* (2005) Purification and characterization of hydantoin racemase from *Microbacterium liquefaciens* AJ 3912, *Biosci. Biotechnol. Biochem. 69*.

26. Larkin, M. A.*, et al.* (2007) ClustalW and ClustalX version 2, *Bioinformatics 23*, 2947-2948.

27. Gouet, P.*, et al.* (2003) ESPript/ENDscript, *Nucl. Acids. Res. 31*, 3320-3323.

28. May, M.*, et al.* (2007) Structural and functional analysis of two glutamate racemase isozymes from *Bacillus anthracis* and implications for inhibitor design, *J. Mol. Biol. 371*, 1219-1237.

29. French, J. B., and Ealick, S. E. (2010) Structural and Mechanistic Studies on *Klebsiella pneumoniae* 2-Oxo-4-hydroxy-4-carboxy-5-ureidoimidazole Decarboxylase *J. Biol. Chem.*, Submitted.

30. Obata, R., and Nakasako, M. (2010) Structural basis for inverting the enantioselectivity of arylmalonate decarboxylase revealed by the structural analysis of the Gly74Cys/Cys188Ser mutant in the liganded form, *Biochemistry 49*, 1963-1969.

31. Glavas, S., and Tanner, M. E. (2001) Active Site Residues of Glutamate Racemase, *Biochemistry 40*.

32. Heras-Vazquez, F. J. L., *et al.* (2003) Overexpression and characterization of hydantoin racemase from *Agrobacterium tumefaciens* C58, *Biochem. Biophys. Res. Commun. 303*, 541-547.

33. Ohtaki, A., *et al.* (2008) Structure of aspartate racemase complexed with a dual substrate analogue, citric acid, and implications for the reaction mechanism, *Proteins 70*, 1167-1174.

34. Otwinowski, Z., and Minor, W. (1997) *Methods Enzymol. 276*, 307-326.

35. Sheldrick, G. M. (2008) A short history of SHELX, *Acta. Cryst. A64*, 112-122.

36. Vonrhein, C., *et al.* (2006) Automated structure solution with autoSHARP, *Methods Mol. Biol. 364*, 215-230.

37. Murshudov, G., *et al.* (1997) Refinement of macromolecular structures by the maximum-likelihood method, *Acta. Cryst. D53*.

38. Laskowski, R. A. (2009) PDBsum new things, *Nucl. Acids. Res. 33*, D266-D268.

39. DeLano, W. L. (2002) The PyMOL Molecular Graphics System, DeLano Scientific, San Carlos, CA.

APPENDIX I

STRUCTURE OF *KLEBSIELLA PNEUMONIAE* 5-HYDROXY ISOURATE HYDROLASE

Summary

5-Hydroxy isourate (HIU) is the product of oxidation of uric acid by uricase. This molecule is converted to 2-oxo-4-hydroxy-4-carboxy-5-ureidoimidazoline (OHCU) by HIU-hydrolase. Presented below is the structure of the HIU-hydrolase from *Klebsiella pneumoniae*, called HpxT. The details of the crystallization and structure solution are provided in addition to the structural results.

Experimental

The HpxT plasmid was provided by the protein production facility and transformed into BL21(DE3) cells using standard techniques. The protein was expressed and purified as detailed previously (see Chapter 6 or 7, Materials and Methods). The crystals were grown using the hanging-drop method, grew in many different conditions and were predominantly rod-shaped. The conditions used for diffraction included: 0.7 - 0.9 ammonia phosphate in 0.1 M imidazole; pH 7.9, 6 - 10 % PEG 3000, 0.2 M $MgCl_2$, in 0.1 M cacodylate, pH 6.5; and 8 - 14% PEG 8000, 0.2 M calcium acetate in 0.1 M imidazole, pH 7.0 - 7.5. Crystals grew in one to two weeks and were cryoprotected with the above solutions supplemented with either 15% PEG 3000, 15% ethylene glycol, or 15% glycerol (little difference noticed in diffraction between cryos). The crystals tested from the above conditions diffracted beyond 2 Å at APS or CHESS and generally yielded high quality data. The structure was solved by molecular replacement with MOLREP using 2IGL as a search model. Refmac5 was used for refinement while manual model building and the addition of water molecules was accomplished using COOT. Data collection and refinement statistics are given in tables A1.1 and A1.2 below.

In attempts to examine ligand binding in HpxT several known ligands have been soaked into crystals or co-crystallized with this enzyme. Uric acid, 8-azaxanthine, 2,6-diaminouracil, allantoin as well as several other purines and analogues have been employed in this manner. To date, all soaks or co-crystallization of these ligands into the enzyme have been unsuccessful. These were attempted under various growth conditions and using crystals grown from different solutions. This work led to the cloning, purification and crystallization of several mutants in order to increase the chance of solving a structure in complex with a ligand.

Several mutants of this protein were provided by the protein production facility. These included the H7N, R41K, H91N, and S105A mutants. All of these were transformed, expressed and purified as mentioned above. While these mutants yielded crystals of similar morphology under the same conditions as native, they diffracted to no better than 3 Å and were highly mosaic. Screens for additional diffraction conditions are under way and, to date, only a single condition (Hampton Screen II, condition 30) has yielded usable data to approximately 2.7 Å.

Table A1.1 Data Collection Statistics

	HpxT-1	HpxT-2
resolution (Å)	2.04	1.76
Wavelength (Å)	0.987	0.987
beam line	24-ID-C	24-ID-C
space group	$P2_12_12_1$	$P2_12_12_1$
a (Å)	42.3	42.3
b (Å)	100.6	100.7
c (Å)	105.6	105.7
no. of reflections	136785	170844
unique reflections	29399	42995
average I/σ	17.8 (4.5)	19.9 (5.9)
Redundancy	4.1 (4.5)	4.1 (3.7)
completeness (%)	99.7 (98.4)	94.2 (89)
R_{sym}[a] (%)	9.2 (34.8)	5.8 (18.6)

*these are the statistics from two of the first data sets collected. They are only two examples of many dozens of datasets with resolutions ranging from 1.6 to 2.3 Å Numbers in parentheses correspond to the highest resolution shell

[a] $R_{\text{sym}} = \Sigma\Sigma_{\text{i}} \left| I_i - \langle I \rangle \right| / \Sigma \langle I \rangle$, where $\langle I \rangle$ is the mean intensity of the *N* reflections with intensities I_i and common indices *h, k, l*

Table A1. 2 Data Refinement Statistics*

	KpHpxT
resolution (Å)	2.04
protein atoms	3110
ligand atoms	0
water atoms	155
reflections in working set	27 847
reflections in test set	1492
R factor[a]	24.4
R_{free}[b]	28.0
rmsd bonds (Å)	0.008
rmsd angles (^{o})	1.21
mean *B* factor (Å^2)	21.1

*these are the statistics from one of the first data sets collected. It is only one example of many dozens of datasets with resolutions ranging from 1.6 to 2.3 Å

[a] $R \text{ factor} = \Sigma_{hkl} \left\| F_{obs} \right| - k \left| F_{calc} \right\| / \sum_{hkl} \left| F_{obs} \right|$, where F_{obs} and F_{calc} are observed and calculated structure factors respectively.

[b] For R_{free}, the sum is extended over a subset of reflections (5%) excluded from all stages of refinement

Structure of HpxT

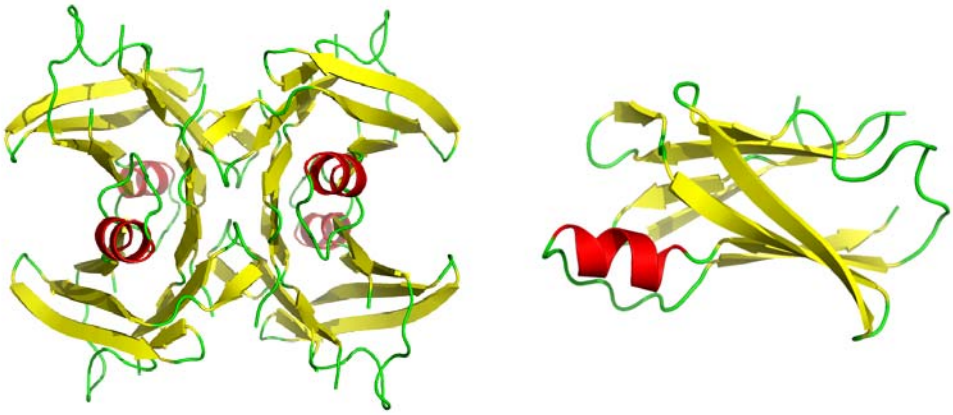

Figure A1.1. Structure of HpxT. HpxT is a tetramer (left) in solution (verified by size exclusion chromatography). The HpxT protomer (right) is also shown.

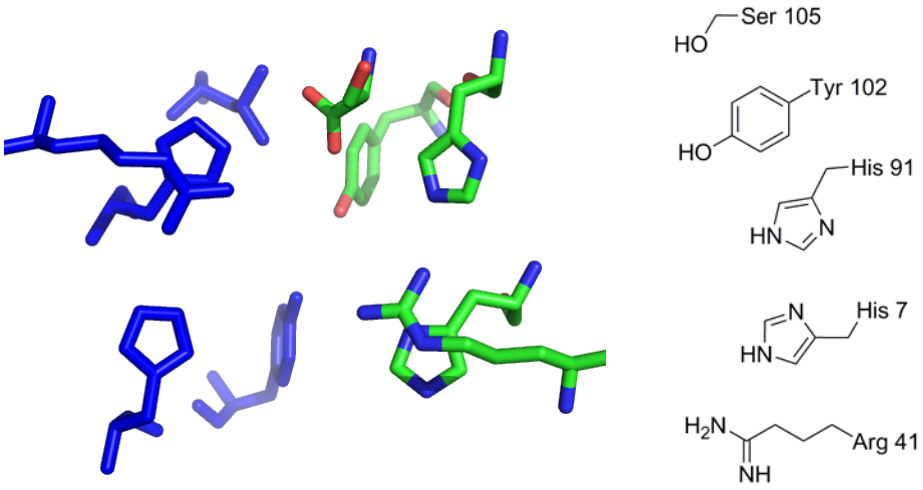

Figure A1.2 Active site of HpxT. The active site occurs at the interface of two protomers and is, consequently, symmetric in structure. The structure of the active site is shown (left) with the residues from one protomer colored blue. The schematic of the active site residues is also shown (right).

Ongoing Work

The goal of this work is to better understand ligand binding for this enzyme, particularly how the symmetric active site can catalyze an asymmetric conversion, and

to examine the mechanism for this conversion. With this in mind, the priority is to solve structures of this enzyme in complex with different ligands. As mentioned above, several mutants have been purified and a new crystallization condition identified that may yield the desired results. Additional optimization of this condition will hopefully yield crystals that will enable us to soak in ligands or provide a new strategy for co-crystallization.

In addition, a UV-based assay has been developed to examine the activity of this enzyme. *In situ* production of the substrate, HIU, and the difference between the spectra of HIU and the product, OHCU, enable us to measure the rate of turnover of this enzyme. Measurements of the relative rates of reaction for the native enzyme and the mutants will provide additional insights into the mechanism of reaction.

APPENDIX II

STRUCTURE OF *LEISHMANIA DONOVANI* OROTODINE MONOPHOSPHATE DECARBOXYLASE-OROTATE PHOSPHORIBOSYLTRANSFERASE

Summary

The *de novo* biosynthesis of pyrimidine nucleotides is a highly conserved pathway that acts, along with the recycling pathway, to maintain cellular pyrimidine levels. While a small number of micro-organisms lack the *de novo* pathway some, such as *Plasmodium falciparum* (the causative agent of malaria), depend solely on the *de novo* biosynthesis pathway for pyrimidines. The biosynthesis of uridine 5'-monophosphate (UMP) from glutamate requires six enzymatic reactions. The pathway and the enzymes that catalyze the six reactions are shown in Figure A2.1.

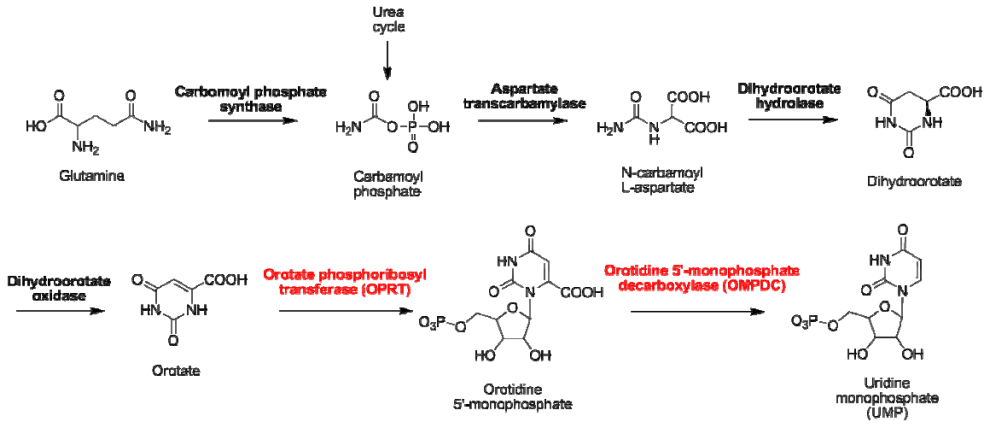

Figure A2.1. Biosynthesis of UMP.

The final two steps of UMP biosynthesis require a transfer of ribose-5-phosphate to orotate and then a subsequent decarboxylation reaction. These reactions are catalyzed by orotate phosphoribosyl transferase (OPRT) and orotidine monophosphate decarboxylase (OMPDC) respectively.

In most prokaryotes OPRT and OMPDC are encoded by separate genes, while in plants and animals these genes are fused and encode a single enzyme called UMP Synthase. A small subset of organisms, including Trypanosomes and Leishmania, also express only a single gene product but the order of the genes is reversed relative to the gene for UMP synthase (Figure A2.2)

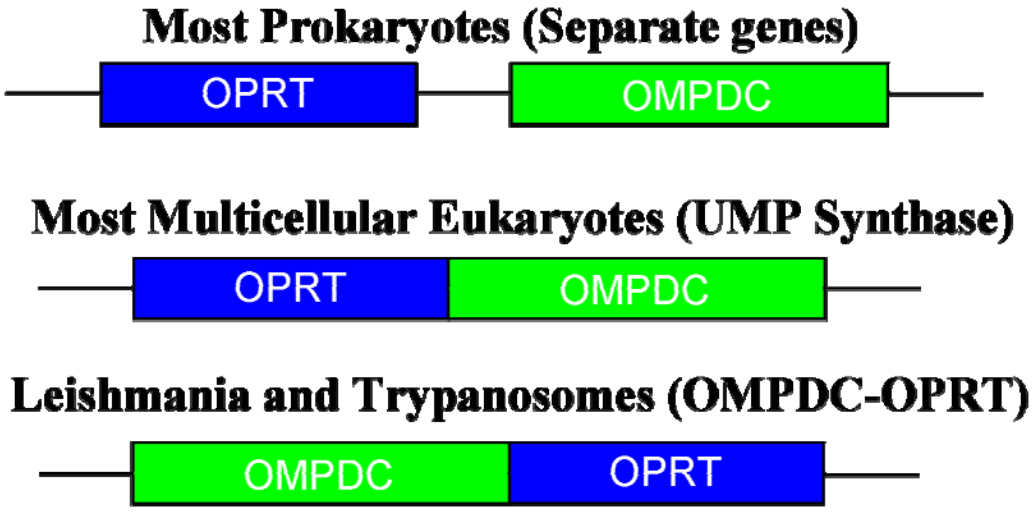

Figure A2.2. Organization of OPRT and OMPDC genes in various organisms.

In order to examine the structural organization of the OMPDC-OPRT enzymes and how this relationship influences function, we solved the structure of the *L. donovani* OMPDC-OPRT bifunctional enzyme in complex with UMP and also that of the truncated protein containing only OMPDC from the same organism.

Experimental

The LdOMPDC-OPRT plasmid was provided by the Ullman lab from Oregon Health and Science University. The plasmid was transformed into BL21 cells and expressed as reported previously (see Chapter 6 or 7, Materials and Methods section). Unfortunately, while the protein expressed well, it was not stable upon buffer exchange into the typical crystallization buffer (10 mM Tris, pH 7.6 and 30 mM NaCl). In order to assure that the protein remained in solution, the purification was

performed under standard conditions with 2 mM DTT and 5 mM UMP added to all buffers. The protein was then either put into trays in the elution buffer (300 mM NaCl, 250 mM imidazole, 5 mM UMP, 2 mM DTT, pH 8.0) or buffer exchanged into a high salt buffer such as 0.1 M Tris, pH 8.0, with 300 mM NaCl, 5 mM UMP and 2 mM DTT.

The protein was crystallized using the hanging drop method and was used at concentrations of 15 - 25 mg/ml. While several conditions gave microcrystals, the only crystals observed with a 3D morphology were under 24 - 38 % PEG-400, 0.2 - 0.4 M NaCl and 0.1 M Hepes, pH 6.8. The crystals were approximately 25 - 100 μm in size and were rectangular or cubic in shape. The crystals were frozen in a solution containing the well solution mentioned above supplemented with 5 mM UMP. Data collection was difficult as the crystals varied in quality and often yielded mosaic data. In addition, the long unit cell access meant that spots were very close together during data collection. By optimizing the detector distance and collecting 0.5° wedges, we were able to collect a complete data set for these crystals that diffracted to approximately 2.9 Å.

All initial attempts to phase using molecular replacement with several homologous structures failed. As a result, SeMet protein was expressed and purified for crystallization trials. Unfortunately, the SeMet crystals did not grow as well as the native and we were unable to collect any usable data from these. In order to facilitate phasing, we then attempted to solve the structure of the two monofunctional proteins, LdOMPDC and LdOPRT. Screens of crystallization conditions for LdOMPDC yielded a large crystal that diffracted well. This crystal grew in 1.6 M ammonium sulfate, 10% 1,4-dioxane and 0.1 M MES monohydrate, pH 6.5. Using this high resolution data from the LdOMPDC crystal and the human OMPDC structure as a model we were able to use molecular replacement to solve the structure. CNS and

Refmac5 were used for refinement, with iterative cycles of manual model building using COOT.

The LdOMPDC structure was used to provide phases for the LdOMPDC-OPRT data by molecular replacement. This enabled the placement of the OPRT domains using yeast OPRT as a model. Using Refmac5 and phenix for refinement, and coot for manual model building, the structure was refined to its current state.

Table A2.1 Data Collection Statistics

	LdOMPDC	LdOMPDC-OPRT
resolution (Å)	1.7	2.99
Wavelength (Å)	0.987	0.987
beam line	24-ID-C	24-ID-C
space group	*C*2	$P4_32_12$
a (Å)	101.38	64.72
b (Å)	98.14	64.72
c (Å)	62.14	477.60
b (°)	106.54	90
no. of reflections	262 430	119 046
unique reflections	62 080	34 461
average I/σ	24.9 (4.4)	11.3 (2.3)
redundancy	4.2 (3.6)	3.5 (1.7)
completeness (%)	98.5 (93.5)	87.7 (39.7)
R_{sym}[a] (%)	6.4 (27.7)	13.1 (37.4)

*these are the statistics from two of the first data sets collected. They are only two examples of many dozens of datasets with resolutions ranging from 1.6 to 2.3 Å
Numbers in parentheses correspond to the highest resolution shell

[a] $R_{\text{sym}} = \Sigma\Sigma_{\text{i}} \left| I_i - \langle I \rangle \right| / \Sigma \langle I \rangle$, where $\langle I \rangle$ is the mean intensity of the *N* reflections with intensities I_i and common indices *h, k, l*

Results

The structure of LdOMPDC-OPRT was solved by MR using the monofunctional LdOMPDC and the yeast OPRT as search models. The data reveals an unusual tetrameric structure shown in Figure A2.3. The presence of this tetramer in solution was verified by size exclusion chromatography (Figure A2.5).

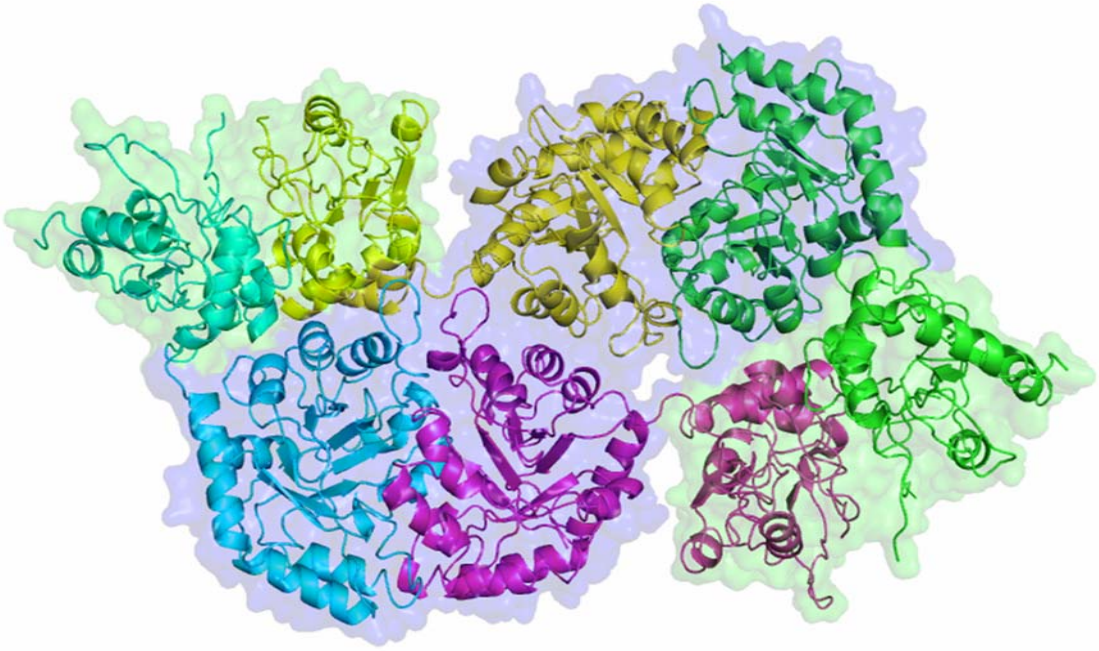

Figure A2.3. *L. donovanii* OMPDC-OPRT overall structure. Individual chains shown in yellow, green, blue and violet, while background surface highlights the two OMPDC dimers in blue and the two OPRT dimers in green

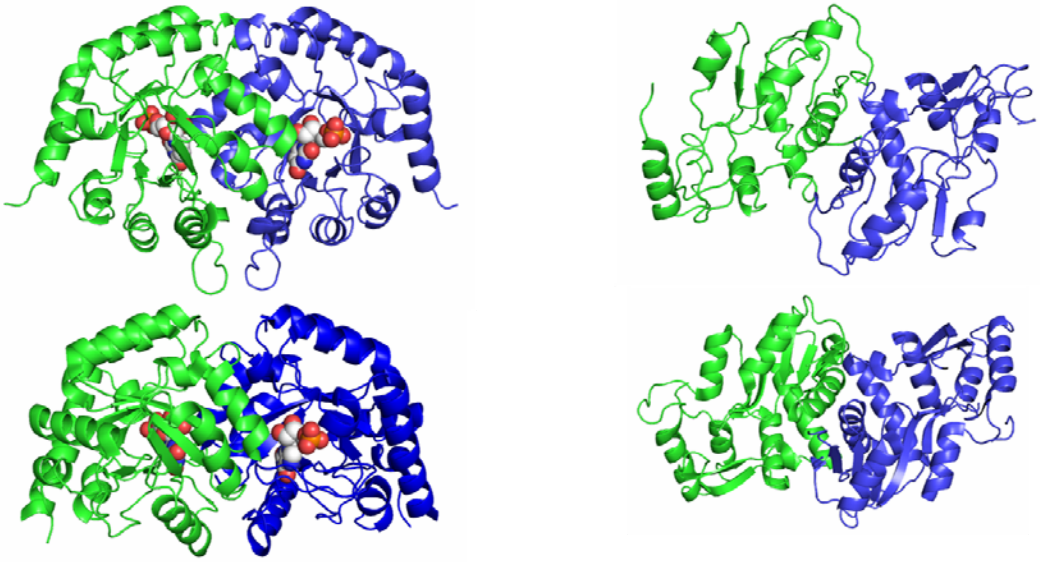

Figure A2.4. *L. donovanii* OMPDC and OPRT dimers compared to homologous enzymes. The OMPDC dimer from *L. donovanii* (top left) is shown above the human homologue (bottom left). Also shown is the *L. donovanii* OPRT dimer (top right) above the homologous enzyme from *S. cerevisiae* (bottom right).

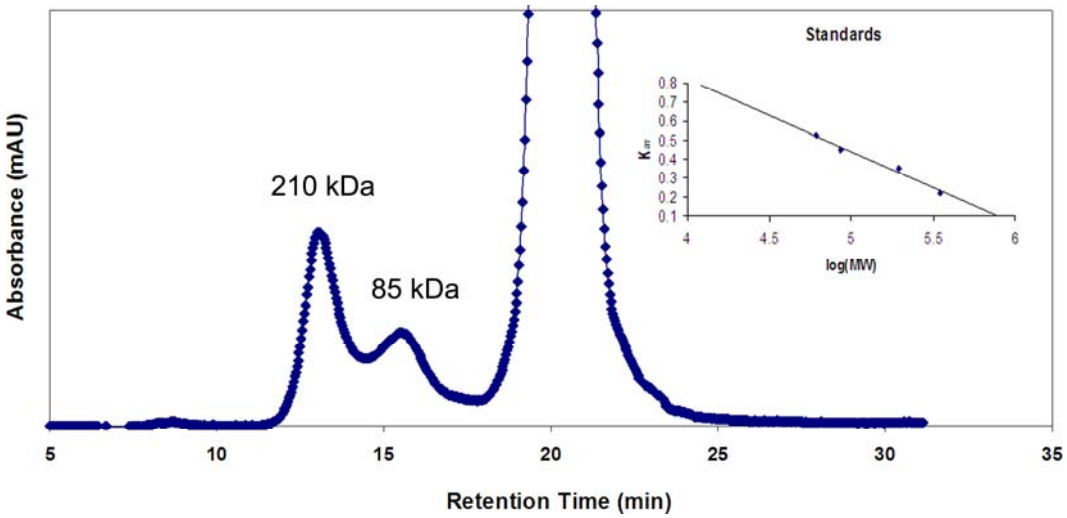

Figure A2.5. Size exclusion chromatography of LdOMPDC-OPRT. Size exclusion chromatography was used to verify the oligomeric state of the protein. The *L. donovani* OMPDC-OPRT fusion monomer has a molecular weight of 53.8 kDa. A peak was observed (210 kDa) that corresponds to a tetrameric species (215.2 kDa expected) as well as a smaller peak (85 kDa) that could be a dimeric state.

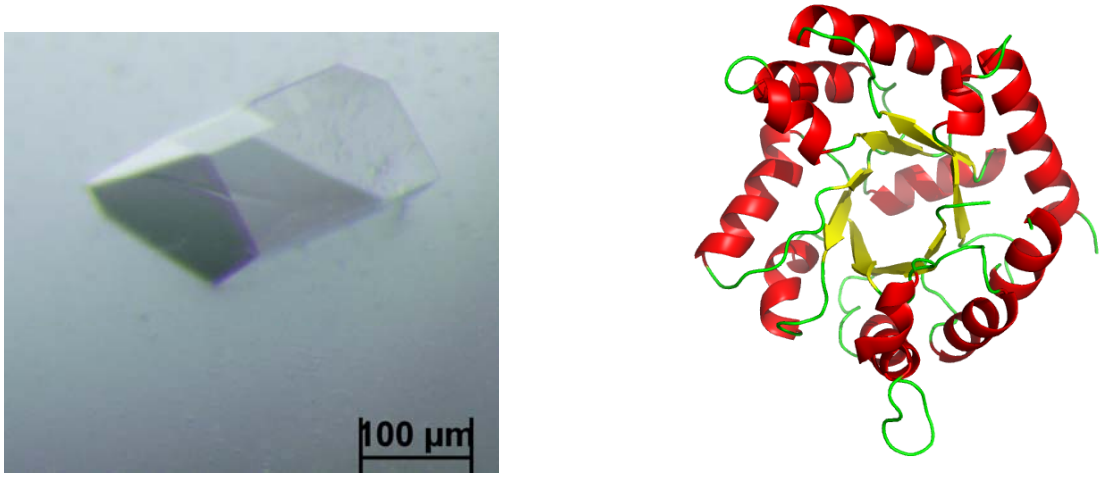

Figure A2.6. Structure of LdOMPDC. In order to use molecular replacement to solve the structure of LdOMPDC-OPRT, a structure of the monofunctional LdOMPDC was solved. The LdOMPDC crystal (left) diffracted to better than 2 Å and allowed for the facile determination of the LdOMPDC structure (right; while the structure was a dimer, only the protomer is shown)

Ongoing Work

The refinement of the structure of LdOMPDC-OPRT is continuing and has nearly converged. In addition, the Human equivalent, HsUMPS, has been purified and will be used to compare the quaternary structures of the two bifunctional enzymes by gel filtration and other means.

APPENDIX III

STRUCTURE OF *SACCHAROMYCES CEREVISIAE* THI20

Summary

Yeast Thi20 is a fusion protein with homology to the bacterial thiaminase, TenA, and to the HMP(P) kinase, ThiD. Although little is know about Thi20, our hypothesis is that it participates in thiamin salvage by catalyzing hydrolysis of HMP precursors. To further understand this protein and its function, we have solved the x-ray crystal structure of the *Saccharomyces cerevisiae* Thi20.

Experimental

Several fungal Thi20 genes were cloned into plasmids, expressed and purified as previously described (see Chapter 6 and 7, Materials and Methods). These constructs, which included *Saccharomyces cerevisiae* Thi20 (ScThi20), *Pichia stipitis* Thi20 (PsThi20) and *Candida glabrata* Thi20 (CgThi20), were expressed with an N-terminal 6-His tag. Of these, only ScThi20 yielded crystals upon screening. The data from these crystals, however, was highly anisotropic and also displayed a high degree of mosaicity. All attempts to optimize the crystallization conditions, cryoprotectants and to find alternative crystallization conditions for these constructs failed. To expand the search, ScThi20 was recloned into a vector with a C-terminal 6-His tag. While screens using this protein were not initially successful, seeding with the crystals formed from the N-terminally tagged ScThi20 yielded diffraction quality crystals. These crystals, formed in 12% PEG 8000, 0.2 M calcium acetate and 0.1 M imidazole, pH 7.5, were diamond shaped and diffracted to approximately 2.7 Å at beamline 24ID-C (data collection statistics provided in Table A3.1).

The ScThi20 structure was solved by molecular replacement using 2GM7 and 1JXH as search models. Molecular replacement in the original space group ($P2_12_12_1$) initially failed, but solutions were found using the subgroup $P2_1$. After a solution was

found in $P2_1$, one fourth of the unit cell (one dimer) was transformed into the higher space group and used without further difficulty. CNS and Refmac5 were used for refinement with manual model building performed using COOT (the refinement statistics are provided in Table A2.2).

Table A3.1 Data Collection Statistics

	ScThi20c
resolution (Å)	2.68
Wavelength (Å)	0.987
beam line	24-ID-C
space group	$P2_12_12_1$
a (Å)	59.70
b (Å)	140.10
c (Å)	143.27
no. of reflections	87 487
unique reflections	31 670
average I/σ	12.2 (1.5)
redundancy	2.8 (1.5)
completeness (%)	92.8 (70.0)
R_{sym}[a] (%)	9.4 (32.9)

[a] $R_{\text{sym}} = \Sigma\Sigma_{\text{i}} \left| I_i - \langle I \rangle \right| / \Sigma \langle I \rangle$, where $\langle I \rangle$ is the mean intensity of the *N* reflections with intensities I_i and common indices *h, k, l*

Table A3. 2 Data Refinement Statistics

	ScThi20c
resolution (Å)	2.68
protein atoms	7902
ligand atoms	0
water atoms	44
reflections in working set	30019
reflections in test set	1606
R factor[a]	24.4
R_{free}[b]	28.9
rmsd bonds (Å)	0.006
rmsd angles ($^{\text{o}}$)	0.974
mean *B* factor (Å^2)	38.6

[a] $R \text{ factor} = \Sigma_{hkl} \left\| F_{obs} \right| - k \left| F_{calc} \right\| / \sum_{hkl} \left| F_{obs} \right|$, where F_{obs} and F_{calc} are observed and calculated structure factors respectively.

[b] For R_{free}, the sum is extended over a subset of reflections (5%) excluded from all stages of refinement

Results

The structure of ScThi20 reveals a dimer (Figure A3.1), a structure which is supported by gel filtration (data not shown). The ThiD portion of ScThi20 dimerizes in a fashion that is similar to known ThiD enzymes (Figure A3.2). The dimer interface between the TenA domains of Thi20, however, is unlike that observed in previously solved TenA structures.

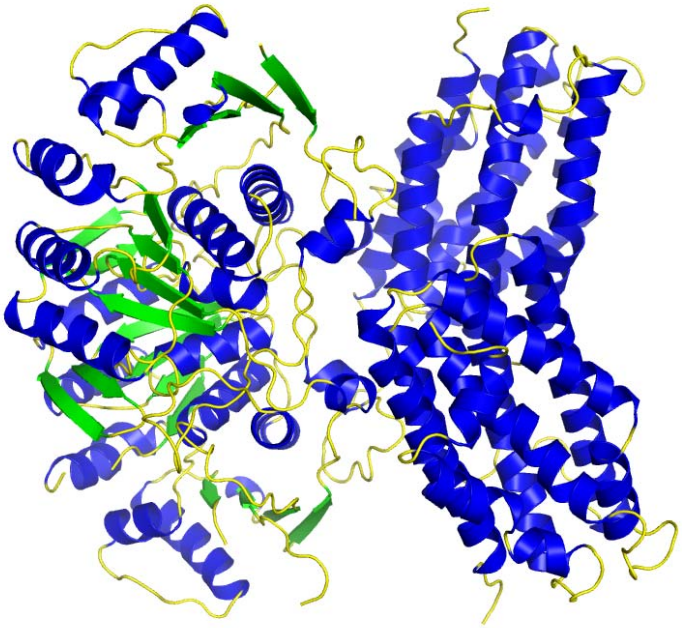

Figure A3.1. Structure of ScThi20. The dimer is shown with helices colored blue and strands colored in green. The ThiD domain is on the left, while the all α-helical domain of TenA is on the right.

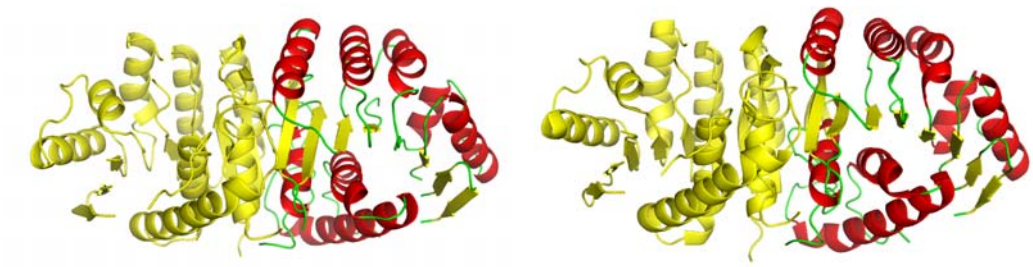

Figure A3.2. Structure of ThiD dimer. The ThiD domain dimer from ScThi20 (left) has a similar interface as that of *S. typhimurium* ThiD (1JXI, right).

Ongoing work

The refinement of ScThi20 is ongoing and is nearly complete. Additional analysis of the structure and comparison to known structures is required in order to learn more about the function of this enzyme. Attempts are underway to improve the quality and diffraction of the ScThi20 crystals and to soak in or co-crystallize ligands.